The University of Nottingham
UNITED KINGDOM • CHINA • MALAYSIA

Development of a Floating Wave Energy Converting Breakwater for Gulf Type Marine Environment

Saad Alsahlawi, MSc

Thesis submitted to The University of Nottingham for the degree of Doctor of Philosophy

March 2017

Abstract

With the increase in human activity associated with the recent rise in Kuwait's oil production, there is greater need for an optimised solution to protect the Kuwaiti coastline and islands from wave attacks and erosion. This thesis describes a programme of research conducted to support the development of a cost-effective method of protecting the Kuwaiti coastline with a breakwater system that also provides an opportunity to generate energy by locally increasing the energy density of waves to make wave energy conversion (WEC) more efficient, cost-effective and commercially competitive.

A comprehensive review of the historical development and current state-of-the-art regarding breakwater and WEC technologies is presented. On the basis of these evaluations, a floating breakwater combined with point absorber device is identified as appropriate for use in the Kuwaiti near shore marine environment. The need for increasing the local energy density at the point absorber is highlighted and the concept of using a parabolic concentrator in combination with point absorber is suggested and developed.

An analytical study extends the understanding of the role of damping in the response of an idealised point absorber device. A steady-state harmonic model is developed to simulate the motion of a single buoy with one degree of freedom (heave) along the vertical axis to optimise its geometrical and control parameters and maximise its power absorption from incident waves. Evaluating different buoy shapes namely: bullet, spike, and bi-cone ($60^o/120^o$) indicates that for each buoy shape, there is an optimum operating range for the power take-off (PTO) that drives the generator where wave energy capture and thus electrical power would be greatest. In the model, comprising a spring-

damper system, the PTO is represented as a damper with a constant damping coefficient (c_1) and the radiation force is represented by a linear radiation damping term (c_2). The model reveals that the best performance is obtained at the optimum value for c_1 which is $c_1 = c_2 = k/\omega$. This condition is met when the buoy with optimum mass is at resonance with the peak frequency of the sea state at $\omega^2 = k/m$. Evaluating the power absorption as a function of c_2 in the model also reveals that at resonance, a buoy of any shape will have two types of behaviour: one driven by low radiation damping and the other by high radiation damping range of values. Operation in the low c_2 region is difficult to achieve in practice, and hence, it is recommended that devices should be designed to operate in the high c_2 region to maximise power capture.

Data is presented from wave tank testing conducted using a flume at the Kuwaiti Institute for Scientific Research (KISR). This is used to evaluate the capability of the proposed parabolic concentrator elements to increase potential wave energy harvesting. A wealth of data, both visualisation and numerical, was obtained and this compares well with the computational analyses. The results indicate that a parabola-buoy system would be capable of absorbing almost 260 kW of power at prototype scale (1:16).

A computational modelling approach using the commercial CFD code ANSYS-Fluent is developed, applying the volume of fluid approach combined with a wave boundary condition. The KISR wave tank was modelled with parabolic element installed and data is compared to that obtained experimentally. Good agreement between CFD and experimental data is obtained validating the modelling choices made. Additional modelling results for the behaviour of waves near an anchored buoy in combination with a parabolic concentrator are presented.

The work presented in this thesis shows that there is the potential for substantial benefit for power absorption through using a combined parabolic concentrator-point absorber device. Future modelling work with fluid-structure interaction and moving buoy will permit further optimisation and development paving the way for full-scale developments in the future.

Declaration of Originality

I hereby declare that the research conducted in this thesis and the thesis itself was composed and originated entirely by myself in the Mechanical Engineering Department at the University of Nottingham, unless otherwise stated. This work has not been submitted for any other degree or professional qualification.

Saad Alsahlawi

Acknowledgements

I would like to thank Kuwait Petroleum Cooperation (KPC) for the financial support they have provided throughout this project.

I would like to express my gratitude to my supervisors Prof Seamus Garvey and Dr. Kathy Simmons for their invaluable guidance and support at every stage of this project. I would also like to thank Dr. Ropes Patel and Dr. Bruce Kakimpa for sharing their technical expertise and for being a great source of knowledge precisely at the times I needed them most.

In addition, I would like to thank Kuwait institute for scientific research (KISR) represented by Dr. Neelamani Subramaniam and his team for letting me use their facility for the experimental work. I would also like to extend my thanks to the University of Nottingham for providing me with this opportunity.

Special thanks to my family and wife for their constant support and encouragement throughout this experience.

Finally, I dedicate this thesis to my precious daughters Kadi and Taleen for their unconditional love.

Contents

Development of a Floating Wave Energy Converting Breakwater for Gulf Type Marine Environment **1**
Abstract ..... **i**
Declaration of Originality ..... **iv**
Acknowledgements ..... **v**
Contents ..... **vi**
List of Figures ..... **x**
List of Tables ..... **xvi**
List of Abbreviations and Terms Used ..... **xvii**
Chapter 1: Introduction **1**
1.1. Background and Motivation for the Work 1
1.2. Research Objectives and Approach 5
1.3. Outline of Thesis Content 6
Chapter 2: Literature Review: Breakwaters and Wave Energy Converters (WECs) **11**
2.1. Introduction 12
2.2. Breakwaters 12
2.3. Floating Breakwaters 18
2.3.1. History of Floating Breakwaters 18
2.3.2. Development of Floating Breakwaters 19
2.3.3. Classification of Floating Breakwaters 24
2.3.4. Floating Breakwater Applications 25
2.3.5. Floating Breakwater Economic Considerations 28
2.3.6. Floating Breakwater Potential for Kuwait 31
2.4. Ocean Wave Energy 34
2.4.1. Wave Energy Converters (WECs) 37
2.4.2. Wave Energy Extraction 41
2.5. Floating Breakwater-WEC Integration 48
2.5.1. Potential Application for Kuwait 54
2.5.2. Cost Sharing 58
2.6. Conclusions 61

Chapter 3: Steady-State Harmonic and Time Domain Point Absorber Modelling 63
3.1. Literature Review 65
3.2. Background Theory 72
3.2.1. Ocean Wave Characteristics 72
3.2.2. Linear Wave Theory 74
3.2.3. Dynamics of a Floating Body in Regular Waves 75
3.2.4. Mass-Spring-Damper System 78
3.2.5. Point Absorber System Features 79
3.3. Generalised Heaving Point Absorber (Buoy) Model 81
3.3.1. Mass-Spring-Damper Representation 81
3.3.2. Newton's Second and Third Laws 82
3.4. Time Domain Model 84
3.4.1. Equation of Motion of a Heaving Point Absorber 84
3.4.2. Power and Energy 86
3.5. Steady-State Harmonic Model 88
3.5.1. Equation of Motion 88
3.5.2. Power Absorption 90
3.5.3. Power Absorption Optimisation 90
3.5.4. Results and Findings 92
3.6. Validation of Steady-State Harmonic Model 94
3.6.1. Power Absorption Optimisation 94
3.6.2. Results and Findings 97
3.7. Steady-State Harmonic Model Optimisation 98
3.7.1. Results and Findings 98
3.8. Buoy Shape Optimisation 102
3.8.1. Statistical Analysis 107
3.8.2. Buoy Power Optimisation 112
3.8.3. Results and Findings 113
3.9. Conclusions 116
Chapter 4: Experimental Wave Flume Tank Testing 119
4.1. Theoretical Background 120
4.1.1. Power Absorption 120
4.1.2. Fourier Series for Analysing Wave Tank Behaviour 122
4.1.3. Froude Scale Ratio 123
4.2. Outline of Experimental Work 124
4.3. Experimental Setup and Measurement 127

4.3.1. Wave Flume Tank 127
4.3.2. Wave Conditions Generated 130
4.3.3. Measurement Instrumentation 133
4.3.4. Calibration 139
4.3.5. Data Acquisition and Collection 140
4.4. Stage-1: Experimental Wave Tank Tests 145
4.4.1. Parabolic Concentrator 145
4.4.2. Stage-1 Test Setup 146
4.4.3. Stage-1 Results 148
4.4.4. Stage-1 Discussion 152
4.4.5. Stage-1 Findings 156
4.5. Stage-2: Point Absorber (Buoy) 157
4.5.1. Stage-2 Buoy Geometry 157
4.5.2. Stage-2 Test Setup 164
4.5.3. Stage-2 Decay Test 166
4.5.4. Stage-2 Results 169
4.5.5. Stage-2 Discussion 172
4.5.6. Stage-2 Findings 174
4.6. Stage-3: Parabolic Concentrator-Point Absorber (Buoy) 175
4.6.1. Stage-3 Test Setup 175
4.6.2. Stage-3 Results 176
4.6.3. Stage-3 Discussion 181
4.6.4. Stage-3 Findings 184
4.7. Conclusions 185
Chapter 5: Computational Fluid Dynamics (CFD) Modelling 188
5.1. Computational Fluid Dynamics (CFD) 189
5.1.1. Computational Fluid Dynamics (CFD) Development 189
5.2. Computational Fluid Dynamics (CFD) Methodology 193
5.2.1. Convergence 193
5.2.2. Boundary Conditions 194
5.2.3. Turbulence 195
5.3.1. Wave generation 200
5.3.2. Mesh Selection 203
5.4. CFD Wave Tank Model 204
5.4.1. Geometry Setup 204
5.4.2. Boundary Conditions 207
5.4.3. Mesh 207

5.4.4. Mesh Sensitivity Study 209
5.4.5. Parabola CFD Model Validation 219
5.5. CFD Wave Tank Model with Buoy 223
5.5.1. Geometry Setup 223
5.5.2. Boundary Conditions 224
5.5.3. Forces 224
5.5.4. Mesh 225
5.5.5. Results for Parabola-Static Buoy Mesh Sensitivity Study 226
5.6. CFD Results for Static Buoy 228
5.7. Future CFD Modelling 239
5.8. Conclusions 241
Chapter 6: Conclusions and Further Research 243
6.1. Main Achievements 243
6.2. Contributions to Knowledge 246
6.3. Project Cost 247
6.3.1. Capital Cost 247
6.3.2. Shipping 249
6.3.3. Installation 249
6.3.4. Operation and Maintenance Cost 250
6.3.5. Mid-life Overhaul 251
6.3.6. Decommissioning 251
6.3.7. Total Lifetime Cost 252
6.4. Future Work 252
References 255
Appendices 277
Appendix 3A 277
A3.1 Time Domain Model 277
A3.2 Steady-State Harmonic Model 281
A3.3 Verification of Steady-State Harmonic Model 283
A3.4 Steady-State Harmonic Model Optimisation 288
Appendix 4A: Hydraulic Motor Calculation 292
Appendix 4B: Calibration Data For Waveprobes 1-6 294
Appendix 4C: Decay Test Results For Each Buoy Shape 296

List of Figures

Fig. 1.1: Location of Kuwait in Arabian Gulf (a) (Baby S., 2011) and Kuwaiti territorial water (b) (Neelamani et al., 2007) 3
Fig. 1.2: Flowchart of the thesis content and chapters 8
Fig.2.1: Steps in selection of breakwater type (Burcharth, 2009) 16
Fig. 2.2: Breakwater type for typical range of wave height and period (PND Engineers Inc., 2015) 17
Fig. 2.3: Protection of offshore crude oil loading terminals 26
(Neelamani and Al Banna, 2017) 26
Fig. 2.4: Floating breakwater used for erosion protection of an island (Neelamani and Al Banna, 2017) 27
Fig. 2.5: Floating breakwater used for marina protection 28
(Neelamani and Al Banna, 2017) 28
Fig. 2.6: Comparison of breakwater costs per running metre as a function of water depth (Fousert, 2006) 29
Fig. 2.7: Capital costs vs safety of breakwaters (Burcharth, 2009) 31
Fig. 2.8: Parabolic concentrator focal point (www.physicsclassroom.com) 33
Fig. 2.9: Global distribution of average annual wave power in kW/m of crest length for various locations around the world (Mamun et al., 2010) 35
Fig. 2.10: Kuwaiti territorial waters (Neelamani et al., 2007) 35
Fig. 2.11: Classification of wave energy converter systems (Hagerman, 1995) 39
Fig. 2.12: Classification according to: (a) location (b) size, orientation and energy-extracting method (adapted from Falnes, 2006) 41
Fig. 2.13: Pelamis (Oregon State University, 2011) 43
Fig. 2.14: PowerBuoy (Ocean Power Technologies, 2011) 44
Fig.2.15: LIMPET OWC (The Queen's University of Belfast, 2002) 44
Fig.2.16: Left: Oyster (Aquamarine Power), top right: WaveRollers (AW-Energy Ltd.) and bottom right: Oceanus 2 (Seatricity) 47
Fig. 2.17: Parabolic focusing device (Denniss, 2007) 51
Fig. 2.18: Moving curved CCell paddle (http://www.ccell.co.uk) 52
Fig. 2.19: CCell paddle operation (http://www.ccell.co.uk) 52
Fig. 2.20: Curved CCell paddle (http://www.ccell.co.uk) 54

Fig. 2.21: The hourly variation (a) and probability density (b) of wave power around Qaru Island for 3 years (Neelamani, 2009) 56
Fig. 2.22: Material ratio flat/CCell structure 60
Fig. 3.1: Power transfer in a generic WEC (Price, 2009) 66
Fig. 3.2: Ocean wave characteristics (Anon, 1984) 72
Fig. 3.3: Wave depth propagation (www.slideplayer.com) 73
Fig. 3.4: Definition of the 6 degrees of freedom (Journee and Massie, 2001) 75
Fig. 3.5: Superposition of hydromechanical and wave loads 77
(Journee and Massie, 2001) 77
Fig. 3.6: Basic design of a point absorber system 80
Fig. 3.7: Motion curves of an underdamped, overdamped and critically damped system (De Backer, 2008) 81
Fig. 3.8: Schematic representation of mass-spring-damper system (modified from Price, 2009) 82
Fig. 3.9: Newton's second and third laws applied to a buoy moving in heave motion (Price, 2009) 83
Fig. 3.10: Schematic representation of the simulated heaving point absorber in the time domain model (Modified from Price, 2009) 85
Fig. 3.11: Power capture by a point absorber (Price, 2009) 87
Fig. 3.12: Schematic representation of a heaving point absorber in the steady-state harmonic model (Modified from Price, 2009) 88
Fig. 3.13: Power capture at $\boldsymbol{c1} = 1592.50$ Ns/m and $\boldsymbol{m} =$ (a) 100 kg (b) 253.4549 kg and (c) 500 kg 93
Fig. 3.14: Power capture at $\boldsymbol{m} = 253.4549$ kg and $\boldsymbol{c1} = 1592.50$ Ns/m 95
Fig. 3.15: Maximum power absorption vs $\boldsymbol{c1}$ and $\boldsymbol{c2}$ at $\boldsymbol{m} = 1783.33$ kg ... 97
Fig. 3.16: Maximum power capture model difference (%) at $\boldsymbol{m} = 1783.33$ kg 98
Fig. 3.17: Power capture at $\boldsymbol{c1} = 6.54 \times 10^5$ Ns/m and $\boldsymbol{c2} = 6.54 \times 10^5$ Ns/m 99
Fig. 3.18: Contour plot for the relationship between $\boldsymbol{c1}$ and $\boldsymbol{c2}$ at $\boldsymbol{m}$ 99
Fig. 3.19: Log power vs c_1 and c_2 at $\boldsymbol{m} = 253.4549$ Kg 100
Fig. 3.20: The relationship between $\boldsymbol{c1}$ and $\boldsymbol{c2}$ with $\boldsymbol{m}$ 101
Fig. 3.21: Shapes and dimensions of prototype buoys 103
Fig. 3.22: Profiles of $\boldsymbol{c2}$ for the bullet buoy 110
Fig. 3.23: Profiles of $\boldsymbol{c2}$ for the spike buoy 111

Fig. 3.24: Profiles of $c2$ for the bi-cone buoy 112
Fig. 3.25: Mean $c2$ for the bullet, spike and bi-cone buoys..... 114
Fig. 3.26: Maximum power capture at $c2$ for zero damped buoys 115
Fig. 4.1: Schematic of wave flume tank and position of parabola 128
Fig. 4.2: Stages of wave flume tank testing 129
Fig. 4.3: Wave flume tank facility and data acquisition setup at KISR 130
Fig. 4.4: Wave probes in the concrete flume tank measuring regular waves for wave characterisation 134
Fig. 4.5: Potentiometer mounted on the frame at the concrete flume tank 135
Fig. 4.6: Load cells to measure forces acting on the buoy..... 136
Fig. 4.7: PTO motor system 137
Fig. 4.8: Polystyrene beads scattered around the area of interest..... 138
Fig. 4.9: Reflection analysis: data acquisition time selection of a suitable window for the wave analysis..... 142
Fig. 4.10: Types of wave reflection: longitudinal and cross waves..... 142
Fig. 4.11: Incident wave height: data acquisition time selection of a suitable window for the wave analysis with wave probes WP1, WP2 & WP3 144
Fig. 4.12: Incident wave height: data acquisition time selection of a suitable window for the wave analysis with wave probes WP4, WP5 & WP6 145
Fig. 4.13: Proposed design for shallow parabolic concentrator (Model 1) 147
Fig. 4.14: Proposed design for deep parabolic concentrator (Model 2) ... 147
Fig. 4.15: Fabrication and installation stages of parabola models at KISR: a) fabrication of stainless steel beams structure b) Fabrication of parabola stainless steel sheet c-d) Installation of parabola structure 148
Fig. 4.16: Parabola-1 response (a), Parabola-2 response (b)..... 151
Fig. 4.17: Photographs of the maximum wave amplification zones for parabola models 1&2 152
Fig. 4.18: Parabola-1 and parabola-2 model responses-(a, b, c, d)..... 154
Fig. 4.19: Bi-cone ($60^o/120^o$) buoy shape (model scale in mm) 161
Fig. 4.20: Zero damped, damped and extra damped bullet buoy 162
Fig. 4.21: Zero damped, damped and extra damped spike buoy..... 163
Fig. 4.22: Test Setup for point absorber (buoy) and the heaving mechanism 164
Fig. 4.23: Schematic of test setup for the cable and pulley arrangement. 166
Fig. 4.24: Experimental setup of cable and pulley arrangement 166

Fig. 4.25: Measured zero damped buoy position during decay test and curve fit 167
Fig. 4.26: Measured half damped buoy position during decay test and curve fit 168
Fig. 4.27: Measured fully damped buoy position during decay test and curve fit 168
Fig. 4.28: Efficiency of power absorption, η , (%) as a function of wave period (a,b and c) 170
Fig. 4.29: Power absorbed by the buoy (W) as a function of wave height (a, b, c) 171
Fig. 4.30: Test setup for parabolic concentrator-point absorber and motion tracking using orange polystyrene beads 176
Fig. 4.31: Efficiency of power absorption, η , (%) as a function of wave period for parabolic concentrator-point absorber (a,b, c, and d) 178
Fig. 4.32: Power absorbed by the buoy (W) as a function of wave height for parabolic concentrator-point absorber-(a,b,c) 179
Fig. 4.32-(d,e): Power absorbed by the buoy (W) as a function of wave height for parabolic concentrator-point absorber 180
Fig. 4.33: Comparison of power absorbed by the buoy (W) as a function of wave height (H = 0.09 m) for parabola 1 and 2 for the same location 180
Fig. 5.1: Schematic of wave tank dimensions 206
Fig. 5.2: Wave tank schematic representation 207
Fig. 5.3: 3D hexahedral structured mesh for wave tank model 208
Fig. 5.4: Plan and isometric views of the 3D hexahedral structured mesh grid 209
Fig. 5.5: Meshing in the interface region 210
Fig. 5.6: Surrounding rough grid for air and water regions 211
Fig. 5.7: Meshing in the vicinity of the parabola-1 amplification zone 212
Fig. 5.8: Calculated air velocity time histories at the focal point from mesh sensitivity study 213
Fig. 5.9a: Calculated water velocity time histories at the focal point from mesh sensitivity study 214
Fig. 5.9b: Calculated water pressure time histories at the focal point from mesh sensitivity study 215
Fig. 5.10: Predictions of wave height at 11 m from mesh sensitivity study 217

Fig. 5.11: Calculated wave height at amplification zone from mesh sensitivity study 218
Fig. 5.12: Physical model wave height at 11m (black) and at amplification zone (pink) 220
Fig. 5.13: 4300 k CFD model wave height at 11m (black) and at amplification zone (red) 220
Fig. 5.14: CFD predictions for pressure contours in the wave tank 222
Fig. 5.15: Physical model bi-cone ($60^o/120^o$) buoy dimensions 224
Fig. 5.16: CFD model bi-cone ($60^o/120^o$) buoy volume fraction contour plot 224
Fig. 5.17: Plan and side views of the wave tank with buoy mesh 225
Fig. 5.18a: Calculated lift force from models with 8 M and 10 M cells 227
Fig. 5.18b: Calculated drag force from models with 8 M and 10 M cells .. 228
Fig. 5.19a: CFD predictions for wave height at amplification zone 229
Fig. 5.19b: CFD predictions for lift and drag forces 229
Fig. 5.20a: Wave height at amplification zone from t = 48 to t = 52 s 229
Fig. 5.20b: Lift and drag force from t = 48 to t = 52 s 230
Fig. 5.21: Pressure and shear stress contours for the static bi-cone ($60^o/120^o$) buoy 231
Fig. 5.22a-b: (a) Wave-buoy interaction response (b) 3D wave tank contours at t = 49.05 s 232
Fig. 5.22c: Wave- buoy vectors of interface velocity field (left). LIC visualisation of the velocity field, coloured by the volume fraction of water on a vertical plane in the middle of the domain (right) at t=49.05 s 233
Fig. 5.23a-b: (a) Wave-buoy interaction response (b) 3D wave tank contours at t = 49.35 s 234
Fig. 5.23c: Wave- buoy vectors of interface velocity field (left). LIC visualisation of the velocity field, coloured by the volume fraction of water on a vertical plane in the middle of the domain (right) at t = 49.35 s 234
Fig. 5.24a-b: (a) Wave-buoy interaction response (b) 3D wave tank contours at t = 49.60 s 235
Fig. 5.24c: Wave- buoy interface vectors of interface velocity field (left). LIC visualisation of the velocity field, coloured by the volume fraction of water on a vertical plane in the middle of the domain (right) at = 49.60 s 236
Fig. 5.25a-b: (a) Wave-buoy interaction response (b) 3D wave tank contours at t = 49.90 s 237

Fig. 5.25c: Wave- buoy interface vectors of interface velocity field (left). LIC visualisation of the velocity field, coloured by the volume fraction of water on a vertical plane in the middle of the domain (right) at = 49.90 s..... 237
Fig. 5.26a-b: (a) Wave-buoy interaction response (b) 3D wave tank contours at t = 50.1 s 238
Fig. 5.26c: Wave- buoy interface vectors of interface velocity field (left). LIC visualisation of the velocity field, coloured by the volume fraction of water on a vertical plane in the middle of the domain (right) at t = 50.1 s..... 238
Fig. 5.27: velocity contour of y-plane wave tank with buoy..... 239
Fig. 5.28: Buoy motion in heave during stage-2 experimental testing..... 240

List of Tables

Table 2.1: Cost estimates in British Pounds (£) (Neelamani and Al-Banna, 2017) 30
Table 2.2: Classification of wave energy device processes (Source: Brooke (2003) with reference to Hagerman (1995) Figure 2.23) 40
Table 3.1: Classification of propagation environment (Anon, 1984)..... 73
Table 3.2: Buoy Shape Selection Criteria..... 104
Table 3.3: Bullet, spike and bi-cone decay tests and statistical results.... 109
Table 3.4: Probability of damping reduction (%) for different buoy shapes 109
Table 4.1: Scale ratio for Froude models (Heller, 2011) 124
Table 4.2: Experimental wave tank tests outline. All experiments were carried out at the Kuwait Institute for Scientific Research..... 126
Table 4.3: Joint distribution of significant wave height and mean wave period for location 1 in Kuwaiti territorial waters (number of occurrences over 12 years) (Neelamani et al., 2007) 131
Table 4.4: Regular wave testing conditions at prototype and model scales 132
Table 4.5: Wave probe calibration constants 139
Table 4.6: Experimental data from parabola-1 and parabola-2 tests 149
Table 4.7 Bi-cone ($60^o/120^o$) buoy dimensions (prototype and model) 160
Table 5.1: Characteristics of generated waves..... 207
Table 5.2: Outline of all input parameters in the mesh sensitivity study for the wave tank parabola model 211
Table 5.3: Mesh sensitivity study results (P = pressure, V = velocity)..... 216
Table 5.4: Percentage difference in wave height calculated during the mesh sensitivity study from the 6900 k mesh case 219
Table 5.5: Outline of all input parameters in the mesh sensitivity study for the wave tank model with buoy 226
Table 5.6: Drag and lift forces in the mesh sensitivity study for the wave tank model with buoy 227
Table 6.1: Parabolic concentrator-buoy device capital cost summary 250
Table 6. 2: Total lifetime cost of parabolic concentrator-buoy device 252

List of Abbreviations and Terms Used

Abbreviations

CFB	Cylindrical floating breakwater
CFD	Computational fluid dynamics
CROWN	Circular ramp overtopping wave energy converter
CSF	Continuum surface force
CWR	Capture width ratio
DBFB	Double barrier floating breakwater
DHI	Danish Hydraulic Institute
DPM	Discrete phase model
FB	Floating body
FBT	Floating breakwater with trusses
FBW	Floating breakwater
FE	Finite element
FEM	Finite element method
FFB	Flexible floating breakwater
FPM	Fine point method
FVM	Finite volume method
HRIC	High resolution interface capturing
KISR	Kuwait Institute of Scientific Research
LIC	Line integral convolution
LSM	Level set method
MCFB	Mesh cage floating breakwater
NS	Navier–Stokes

OWC	Oscillating water column
PFB	Porous floating breakwater
PFEM	Particle finite element modelling
PIV	Particle image velocimetry
PTO	Power take off
RANS	Reynolds averaged Navier–Stokes
RBF	Radial basis functions
RNG	Renormalisation group
SIMPLE	Semi-implicit method for pressure-linked equations
SPH	Smooth particle hydrodynamics
UDF	User defined function
VLFS	Very large floating structure
VOF	Volume of fluid
VOF-LES	Volume of fluid – large eddy simulation
WEC	Wave energy converter

Symbols

Wave parameters

A	Wave amplitude [m]
AF	Amplification factor
A_w	Area occupied by the buoy in the sea water [m^2]
C	Wave speed [m/s]
D	Water depth [m]
B_d	Buoy draft [m]
D	Waterline diameter of buoy [m]
D_{ij}	Diameter of maximum amplification zone [m]
E	Energy stored in waves per unit of sea surface [J/m^2]

$\overline{E}$	Total energy stored in waves per unit area of sea surface [J/m^2]
F	Wave frequency [Hz]
F_i	Force in the heaving direction [N]
$f(t)$	Signal in the time domain
l	Distance from the wave maker to WP1 [m]
k_n	Wave number (2π / λ)
G	Acceleration due to gravity [m/s^2]
H	Wave height [m]
H_f	Amplified wave height [m]
H_g	Significant wave height [m]
H_i	Incident wave height [m]
H_{model}	Wave height at model scale [m]
$H_{prototype}$	Wave height at prototype scale [m]
H_r	Reflected wave height [m]
H_T	Total cylinder height [m]
L	Wave length [m]
L_{ac}	Length from the centre of the parabola to the centre of the maximum [m]
L_o	Deep water wave length [m]
L_{fe}	Length from edge of parabola to centre of maximum amplification zone [m]
L_{fc}	Length from centre of parabola to centre of maximum amplification zone [m]
L_{Tank}	Width of flume tank in power calculations [m]
P	Power in the wave front [W]
P_a	Power absorbed by a heaving buoy [W]
P_i	Average incident wave power per unit crest width[W/m]
R_c	Reflection coefficient
T	Wave period [s]
T_i	Incident wave period [s]

T_{model}	Wave period at model scale [s]
T_p	Periodic time of the wave in Fourier Series [s]
$T_{prototype}$	Wave period at prototype scale [s]
T	Time [s]
t_s	Signal time [s]
v_i	Buoy velocity in the heaving direction [ms^{-1}]
V_{out}	Output voltage [V]
v_g	Group velocity of waves [ms^{-1}]
λ	Froude scaling factor
η	Absorption efficiency [%]
ρ	Density [kg/m^3]
ω	Wave angular frequency [rad/s]
ω_a	Natural angular frequency [rad/s]
ω_n	Natural resonance frequency of the device [rad/s]
ω_i	Incident wave frequency [rad/s]

Newtonian mechanics terms

A_M	Added mass matrix
C_M	Hydrodynamic damping coefficient matrix
$\overrightarrow{f}$	Excitation force [N]
$\overrightarrow{F}$	Resultant external force [N]
$\overrightarrow{H}$	Instantaneous angular momentum [Nms]
K_M	Hydrodynamic spring constant matrix
M	Mass [kg]
M_M	Mass and inertia matrix
$\overrightarrow{M}$	Resultant external moment [Nm]
T	Time [s]
$\overrightarrow{U}$	Instantaneous velocity [m/s]

$\vec{\ddot{y}}$	Acceleration [m/s^2]
$\vec{\dot{y}}$	Velocity [m/s]
$\vec{y}$	Location with respect to reference frame [m]

Analytical modelling terms

A	Amplitude of excitation force [m]
A_w	Area occupied by the buoy in sea water [m^2]
c	Damping coefficient [Ns/m]
c_1	PTO damping coefficient [Ns/m]
$\tilde{c}_1$	Optimum PTO damping coefficient [Ns/m]
c_2	Radiation damping coefficient [Ns/m]
$\tilde{c}_2$	Optimum radiation damping coefficient [Ns/m]
c_a	Actual damping coefficient [Ns/m]
c_c	Critical damping coefficient [Ns/m]
$f(t)$	Force across damper [N]
F_{exc}	Wave excitation force [N]
F_{net}	Net force [N]
F_{PTO}	PTO damping force [N]
F_{rad}	Radiation force [N]
F_{res}	Restoring force [N]
F_{spring}	Mechanical spring force [N]
G	Acceleration due to gravity [m/s^2]
K	Spring constant, used to represent buoyancy-stiffness [N/m]
M	Mass [kg]
$\tilde{m}$	Optimum mass [kg]
P	Power absorbed by the PTO [W]
S	Standard deviation in results
T	Time [s]

$u(t)$	Wave vertical velocity [m/s]
V	Velocity across damper [m/s]
$x(t)$	Wave displacement [m]
Y	Vertical displacement [m]
$\dot{y}$, v	Vertical velocity [m/s]
$\ddot{y}$, $\dot{v}$	Vertical acceleration [m/s^2]
ξ	Damping ratio
λ	Frequency of displacement for calculating time constant
ϕ	Amplitude of displacement for calculating time constant
τ	Time constant representing time to settle to steady state
η	Overall power absorption efficiency [%]
ω_α	Angular frequency of excitation force [rad/s]

CFD

A	Wave amplitude [m]
A_c	Wave amplitude at the crest [m]
A_t	Wave amplitude at the trough [m]
C	Wave speed [m/s]
F_D	Drag force [N]
F_L	Lift force [N]
F_γ	Side force [N]
G	Acceleration due to gravity [m/s^2]
H	Generated wave height [m]
k_i	Curvature from the surface normal
k_n	Wave number
L	Wave length [m]

L_c	Characteristic length in Reynolds no. calculations [m]
N_{faces}	Number of faces on the cell
P_p	Pressure [Pa]
P_{Total}	Total pressure [Pa]
P_s	Static pressure [Pa]
S	Source term
σ_{ij}	Surface tension coefficient
T	Time [s]
T	Wave period [s]
u_a	Time averaged velocity [m/s]
U_f	Volume flux through the face
M	Kinematic viscosity [Ns/m^2]
μ_t	Eddy viscosity [Ns/m^2]
α	Volume fraction [%]
v_a	Absolute dynamic viscosity [Ns/m^2]
V_c	Control volume [m^3]
V_{cell}	Cell volume [m^3]
ϕ	Scalar variable
ρ	Volume average density [kg/m^3]
ω	Wave angular frequency [rad/s]
ω_e	Effective wave frequency [rad/s]
$\hat{\chi}$	Reference wave propagation direction
$\hat{y}$	Direction opposite to gravity
$\hat{z}$	Direction normal to $\hat{x}$ and $\hat{y}$
$z(t)$	Buoy motion at damped oscillation [m/s]

Chapter 1: Introduction

This thesis describes a programme of research conducted to support the development of a cost-effective method of protecting the Kuwaiti coastline with a breakwater system that also provides an opportunity to generate energy at this site, by locally increasing the energy density of waves to make wave energy conversion more efficient, cost-effective and commercially competitive.

1.1. Background and Motivation for the Work

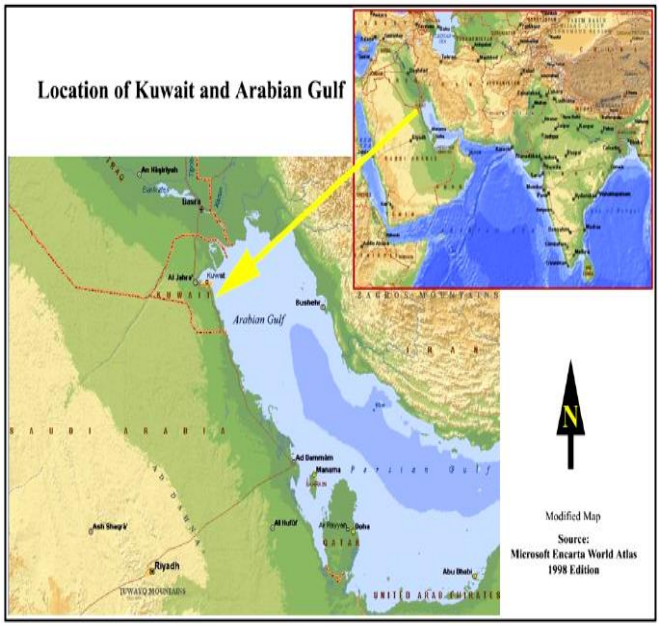
The recent growth of the world's population combined with the rise in living standards has led to an increase in global energy usage since the beginning of this century. Concerns over global warming have prompted an urgent search for alternative energy sources to meet global demands in the near future and for generations to come. Renewable energy resources represent one the best hopes for reducing mankind's contribution to global warming and meeting global demands for energy (Krupp and Horn, 2008). Renewable energy can be defined as "energy obtained from natural and persistent flows of energy occurring in the immediate environment" (Twidell and Weir, 2006). There are numerous types of renewable energy available including solar, wind, geothermal, biomass fuel and ocean waves. Compared to wind and solar energy, ocean wave energy presents considerable technical advantages, because it is more predictable, persistent and spatially concentrated (Clement et al., 2002). The oceans are a vast and powerful source of energy which could potentially be harnessed to supply more than enough energy to meet worldwide demand for electricity (Pelc and Fujita, 2002). Ocean wave energy may not be the sole solution to global warming problems, but it

has the capability to make a substantial contribution towards future energy supply.

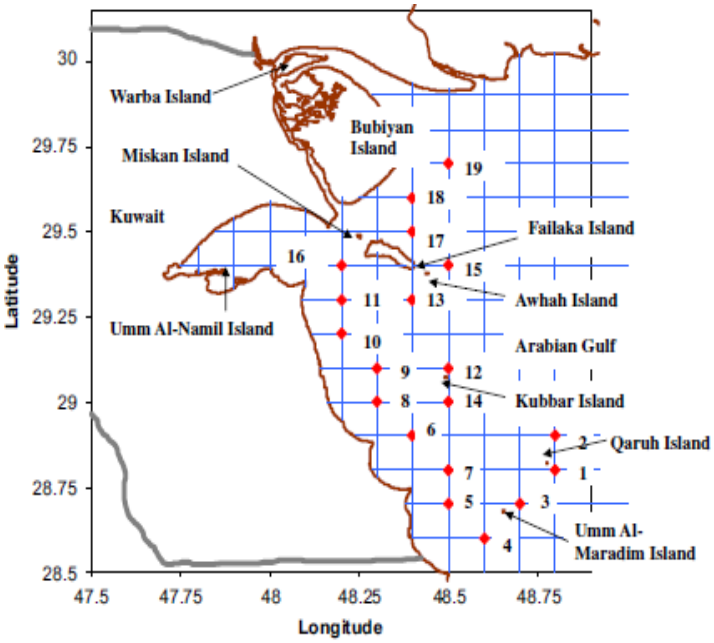
The idea of converting ocean wave energy into useful energy forms is not new. According to Leishman and Scobie (1976), the first British patent for a wave energy device dates back to 1855, while in France, Girard and Son patented their ideas as early as 1799. Intensive research and development in this field began after the dramatic increase in oil prices in 1973. In the 1980s when oil prices declined, the interest in wave energy nearly disappeared. Funding for wave energy research increased again in the late nineties following the Kyoto conference on the reduction of CO_2 emissions and the growing awareness of the limited and insecure nature of the world's energy supply. At present, in many areas of the world, ocean wave energy has great promise. However, many of the technologies to harness this energy remain to be developed to commercial standards. Further research is still needed to develop reliable wave power conversion technologies which could be economically competitive in the global energy market. The enormous potential of ocean wave energy strongly supports efforts to find viable and profitable engineering solutions for capturing energy from waves.

The global wave power resource in deep water (> 100 m depth) is estimated to be approximately 1–10 TW or 8,000–80,000 TWh/yr (Panicker, 1976). A detailed examination of the global potential shows that the most promising locations for wave energy production are located off the western coasts of continents in the moderate to high latitudes where there is deep water (> 40 m), since wave energy is found to reach power densities of 60–70 kW/m in these locations (IRENA, 2014). For example, countries like Australia, Chile, Ireland, New Zealand, South Africa, the UK, and the US have excellent wave resources with average power densities in the range of 40–60 kW/m (ABP, 2008; IRENA, 2014). Iranian seas also have great wave energy potential. For instance, the Caspian Sea has a maximum wave power density of 30 kW/m (Alamian et al., 2014). Much lower ocean wave

power densities were reported for the State of Kuwait at the Engineering Congress on Alternative Energy Applications in 2009 (Neelamani, 2009). For example, it was reported that the wave power density available around Qaru Island (Figure 1.1.b) varies between 0 and 16 kW/m.



(a)



(b)

Fig. 1.1: Location of Kuwait in Arabian Gulf (a) (Baby S., 2011) and Kuwaiti territorial water (b) (Neelamani et al., 2007)

The State of Kuwait is situated in the north western coastal plain of the Arabian Gulf (Figure 1.1a). Kuwait occupies an area of approximately 17,800 km^2 at latitudes of 28° 30' N to 30° 05'N and longitudes of 46° 3' E to 48° 35' E (Neelamani et al., 2007). Its territorial water is about 500 km in length and has depths of up to 25 – 30 m (Neelamani et al., 2007). There are nine islands in Kuwait, namely: Bubiyan, Warba, Failaka, Miskan, Umm Al-Namil, Awhah, Kubbar, Qaru and Umm Al-Maradim. The Kuwaiti territorial waters can be divided into two regions: the shallow Northern area which is less than 5 m deep in most places and has a muddy sea bed; and the relatively deep Southern area which has a bed of sand and silica deposits. Although the area of the Kuwaiti territorial waters is only about 7611 km^2, the wave climate varies significantly between different areas.

Wave energy potential and significant wave heights and periods have been predicted statistically for 19 different locations (Figure 1.1b) in the Kuwaiti territorial waters based on 15 years' worth of historic wave data, denoting the average recurrence interval over 100 years (Neelamani et al., 2007). Among these 19 locations, the significant wave height varies from 1.86 to 4.02 m and the mean wave period is between 4.2 and 6.3 s for the significant wave heights corresponding to a 100 year return period. Based on the hydrodynamic atlas and the extreme wave analysis for Kuwaiti territorial waters, the marine area surrounding Qaru Island and Umm Al-Maradim are the most suitable for wave energy power plants (Neelamani et al., 2007). It was estimated that for a period of 1 year, the total incident wave power per metre of wave is about 6000 kWh around Qaru Island. Water depths in the area reach 25 to 30 m about 1000 m away from the island (Neelamani, 2009). Wave power greater than 1 kW/m around Qaru Island is available for more than 12% of the year (Neelamani, 2009).

The coastal zone in Kuwait is considered to be of special importance as almost all the residential, commercial, industrial, and tourist areas are concentrated along the coastline and the entire population lives within 15 km of the coast. Moreover, the majority of Kuwait's oil ports and

harbours are located on the Southern shore. With the increase in human activity associated with the recent rise in oil production, there is greater need for an optimised solution to protect the Kuwaiti coastline and islands from wave attack and erosion. As the wave climate, for example around Qaru Island, has been found suitable for the installation of a floating wave energy conversion (WEC) device (Neelamani, 2009), this provides an opportunity to consider using a combined protective and energy generating system at this site. However with the low wave power density, a coastal protection structure is needed that is also capable of locally increasing the energy density of waves to make wave energy conversion more efficient, cost-effective and commercially competitive.

1.2. Research Objectives and Approach

The main objective of the research presented in this thesis is to support the development of a viable and validated solution to protect the Kuwaiti coastline and islands from wave attacks and erosion. The programme of research conducted aims also at supporting the development of a method of protecting the Kuwaiti coastline with a breakwater system that also provides an opportunity to generate energy by locally increasing the energy density of waves to make wave energy conversion (WEC) more efficient, cost-effective and commercially competitive. The study provides the first evaluation of the potential of a parabolic concentrator to enhance wave energy conversion in mild wave climates such as that found in the State of Kuwait.

The objectives of the research can be summarised as follows:

- Conduct a thorough literature review to identify WEC and breakwater concentrator combinations suitable for Kuwait,
- Conduct analytical modelling of a point absorber to better understand how to optimise its dynamic behaviour and design geometry,

- Develop and apply a Computational Fluid Dynamic (CFD) modelling approach suitable for analysing wave behaviour in the presence of a geometrically representative parabolic concentrator-point absorber device,
- Use experimental testing to generate data to validate the CFD modelling work, and
- Use experimental testing to increase understanding of wave and point absorber behaviour to support the optimisation of the proposed prototype system,
- Reassess the viability and cost effectiveness of the proposed prototype system.

1.3. Outline of Thesis Content

A flowchart of the research discussed in this thesis is given in Figure 1.2. A brief description of the scope and content of each chapter is also provided. The bulk of the literature review covering breakwater-wave energy conversion systems is given in Chapter 2. Additional literature review sections are included in each chapter separately. These sections focus specifically on the research presented in the related chapters.

A review of the literature on state of the art breakwater structures and WEC devices is given at the beginning of the second chapter. The review indicates that a point absorber WEC is an appropriate type of device to be combined with a breakwater. A thorough literature review was conducted examining all existing breakwater-wave energy conversion systems that are appropriate for mild wave climates such as that found around Qaru Island. In addition, to finding a method of increasing wave energy density. The innovative research on focusing waves using a bottom step or reflector wall with a parabolic shape in the horizontal plane conducted and published by Monopolis et al. (1980) and others (Helstad, 1980; Kudo et al., 1987; Murashige and Kinoshita, 1992; Yang and Ertekin, 1991; Cheung et al., 1995) was of particular interest as it presented a viable option for increasing wave

energy density. Based on an analogy with optics (Mehlum and Stamnes, 1980; MacCormick et al., 1980), it can be seen that a parabolic reflector causes waves to amplify at the focal point of the step. This attribute is very attractive in view of the wave climate at Qaru Island, and as such a parabolic concentrator could function as a breakwater, part of a WEC device and as a mooring facility which would be highly cost effective. The amplified and focused wave energy inside the parabola structure could be converted into usable power using a wave energy device such as a point absorber (buoy). In Chapter 2, various types of breakwater construction are discussed, and a solution based around a parabolic concentrator combined with a point absorber moored to the sea bed was selected to be developed as part of this study. Aspects related to cost sharing during construction by incorporating WECs into breakwaters are also discussed at the end of the chapter.

In the third chapter, the heaving motion of a point absorber WEC is modelled analytically. The model considers a single point absorber system with one degree of freedom (heave) along the vertical axis. The novel approach in this chapter is based on examining the system's damping profiles, and parameters that are initially assigned to give a linear damping profile are optimised to maximise the energy absorbed per wave cycle. The approach used is numerical and the dynamic equations are formulated and results calculated in the time domain using the software MATLAB which offers a fast solver with high numerical accuracy. In order to calculate the steady-state harmonic response, the model is initially simplified and an optimal damping profile is determined through numerical optimization in the time domain. Having determined the optimal damping profile numerically, a steady-state harmonic solution methodology is developed and matched to the time domain solution. Further calculations using the steady-state harmonic model are carried out to determine optimal damping profiles for different buoy shapes. The results of these analyses provide the necessary input for key decisions regarding optimal damping profiles

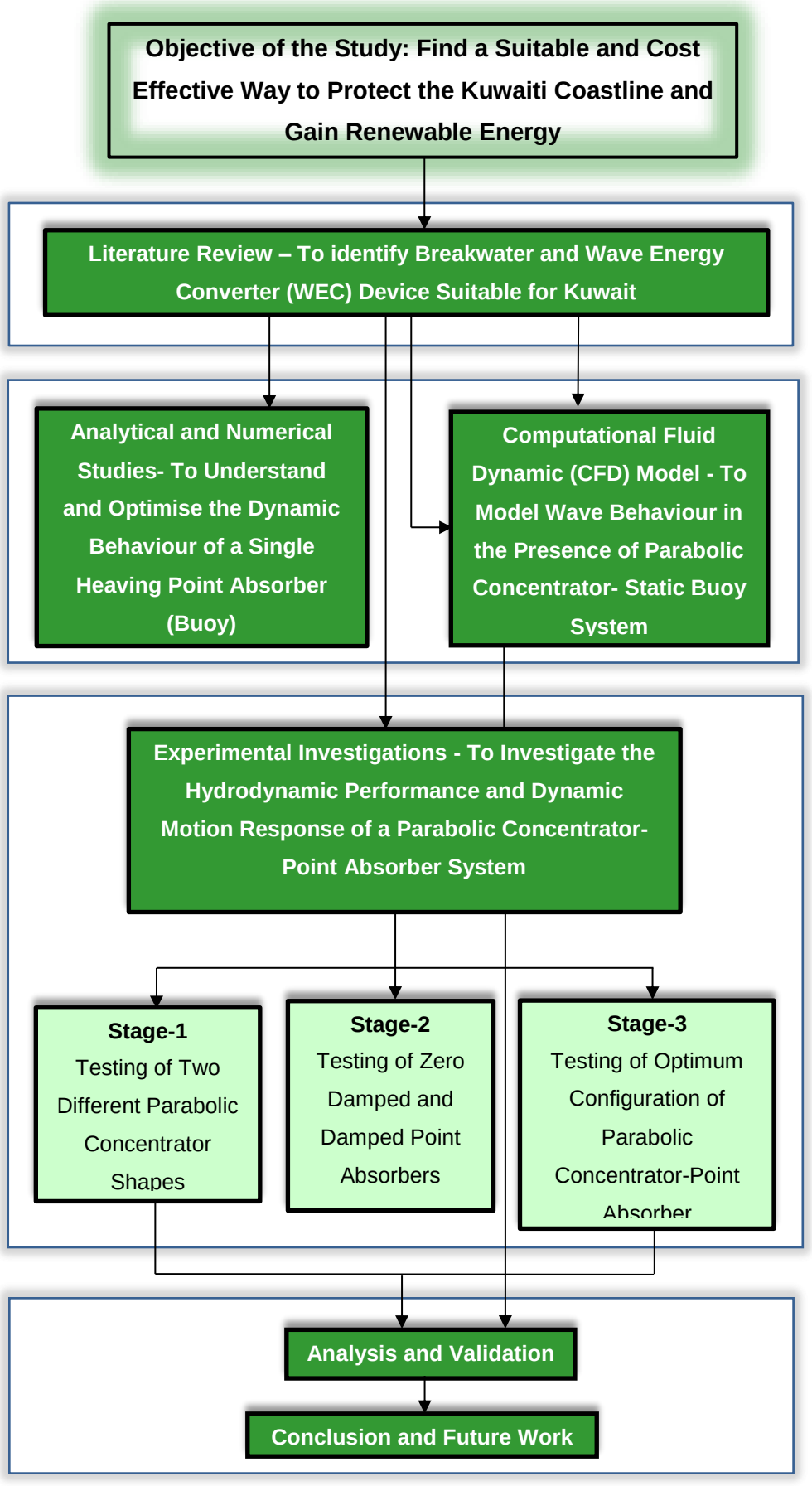


Fig. 1.2: Flowchart of the thesis content and chapters

and maximum power extraction for three different buoy shapes which can be tested experimentally.

The fourth chapter contains a detailed description of the experimental programme carried out to investigate the hydrodynamic performance and dynamic motion response of a parabolic concentrator-heaving buoy system. The Kuwait Institute for Scientific Research (KISR) wave flume tank was utilised for these experiments. The motivation for the experimental investigation and a description of the test facility, measurement techniques and testing procedures are presented in the first part of the chapter. This is followed by a description of some specific aspects related to the geometry of the buoy and parabolic concentrators tested and the methods of data collection. In addition, an analysis of the physical quantities measured during the preliminary stages of testing is provided to understand the phenomenon under investigation. Two candidate parabolic geometries were tested and the results presented demonstrate the effect of the incoming wave characteristics on their performance. Based on the results obtained, one of the parabolas was selected for future testing.

The final part of the experimental chapter details the wave tank tests in which the performance of the optimum combined parabola-buoy configuration was examined for the following two cases: (i) parabolic concentrator-heave only zero damped point absorber and (ii) parabolic concentrator-heave only damped point absorber. The results are analysed to generate an understanding of the hydrodynamics and potential power output of the novel technology.

In the fifth chapter, the focus of the theoretical study moves to less idealised systems than those considered in Chapter 3. In this chapter, the numerical simulation methods available for modelling fluid flows with interfaces are reviewed. The commercial computational fluid dynamics (CFD) code ANSYS-FLUENT is used to model the essential elements of the KISR wave tank with a parabolic concentrator. A mesh sensitivity study is presented and the optimum mesh for this study

identified. Experimental data from the KISR wave tank is then compared to the CFD data and good agreement is demonstrated. In the final section of Chapter 5, a model of the wave tank with a static buoy is presented with predictions for the forces acting on a buoy due to wave motion. This work forms an essential precursor to possible future work involving fluid-structure interactions where the behaviour of a moving buoy would be evaluated.

In the final, sixth chapter, the most important findings of this research are highlighted and a summary of the main achievements and contribution to the body of knowledge in this area are given. In addition, some recommendations for future work are proposed.

Chapter 2: Literature Review: Breakwaters and Wave Energy Converters (WECs)

The aim of the first sections of this chapter is to conduct a thorough literature review:

- To identify breakwater and WEC combinations suitable for Kuwait,
- To address the general purpose of breakwaters and list their selection criteria,
- To justify the view that the floating types are superior to other breakwater types,
- To summarise recent literature reviews of floating breakwaters design and performance aspects, and
- To identify a suitable coastal protection structures that are capable of locally increasing the energy density of waves.

The remainder of this chapter explains the concept of ocean wave energy and conducts an investigation into the main types of existing WECs. The devices are classified according to their size, orientation, location and mode of operation. The chapter extends further to detail aspects related to wave energy extraction and review the current market for wave energy systems. The potential suitability of the various WEC devices for use with parabolic concentrator technology is assessed within the chapter. The last section of the chapter aims to provide a preliminary assessment of the effectiveness and applicability of a parabolic concentrator-WEC structure for an ocean wave spectrum representative of the operational wave environment of Kuwait.

2.1. Introduction

The basic purpose of any breakwater is to provide protection to shorelines, harbours and structures and prevent damage from excessive waves. Breakwaters are also used to protect coastlines against erosion caused by waves. Technological improvements within the last 100 years and changes in societal focus have led to alterations in the design and purpose of breakwaters. Although their purposes may vary, the common link between all breakwaters is their use for providing protection against waves.

Following the introduction of the concept of wave energy over a decade ago, there has been a substantial amount of research and development carried out on wave energy conversion concepts and technologies. Today, the main aims for the development of ocean wave energy systems are ensuring the reliability of the WEC technology employed and reducing costs. A significant amount of experience has been gained which can be drawn upon to improve the design and performance of ocean power techniques. More recently, the design goals for coastal engineers have started to shift from protecting against towards harvesting wave energy, and in some cases both. Climate change, evidenced by storms and the observed rise in sea level, and the demand for high energy harvesting rates challenge the effectiveness and sustainability of existing coastal structures. In particular, seawalls and breakwaters need to be higher, stronger and more efficient. This requirement for more efficient and sustainable coastal structures can be potentially fulfilled through the combination of WECs with other coastal and ocean engineering facilities such as breakwaters.

2.2. Breakwaters

The history of breakwaters goes back to ancient times where simple mounds were constructed with stones. As early as 2000 B.C., a stone masonry breakwater was constructed in Alexandria, Egypt (Takahashi,

2002). The Roman Emperor Trajanus (A.D. 53-117) constructed what is believed to be the oldest existing rubble mound breakwater. It reached its equilibrium slope after a long history of damage and subsequent repairs and it triggered the beginning of coastal modification. There has been much discussion of breakwaters after the construction of the first modern breakwater at Cherbourg, France, around the end of the 18th century. The historical development of breakwater structures was originally summarised by Ito in 1972 and later rearranged and slightly modified by K. Tanimoto in 1987. Beginning with the ancient dyke-style breakwaters comprised of natural stone, various trends were seen in structural development towards increasing both stability against waves and savings in cost.

Although there are several types of breakwater structure used throughout the world, three main types can be distinguished, namely (Takahashi, 2002):

(1) Mound Type: Mound breakwaters essentially consist of a large mound of loose elements such as rocks, stones or concrete blocks. The most basic type is a mound of randomly placed stones. This type of breakwater is particularly attractive if the loose elements required are available in the vicinity of the breakwater location and the water is shallow (depth < 10 m) (Fousert, 2006).

(2) Vertical Type, including the monolithic and composite types: Monolithic breakwaters have a cross-section which acts as a single large solid block. Structures of this type include block walls, masonry walls and the caisson. These breakwaters are generally suitable for use in medium water depths (10 m – 24 m) (Fousert, 2006), where it is cheaper to construct than a mound type. A composite breakwater comprises a monolithic breakwater with a low-crested berm. This type of breakwater is particularly suitable for deeper waters (24 m–32 m) (Fousert, 2006) and in areas which have appropriate soil conditions for a stable foundation. This type is very similar to a rubble mound breakwater armoured with

concrete blocks. The main difference is that the concrete blocks in the rubble mound breakwater act to protect the rubble foundation, while the concrete blocks of the horizontally composite breakwater function to reduce the wave force and size of the reflected waves (Takahashi, 2002).

(3) Special Non-Gravity Types: Common unconventional breakwaters come under the categories of non-gravity, such as pneumatic/hydraulic breakwaters, floating and pile (Verhagen et al., 2009). In most standard cases, these types of breakwater are uneconomical because of the high structural strength required for the breakwater elements. A floating breakwater is very useful in deep waters (depths > 20 m) (Elchahal et al., 2008), but is only effective for relatively short wavelength waves. In the next section, the selection criteria for breakwaters are detailed.

2.2.1. Breakwater Selection Criteria

The main factors to be considered in the selection of a suitable breakwater design have been listed by Takahashi (2002):

1. **The availability of construction materials at or near the site:** If construction materials are easily accessible then this is a big advantage for the rubble mound breakwater for example since this reduces material costs, especially when a large supply of rubble stones is readily available.

2. **The depth of water and condition of the sea floor:** If water depths are not very large, sea bed soils are weak and restrictions on wave reflection exist, then the initial choice would be for a rubble mound structure. On the other hand, if, sea bed soil strength is reasonably good and water depths are medium to large, then a composite structure would be the obvious initial choice.

3. **The equipment suitable/available for its construction:** Some types of breakwaters can be constructed on land such as the rubble mound breakwater which doesn't require large-scale construction equipment such as work barges.

4. **Cost of construction:** The composite breakwater can be rapidly constructed and is fully stabilised once its caissons are filled with sand. In comparison, the rubble mound type is more unstable and its inner layers may be subjected to damage during construction.

5. **Maintenance:** Some breakwaters such as the composite type require less maintenance where others tend to require relatively frequent maintenance efforts such as maintaining the blocks of rubble mound breakwaters.

Once the functional criteria for the breakwater structure are defined and the environmental and construction conditions are investigated, a breakwater type can be selected for further analysis in terms of conceptual design and costing. The selection of breakwaters involves the steps indicated in the diagram shown in Figure 2.1.

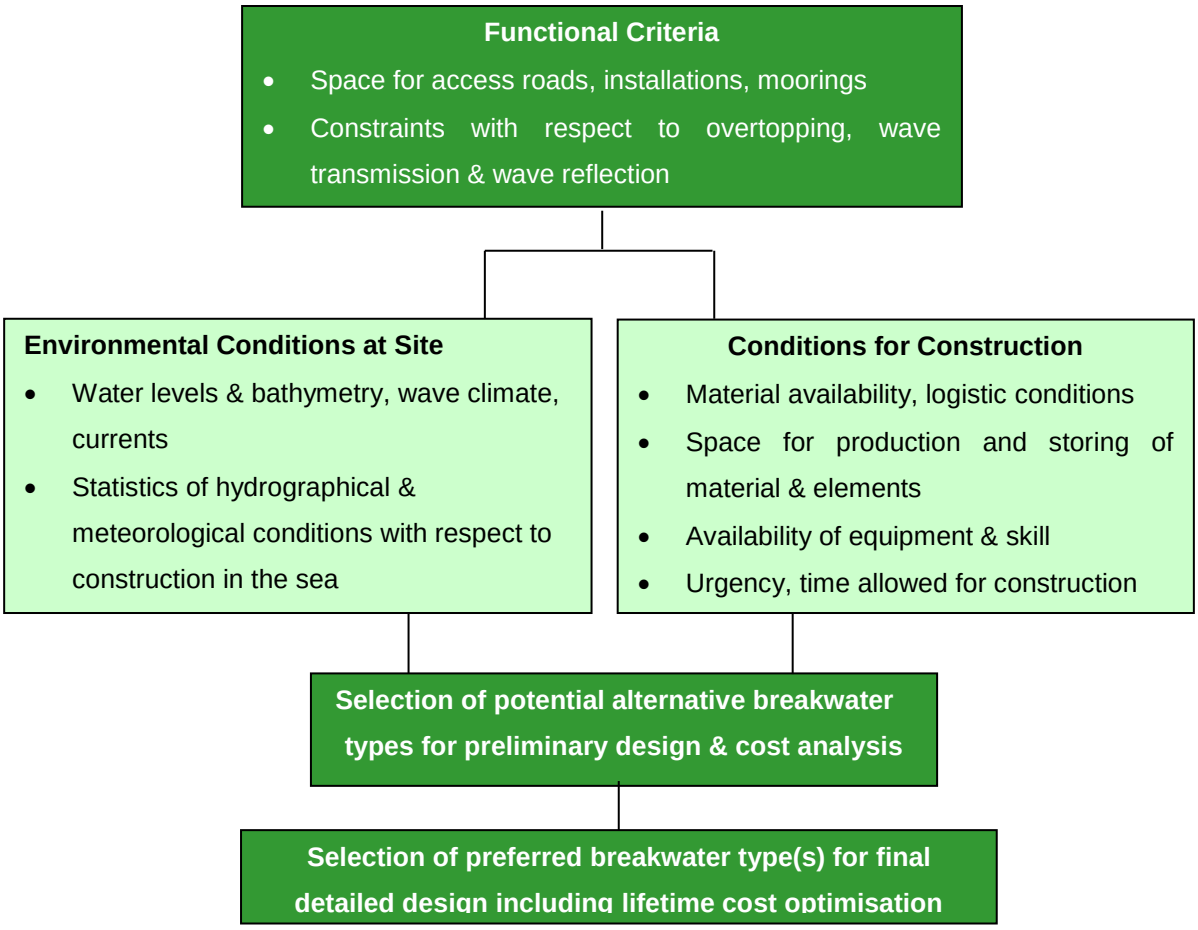


Fig.2.1: Steps in selection of breakwater type (Burcharth, 2009)

In practice, breakwater selection conditions are almost never clear, as breakwaters tend to have different characteristics, especially with respect to function, constructability and environmental impact. Due to the large number of aspects to consider, there are no simple rules for the choice of breakwater type. The actual combination of functional and environmental conditions varies considerably from location to location, and in practice determines the final choice. Lamberti and Franco, (1994) have compared the use of a caisson (composite) breakwater with a rubble mound breakwater armoured by concrete blocks for applications where both types are strong contenders. In addition, Hales, (1981) has evaluated and discussed the existing technical literature on floating breakwater concepts and noted that the four fundamental factors that greatly influence their design are: buoyancy and floating stability, wave transmission, mooring forces and structural integrity.

Furthermore, the choice of breakwater type is largely dependent on wave height and period. Large waves require rubble mound structures that are able to absorb wave energy. Floating breakwaters, on the other hand, can be used for smaller wave heights and periods. Vertical wall types are used to cover the range between rubble-mound and floating breakwaters, as shown in Figure 2.2.

Floating breakwaters are not suitable for cyclone and Tsunami dominated sea conditions, however they work well in marine conditions with moderate and short period waves. They are particularly suitable for the Kuwaiti territorial waters where the extremely significant wave height varies from 1.86 to 4.02 m and the mean wave period is in the range 4.2 to 6.3 sec (Neelamani et al., 2007). For a country like Kuwait which has short waves, deep waters and a limited supply of good quality stone, floating breakwaters are the most appropriate coastal protection structures. Although the advantages of floating structures appear obvious, the use of these structures is limited, mainly due to their complex hydrodynamic behaviour, reliability and cost. Section 2.3 will provide insight into all aspects related to floating breakwaters.

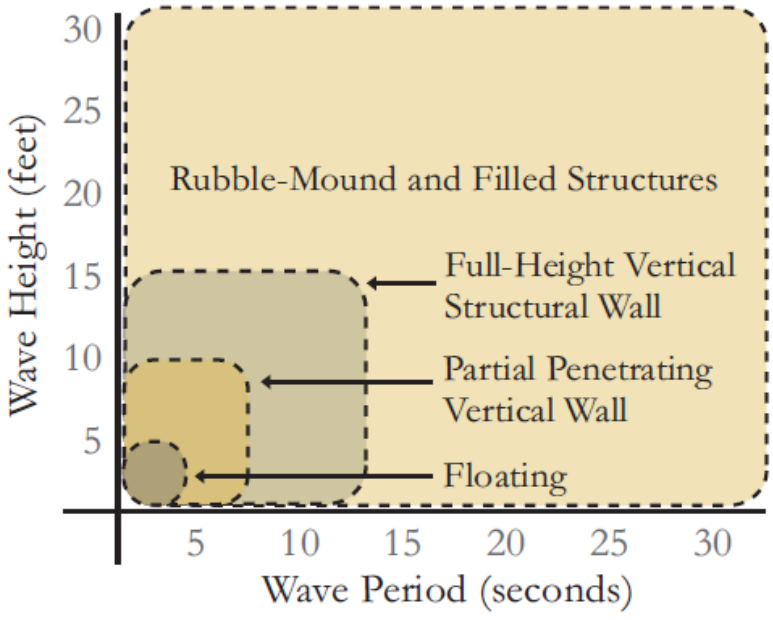


Fig. 2.2: Breakwater type for typical range of wave height and period (PND Engineers Inc., 2015)

2.3. Floating Breakwaters

Based on the selection criteria given in section 2.2.1, the floating breakwater type was identified as the most suitable for applications within the Kuwaiti territorial waters. Therefore, this section will focus solely on floating breakwaters.

2.3.1. History of Floating Breakwaters

One of the first floating breakwaters was constructed in 1811, where it was used to provide shelter for the fleet at Plymouth in Great Britain (Morey, 1998). However, their application for the reduction of surface gravity waves was first considered by Joly in 1905. Interest in their use increased during the Normandy invasion in World War II. At that time, Great Britain developed a floating breakwater called the `Bombardon' to protect men and materials during offloading on the Normandy coast. The design consisted of several iron elements; unfortunately it failed during a severe storm which occurred after the invasion. As a result, the interest in floating breakwaters declined until 1975, when it rose again due to their potential for naval and military applications.

During the 1970s the demand for floating breakwaters for the protection of marinas increased. With space becoming very scarce in coastal zones and the large demand for new marinas, floating breakwaters were used to create appropriate areas for the construction of these marinas. After the potential of floating breakwaters was recognised, there was a growth in research examining wave transmission, reflection, energy dissipation, dynamic response, mooring forces, and the effect of the width of the floating breakwater on its hydrodynamic characteristics.

Over the years, many different types of floating breakwater have been developed and many conclusions have been drawn as to their effectiveness. Some of the advantages of floating breakwaters include the following:

1. Floating breakwaters are less expensive than fixed structures in deeper waters (depths > 10 feet) (Hales, 1981).
2. Floating breakwaters can effectively attenuate moderate wave heights (wave heights < 6.5 feet) (Tsinker, 1995).
3. Poor soil conditions may make floating breakwaters more feasible to use than heavy rubble fixed breakwaters (McCartney, 1985).
4. Floating breakwaters have minimal effects on water circulation, sediment transport and fish migration. (McCartney, 1985)
5. Floating breakwaters can be easily moved, rearranged in different layouts, or transported to other sites (Hales, 1981).
6. If ice formation presents a problem, floating breakwaters can be removed easily (McCartney, 1985).

Some of the disadvantages of floating breakwaters are the following:

1. Floating breakwaters are less effective than fixed structures at reducing wave heights for slow waves; a practical upper limit for the design wave period is 4 to 6 seconds (equivalent to a minimum frequency of 1.0 rad/s to 1.6 rad/s) (Tsinker, 1995).
2. Floating breakwaters are susceptible to structural failure during catastrophic storms (Tsinker, 1995).
3. If the structure fails and is detached from its moorings, it may become a hazard.
4. Compared to the more common fixed breakwaters, floating breakwaters require a high degree of maintenance (Tsinker, 1995).

2.3.2. Development of Floating Breakwaters

Recent developments in floating breakwater technology have come about as a consequence of worldwide research efforts. Studies have included numerical modelling of floating breakwaters aiming to assess the wave characteristics around a floating breakwater (either moored or freely floating), the dynamic response of the breakwater (heave, pitch, roll, surge, sway and yaw) and to enable estimation of mooring forces

for different incident wave characteristics and different mooring configurations. As experimental data is essential for verifying mathematical model results, this has usually been obtained from physical modelling experiments either in the laboratory or in the field. Some of the key publications in this area are by Stiassnie (1980), Yamamoto (1981), Drimer et al., (1992), Abul-Azm, (1996), Williams (1997; 2000) and Stiassnie and Drimer (2003). Some researchers, such as McCartney, (1985), have carried out detailed physical model studies using a laboratory wave flume and basin to understand the wave transmission, reflection, energy dissipation, mooring and dynamic response characteristics of floating or special type breakwaters.

There has been a significant amount of interesting research completed around the world on floating breakwaters during the last decade. For example, Gozo et al., (2009) carried out a visualisation study of the flow field around Double Barrier Floating Breakwaters (DBFB) using the particle image velocimetry (PIV) technique. Their model predicted the wave height distribution behind a DBFB with good accuracy. Wang and Sun, (2010) carried out a physical model study on porous floating diamond-shaped blocks. This breakwater type was found to dissipate more wave energy and more effectively reduce mooring forces than conventional designs.

Uzaki et al., (2011) experimentally investigated the wave absorption performance of a novel steel floating breakwater with trusses (FBT), which is composed of a box-type pontoon and truss structures. Flow visualisation revealed that the front truss structure breaks incident waves and converts wave energy to turbulent energy effectively. Peña et al., (2011) also carried out laboratory experimental investigations on four different pontoon floating breakwater types. In their study, a basic pontoon type model with twin fins was modified by reducing the breakwater width and increasing the depth of the fins. It was concluded that the width of the pontoon is the key design parameter, and small modifications in cross-sectional shape have less effect on hydrodynamic behaviour and mechanical loads.

Despite the large amount of literature on floating breakwaters in general, Ozeren et al. (2011) noted that there is still a lack of knowledge about the performance of cylindrical breakwaters, which as a result of their simplicity, can minimise construction and material costs. They carried out a laboratory investigation of the hydrodynamic interaction of cylindrical breakwaters with monochromatic waves in deep and transitional water depths. The tested breakwater models featured single and multiple-cylinder cross-sections combined with bottom-moored, arm-restrained (connected to shoreline), and pile-restrained configurations. When the breakwater models were fixed, the reflection was higher than for the partially restrained models, and efficiency was found to be strongly dependent on draft ratio (z_d/d, where z_d is the draft and d is the height of the structure). For partially restrained models, dissipation strongly influenced transmission coefficients. Furthermore, horizontal restraint was found to be more important than vertical restraint in terms of improving breakwater efficiency.

The effect of introducing skirt walls to a floating breakwater was studied by Koutandos and Prinos (2011). Non-porous skirt walls were found to be better at reducing wave transmission than porous skirt walls (Koutandos and Prinos, 2011). In 2012, Shih experimentally studied the transmission and dissipation characteristics of porous perpendicular pipe breakwaters under different wave conditions for various combinations of pipe diameters and lengths. It was found that wave energy was mainly dissipated due to drag and interception of the resultant motion by the pipe breakwaters. It was also revealed that attenuation is much more effective with smaller pipe diameters than with longer lengths. Li and Lin, (2012) carried out regular and random wave impact tests on floating bodies using a numerical wave tank. The wave impact forces were obtained for different wave heights, periods and water depths. Zhao et al., (2012) also investigated both theoretically and experimentally the interaction between waves and an array of porous circular cylinders with and without an inner porous

plate. The draft of the cylinders, the location of the inner porous plate, and the spacing between adjacent cylinders were adjusted to investigate their effects on wave dissipation. He et al., (2012; 2013) examined the hydrodynamic performance of floating breakwaters with and without pneumatic chambers. Their experimental results showed that pneumatic chambers can significantly enhance wave energy dissipation and reduce wave transmission. A two dimensional numerical wave tank model was used by Wei et al., (2013) to simulate interactions between water waves and inclined-moored submerged floating breakwaters; the applicability and validity of their model were further confirmed by comparing numerical and experimental results. Koraimaand Rageh (2013) studied the hydrodynamic performance of a floating breakwater with under-connected plates. Their experimental results showed that the efficiencies of transmission and reflection increase with the number of the plates.

Zhou et al., (2014) investigated the effects of different floating breakwater shapes on wave absorption and provided a basis for the design of a floating breakwater for an offshore project. Three different floating breakwater shapes were studied experimentally, namely: a soft wall-sided pontoon, a solid wall-sided pontoon and a circular cross-section breakwater filled with water. Various factors including wave period, wave steepness and geometrical characteristics were considered. The circular cross-section breakwater provided greater wave absorption compared to the other two types and proved to be the most efficient. More detailed experiments were conducted on the circular cross-section breakwater where a V-shaped floating breakwater consisting of two single circular cross-section breakwaters was studied. The effects of the angle between the two sections, the wave period and the wave height were examined. The results revealed that geometrical configuration and water depth significantly impact on wave attenuation and mooring forces. Another new types of floating breakwater has also been tested in a wave flume tank. Similar to the cylindrical floating breakwater (CFB) consisting of two parts, this design had a main body

of rigid cylinders, and a flexible mesh cage containing a number of suspended balls intended to absorb wave energy by converting it to mechanical energy (Ji et al., 2015). A series of experiments were carried out to compare the performance of this floating breakwater design with traditional double pontoons and box floating breakwaters. Results showed that the new design performed better than the more traditional designs in that wave transmission was significantly reduced by the mesh cage and balls, especially in the case of long waves. Ji et al. (2016) also conducted flume tank experiments on four types of floating breakwater, namely cylindrical floating breakwaters (CFB), porous floating breakwaters (PFB), mesh cage floating breakwaters of type-I (MCFB-I) and mesh cage floating breakwaters of type-II (MCFB-II). The hydrodynamic performance of each type was tested to identify the most effective configuration for wave attenuation. The incident and transmitted waves, the tensions in the mooring lines and the motion responses of all of the four types were measured. Among them, MCFB-I was found to have the greatest attenuation effect on the incident wave amplitude.

In March 2016, Neelamani and Al-Banaa patented an innovative floating breakwater design with skirt walls with a defined porosity which gives material savings of up to 50% or more compared to more conventional designs (US Patent No. US 9,340,940 B2). Wang et al. (2016) tested an arc plate breakwater, which consisted of several horizontal arc plates suspended on supporting piles. The damped performance of the breakwater was explored using two-dimensional regular wave model tests. The hydrodynamic performance of the breakwater was compared with that of a similar breakwater which consisted of several horizontal plates. The surface arc plate was found to be a better wave attenuator and a stronger reflector than the submerged plate. Moreover, when the arc gap was equal to the arc height, the arc plate breakwater with a smaller relative height was found to dissipate more waves than the one with a greater relative height. The performance of an offshore circular ramp overtopping wave energy

converter (CROWN) was investigated very recently by Liu et al. (2017). The converter consisted of a reservoir surrounded by a circular ramp and an outflow duct installed with a low water head turbine. Experiments were conducted to examine wave overtopping behaviours and demonstrated that guide vanes can effectively control the wave water motion on the ramp for overtopping into the reservoir. An analysis of the overtopping discharge showed that the resonant zone is located in the smaller relative wave length domain. Guide vanes and milder ramp slopes were found to significantly enhance the overtopping discharge of the device.

From the research discussed above, it is clear that significant effort has been made worldwide to optimise floating breakwater configurations with a view to reducing costs while at the same time increasing hydrodynamic performance. Both theoretical and experimental tools have been used to tackle the issues related to floating breakwaters. Many floating breakwater concepts have been patented and some have been field tested. To date, they have been used for different purposes such as the creation of temporary calm water conditions for construction or war-related activities, coastal protection, marinas, floating airports, yacht harbours, etc.

2.3.3. Classification of Floating Breakwaters

Over the past two decades, floating breakwaters have mostly been used in conjunction with marinas, particularly in areas with large water depths (Elchahal et al., 2008). The application of floating breakwaters for ports, however, is less common because ports are often located near seas or oceans where there are higher and longer waves and floating breakwaters have historically been ineffective in these harsher ocean conditions (Briggs et al., 2002). The main reason is that wave lengths are large relative to the width of the floating breakwater, causing the breakwater to move up and down on the wave rather than acting to reduce wave energy. Richey and Nece (1974) recognised there are at least 60 different floating breakwater configurations in

existence. Based on the principle on how they attenuate waves, they are classified by the Permanent International Association of Navigation Congress (PIANC, 1994) into two classes:

- Reflective structures: these reflect incoming waves and are often rigid structures so they do not deform under wave loads. The most common reflective types include the pontoon, A-frame, Hinged types.
- Dissipative structures: these dissipate wave energy through turbulence, friction and non-elastic deformation, and are often flexible. These structures include the scrap-tyre, tethered-float, porous-walled, flexible membrane types.

2.3.4. Floating Breakwater Applications

A floating breakwater can provide a versatile means of protecting a marina or dockage area, and offers the best defence from short waves or boat wakes in reservoirs, marinas, lakes and rivers. In addition to applications in deep waters with short waves, there are some other applications where floating breakwaters may be suitable.

Floating ports: Currently, interest in floating breakwaters mainly comes from military port construction, the pleasure boat market and the expansion of commercial harbours. Ports are often very expensive to construct in areas of deep water and it might prove advantageous to build floating ports in these areas. In order to make a floating port feasible, the structure needs to attenuate the wide spectrum of waves which occur in oceans and large seas (Ali, 2006). In a storm, wave heights can reach 6 m with associated periods of up to 18 sec (Briggs et al., 2002), thus a very large floating breakwater is required which in most cases is not an economically viable solution.

Offshore engineering: One of the more interesting examples in this category is the pier extension of Port Hercule in Monaco which was designed to provide sea defences for a large harbour. With a total weight of 160,000 tons, it is a multi-purpose breakwater as it houses a

parking garage, mooring facilities and 25,000 m^2 of free space, divided into two levels. The option of a floating breakwater was chosen because of the combination of deep water and poor soil conditions at the site. The structure of a floating breakwater is relatively easy to transport and may be suitable for reducing large wave heights to acceptable levels such that they do not hinder maintenance activities. Another example of an offshore application is floating transhipment container terminals as these can offer increased efficiency for the loading and unloading of large container vessels (Fousert, 2006). Floating breakwaters can also be used to protect offshore crude oil loading terminals from wave activity as illustrated in Figure 2.3.

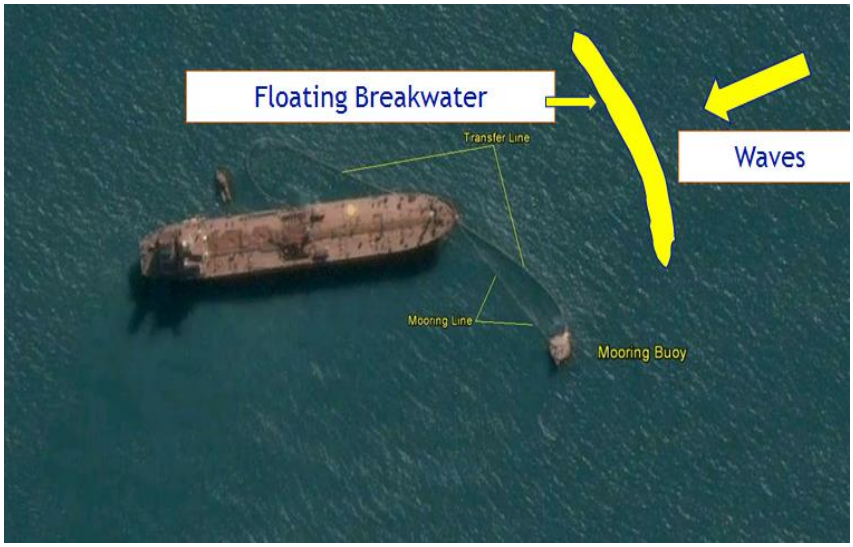


Fig. 2.3: Protection of offshore crude oil loading terminals (Neelamani and Al Banna, 2017)

Local regulations: In some cases, floating breakwaters have been installed at locations at which local regulations restrict the use of more conventional designs. For example, in Bulgaria, a permit is required for the construction of a conventional breakwater, which is a time consuming and costly to obtain. In contrast, a floating breakwater only requires a mooring permit, which is much easier to arrange (Drieman, 2011).

Other applications: Floating breakwaters can also provide a certain amount of shoreline erosion protection for islands, e.g. Qaru Island in Kuwait where there are large areas of coral as illustrated in Figure 2.4. In such locations, breakwaters can reduce or prevent the costly consequences of seashore erosion. Some types of floating breakwater, for example the pontoon type, are suitable for use as docks for mooring boats in calm wave conditions. In addition, floating breakwaters can be of use for defining swimming areas, for protecting open sea fish cages from strong waves and for protecting marinas as illustrated in Figure 2.5. They can also be useful even in the most unusual applications such as sewage ponds or by simply helping to moderate the wave or providing accesses from one place to another.



Fig. 2.4: Floating breakwater used for erosion protection of an island (Neelamani and Al Banna, 2017)

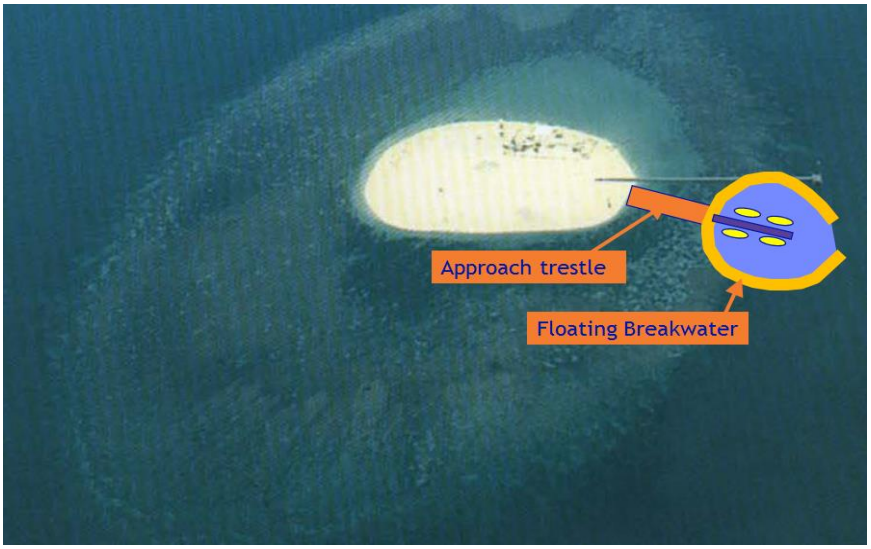


Fig. 2.5: Floating breakwater used for marina protection (Neelamani and Al Banna, 2017)

2.3.5. Floating Breakwater Economic Considerations

The optimum choice of design for any breakwater is very complicated as a wide range of both functional and environmental factors must be considered. Both the breakwater's structural integrity and wave transmission performance depend on its geometry, mass, and mooring properties. The final choice often comes down to the results of a cost analysis and economic evaluation of the various alternatives. From the sections above, it is clear that the applicability of each type of breakwater strongly depends on water depths, availability of materials and local soil conditions.

The construction costs of the various conventional breakwaters have been discussed extensively in the literature. Fousert (2006) compared values from the literature with the cost of a floating breakwater, as shown in Figure 2.6. While higher maintenance costs are a disadvantage of floating breakwaters, the independence of their costs from water depth is in their favour.

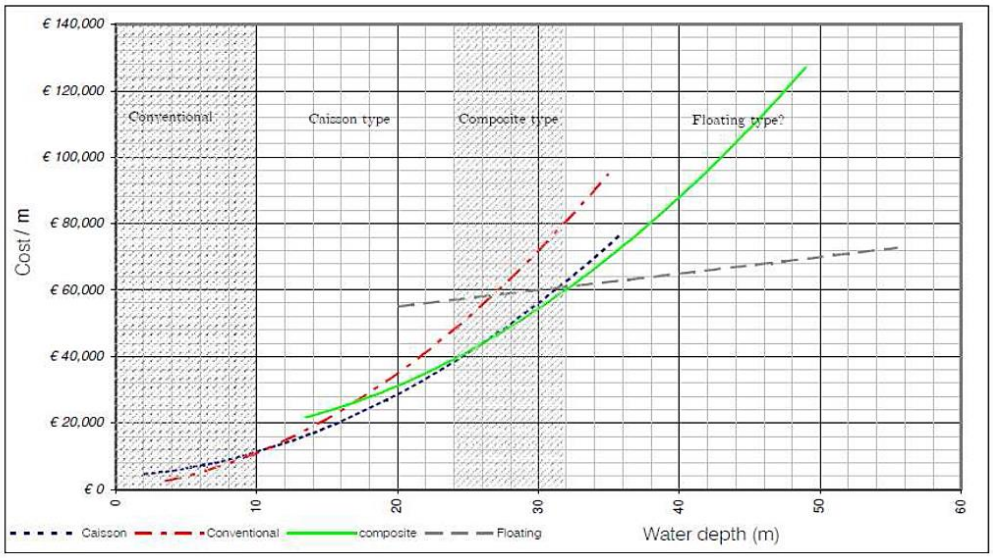


Fig. 2.6: Comparison of breakwater costs per running metre as a function of water depth (Fousert, 2006)

According to d'Angremond, (2001), from a conventional point of view, conventional breakwaters are preferred for water depths up to around 8 m. For depths ranging from 8 to 20 m, a caisson breakwater is more cost effective than the conventional rubble mound breakwater types due to the increase in volume of rocks required at the base. Between 20 and 30 m, composite breakwater designs become the most cost effective, as the increase in the height of caisson required would need a corresponding increase in its width. In contrast, the costs of floating breakwaters barely increase with increasing depths and in general, they are regarded as more economical than fixed breakwaters (Grinyer, 1995). Moreover, there are additional advantages such as they can be constructed on soft ground without the need for ground improvement. According to Grinyer, (1995), floating breakwaters have exceeded expectations with regards performance and are often used to allow the temporary berthing of large visiting craft and the loading and unloading of passengers from the Hythe ferry. As an example of the cost effectiveness of floating breakwaters, the total cost of the 205 m floating pontoon breakwater for the Town Quay Marina at Southampton was approximately £481,000 which equates to a price of less than £2,400 per metre (Grinyer, 1995). The construction of this breakwater

commenced in January 1993 and was already completed by July of the same year.

A recent economic study was conducted and presented by Neelamani at the Innovation in Wave Breakwaters Forum 2017 which focused on the Arabian Gulf marine environment and conditions (Neelamani and Al Banna, 2017). The study summarised in Table 2.1, compared cost estimates for the construction and mobilisation of a rubble mound breakwater with concrete armour, and a floating breakwater with 5 skirt walls. The floating breakwater was 8 m wide, 12 m long and 5 m deep. Each skirt wall was 2 m deep and 20 cm thick. The rubble mound breakwater had seaside and leeside slopes of 1:2 and 1:1.5, respectively. Its height was 11 m and its bottom and top levels were 4 m and 42.5 m wide, respectively. The water depth with reference to mean water level was 6 m. Costs were estimated for a total run of 200 m.

Despite the expensive maintenance costs (about 5% of the initial costs) associated with the floating breakwater, the floating design gave cost savings of 40% compared to the rubble mound design. The material cost estimates in 2017 were based on: cost of stone/cubic m = £53, cost of plain concrete/cubic m = £107 and cost of reinforced concrete/cubic m = £214.

Table 2.1: Cost estimates in British Pounds (£) (Neelamani and Al-Banna, 2017)

Rubble mound with concrete armour	Floating breakwater with 5 skirt walls
Cost of rubble for 200 m = £2,184,509 Cost of plain concrete for 200 m = £1,092,349 Sea bed preparation (10%) + Engineering study (3%) = £425,991	Cost of reinforced concrete for caissons to cover 200 m = £ 620,300 Mobilization (50%) + Mooring cost (20%) + Scaffolding cost (20%) + Transport cost (10%) + Cranes for erection (20%) + Engineering study (10%) + Miscellaneous cost (20%) = £930,451
Total cost = £ 3,702,859	**Total cost = £ 1,550,751**

Generally speaking, a true economic evaluation of any breakwater must consider total expenditure for the full service lifetime; lifetime expenditure tends to depend on the chosen safety level of the structure. The safety levels related to minimum total costs over the service life of a breakwater should take into account capital costs, maintenance and repair costs, and downtime costs as illustrated in Figure 2.7 (Burcharth, 2009).

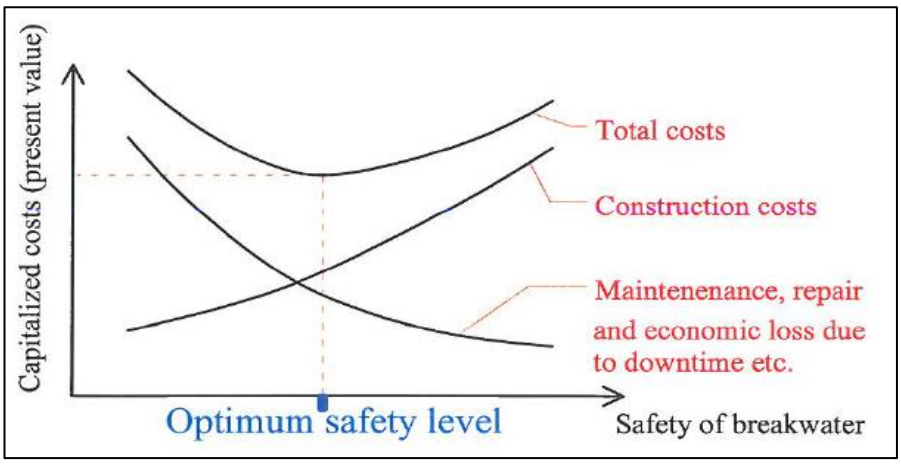


Fig. 2.7: Capital costs vs safety of breakwaters (Burcharth, 2009)

2.3.6. Floating Breakwater Potential for Kuwait

As stated in Chapter 1, with the low wave power density at Qaru island in Kuwait and the limited local sources for good quality stone, there is a need to find a suitable coastal protection structure that is also capable of locally increasing the energy density of waves in order to make wave energy conversion a more efficient, cost effective and commercially competitive technology. Considerable engineering effort has been devoted to WEC design concepts and technologies. In particular, research has focused on increasing the local energy density of waves and confining this energy to a localised area in order to make WEC systems more efficient. The necessary tools to focus wave energy are not yet available, but the similarity between the analytical representation of water waves and light waves instantly provides some interesting ideas for their development derived directly from optics.

Pioneering researchers in the use of the Fresnel lens concept for focusing wave energy are Mehlum and Stamnes (1980) and MacCormick et al. (1980). By analogy with optical theory, it is possible to show that wave reflection can be maximised or wave transmission minimised with a parabolic step on the sea floor (Mehlum and Stamnes, 1980). Wave energy focusing structures to amplify the incident wave height at a predetermined focal point have been proposed. A number of studies have been carried out examining various wave energy focusing techniques to investigate their performance under different wave conditions. A horizontal thin plate submerged under the surface of the water was initially proposed by Helstad, (1980) and examined further both numerically and experimentally by Kudo et al. (1987). Murashige and Kinoshita (1992) looked at thin plates of different shapes and dimensions. An innovative experimental study in which focusing of waves was carried out by means of a bottom step or wall with a parabolic shape in the horizontal plane was conducted and published by Monopolis et al. (1980). By analogy to optics, such a step should cause waves to amplify at the focal point of the parabola. This concept was studied further by Ertekin and Monopolis (1985) whose experimental results showed wave amplification by a factor of eight could be achieved. This concept is very attractive in view of the issue with low power density at Qaru Island. A parabolic concentrator breakwater appears to be the best and most cost effective candidate for this location as it can function as a breakwater, WEC focusing device and mooring facility.

A parabolic concentrator is a reflective wall used to collect wave energy. It transforms an incoming plane wave travelling along its axis into a spherical wave converging towards its focal point as illustrated in Figure 2.8. In other words, a series of incoming waves parallel to the axis of the parabola will reflect, amplify and concentrate at the focal point. Conversely, a spherical wave generated by a point source placed at the focal point will be reflected into a plane wave propagating along the axis.

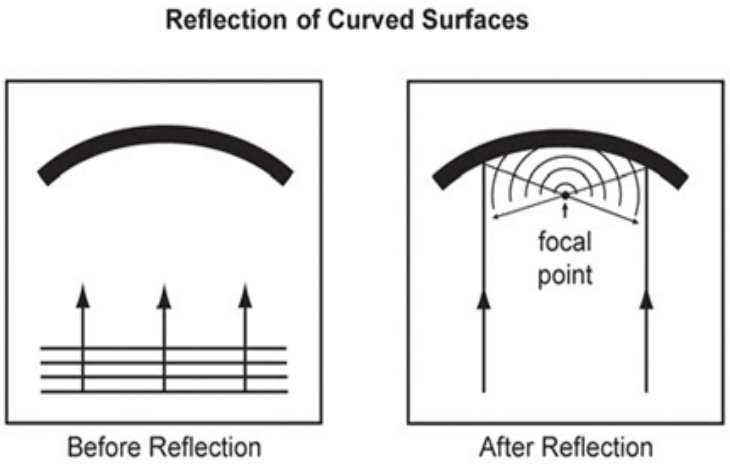


Fig. 2.8: Parabolic concentrator focal point (www.physicsclassroom.com)

Wave behaviour at the focal point of a parabolic step was studied by Yang and Ertekin (1991) using a three-dimensional numerical model based on the boundary element method. The model was used to solve a linear boundary value problem to predict wave behaviour. It was found that the energy density of waves increases at the focal point. It was also found that wave amplitude amplification not only occurred at the focal point, but also at a series of locations along the parabolic step discontinuity. The magnitude of wave amplification was found to depend on the focal length, location of the side walls, water depth ratio (of the deep region to the shallow region), and the incoming wave length. Another wave focusing structure was studied by Cheung et al., (1995), using time domain modelling. In their model, the wave energy was reflected by a much smaller submerged narrow structure defined by a parabola similar to an optical reflector. Their results also illustrated that wave amplification not only occurs at the focal point of the structure but at a series of locations in front of the structure.

The amplified and focused wave energy inside a parabolic breakwater structure can be converted into usable power, e.g. pneumatic power, and a wave energy device can produce more power if waves are amplified since, according to linear wave theory, power is proportional to the square of the wave amplitude (Airy, 1841). With this in mind, a

detailed review of existing WEC device designs will be conducted in section 2.4 and their potential suitability for use in conjunction with parabolic concentrator technology will be assessed.

2.4. Ocean Wave Energy

The fast depletion of fossil fuel resources worldwide has required an urgent search for alternative energy sources to meet global demands both in the near future and for generations to come. It is clear that no single renewable energy source can meet the world's requirements, but out of the many alternatives, ocean energy stands out as a promising option to make a contribution towards meeting these needs. Ocean wave energy has several advantages over other forms of renewable energy since waves are: more constant, more predictable and have a high energy density, enabling devices to extract more power from smaller volumes at lower cost with reduced visual impact (Brekken, 2009).

Although the need to find other solutions to satisfy the growing global demand for energy was emphasised by the oil crisis in the 1970s, relatively few people have recognised wave energy as a feasible alternative. Wave energy is usually expressed in terms of power level, or the amount of energy available in each metre of a wave crest. The usual units of measurement are kilowatts per metre (kW/m) for a local area or megawatts per kilometre (MW/km) for a larger area. The global wave power available in deep water (depth > 100 m) is approximately 1–10 TW or 8,000–80,000 TWh/yr (Panicker, 1976). The distribution of average annual wave energy density in different parts of the world can be seen in Figure 2.9. The power density along the west coast of Europe, Scotland and Ireland is 75 kW/m (Mork et al., 2010). For the State of Kuwait, much lower power densities have been reported (Neelamani, 2009). The wave power available around Qaru Island, for example, is found to vary from 0 to 16 kW/m (Figure 2.10) with wave powers greater than 1 kW/m available for more than 12% of the year.



Fig. 2.9: Global distribution of average annual wave power in kW/m of crest length for various locations around the world (Mamun et al., 2010)

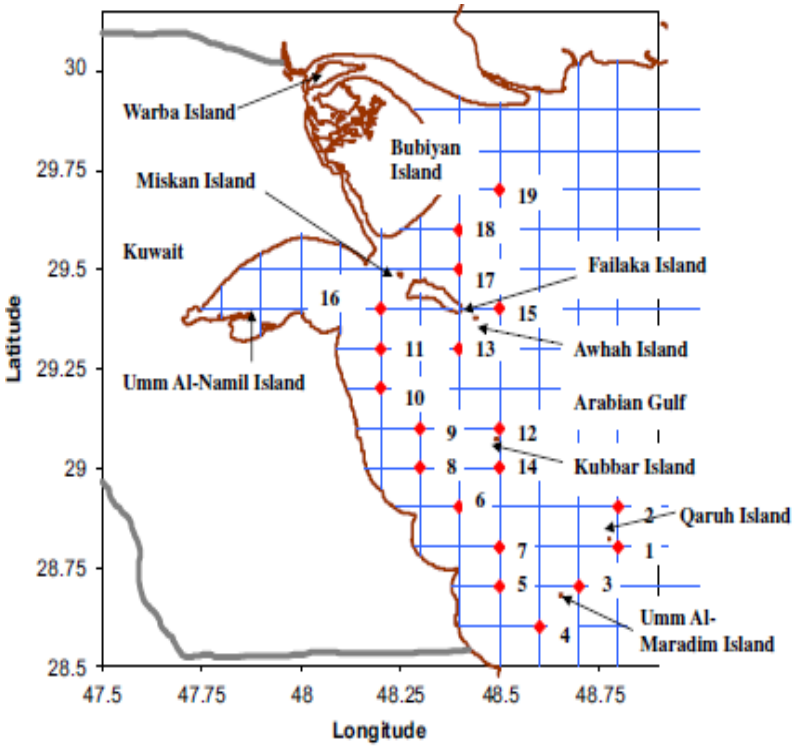


Fig. 2.10: Kuwaiti territorial waters (Neelamani et al., 2007)

The idea of converting ocean wave energy into useful energy forms is not new. Leishman and Scobie (1976) have documented the historical development of wave power devices. According to them, the first British

patent dates back to 1855, while Girard and Son patented their ideas in France as early as 1799. About 340 patents were obtained in the period from 1855 to 1973. Interest in ocean energy and the need to find other solutions to satisfy the growing global demand for energy was emphasised by the oil crisis in the 1970s. However, in 1980 when gas was cheap, relatively few people recognised it as a feasible alternative energy source and the funding for wave energy projects ceased. Considerable engineering effort has been devoted to WEC design concepts and technologies, yet despite the pioneering works of Salter (1974), Budal and Falnes (1975; 1980), Evans (1976; 1980) and others, very few WEC devices have actually been deployed.

In general, wave energy is harnessed through movement of the device, irrespective of whether it floats on the surface of the ocean or operates below sea level. Unlike other renewable resources, there are a large number of different concepts and techniques for harnessing wave energy. Over 1000 different wave energy harnessing techniques have been patented in Japan, North America and Europe, and all involve three main conversion levels, as reported by Brooke (2003):

- Primary level: At the primary level, wave energy is captured by an oscillating system. Examples of these types of systems include: a floating body, an oscillating solid element, or oscillating water within the structure. The system should be able to store some of the kinetic and/or potential energy extracted from the wave.
- Secondary level: At the secondary level, the stored energy is converted into a useful form. This involves the use of devices for power take-off (PTO) and level control such as controllable valves, hydraulic rams and pneumatic components along with the associated electronic hardware and software. In this secondary conversion, kinetic/potential energy is converted to the rotational energy of a shaft by means of a turbine.

- Tertiary level: This is the last and final level in which the shaft's rotation within a generator is used to convert the harnessed power into electricity.

2.4.1. Wave Energy Converters (WECs)

Wave energy converters (WECs) capture the energy contained in ocean waves to generate electricity. The concept of extracting energy from ocean waves is not a recent phenomenon. Researchers have been studying different concepts and solutions for wave energy conversion since the 1970s. In the following sections, the variety of existing WEC systems and their basic principles will be described.

2.4.1.1. Wave Energy Converter Classification

Due to the diversity in the ways energy can be absorbed from waves, WEC devices can be classified based on various different attributes. One of the most prevalent ways this has been done in the literature is by using the classification system proposed by Falcao, (2010), which groups the devices into three main categories: oscillating water columns, overtopping devices, and wave activated bodies (heaving buoys, pitch/surge devices, surge/heave/pitch devices and yaw/heave devices). Twelve distinct process variations have also been identified by Hagerman (1995) (Figure 2.11) as follows:

- Oscillation mode: heave, surge, or pitch
- Method of force reaction: against the sea bed or against another, differently oscillating body
- Type of wave–oscillator interface: solid or flexible structure, or water–air interface for an oscillating-water column (OWC)

Hagerman's (1995) modified classification in Table 2.2 (from Brooke, 2003) shows the main generic types of wave energy harnessing schemes. These categories have been slightly updated, and a summary of a few of them is given in the following sections. The main

generic types of wave energy harnessing schemes (Brooke, 2003; Hagerman, 1995) can be listed as follows:

1. Oscillating Water Column (OWC) Systems: These systems include a partially submerged, hollow structure open to the sea below the water line and include OWC-onshore, OWC-offshore and OWC-floating systems.
2. Overtopping Systems: In these devices the water in incident waves is collected to create a head to drive one or more low head turbines.
3. Point Absorber Systems**:** These systems are either floating or mounted on the sea bed and are allowed to heave following the action of the incoming waves. They provide a heaving motion which is transformed by mechanical and/or hydraulic subsystems into either linear or rotational motion which is in turn used to drive electric generators. Subtypes include absorber-point, absorber-multipoint and absorber-directional float.
4. Surge Devices: These devices use the particle velocity of the incoming waves to drive a deflector or to generate a pumping effect with a flexible bag facing the wave.
5. Other Devices**:** These devices comprise any that do not fall within the above-mentioned classes.

WEC devices can also be classified according to location; size and orientation; and energy extraction method as described below.

(a) Classification according to location

WECs can be categorised based on their distance from the shore as onshore, nearshore or offshore (Cruz, 2008; Falcao, 2010) as illustrated in Figure 2.12a. Onshore WEC devices are placed on the coastline. Near-shore devices are those that are located in shallow waters 10–25 km from the coastline. Offshore devices can be located at distances greater than 25 km away. Offshore devices take longer to develop as a result of the harshness of the environment.

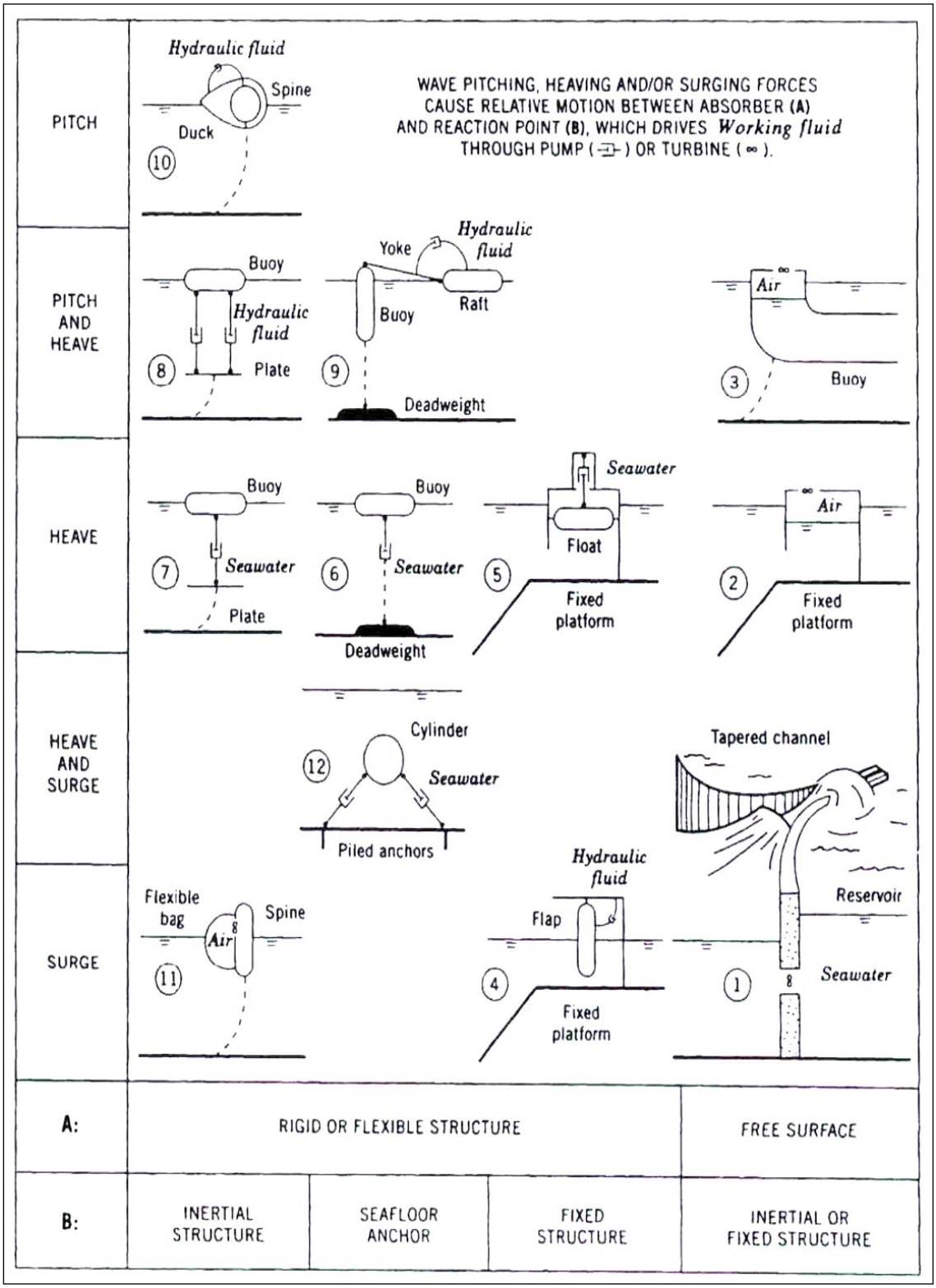


Fig. 2.11: Classification of wave energy converter systems (Hagerman, 1995)

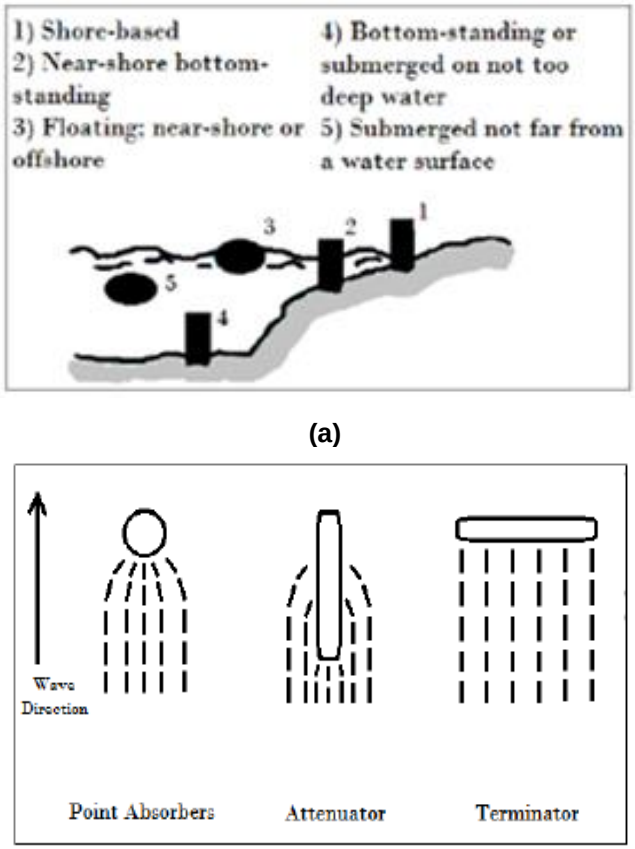
Table 2.2: Classification of wave energy device processes (Source: Brooke (2003) with reference to Hagerman (1995) Figure 2.23)

Location of System	Wave Energy Conversion Process		Reference to Hagerman
Onshore	1.1	Fixed oscillating water column	2
	1.2	Reservoir filled by wave surge	1
	1.3	Pivoting flaps	4
Near shore	2.1	Freely floating oscillating water column	3
	2.2	Moored floating oscillating water column	3
	2.3	Bottom mounted oscillating water column	2
	2.4	Reservoir filled by direct wave action	1
	2.5	Flexible pressure device	11
	2.6	Submerged buoyant absorber with sea floor reaction	12
	2.7	Heaving float in bottom mounted or moored floating caisson	5
	2.8	Floating articulated cylinder with mutual force reaction	-
Offshore	3.1	Freely heaving float with sea floor reaction point	6
	3.2	Freely heaving float with mutual force reaction	7
	3.3	Contouring float with mutual force reaction	8
	3.4	Contouring float with sea floor reaction point	9
	3.5	Pitching float with mutual force reaction	10
	3.6	Flexible bag with spine reaction point	11
	3.7	Submerged pulsating-volume body with sea floor reaction point	-
	3.8	Reservoir filled by direct wave action	1

(b) Classification according to size and orientation, and energy extraction method

If the size of the system is small compared to a typical length of wave, then the WEC is called a point absorber (Budal and Falnes, 1975). This type of system typically has a power rating of a few hundred kilowatts. Hence, a large power plant would need to consist of hundreds or perhaps thousands of such units dispersed in a very long and relatively narrow array along the coast. In contrast, if the system size is large compared to a typical wavelength, then the WEC is called a line

absorber. Line absorbers can be further classified into terminators or attenuators, as illustrated in Figure 2.12b. A wave energy line absorber is a terminator if it is aligned parallel to the main direction of the wave crests, and an attenuator if it is aligned normal to the main wave crests.



(a)

(b)

Fig. 2.12: Classification according to: (a) location (b) size, orientation and energy-extracting method (adapted from Falnes, 2006)

2.4.2. Wave Energy Extraction

The harnessing of wave energy is based on the principle of accumulating water movements to create a small head behind a dam. Extracting energy from ocean waves has been carried out for many years. Nowadays, WEC technology has evolved and several different concepts have been successfully designed and built. It was estimated that in 2013, there were more than a hundred projects at various stages of technological development (Falcao, 2010; Bahaj, 2011). Wave

energy technologies generally consist of a number of components (IRENA, 2014):

1. The structure and prime mover that capture the wave energy,
2. The foundation or mooring that keeps the structure and prime mover in place,
3. The PTO system that converts mechanical energy into electrical energy (of the existing WECs, 42% use hydraulic systems, 30% direct-drive systems (mostly linear generators), 11% hydraulic turbines, and 11% pneumatic systems (IRENA, 2014)),
4. The control systems that safeguard and optimise performance based on operating conditions.

Despite the large variation in their design, WECs can be classified into three main types: attenuator, point absorber and terminator. Attenuators are long multi-segment floating structures that are oriented parallel to the direction of the waves. An example of such a device is the 750 kW Pelamis (Latin for "Sea Snake") shown in Figure 2.13 which was developed by Ocean Power Delivery. The Pelamis consists of four tubular sections (with a diameter of 4.6 m and a total length of 150 m) connected by rams. These sections move relative to each other as a wave passes underneath. The rams pump hydraulic fluid through a hydraulic system, converting kinetic energy into hydraulic and mechanical energy. The Pelamis’s narrow profile enables it to survive extreme weather conditions.



Fig. 2.13: Pelamis (Oregon State University, 2011)

Point absorber devices are floating structures consisting of a buoy connected to a number of components that move relative to each other due to the rising and falling of waves. The mechanical energy generated is used to drive an electrical generator. The electrical energy is then fed down a single cable to a junction on the sea bed. The energy generating capacity of a single point absorber device can be up to 11 MW. There are many examples of point absorbers; one such is Ocean Technology's PowerBuoy, shown in Figure 2.14.



Fig. 2.14: PowerBuoy (Ocean Power Technologies, 2011)

The PowerBuoy system allows the buoy to capture and convert wave energy into low cost clean electricity.

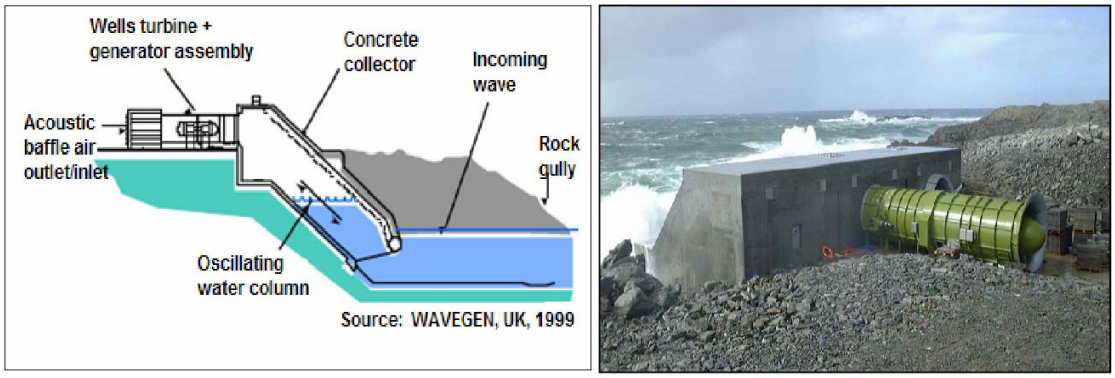


Fig.2.15: LIMPET OWC (The Queen's University of Belfast, 2002)

Terminator devices are floating structures with a floating or bottom-fixed water reservoir. They usually have reflecting arms which ensure that as waves arrive, they spill over the top of the ramp and are restrained in the reservoir. The potential energy of the water collected, due to the height of the water above the sea surface, is transformed into electricity using conventional low head hydro turbines. Examples of terminator devices are the Salter Duck developed at the University of Edinburgh and the LIMPET OWC (Figure 2.15). The energy generating capacity of a single terminator device can be up to 1.5 MW**.** Other representative devices are the WaveDragon (Denmark); Seawave Slot-Cone Generator (Norway); and WaveCat (Spain) (IRENA, 2014).

Most of the energy contained in a wave (95%) is located within the top one fourth of the wave height (IRENA, 2014). This energy can be extracted in different ways depending on the wave's motion. A WEC device that is freely floating can experience up to six degrees of freedom: three translational (surge, sway and heave) and three rotational (roll, pitch and yaw). Some devices are not freely floating, but are restrained to fewer degrees of freedom, for example, due to their connection to the sea bed. In general, the following rules for the extraction of wave energy apply (IRENA, 2014):

- A horizontal front/back wave motion, "surge", can be harnessed with technologies which use a "roll rotation".
- A horizontal side-to-side wave motion, "sway", can be harnessed with technologies using a "pitch rotation".
- A vertical (up/down) wave motion, "heave", can be harnessed with technologies using a "yaw rotation" or "translation".

Another way to categorise wave energy technologies is thus by how the surge, heave, sway or a combination of motions is harnessed (EMEC, 2014). In general, point absorbers use a heave motion to drive a piston up and down; terminators and OWCs convert surge motion, and attenuators use pitch motion to drive a rotor. Despite the fact that these systems are simple (there are no moving parts other than the air

turbine) and reliable, their performance level is not high. The development of new control strategies and turbine concepts are seen as ways to notably increase their power generating capacity. A new generation of floating OWCs integrated on spar-buoys have exhibited substantial improvements in performance. Representative devices include: GreenWave (Scotland/UK); Mutriku (Basque Country/Spain); Ocean Energy Buoy (Ireland); Oceanix (Australia); Pico Plant (Azores/Portugal) and Wavegen Limpet (Scotland/UK) (Papaioannou, 2011; SI Ocean, 2012; IRENA, 2014).

In general, Europe is still the leading market for all wave energy technologies, nevertheless the markets in other countries and regions are growing rapidly. As summarised in the wave technology brief (IRENA, 2014), the first WECs deployed were the 750 kW Pelamis prototypes in the UK and the 2 MW Archimedes Wave Swing 2 prototype in Portugal in 2004. (In 2013, Alstom announced that it would not be investing further in the Archimedes Wave Swing.) In Portugal in 2008, the first wave energy farm (2.25 MW) comprising three Pelamis prototypes were tested. Aquamarine Power has a 315 kW Oyster installed in the Orkney Islands in 2009, and an 800 kW Oyster in 2011 (Figure 2.17 – left). The Danish company Dexawave is running projects in Denmark and Malta. In 2011, the Basque Energy Board (EVE) opened the first commercially-operated wave power plant at Mutriku's breakwater, with sixteen 18.5 kW OWC wave turbines and a total installed capacity of 296 kW (Papaioannou, 2011; SI Ocean, 2012). The Finnish company AW-Energy Ltd. has deployed three, 100 kW WaveRollers in Portugal, and is planning a 1.5 MW farm in France (Figure 2.17 – top right). Another Finnish company, Wello Ltd., is testing its Penguin design (using a rotating mass) in UK waters. The Norwegian company Langlee Wave power moved its activities to the Canary Islands and started pilot projects in 2014. Seatricity installed their 162 kW Oceanus 2 at the Wave Hub Facility in the UK in 2016 (Figure 2.16 – bottom right).



Fig.2.16: Left: Oyster (Aquamarine Power), top right: WaveRollers (AW-Energy Ltd.) and bottom right: Oceanus 2 (Seatricity)

In addition, there are a number of companies working on development of WECs in America, Australia and Canada including Ocean Power Technologies (with pilot projects in Australia, the UK and the US with expansion into Japan), Oceanlinx (with a 1 MW OWC launched in October 2013, in South Australia), Carnegie Wave Energy (with projects in Australia, Bermuda, Canada, Ireland and La Reunion), and Eco Wave Power (with projects in China, Cyprus, Mexico, and the UK). Additionally, China (Guangzhou Institute of Energy Conversion, National Ocean Technology Center, South China University of Technology, Sun Yat-sen University), Japan (Mitsui, Japan Marine Science and Technology Centre) and Korea (Maritime and Ocean Energy Engineering Research Institute (KORDI), Korea Maritime University) have also shown a strong interest in wave energy. All the companies listed above have initiated and continued to support new research, development, pilot testing and demonstration projects (Papaioannou, 2011).

2.5. Floating Breakwater-WEC Integration

The idea of integrating WECs into breakwaters is not new. The world's first wave power extracting breakwater system was installed in Sakata Port in front of the Sea of Japan in the winter of 1989 (Takahashi et al., 1992). Its structure is composed of a special caisson with an innovative configuration which can accommodate Oscillation Water Columns (OWCs) and an engine room with turbines coupled to a generator with an output power of 60 kW. A trial system with harbour walls was also installed in front of the breakwater at Vizhinjam in India in 1991 (Raju and Neelamani, 1992). This wave energy plant was equipped with Wells turbines with a power of 150 kW. It has also been used to test different types of air turbine, including impulse turbines. Research into integrating OWC-type wave energy extraction systems into caisson breakwaters has also been carried out by Matrins et al. (2005), Boccotti (2007), and Arena et al., (2013), among others.

Vicinanza et al., (2014) combined rubble mound breakwaters and WECs in an innovative way such that wave energy is extracted by collecting wave overtopping in a front reservoir and turbines are driven as the water collected returns to the sea. Orer and Ozdamar (2007) investigated the efficiency of a plate wave energy converter which can also perform the function of a breakwater. In their design, a pulsating flow occurs below the plate opposite to the direction of wave propagation, which can be used to drive turbines. An efficiency of approximately 60% can be achieved by modifying the structure below the plate. He and Huang (2014) experimentally investigated the hydrodynamic performance of a pile-supported OWC structure which can act as a breakwater and has the potential to utilise wave energy. As their design incorporates a fixed structure, the cost of installation would rise with increasing water depth.

The integration of wave energy devices into floating breakwaters has not been studied extensively as yet. Hong et al., (2006) theoretically investigated the hydro-elastic response of a very large floating structure

(VLFS) placed behind a reverse T-shaped freely floating breakwater with an OWC. Hong et al., (2006) claimed that if the reverse T-shaped floating breakwater is connected to the very long floating structure (VLFS) by a pin, it will likely act as an anti-motion device. Using a fully nonlinear numerical model, Koo (2009) investigated the motion response of a floating box-shaped breakwater that serves as a WEC. The pneumatic damping system in the breakwater is provided by an airflow nozzle at the top of the chamber whereby energy is dissipated as the air passes through the outlet. Koo (2009) reported that the maximum body displacement occurs for frequencies near the resonance period of the column. He et al., (2012; 2013) integrated an OWC-type device with a slack-moored floating breakwater and found that with this system, a broader frequency range for energy extraction was created and there was also an improvement in wave attenuation for longer-period waves. Michailides and Angelides (2012) introduced a new type of flexible floating breakwater (FFB), which acts not only as a shore protection structure, but also as a wave energy device. The structure captures wave energy through the relative motion between adjacent floating modules. The authors also theoretically investigated the hydrodynamic performance of the FFB under PTO damping using linear hydro-elastic theory. Zanuttigh et al., (2010; 2013) experimentally investigated the feasibility of using the DEXA WE device as a wave attenuation structure. The device consists of two rigid pontoons with a hinge in between, which allows the pontoons to pivot in relation to each other. The study focused on the wave field around the device, the wave transmission and reflection. The results suggested that the DEXA structure can be integrated into coastal protection schemes.

Ning et al., (2016) conducted an experimental study on a novel integrated system comprising a vertical pile-restrained floating breakwater which works on the same principle as an oscillating buoy WEC. Their integrated system has a box-type floating breakwater as its base structure. A PTO system is installed above the floating breakwater body with no requirement to change the geometry of the original base

structure. The heave motion of the floating breakwater is controlled by the PTO system through the transmission mechanism, and wave energy is captured from the kinetic energy related to the heave motion of the floating breakwater. However, the magnitude of the PTO damping force could potentially affect the motion of the floating breakwater, and in turn alter the transmission coefficient. It may thus be possible to optimise the capture width ratio (CWR) and transmission coefficient of the integration system. The PTO damping characteristics and the effects of various parameters including the wave period, wave height, system dimensions and excitation current, on the hydrodynamic performance were investigated. Results indicated that the PTO damping force, the draft and the ratio between the width of the floating breakwater and the wavelength have a significant influence on hydrodynamic performance. It was concluded that the floating breakwaters examined perform more efficiently under larger PTO damping forces and there is no need to modify the geometry. It was also found that breakwaters can be utilised for energy extraction if the appropriate dimensions and PTO damping force are selected based on the dominant sea state at the deployment site. Incident wave height was found to have little influence on reflection and transmission coefficients but it was found to have a significant effect on the capture width ratio (CWR = $P_{average}/P_{incident}$). It was found that with careful adjustment of the PTO damping force, the CWR of the system can reach 24% while the transmission coefficient remains lower than 0.50 and as such the design is effective.

An invention similar to a parabolic concentrator was proposed by Energetech Australia Pty. Limited in 2005. In 2007, the company changed its name to Oceanlinx and patented the concept (Denniss, 2007). This design includes a plane wave focusing and amplifying structure comprised of an open sided bay bounded by a generally upright wall. The wall is oriented such that it admits advancing wave fronts in a direction generally parallel to the axis of symmetry. Upon reflection from the wall, the waves converge to an energy harnessing

region near the apex or adjacent to the focal point of the parabola, thereby amplifying the vertical displacement of the waves in that region. The parabolic-shaped wall allows capture of a wide band of incident wave energies, thus increasing the production capacity of the device. The conceptual design also includes an oscillating water column (OWC) at the focal point of the parabolic wall such that the amplified waves are concentrated at the chamber allowing efficient energy conversion from incident waves over a range of angles. The parabolic focusing device is shown in Figure 2.17. The current Oceanlinx products do not include the curved wall collector element.

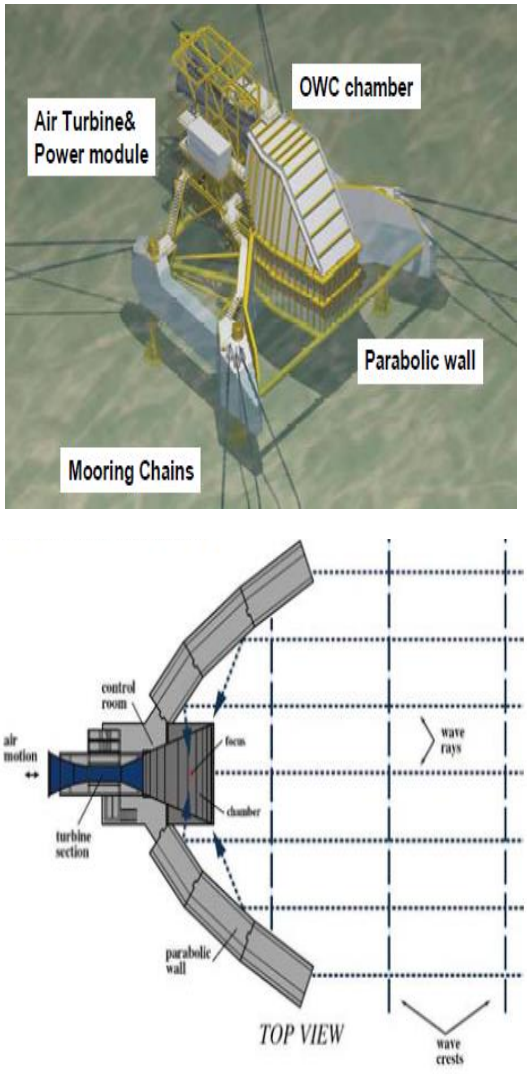


Fig. 2.17: Parabolic focusing device (Denniss, 2007)

The concept of a parabolic concentrator element was also included in a more recent project that promised to deliver the next generation of floating WEC devices called the Curved CCells paddle. This device is made from composite materials and controlled by a new type of dynamic PTO system. In order for the curved paddle wall illustrated in Figure 2.18 to adsorb incident wave energy, it needs to move so it creates a wave that is exactly out of phase with the incident wave. When the waves cancel each other out, no energy remains in the water at the paddle wall's boundaries and the original wave energy is transferred to the moving wall.

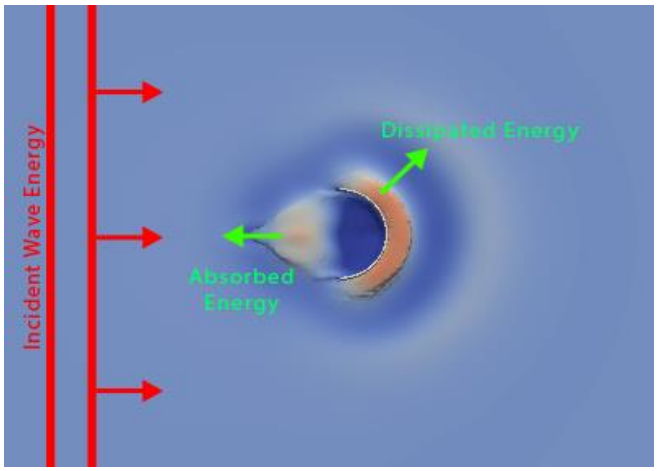


Fig. 2.18: Moving curved CCell paddle (http://www.ccell.co.uk)

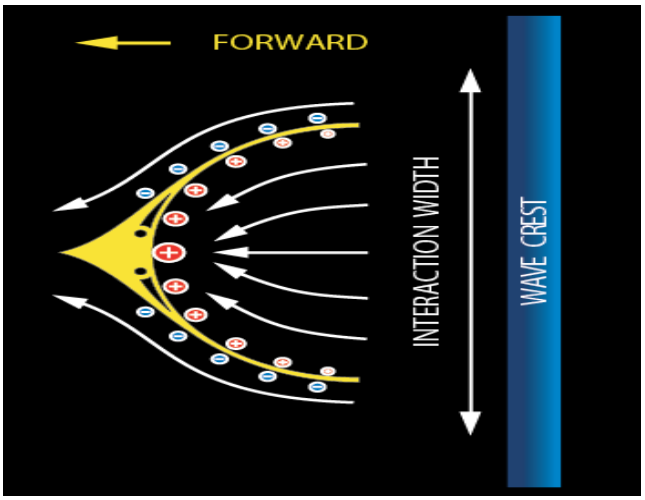


Fig. 2.19: CCell paddle operation (http://www.ccell.co.uk)

The CCell collects energy by harvesting power from the open sea. Flexible curved guides focus the incoming waves towards a strong central core, illustrated in Figure 2.19, which drives hydraulic pistons that extract the power. The curved shape also creates a beneficial pressure on the shore face of the paddle, dramatically increasing the net force across the paddle when the paddle is within both wave crests and wave troughs. Much like the wing of a plane, this effect dynamically increases the catchment width of the CCell, leading to an estimated effective width of over 120%.

In 2012, laboratory tests were performed in the wave flumes at UCL on a selection of curved and flat paddle shapes, to assess the importance of the curvature of the CCell for absorbing wave energy. The curvature illustrated in Figure 2.20 was found to not only increase the forces and power delivered to the piston, but also caused a noticeable reduction in turbulence around the paddles. The tests demonstrated that the curved CCell paddles would extract energy from waves within both a wave crest and a wave trough. Through the use of rapid prototyping and short development cycles, the project is aiming to deploy nine 20 kW units within three years. Several of these will be deployed to provide power to two remote islands. A curved CCell paddle 0.5 m wide (1/5th the width of the tank in the experiments) was found to deliver 2 to 3 times more power than an equivalent flat paddle. In 2015, the CCell project won £1.8M to develop the next generation of CCell units. No further information is available on the current status of the CCell project.



Fig. 2.20: Curved CCell paddle (http://www.ccell.co.uk)

Findings from the literature concerning breakwater-WEC integration and projects such as the Oceanlinx wave focusing WEC and the curved CCell paddle are encouraging for the idea of utilising wave energy cost effectively in the coastal areas of Kuwait.

2.5.1. Potential Application for Kuwait

Neelamani et al., (2007) have encouraged the use of floating breakwaters for erosion protection of the Kuwaiti islands and for new harbour breakwaters, particularly from an environmental point of view. Wave energy potentials and significant wave heights and periods have been predicted statistically for 19 different locations in the Kuwaiti territorial waters based on 15 years' worth of historic wave data (Neelamani et al., 2007). For the 19 locations considered, the extremely significant wave height varies from 1.86 to 4.02 m and the mean wave period in the Kuwaiti sea was found to range from 4.2 to 6.3 sec for the significant wave heights corresponding to a 100-year return period. It is essential to consider the wave power potential of Kuwaiti territorial waters before planning any WEC installations. From the Hydrodynamic

Atlas and the extreme wave analysis for Kuwaiti territorial waters discussed above, it is clear that the marine areas surrounding Qaru Island and Umm Al-Maradim could be potential sites for wave energy power plants (Neelamani et al., 2007). The water depths about 1000 m away from the islands reach 25 to 30 m, hence floating wave energy devices would be the most appropriate.

Three years' worth of data for the hourly variation of wave power around Qaru Island was collected and indicate that the wave power available varies from 0 to 16 kW/m (data reproduced in Figure 2.21a) (Neelmani, 2009). Furthermore, from the graph showing the probability of exceedence of wave power around Qaru Island (reproduced in Figure 2.21b), it can be seen that a wave power greater than 1 kW/m is available for more than 12% of the year. It is estimated that over a period of 1 year, the total incident wave power is about 6000 kWh at this location. The wave climate around Qaru Island is thus suitable for the installation of a wave power device with the extracted power sufficient for the utility services on Qaru Island. However, with the low wave power density and limited resources of good quality stone in the area, there is a need to find a suitable coastal protection structure which can protect the island from wave attacks and erosion as well as locally increase the energy density of the waves. In order to attenuate the waves, the floating breakwater must have a dimension extending in the direction of waves, typically on an order of the wave length. Also, the floating breakwater must have a reasonably deep draft to extend to depths equal if not greater than the amplitude of the waves. In addition, a hydrodynamic resistive shape is desirable, rather than a more streamlined shape. As discussed in section 2.3.6, wave focusing by the introduction of a parabolic shape element is very attractive for this site. A parabolic concentrator would be the best solution as it can function as a breakwater, a WEC device and a mooring facility. The amplified and focused wave energy inside the parabolic breakwater structure could be converted into usable power using a wave energy device.

It is not necessary to construct the concentrator to extend up from the sea floor, as wave action is typically confined to the upper strata of the water. Accordingly, it has been found that the proposed floating concentrator can also provide the desired attenuation of wave action, when provided with the proper characteristic and moored in appropriate locations.

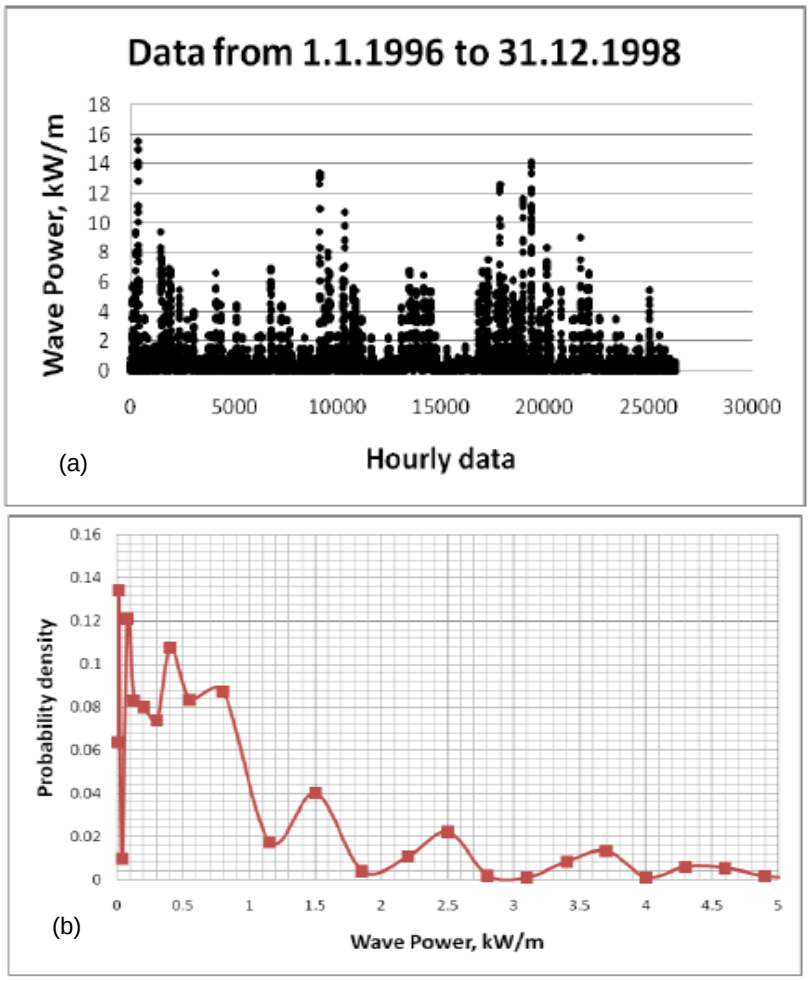


Fig. 2.21: The hourly variation (a) and probability density (b) of wave power around Qaru Island for 3 years (Neelamani, 2009)

There are a wide range of wave energy technologies which can be applied in combination with floating breakwaters depending on water depth and location (shoreline, near shore, offshore) (Cruz, 2008; Falcao, 2010). Kuwaiti territorial waters are up to 25–30 m deep

(Neelamani et al., 2007). Bottom-fixed near shore devices are intended for use in shallow waters typically 20–25 m deep. These have nearly the same advantages as onshore devices in that they are relatively easy to install and maintain, however they tend to be exposed to higher power waves. Offshore wave energy devices are intended to make use of the greater energy content of waves found in deeper water (depth > 25 m). Furthermore, 67% of the current WEC concepts are floating, and only 19% are fixed (IRENA, 2014).

Despite the numerous integrated WEC-breakwater concepts that are detailed in section 2.5, the idea of integrating WE devices into floating breakwaters has not been the studied extensively. The research which has been carried out on floating breakwaters in combination with OWCs and oscillating buoys was discussed earlier. Babarit et al., (2012) conducted a study on the selection of WECs and eight wave energy converters with different working principles were considered. Their performance at five prospective locations with depths ranging from 40 to 100 m was estimated. For each device, a numerical Wave-to-Wire time-domain model was built and the power matrices of each device were computed. By multiplying these power matrices with the wave scatter diagrams at each site, the annual mean absorbed power for each device at each site was derived. The devices considered were: a small bottom-referenced heaving buoy, a bottom-referenced submerged heave-buoy, a floating two-body heaving converter, a bottom-fixed heave-buoy array, a floating heave-buoy array, a bottom-fixed oscillating flap, a floating three-body oscillating flap device and a floating oscillating water column. The aim was to compare the devices in terms of annual absorbed energy per unit of characteristic mass, per unit of characteristic surface area and per unit of characteristic PTO force. The power matrices of each WEC were computed from numerical models in order to calculate the annual absorbed energy. It was found that the annual absorbed energy differed significantly from the lowest, 2 kW for the small bottom-referenced heaving buoy at the least energetic site, to the highest, 800 kW for the bottom-fixed oscillating flap at the

most energetic site. This was expected as the devices compared differ greatly in their size and working principles.

The performance measures estimated in the study by Babarit et al., (2012) reflect the main cost drivers to be considered when selecting a WEC to combine with a parabolic breakwater. Babarit et al., (2012) stated that the absorbed energy relative to the dimension-related parameters of the device is of primary concern. A point absorber has a relatively low capital investment and high power capture to mass ratio (Budal and Falnes, 1975). Being much smaller than the incident wavelength, a point absorber also has the added benefit of being capable of converting more power than is directly incident on its body and the power it produces is greater if the waves are amplified since, according to linear wave theory, power is proportional to the square of the wave amplitude (Yang and Ertekin, 1991).

Pioneering experimental research on point absorbers was performed by Budal et al., (1975; 1980). Although there has been a significant amount of research since on point absorbers by Budal, Falnes and others (detailed in chapter 3), to date there are no parabolic concentrator-point absorber WEC devices in use which highlights the need for development of this innovative conceptual design. The research presented in this thesis aims to optimise the configuration of this type of device and assess its potential for power production and commercial application based on the wave conditions in Kuwait.

2.5.2. Cost Sharing

Cost sharing is an effective way of reducing the capital costs of an engineering installation, and integrating WECs into breakwaters provides a promising way to realise cost-sharing in wave energy technology (Ning et al., 2016). In 1996, Graw discussed the advantages of sharing the construction costs of a breakwater-WEC system. With breakwater-WEC integration, installation costs are reduced for both the

electricity producer and the authorities who wish to provide shelter for the coastal area or structure.

On the basis of a designed breakwater-WEC's characteristics, the economic feasibility of the structure can be assessed by first measuring the amount of material which is active in carrying load in the structure and then determining how much material is required for a large-scale structure. This is defined as the structural capacity (Garvey, 2010). The capacity of a structure is related to the magnitude of the force that it carries and the distance over which this force is transmitted. The unit of structural capacity is thus force × distance (with units of Newton metre). Although dimensionally structural capacity has the same units as work and torque, physically it is quite different. Very few studies on structural design have referred to this measure (Garvey, 2010) and no discussion has been provided as to what materials provide the greatest value in terms of (force × distance) capacity per unit cost. The total potential of a structure to carry load is related to the product of the total volume of structural material and the maximum allowable stress that the material can withstand.

In the study in which the curved CCell paddle was developed, a curved structure was found to be naturally stiffer than a flat structure with the same width (CCell, Zyba Ltd). By curving a flat paddle, 90% less material is required to achieve the same overall stiffness, or alternatively, peak stresses can be reduced by 80% using the same plate thickness, as illustrated in Figure 2.22 (CCell, Zyba Ltd). Moreover, the CCell paddle is designed to be flexible within the guides of the unit and strong in the centre. This is achieved through a variation in thickness which further reduces the overall mass and improves the life of the paddle by reducing fatigue. An economic analysis conducted by Zyba Ltd. showed that the CCell can deliver a four-fold improvement in installation costs in £/W; a small unit can be installed at a price of £2.5/W and OPEX costs below £50/MWh are achievable. The CCell is thus one of the few concepts that could make wave energy economically viable.

The most significant cost after the cost of the structure is related to the PTO system (Naty et al., 2016). The latest estimates from European wave energy projects also suggest that the PTO system accounts for 22% of the total lifetime project costs with installation 18%, operation and maintenance 17%, foundations and mooring 6%, and grid connection 5% (SI Ocean, 2013). Hence the economic viability of a breakwater that will be utilised for energy extraction not only depends on the structure's optimum geometry but also on the PTO system employed. In section 2.5.1, a point absorber was identified as the most appropriate wave energy device for harnessing the amplification effects provided by a parabolic structure. In order to increase device efficiency and minimise energy production costs, it is necessary to optimise buoy geometry and PTO system configuration. This will be investigated in depth in Chapter 3 based on the dominant sea state at the proposed deployment site in Kuwait.

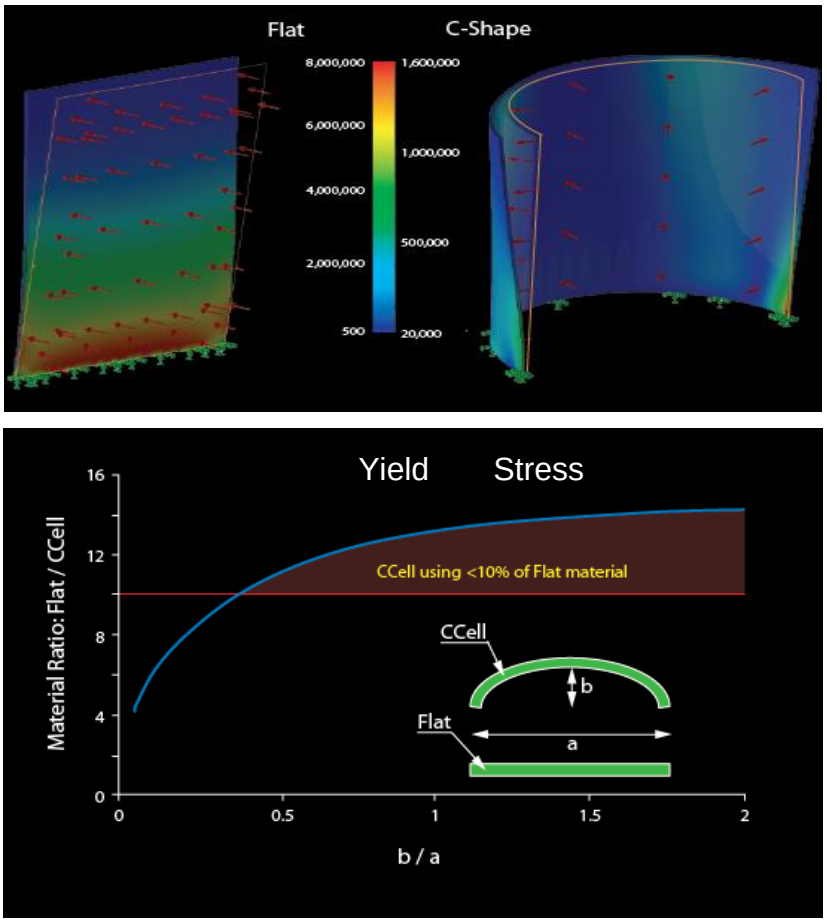


Fig. 2.22: Material ratio flat/CCell structure (http://www.ccell.co.uk)

2.6. Conclusions

The purpose of the comprehensive literature review presented in this chapter is to identify a viable solution to protect the Kuwaiti coastline and Qaru island in particular from wave attacks and erosion. The conducted literature also aimed at finding a method of protecting the island with a breakwater system that also provides an opportunity to generate energy by locally increasing the energy density of waves to make wave energy conversion (WEC) more efficient, cost-effective and commercially competitive. The wave climate around Qaru Island was found to be suitable for the installation of a WEC device and a floating breakwater was identified as the most appropriate type to be combined with the WEC device.

In addition, with the low wave power density and limited resources of good quality stone in the area of interest, the chapter provided the first evaluation of the potential of a parabolic concentrator to enhance wave energy conversion around the island. A parabolic concentrator was found to be the best solution as it can function as a breakwater, a WEC device and a mooring facility. The amplified and focused wave energy inside the parabolic breakwater structure could be converted into usable power using a wave energy device.

The main objective of the work presented in this thesis relates to the development of various WEC elements to be combined with a floating parabolic breakwater with a particular focus on optimising conversion efficiency and the concept of focusing waves. The combination of a parabolic concentrator with a point absorber was assessed further in section 2.5. Selection of a suitable point absorber WEC and optimisation of its geometrical and control parameters will be conducted in chapter 3. The will be done by developing a steady-state harmonic model that can simulate the motion of a single buoy with one degree of freedom (heave) along the vertical axis. The model will be used to identify the best point absorber configuration at which power absorption from incident waves is maximised. This concept is developed in more

detail in Chapter 4 where design of a parabolic concentrator-point absorber geometry is proposed and the likely impact/benefit of such a technology is investigated experimentally. A CFD modelling approach suitable for analysing wave behaviour in the presence of a geometrically representative parabolic concentrator-point absorber device will be developed in chapter 5. The experimental testing will be used to generate data to validate the CFD modelling work. Reassessment of the viability and cost effectiveness of the proposed prototype system will be provided in chapter 6.

A theoretical background to aspects related to the hydrodynamics of waves and floating body theory, ocean wave characteristics and wave energy density will be provided in chapter 3. There are additional literature review elements incorporated in Chapters 3, 4 and 5 of this thesis as they are related specifically to the research topics presented within these chapters and are particularly intended for the reader who is not familiar with these topics.

Chapter 3: Steady-State Harmonic and Time Domain Point Absorber Modelling

A point absorber system is a complicated dynamic system in which the buoy is connected to a PTO-driven generator in order to capture the wave induced motion to turn it into electrical power.The buoy motion depends on the buoy geometry and dimensions, the mass of the moving parts of the system and on the damping force from the generator. The damping in the generator depends on both the generator specifications, the connected load and the buoy velocity. In this chapter the buoy geometrical and control parameters have been used to study how the buoy geometry, assuming constant PTO damping coefficient, affects the motion and the energy absorption of a WEC. The geometrical parameters include a linear radiation damping term c_2 which defines the geometry of the buoy. The control parameters relate to the PTO damping mechanism, c_1.

The aim of this chapter is to develop a steady-state harmonic model that can simulate the motion of a single buoy with one degree of freedom (heave) along the vertical axis. The model can be used to optimise a buoy's geometrical and control parameters to maximise its power absorption from incident waves. To increase wave device efficiency and consequently minimise energy production costs, a novel approach to optimising the geometry and performance of heaving point absorbers was utilised by fixing buoy mass and using the values for c_1 and c_2 which gave the greatest power absorption. The power response was thus maximised by using the best value for c_2 from the region driven by high c_2 for determining the best value of c_1 for a mass equal to the optimum mass.

The steady-state harmonic model developed was verified against results from a time domain model after the models' transient responses were allowed to settle down to steady state. The optimisation approach developed within the chapter could be used to help realise major economic design benefits for a point absorber buoy of any shape for a given sea state. Buoy behaviour is simulated based on the assumptions of regular waves and a constant PTO damping coefficient. This approach is standard practice for this type of modelling and hence was a natural starting point for this work.

A literature review of the proposed methods for increasing the efficiency and power absorption of wave devices, and consequently to minimise energy production costs, is given in section 3.1. In the second section, a theoretical background to aspects related to the hydrodynamics of waves and floating body theory, ocean wave characteristics and wave energy density is provided. This section is particularly intended for the reader who is not familiar with these subjects. The basics of linear wave theory as well as the supporting assumptions are reviewed and the dynamics and forces acting on a floating body in regular wave conditions are illustrated. The third section of the chapter goes on to determine the solution to the differential equation describing the heaving motion of a point absorber. At first, the solution for a simple mass-spring-damper system is considered. This is then extended for a point absorber subjected to external control forces such as the wave and damping forces which act on a buoy. The analysis method for the time domain model is described in section 3.4. A numerical approach was employed, and the dynamic equations describing the motion of the buoy were formulated and analysed in the time domain using the software MATLAB. The differential equations describing the motion of the buoy were derived and solved using the common 4th order Runge-Kutta method. In section 3.5, a steady-state harmonic model describing the motion of a buoy is developed in MATLAB. Validation of the steady-state model against the time domain model is presented in section 3.6 using the steady-state results from both models. In section 3.7, the

validated steady-state harmonic model is developed further and in section 3.8 it is used to optimise the geometrical parameters of different buoy shapes to maximise their power capture. Details of the codes developed in MATLAB are given in Appendix 3.

3.1. Literature Review

To date, research into increasing the energy absorption of heaving point absorbers under regular waves has focused on tuning the WEC system to oscillate in resonance with the incoming waves. If a point absorber buoy is in resonance with incident waves, it will see increased displacement amplitudes and velocities, and therefore absorb more energy than when it is not (Budal and Falnes, 1975; Falnes, 2002). To achieve resonance, the phase and amplitude of the point absorber oscillation have to be chosen carefully to ensure optimal performance. Phase and amplitude can be varied independently through phase and amplitude control factors (Cruz, 2008). These control factors are considered optimal for a desired point absorber motion when maximum power absorption is achieved. This can be calculated for a single buoy in multiple degree of freedom motion or in single degree of freedom motion. An optimal result can be obtained by forcing both the amplitude and phase to take particular values. As summarised by Price (2009), the various stages required to convert the power absorbed from a wave to the final useful energy are as follows (see Figure 3.1):

- **Stage One:** is the flow of power between the wave (0) and the primary interface (1), giving the intercepted power.
- **Stage Two:** is the flow of power between the primary interface and the (PTO) (2), giving the captured power.
- **Stage Three:** is the flow of power between the PTO and the final stage of power conversion (3), giving the delivered power.

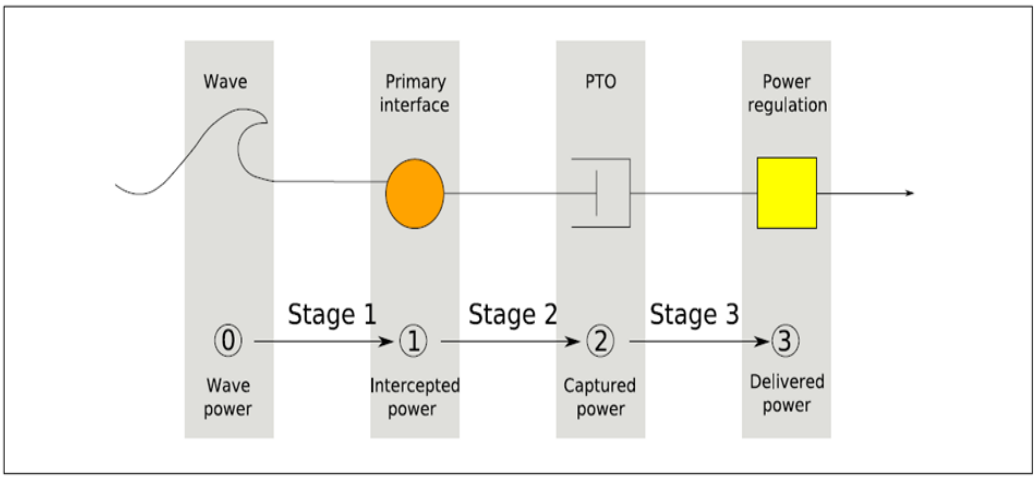


Fig. 3.1: Power transfer in a generic WEC (Price, 2009)

In a point absorber system, the buoy is connected to a PTO-driven generator in order to capture the wave induced motion to turn it into electrical power. A point absorber can be considered as a mechanical system with two sets of parameters, namely geometrical parameters and control parameters. The geometrical parameters define the structure of the buoy and cannot be changed once the buoy is built. The control parameters are related to the PTO damping mechanism and are usually variable parameters that can be tuned to match a given sea state. Motion control of WEC devices has been the focal point of much research with the view to increasing performance and thus the competitiveness of particular devices in the energy market. Hence, numerous techniques mainly based on latching, unclutching or phase control (Salter et al., 2002) have been developed and applied to wave devices to improve efficiency and minimise energy production costs. These will be discussed in detail below.

With regular waves, the maximum power absorption for a heaving point absorber WEC can be achieved when:

1. The velocity profile of the device is in phase with the excitation force of the waves (Falnes, 2002).

2. Energy is supplied during the wave cycle to maximise the velocity excursion (Falnes, 2002).

As the second condition requires very complex PTO mechanisms, it is rarely considered. However, a limited number of solutions have been proposed for condition one. These include:

- Linear damping: by applying a constant linear damping coefficient (Nolan et al., 2005).
- Freewheeling or Declutching: by allowing the device to freewheel (unloaded) from the extrema (i.e. allowing velocity to increase and then applying load only after a certain velocity threshold is reached) (Salter et al., 2002; Wright et al., 2003; Babarit et al., 2009).
- Latching: by locking the buoy in a position at the instant when its velocity becomes zero and then releasing it after a fixed period of time (Budal and Falnes, 1975; Falnes and Lillebekke, 2003; Babarit et al., 2004; Korde, 2002; Wright et al., 2003; Greenhow and White, 1997).

Early theoretical work by Budal and Falnes (1975), Newman (1976), and Evans (1976) showed that a single point absorber is able to capture power from a wave crest width greater than the width of the buoy itself, giving potential greater power extraction when collecting power from a given length of beach. Budal and Falnes (1975) demonstrated that a single point absorber (buoy) in simple heave motion can extract maximum power from a crest length of $1/2\pi$ wavelengths of an incident wave. For real buoys, the heave amplitudes required for maximum power extraction are available only in resonant conditions. Outside resonant frequencies, the power absorbed decreases markedly. This was illustrated in Budal and Falnes' (1975) work where the power absorption of a semi-submerged sphere was plotted as a function of wave frequency. At resonant frequencies with no frictional damping, the power recovery of a linear PTO damper (generator) was seen to reach the theoretical maximum. However, on

either side of the resonant frequency, the dynamic heaving response of the buoy was insufficient to reach the levels required for maximum theoretical power recovery (Duncan and Brown, 1982). Lighthill (1979) reviewed the physical aspects related to this behaviour and noted that in order to broaden a buoy's frequency response, the external PTO damping coefficient should be set higher than the optimum at resonance. Evans (1976) found that while working in a single mode with a linear PTO mechanism, wave power extraction characteristics can be controlled through added damping alone without any requirement for added mass. The absorption length of the device was calculated by applying an added damping approximation curve to the linearly controlled heaving sphere. The absorption length was defined as the length of wave frontage for which the power equals the time averaged power absorbed by the sphere. Parameterisation of the added damping was also carried out by Greenhow (1982) to calculate the wave absorption characteristics of a heaving sphere with linearly and non-linearly phase controlled motion. By parametrising the added damping for 2D and axially symmetric 3D wave power devices, the main features of power extraction with linear and non-linear PTO mechanisms was modelled very easily.

The need for reducing WEC device costs is mainly due to their high costs of installation and maintenance. Studies have been undertaken to optimise the hydrodynamic performance of various WEC devices to increase their efficiency of energy extraction from waves. Vantorre et al. (2004) varied buoy geometry, PTO damping and the supplementary inertia required for phase control, maximising efficiency and increasing the capture width of a heaving point absorber device intended for deployment in the North Sea off Belgian coastlines. In Babarit and Clement (2006), three different latching control strategies were compared to show their effectiveness in different sea states with all three strategies giving a considerably increased efficiency in irregular waves. Nolan et al. (2005) proposed latching as an optimal strategy to bring a device's velocity profile back in phase with the wave excitation

force. The most important control variable was found to be the latching period which was determined based on the excitation force and system parameters. The study also revealed that the system must be designed so that the device's resonant frequency is equal to the predominant wave frequency at the deployment location, and some type of provision must be made for when the wave frequency deviates away from the predominant value. Yavuz et al. (2006) assessed the performance of a point absorber where the resonance was tuned by varying the PTO characteristics. Results showed a maximum power capture of 50% of the rated power in regular waves. This work was continued in Yavuz et al. (2007) to consider irregular waves, where it was shown that power capture can be maximised by continuously tuning the natural frequency of the device to the incoming wave frequency. Falcao (2007) performed a time-domain analysis to evaluate the hydrodynamic performance of a heaving floating device coupled to a hydraulic PTO unit. He developed an algorithm to optimise the device which showed its performance to be weakly dependent on wave period and independent of wave height when simulated in real sea conditions. It was also found to produce power output at similar levels to a fully linear PTO unit. Falcao (2008) continued the study, and included a strategy for phase control of latching in the frequency domain to further increase the power absorbed. In Falcao (2009) paper, the geometrical configuration of a two-body heaving point absorber was optimised through phase control in the frequency domain.

Folley and Whittaker (2009) proposed a new control method called active bipolar damping or declutching. In this method the buoy's velocity is shifted so it is in phase with the wave force. Theoretically, this method showed potential for higher power capture than that achievable with optimum linear damping without the requirement of reactive energy storage. A linearised model was investigated by Babarit et al. (2009) which included a hydraulic PTO. Results showed greater power levels could be achieved with the declutching control method which provided the added advantage of requiring a less complex system. The

recommendations in Babarit et al., (2009) for the use of the economical declutching method were confirmed by Teillant et al., (2010). Teillant et al., (2010) determined the best control strategy to apply based on the relative resonant frequency of the device and the monochromatic wave frequency set. Both latching and declutching strategies were considered via a general parametrisation of the damping force. The optimal damping profile was calculated for a range of incident wave frequencies, including the resonant frequency of the device. A set of 11 successive wave frequencies were examined (ω = 0.4 – 1.3 rad/s plus the resonance case). For frequencies on either side of the resonant value, the results for maximum energy absorbed clearly indicated there was an optimal strategy for control. The optimal damping strategy moved from a latching strategy when $\omega_i < \omega_n$ to a declutching strategy when $\omega_i > \omega_n$ where, ω_n is the natural resonant frequency of the device, and ω_i is the incident wave frequency. Interestingly, a hard switching function for PTO damping was preferred in both cases. In most of the above investigations, linearised models with idealised hydraulic circuits were used. Cargo et al., (2016) conducted an extensive study on the modelling of a PTO system considering real hydraulic circuits and components. He demonstrated that over-simplification of the PTO during the simulation phase of WEC development could lead to incorrect design decisions and subsequent additional delays and costs. Bachynski et al., (2012) investigated the effects of geometry, mooring system and mass distribution on a tethered WEC in irregular waves through linear frequency domain analysis of coupled pitch and sway motions. Their results highlighted the importance of tuning the system for a specific wave climate in order to maximise the total energy capture and avoid potential WEC failure. The effect of WEC geometry was also investigated by Sjokvist et al., (2014). In this study, a velocity ratio (B) was used to study how the buoy draft and radius, assuming constant PTO generator damping coefficient, affected the motion and the energy absorption of a WEC. It was concluded that an optimal buoy geometry can be identified for a

given generator damping. When B was used to analyse experimental results from two WECs with identical generators but different buoys, it was found that the difference in output power derived partly from the buoy draft, but was independent of the buoy radius. It was concluded that the B is more informative than the capture width ratio (CWR) when designing and analysing data for point absorber WECs. CWR is defined as the ratio between the power absorbed by the WEC's generator and the total in time average incident wave power that is travelling through the buoy. It was also concluded that optimal buoy radius can be identified for a specific PTO generator damping. For example, the optimum buoy radius for 7.4 kNs/m, 20 kNs/m and 30 kNs/m of damping are around 1.75 m, 2.5 m and 3 m, respectively. For damping of 20 kNs/m and 30 kNs/m, however, there was no difference in the results for buoy radius values of 2.5 m, 3 m or 3.5 m. Smaller buoys were found to be more favourable with lower damping, while larger buoys were more favourable as the damping increased. Considering the cost of manufacturing, a buoy with a lower radius would be preferred.

Using phase control to shift a point absorber's natural frequency close to the resonance condition by adding a supplementary mass (Vantorre et al., 2004; De Backer, 2008) or a negative mechanical spring (Falcao, 2010) has also been studied. Phase control by adding a fully submerged body to suitably tune the device's natural frequency based on PTO damping has been investigated by several authors (De Backer, 2008; Engstrom et al., 2011; Waters et al., 2011). Passive control was also studied by Piscopo et al. (2016) combined with the development of a new optimisation procedure for heaving point absorber hydrodynamic performance with the aim of maximising yearly energy production. Their optimisation procedure allows for varying the fully submerged added mass and the PTO damping until the optimum configuration is detected. It was concluded that the deployment site plays a fundamental role in the assessment of WEC optimum configuration.

3.2. Background Theory

3.2.1. Ocean Wave Characteristics

The simplest ocean wave form is a regular sine wave. The main parameters which are used to describe such a wave are the period, T, height, H, and water depth $,d,$ over which it is propagating. The propagation environment depends mainly on the depth (shallow, transitional or deep). All other parameters, such as water velocities, accelerations, and kinematics (motions) can be determined theoretically from these quantities. The principal types of sea waves are deep water waves and inshore waves, and these are either destructive, constructive or refracted. In addition, there are two main groupings of waves: regular (sinusoidal) and irregular. Although ocean waves are never actually sinusoidal, low amplitude swells may come close to being sinusoidal as shown in Figure 3.2.

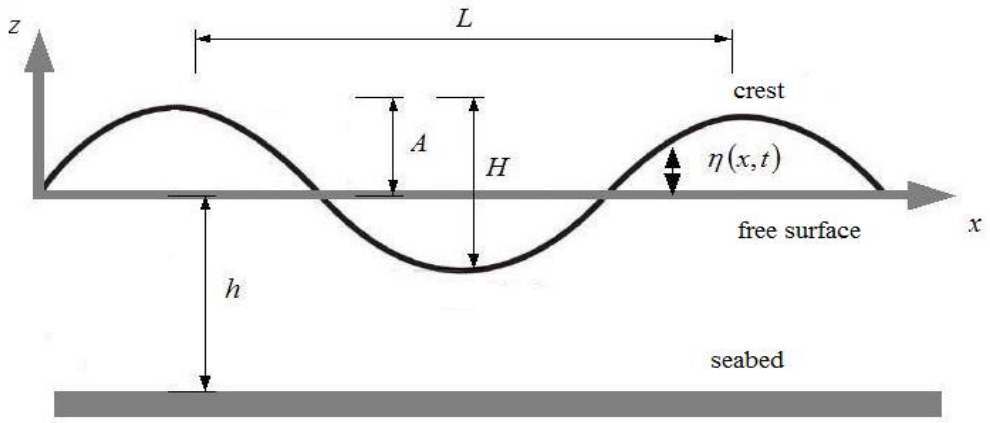
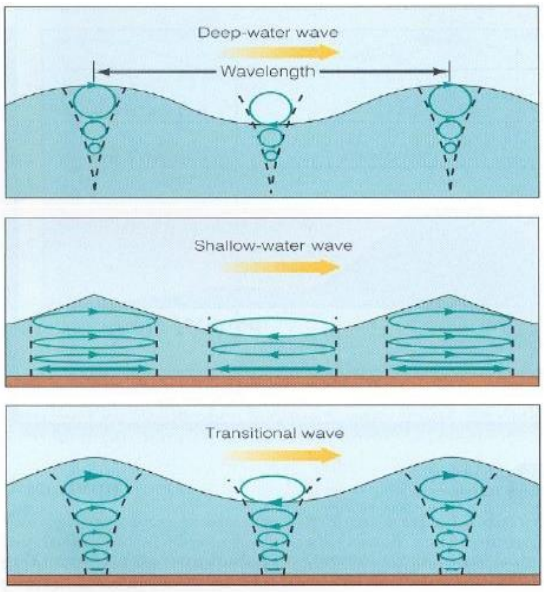


Fig. 3.2: Ocean wave characteristics (Anon, 1984)



Crest: the high point of a wave.
Trough: the low point of a wave.
Wave Height (H): vertical distance from trough to crest.
Wave Length (L): horizontal distance between adjacent crests.
Wave Period (T): the time for a wave crest to travel a distance equal to one wave length.
Wave Frequency (f): the inverse of the wave period.
Wave Speed (C): the ratio of wave length and wave period.

Fig. 3.3: Wave depth propagation (www.slideplayer.com)

Classification of the propagation environment is illustrated in Figure 3.3 and summarised in Table 3.1. There are three categories of wave: deep water, transitional and shallow water. This classification is based on the ratio between the depth, d, and length, L, of the wave and the regulating limiting values given by $tanh\,(kd)$.

Table 3.1: Classification of propagation environment (Anon, 1984)

Classification	d/L	kd	$tanh(kd)$
Deep water	>1/2	>π	≈1
Transitional	1/25 to 1/2	¼ to π	$tanh(kd)$
Shallow water	<1/25	<1/4	$\approx kd$

Gravity waves, also called surface waves, are regular waves which are small in amplitude, sinusoidal, and progressively definable by their wave height and period in a given water depth. There are two theories which model gravity waves, namely the linear Airy wave theory that applies to waves of small amplitude and length and the nonlinear Stokes 2nd order theory which applies to waves of large amplitude and length. The linear theory developed by Airy (1841) gives a reasonable

linearised approximation of the propagation of gravity waves with small ratios of wave height to water depth (shallow water) and wave height to wavelength (deep water). On the other hand, Stokes (1847) was the first to develop a finite amplitude wave theory to take into account the nonlinear terms. The theory considered waves of small, but finite, height propagating over water of finite depth. All linear terms in the ideal fluid equations of motion have been retained up to second order enabling the determination of hydrodynamic characteristics for waves of greater steepness (H/L). When the wave steepness is assumed to be small then linear Airy waves theory applies. However, when wave steepness value is high or finite (but always < 1) then we are talking about finite amplitudes and the theory of linear wave becomes no longer valid. For this reason, and to take into account the nonlinear aspect of the wave, it becomes necessary to use higher-order approximation such as the Stokes 2nd order theory. A very thorough account of the historical development of water wave theory was presented by Craik (2004). The properties of a simple sinusoidal wave can be understood using linear wave theory which is described in section 3.2.2.

3.2.2. Linear Wave Theory

In order to understand the behaviour of waves and their characteristics, an explanation of linear wave theory is given here. The linear wave theory developed by Airy (1841) is considered to be the first attempt at a complete theoretical description of wave behaviour. In this theory, water waves are considered as being oscillatory, and water particle motion is described by orbits which are closed or nearly closed for each wave period. Linear wave theory is based on two equations: a mass balance equation and a momentum balance equation. These two equations describe the kinematic and dynamic aspects of waves. Waves can be described by linear wave theory by assuming non-linear effects are negligible and water is an ideal fluid. This implies that water: is incompressible, has constant density, has no viscosity and there is

no rotation of the water particles around their own axes. In addition, the following assumptions are made:

(a) Surface tension can be neglected.
(b) Coriolis effects can be neglected.
(c) Pressure at the free surface is uniform and constant.
(d) The sea bed is horizontal, fixed, and impermeable (which implies that the vertical velocity at the sea bed is zero).
(e) Wave amplitudes are small and the wave form is invariant in time and space.
(f) Waves are plane or long crested (two-dimensional).

3.2.3. Dynamics of a Floating Body in Regular Waves

A structure that is freely floating in ocean waves has six degrees of freedom: three translational (surge, sway and heave) and three rotational (roll, pitch and yaw) as shown in Figure 3.4. The analysis described in this section will consider all six modes of motion in regular waves only.

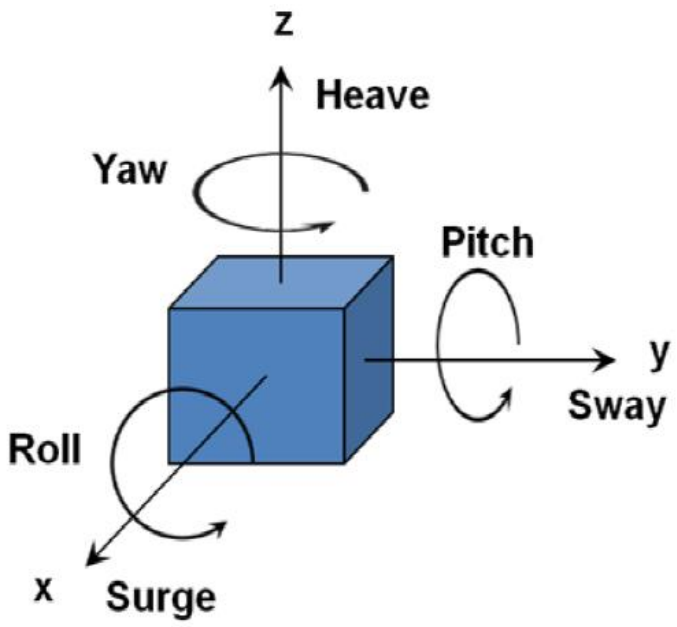


Fig. 3.4: Definition of the 6 degrees of freedom (Journee and Massie, 2001)

The equation describing the motion of a floating rigid body is derived from Newton's second law. Based on this law, two vector equations can be derived, one for describing translations (Equation 3.1) and one for describing rotations (Equation 3.2).

$$\overrightarrow{F} = \frac{d}{dt}(m\overrightarrow{U}) \tag{3.1}$$

$$\overrightarrow{M} = \frac{d}{dt}(\overrightarrow{H}) \tag{3.2}$$

where $\overrightarrow{F}$ is the resultant external force acting on the centre of gravity, m is the mass of the rigid body, $\overrightarrow{U}$ is the instantaneous velocity of the centre of gravity, $\overrightarrow{M}$ is the resultant external moment acting about the centre of gravity, $\overrightarrow{H}$ is the instantaneous angular moment about the centre of gravity, and t is time.

The motion of a floating body has a linear behaviour which implies that when the amplitude of the excitation force is doubled, the amplitude of the response will be doubled as well, while the phase shift between the response and excitation remains unchanged. Due to this linear behaviour, the oscillation of a body in still water, and the forces acting on a restrained body in waves can be used to derive the resulting motion (illustrated in Figure 3.5). The following two assumptions are made:

- The linear hydrodynamic reaction forces and moments, e.g. damping and spring forces, are induced by the harmonic oscillations of the rigid body.
- The wave excitation forces and moments are produced by waves acting on the restrained body.

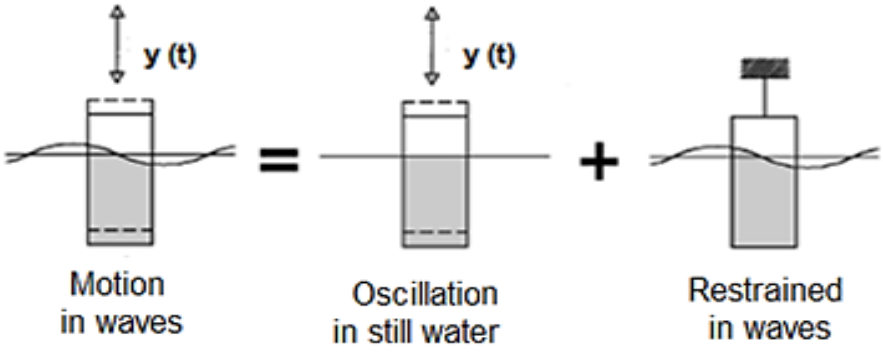


Fig. 3.5: Superposition of hydromechanical and wave loads (Journee and Massie, 2001)

The resultant force, F_i, equals mass × acceleration (Newton's second law), in which the acceleration is defined as the second derivative $\ddot{y}_j$ of location as a function of time, $y(t)$. From this equation, the six equations of motion can be derived and the coupled equations of motion in six degrees of freedom in waves can be written as:

$$\sum_{j=1}^{6} m_{ij}\,\ddot{y}_j = F_i \qquad \text{for } i = 1,\ldots,6 \tag{3.3}$$

where m_{ij} is the solid mass and inertia of the structure (6 × 6 matrix), $\ddot{y}_j$ is the acceleration of the structure in direction j (6 × 1 vector), and F_i sum of the forces or moments acting in direction i (6 × 1 vector). The resultant force, F_i, consists of the following components:

- Harmonic (regular) wave exciting forces and moments, $\overrightarrow{F}$,
- Linear hydrodynamic damping force $c\vec{\dot{y}}$, and
- Linear hydrostatic spring force $k\vec{y}$.

Substituting these variables for the components in Equation (3.3) gives an equation for a damped mass-spring system. The additional fluid inertia resulting from the fluid acting on the buoy must be considered when formulating the system equation of motion. This added effect is the added mass. The equation of motion is a coupled 2nd order differential equation which governs the six degrees of freedom:

$$(M_M + A_M)\ddot{\vec{y}} + C_M\dot{\vec{y}} + K_M\vec{y} = \overrightarrow{F} \quad (3.4)$$

where

M_M = 6 × 6 matrix of solid mass and inertia of the structure

A_M = 6 × 6 matrix of the added mass

$\ddot{\vec{y}}$ = acceleration of the structure (6 × 1 vector)

$\dot{\overrightarrow{y}}$ = velocity of the structure (6 × 1 vector)

$\overrightarrow{y}$= location of the structure with respect to reference frame (6 × 1 vector)

c_M = 6 × 6 matrix of hydrodynamic damping coefficient

K_M = 6 × 6 matrix of hydrodynamic spring constant

$\overrightarrow{F}$ = excitation force acting on the structure (6 × 1 vector)

3.2.4. Mass-Spring-Damper System

The model that is most widely used for describing the motion of floating bodies is the mass-spring-damper system. The derivation of the model comes from the analysis of the forces or moments acting on a floating object and is based on a number of assumptions. The wave and damping forces acting on a buoy are described as follows:

- **Radiation Force (F_{rad}):** is the force exerted on a buoy as a result of its oscillatory motion through the water's surface. This motion results in the creation of waves radiating away from the buoy. The amount of energy of the radiated waves equals the amount of the energy loss (damping) of the buoy.
- **Restoring Force (F_{res}):** according to Archimedes' law, as a buoy moves through the water's surface, it experiences a buoyancy force proportional to the volume of water displaced by the buoy. This force tends to restore the buoy to its equilibrium position where the buoyancy force equals the gravitational force.
- **Wave Excitation Force (F_{exc}):** as waves approach a buoy, they create a disturbance in the pressure field around the solid

surface and pressure deviates from its hydrostatic state. In linear wave theory and for undisturbed waves, this disturbance is represented by a non-hydrostatic part. The hydrostatic part is accounted for in the restoring force.

- **PTO Damping Force (F_{PTO}):** a buoy is connected to a PTO damper to capture the wave induced motion and turn it into electrical power. This damper exerts a force on the buoy which acts in the opposite direction to buoy's velocity.
- **Mechanical Spring Force (F_{spring}):** a mechanical spring is also connected to the buoy parallel to the PTO device to keep the whole system in line. This mechanical spring exerts a force similar to the restoring force called the spring force.

3.2.5. Point Absorber System Features

The basic design and functional principles of a point absorber system are illustrated in Figure 3.6, which shows a rigid floating body (buoy) attached to the sea bed. The purpose of the floating buoy is to act as the energy absorbing body of the system; it also acts to hold the system upright. These two functions result from the buoyancy of the buoy and the induced pressure forces due to water particle movement in the wave front. The generator consists of a spring-damper system where the damping is provided by the PTO. The generator's primary function is to take the energy captured from the wave induced motion of the float by the PTO and convert it into electricity. The PTO device is placed somewhere between the sea bed and the buoy so that it can determine the direction of the buoy's motion which is crucial for power production. The generator also contains a spring which acts as a pre-tensioner to keep the line straight. The point absorber buoy system can be treated as a mass-spring-damper system which in classical mechanics has a mass, a damping coefficient and a stiffness coefficient.

The buoy system is modelled as rigidly attached to the generator such that the entire system moves in phase. This is one of the main assumptions used in the analysis presented in this chapter.

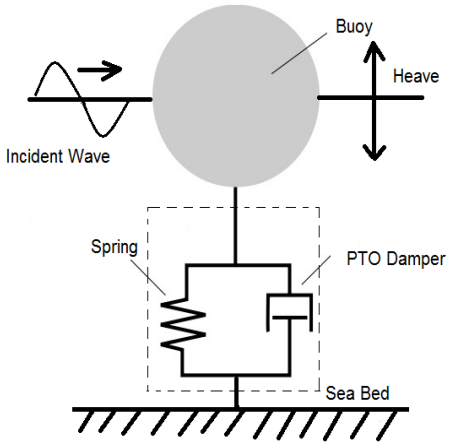


Fig. 3.6: Basic design of a point absorber system

When the point absorber buoy system is displaced from its equilibrium position, it experiences a restoring force proportional to its displacement. If the restoring force is the only force acting on the system, the system is called a simple harmonic oscillator. This means that it undergoes simple harmonic motion with a constant amplitude and frequency. If a damping force proportional to the velocity is also present, the harmonic oscillator is described as a damped oscillator. Depending on the damping coefficient, the system can:

- Oscillate with a frequency lower than in the non-damped case and the amplitude of the displacement decreases with time (underdamped system).
- Decay to the equilibrium position without any oscillation (overdamped system).

The boundary between underdamped and overdamped behaviour occurs at a particular value of damping coefficient where the system is called "critically damped". The damping coefficient in this case, called the critical damping coefficient, c_c (Ns/m), is given by:

$$c_c = 2\sqrt{km} \tag{3.5}$$

The ratio of the actual damping coefficient, c_a , to the critical damping coefficient is called the damping ratio, ξ, and is given by:

$$\xi = \frac{c_a}{c_c} \tag{3.6}$$

The different responses of an overdamped, underdamped and critically damped system are shown in Figure 3.7.

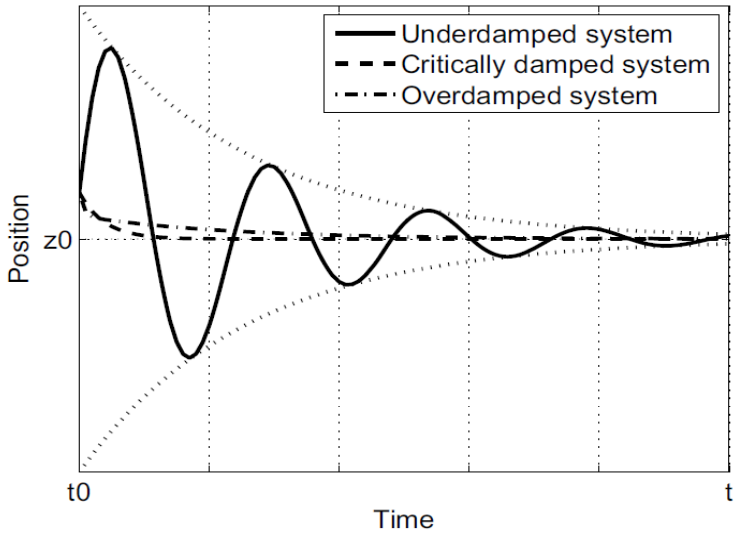


Fig. 3.7: Motion curves of an underdamped, overdamped and critically damped system (De Backer, 2008)

3.3. Generalised Heaving Point Absorber (Buoy) Model

3.3.1. Mass-Spring-Damper Representation

In this model, the simple motion of a point absorber is compared to that of a mechanical oscillator consisting of a mass-spring-damper system with a single degree of freedom of motion subjected to an external force in the direction of the degree of freedom. A schematic representation of the system is shown in Figure 3.8.

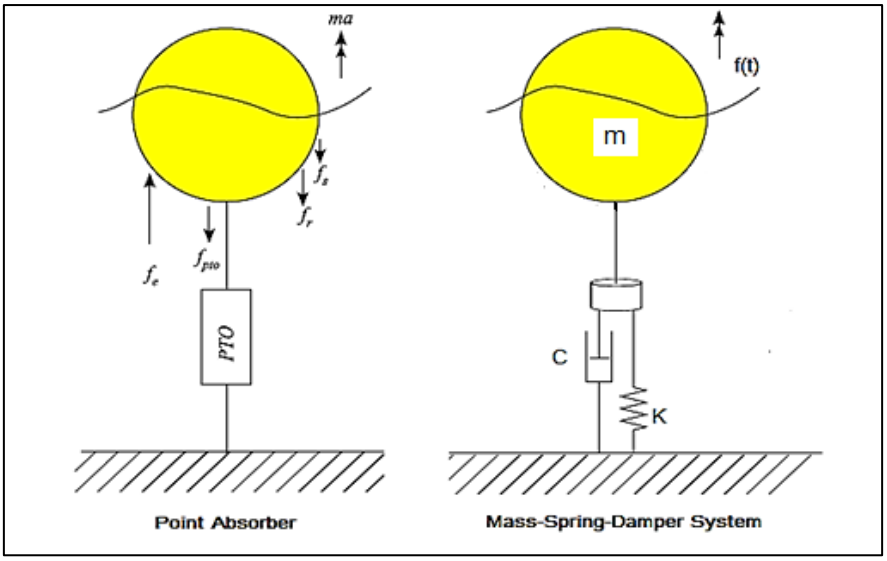


Fig. 3.8: Schematic representation of mass-spring-damper system (modified from Price, 2009)

The system is linearly damped with damping coefficient, c (Ns/m). An external harmonic force is applied to the system, with amplitude A (m) and angular frequency, ω (rad/s). The spring constant, k (N/m), acts as a restoring mechanical force which is proportional to the system's vertical displacement, y, from its original position.

3.3.2. Newton's Second and Third Laws

The equation of motion is expressed from Newton's second law such that the sum of all the forces acting on a body is equal to the mass of the body times its acceleration. For a point absorber, the forces include the restoring force, the damping forces and the external excitation force. All the forces, apart from the excitation, are linear functions of the displacement and can be linked to the acceleration by:

$$F_{net} = m\ddot{y} = F_{exc} + F_{rad} + F_{res} + F_{spring} + F_{PTO} \quad (3.7)$$

Equation (3.7) can be linearised by writing all the forces, apart from the excitation, as linear functions of the displacement. It can then be rearranged into the conventional form of an equation of motion:

$$F_{net} = m\ddot{y} - F_{exc} - F_{rad} - F_{res} - F_{spring} - F_{PTO} = 0 \qquad (3.8)$$

where F_{net} is the sum of all the forces acting on the buoy (N), m is the mass of the buoy (kg), and $\ddot{y}$ is the net vertical acceleration of the buoy (m/s^2).

Equation (3.8) can be used to calculate the motion of a point absorber; it applies to a system with a constant mass. The forces acting on a buoy are illustrated in Figure 3.9. According to Newton's second law, the sum of the forces on the heaving buoy equals mass x acceleration (shown on the left). Newton's third law states that every force has a reaction force equal in magnitude and opposite in direction.

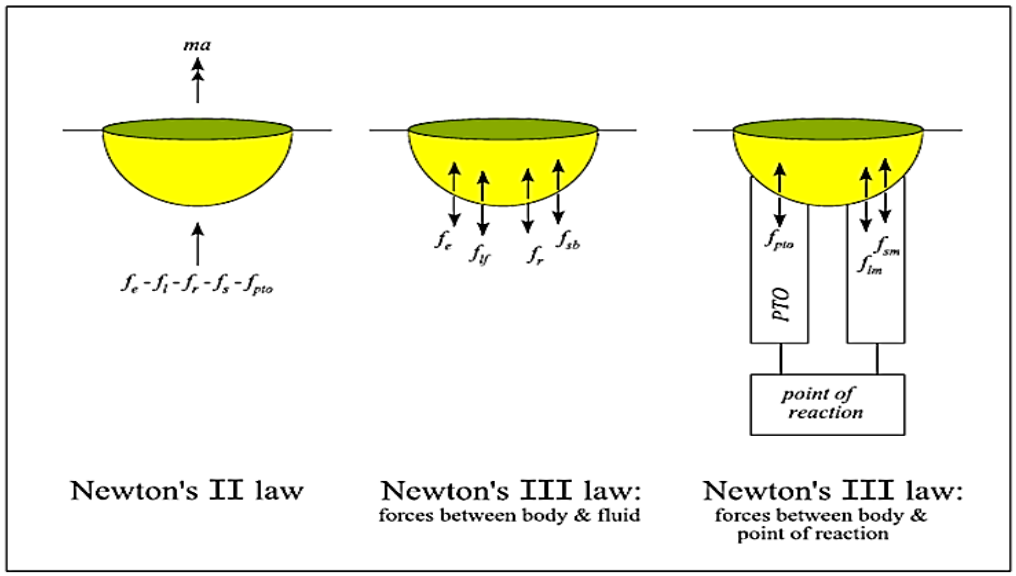


Fig. 3.9: Newton's second and third laws applied to a buoy moving in heave motion (Price, 2009)

In Figure 3.9, forces are shown between the buoy and the fluid in the centre and between the buoy and the point of reaction on the right. All the forces experienced by the buoy are associated with reaction forces; only those forces acting on the buoy that are of interest will be included when modelling its motion.

3.4. Time Domain Model

In this section the governing equation of motion for a single degree of freedom (heave) buoy is presented and the governing equations and assumptions used in the time domain simulation are introduced. The steps involved in the development of the model were:

(a) Writing the differential equation of motion for a buoy

(b) Linearising the equation of motion

(c) Solving the differential equations for the relative velocity of the buoy (using the 4th order Runge-Kutta method in MATLAB)

(d) Computing the rate of energy dissipation

3.4.1. Equation of Motion of a Heaving Point Absorber

For a buoy in heave motion, the vertical displacement $y(t)$ is defined as the vertical displacement of the buoy with respect to the effective centre of the wave displacement $x(t) = A\,cos(\omega t)$ where A is the wave amplitude and ω (rad/s) is the angular frequency. It is assumed that one end of the system is fixed to an inertial frame. In reality this “fixing” would be provided by a large heave-plate located well below the level of the waves. The linear damping in the system is partially due to radiated waves and partially due to friction. In the diagram, the PTO damper c_1 is the main power extraction unit; the PTO system is assumed to be linear for simplicity. The radiation force can be decomposed into a linear radiation damping term c_2. The radiation damper, c_2, acts to prevent the mass, m, from moving relative to the wave. No mass is added to the buoy's absolute mass in the model. A schematic view of the simulated point absorber system is given in Figure 3.10.

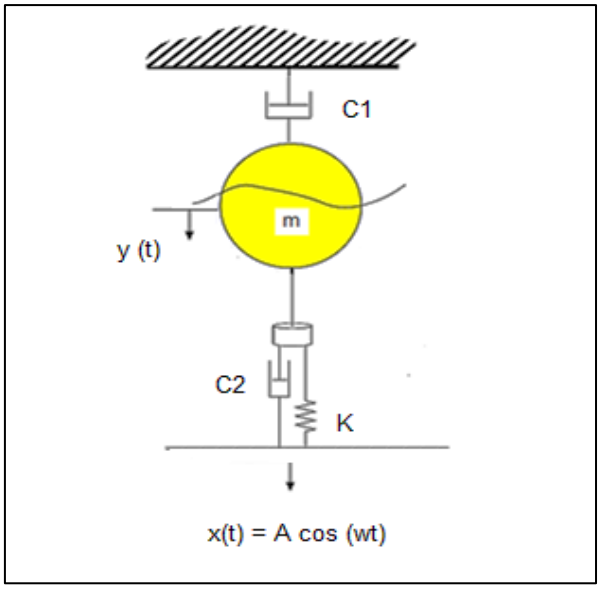


Fig. 3.10: Schematic representation of the simulated heaving point absorber in the time domain model (Modified from Price, 2009)

The mechanical spring force acting on the buoy (similar to the restoring force) is assumed to be linearly proportional to displacement and the damping forces are assumed to be linearly proportional to velocity. In the model, the buoy is allowed to respond to the harmonic excitation forces caused by the wave. The differential equation of motion for the heaving buoy can be obtained from the following forces:

The mechanical spring force (F_{spring}) = ky (3.9)

The PTO damping force (F_{PTO}) = $c_1\dot{y}$ (3.10)

The radiation force (F_{rad}) = $c_2\dot{y}$ (3.11)

The excitation force (F_{exc}) =

$$kx + c_2\dot{x} = kAcos(\omega t) - c_2\omega Asin(\omega t) \quad (3.12)$$

The equation of motion of this buoy can thus be found from Newton's second law:

$$m\ddot{y} + (c_1 + c_2)\dot{y} + ky = A[kcos(\omega t) - c_2\omega sin(\omega t)] \quad (3.13)$$

where m is the mass and $\ddot{y}$ is the acceleration of the buoy. The buoyancy-stiffness k is expressed as $k = \rho g A_w$, where A_w is the wetted plane cross sectional area occupied by the buoy (assumed sphere) in the sea water. The buoyancy-stiffness for an occupied area in seawater of 1 m^2 is k = 10006 N/m (at $\rho_{sea\ water}$= 1020 kg/m^3, g = 9.81 m/s^2 and $A_w = 1$ m^2). The PTO and radiation damping coefficients are c_1 (Ns/m) and c_2 (Ns/m), respectively.

A reference value for c_1 is used and is taken as half of the critical damping which equals to k/ω at optimum mass. While the buoyancy-stiffness is kept constant at 10006 N/m, the parameters m, c_1 and c_2 are easily varied and can thus be optimised in order to maximise buoy power absorption or extraction rate. Equation (3.13) can be solved for the vertical displacement of the buoy, $y(t)$, in the time domain given the values of the coefficients c_1 and c_2 and the wave excitation forces.

3.4.2. Power and Energy

The term “power absorption” is generally used to refer to the average power absorption which is normally expressed as the power absorbed by the PTO system. When there is no damping (i.e. no losses or PTO), all the power in the incident wave remains in the sea in the form of radiated, diffracted and transmitted waves. On the other hand, with PTO damping, as shown in Figure 3.11, some of the intercepted power is captured and some returns to the sea as radiated power.

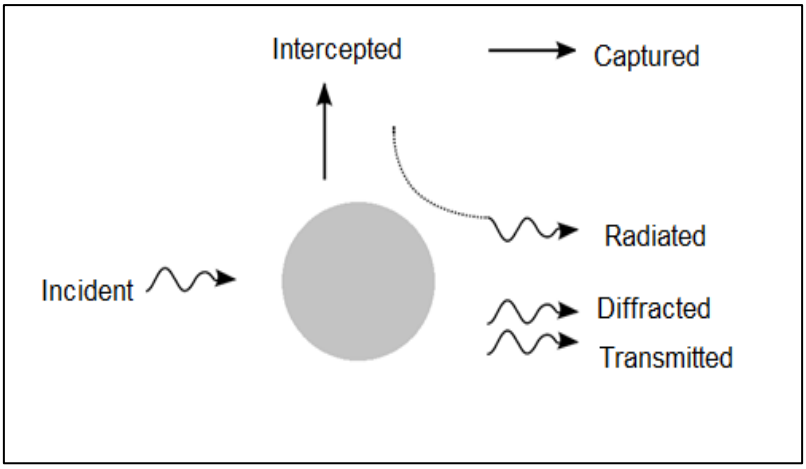


Fig. 3.11: Power capture by a point absorber (Price, 2009)

A harmonically oscillating buoy is assumed to have a velocity $v = \dot{y}$ which generates a force in the damper c_1. In a heaving system, the power P absorbed by the buoy and converted through the PTO damper, c_1, is calculated from the force and velocity as given by:

$$P = c_1 \dot{y}^2 \tag{3.14}$$

The energy collected in the damper over a period of time t_1 is:

$$E_d(t_1) = \int_0^{t1} P_1 dt = \int_0^{t1} c_1 \dot{y}^2 dt \tag{3.15}$$

The objective of this study is to maximise the energy developed in damper c_1 . In theory, this energy is maximised when Equation (3.15) is maximised over one period of the excitation wave force. This results in the condition:

$$\omega_n = c_1 \sqrt{\frac{k}{m}} = \omega_i \tag{3.16}$$

where ω_n is the resonance frequency of the device and ω_i is the incident wave frequency. When this condition is met, the velocity profile of the device is in phase with the excitation wave force which is consistent with condition one for maximising the power absorption discussed in section 3.1.

3.5. Steady-State Harmonic Model

In this section the governing equation of motion for a single degree of freedom (heave) buoy is presented and the equation and assumptions used in the steady-state harmonic model are introduced. The following steps were required for analysing the buoy motion:

(a) Differentiating the equation for power using c_2, optimum m and reference c_1 value, and

(b) Calculating the optimum power extraction rate of the buoy.

3.5.1. Equation of Motion

In this section the analytical model is presented and the response of a point absorber oscillating in a harmonic wave with respect to a fixed reference is discussed. The buoy is restricted to heave motion only. It is assumed that one end of the system is fixed to an inertial frame similar to the time domain model discussed in the previous section. A schematic of a point absorber system under vertical wave velocity $u(t)$ is shown in Figure 3.12.

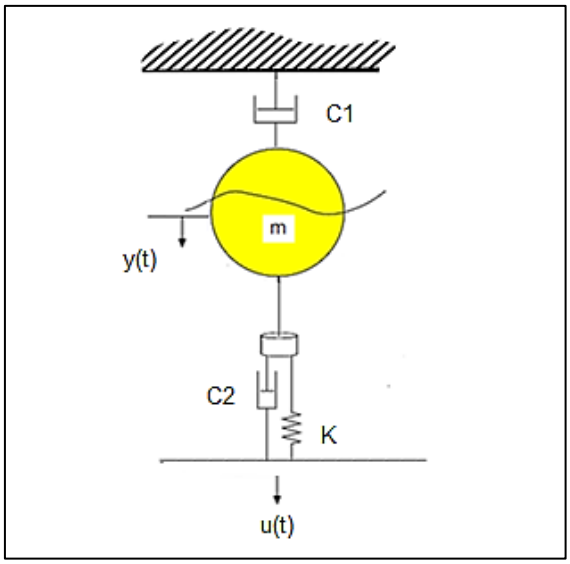


Fig. 3.12: Schematic representation of a heaving point absorber in the steady-state harmonic model (Modified from Price, 2009)

In the diagram in Figure 3.12, the PTO damper c_1 is the main power extraction unit and is assumed to be linear for simplicity. The term c_2 represents the radiation damping. No mass is added to the buoy's absolute mass in the model.

Due to the vertical wave velocity $u(t)$, the buoy is displaced from its equilibrium position to an actual position of $y(t)$. The differential equation of motion of the point absorber can be found from Newton's second law:

$$m\ddot{y} + c_1\dot{y} = k\,(u - y) + c_2\,(\dot{u} - \dot{y}) \tag{3.17}$$

The spring force in expressed in Equation (3.17) as $k\,(u - y)$. The damping force exerted by the PTO system is expressed in Equation (3.17) as $c_1\dot{y}$. The damper c_1 is the main power extraction unit and the PTO system is assumed to be linear for simplicity. The radiation force is expressed in Equation (3.17) as $c_2\,(\dot{u} - \dot{y})$. The equation of motion for a heaving point absorber (Equation 3.17) can thus be rewritten as:

$$m\ddot{y} + (c_1 + c_2)\,\dot{y} + ky = ku + c_2\dot{u} \tag{3.18}$$

It is assumed throughout this study that all time dependence is harmonic with an angular frequency of ω (rad/s). The time dependence of the quantities $u(t)$ and $y(t)$ can then be removed by the introduction of the complex variables U and Y where:

$$u = Re\left(U \times e^{j\omega t}\right) \tag{3.19}$$

$$y = Re\left(Y \times e^{j\omega t}\right) \tag{3.20}$$

Equation (3.18) thus becomes:

$$(-m\omega^2 + (c_1 + c_2)\,j\omega + k)\,Y = (k + j\omega c_2)\,U \tag{3.21}$$

Equation (3.21) can be rearranged to give:

$$Y = \frac{(k+j\omega c_2)\,U}{(-m\omega^2+(c_1+c_2)\,j\omega+k)} \tag{3.22}$$

3.5.2. Power Absorption

The velocity, v, in the power extraction damper c_1 is expressed as:

$$v(t) = y\dot{(t)} = Re\left(V \times e^{j\omega t}\right) \tag{3.23}$$

The time dependence of quantity $v(t)$ can be removed by the introduction of the complex variable, V, where:

$$V = jwY \tag{3.24}$$

The mean power extracted by damper c_1 is given by:

$$P = \frac{1}{2}c_1|j\omega Y|^2 = \frac{1}{2}\,c_1\omega^2\,|Y|^2 \tag{3.25}$$

Substituting Equation (3.22) into Equation (3.25) gives:

$$P = \frac{1}{2}\omega^2 c_1 \times \frac{\left(k^2+\omega^2c_2^2\right)}{((k-\omega^2m)^2+\omega^2\,(c_1+c_2)^2)} \times U^2 \tag{3.26}$$

It can be seen that although the wave magnitude, U, does not affect the optimal values of $m, c_1\ and\ c_2$, it can affect the value of the extracted power.

3.5.3. Power Absorption Optimisation

In order to optimise the buoy power extraction rate, the term H defined below, needs to be differentiated with respect to m, c_1 and c_2. The partial derivatives $\frac{\partial H}{\partial m}$, $\frac{\partial H}{\partial c_1}$ and $\frac{\partial H}{\partial c_2}$ are then set equal to zero and their stationary values obtained.

$$H = \frac{c_1\left(k^2+\omega^2c_2^2\right)}{((k-\omega^2m)^2+\omega^2\,(c_1+c_2)^2)} \tag{3.27}$$

The derivatives can be written in their simplified forms as:

$$\frac{\partial H}{\partial m} = \frac{2c_1\omega^2(c_2^2\omega^2+k^2)(-m\omega^2+k)}{((k-\omega^2 m)^2+\omega^2\,(c_1+c_2)^2)^2} \tag{3.28}$$

$$\frac{\partial H}{\partial c_1} = \frac{(c_2^2 2\omega^2+k^2)(-c_1^2\omega^2+c_2^2\omega^2+k^2-2km\omega^2+m^2\omega^4)}{((k-\omega^2 m)^2+\omega^2\,(c_1+c_2)^2)^2} \tag{3.29}$$

$$\frac{\partial H}{\partial c_2} = \frac{2c_1\omega^2(c_1^2c_2\omega^2+c_1c_2^2\omega^2-c_1k^2-2c_2km\omega^2+c_2m^2\omega^4)}{((k-\omega^2 m)^2+\omega^2\,(c_1+c_2)^2)^2} \tag{3.30}$$

Setting the numerator in Equation (3.28) equal to zero gives the stationary values for m as follows:

$$m = \frac{k}{\omega^2} \tag{3.31}$$

Setting the numerator in Equation (3.29) equal to zero, substituting for $m = k/\omega^2$ and rearranging gives:

$$c_1 = c_2 \tag{3.32}$$

Setting the numerator in Equation (3.30) equal to zero and rearranging gives:

$$c_2 = \frac{k^2}{\omega^2 c_1} \tag{3.33}$$

From Equations (3.32) and (3.33) the optimum damping coefficient becomes $c = \frac{k}{\omega}$. By substituting for m from Equation (3.31) and c_2 from Equation (3.33) into Equation (3.26), the expression for the optimum power extraction rate was obtained as follows:

$$P = \frac{1}{2} \times \frac{\omega^2 c_1 k^2}{(\omega^2 c_1^2+k^2)} \times U^2 \tag{3.34}$$

The system has 5 dimensions: k, m, c_1, c_2 and ω. In order to reduce the number of dimensions when calculating the buoy optimum power response, m was fixed at its optimum value and c_1 was fixed at its reference value. The unknown parameter c_2 was varied for a wave magnitude $U = 1$ m. The buoyancy-stiffness and wave natural

frequency were also kept constant at k =10006 N/m and $\omega = 2\pi$ rad/s. The natural frequency of the buoy was assumed to be equal to the peak frequency of the sea state, i.e. it was assumed to be in resonance. Optimisation of the buoy power response was carried out in MATLAB using the following:

- PTO external damping coefficient $c_1 = {}^{k}/_{\omega}$ (Ns/m).
- Buoy mass $m = {}^{k}/_{\omega^2}$ (kg).
- Radiation damping coefficient $c_2 = c_c[10^{-8}\ to\ 10^{8}]$ (Ns/m). The c_2 value was varied using 500 time steps.

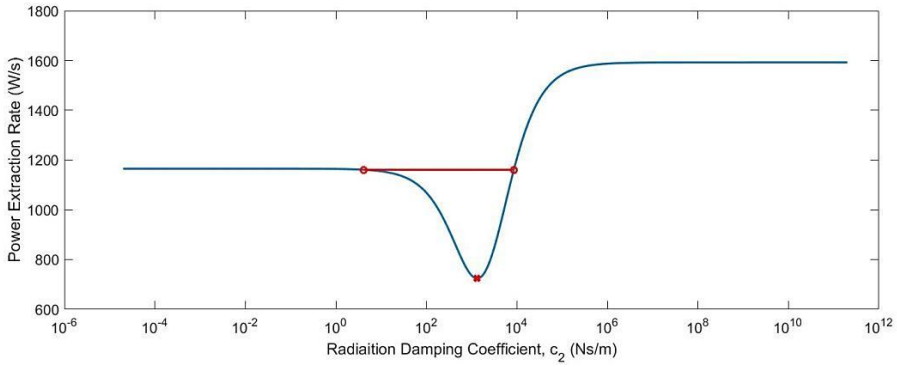
3.5.4. Results and Findings

The first set of simulations were performed by fixing m and c_1 at their optimum values and varying c_2 in order to determine the optimum power extraction rate over the range of regular wave conditions. The mean power extracted was determined using Equation (3.26) and the results are plotted in Figure 3.17. The results indicate that there are two power extraction rate regions: the left region is driven by the low value of c_2 and right region is driven by the high value of c_2 as seen in Figure 3.13. With this model, the optimum mass $(m = {}^{k}/_{\omega^2})$ and value of c_1 were found to be 253 kg and 1592.50 Ns/m, respectively.

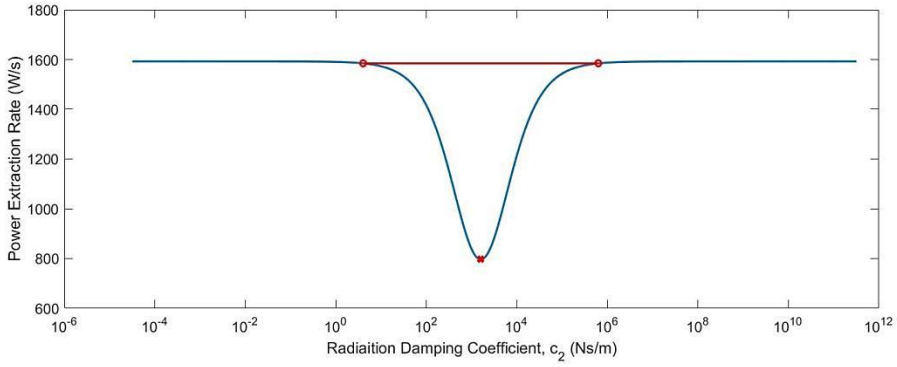
It was clear from the simulations that using the optimum mass gave the highest power extraction rates in the right and left regions of the graph (Figure 3.13b). The power extraction rate was constant for $c_2 < 10^2$ and $c_2 > 10^4$ (Ns/m) and the lowest power extraction rates occurred for c_2 values between 10^2 and 10^4 (Ns/m). These results are similar to the results from the time domain model.

Further analyses were conducted with mass values above and below the optimum mass. Mass values of 100 kg (Figure 3.13a) and 500 kg (Figure 3.13c) resulted in lower power capture in the left region only.

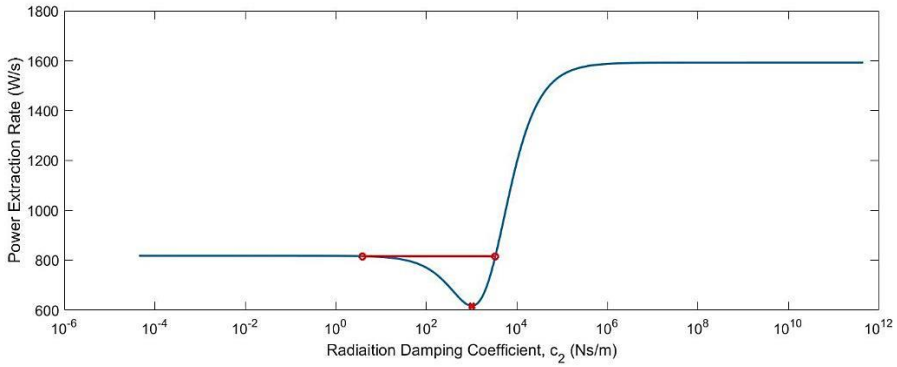
This showed that there is no visible effect of increasing the mass to 500 kg when the c_2 value is high. Mass was only found to play a significant role for low values of c_2. The maximum power extraction rate of a buoy with optimum mass $\widetilde{m}$ and $\widetilde{c_1}$ was 1585 W/s.



(a) Buoy mass = 100 kg



(b) Buoy mass = 253.4549 kg



(c) Buoy mass = 500 kg

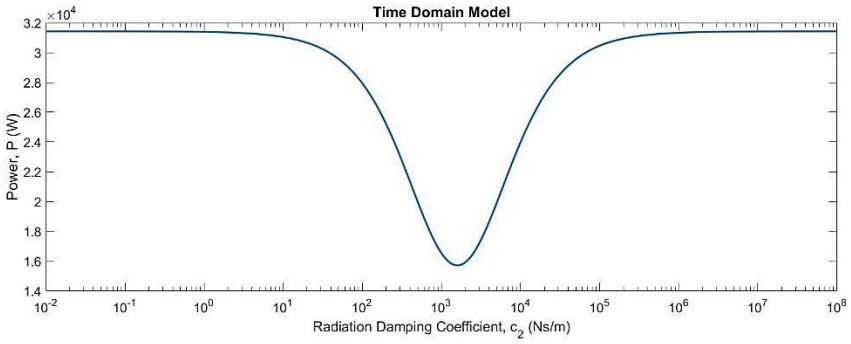
Fig. 3.13: Power capture at $c_1 = 1592.50$ Ns/m and $m =$ (a) 100 kg (b) 253.4549 kg and (c) 500 kg

3.6. Validation of Steady-State Harmonic Model

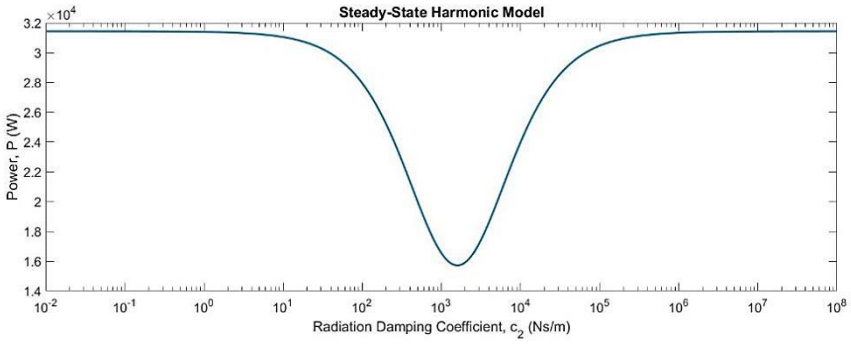
In order to achieve the modelling objectives of this chapter it was important to verify the steady-state harmonic model by comparison with the time domain model. For this purpose, the time taken for the time domain and steady-state harmonic models to settle down from transient to steady-state was compared along with the predictions from both models for steady-state behaviour.

3.6.1. Power Absorption Optimisation

Before verifying the steady-state model, an initial assessment of the agreement in the predictions of power absorption from the time domain model implemented in section 3.4 and the steady-state harmonic model implemented in section 3.5 was made in terms of c_2 values at optimum $\widetilde{m}$ and reference c_1 value. The comparison showed that the values for c_2 at which the least power is produced are in the region 4.00 Ns/m to 6.54×10^5 Ns/m for both models as seen in Figure 3.14. The optimum $\widetilde{m}$ and reference c_1 values were found to be equal to 253.4549 kg and 1592.50 Ns/m, respectively, for both solutions which produced power of 3.14×10^4 W.



(a) Time domain



(b) Steady-state harmonic

Fig. 3.14: Power capture at $\tilde{m} = 253.4549$ kg and $c_1 = 1592.50$ Ns/m

Any system response is known to have two components: transient response and steady-state response. The transient response is presented by the short period of time immediately after the system starts. If the system is asymptotically stable, the transient response disappears. However, if the system is unstable the transient response will increase very quickly in time. Even if the system is stable, some phenomena like high frequency oscillations may occur. Assuming the system is asymptotically stable; the system response in the long run is determined by its steady-state component only. Therefore, for transient and steady-state responses systems it is important that the steady-state response values are as close as possible to desired values. This allows the corresponding errors of the difference between the actual and desired system reponses at steady-state to be determined for the time domain and harmonic both models. Therefore, the time taken for both models to settle down from transient to steady-state was calculated.

This was done by finding the time constant required for the system response of each model to decay to zero as follows:

Let $\mathrm{y(t)}=\emptyset\exp(\lambda \mathrm{t})$ (3.35)

where $\emptyset$is Amplitude and λ is frequency.

Substituting $y(t)$ into Equation (3.17) and rearranging the equation gives:

$$m\lambda^2(c_1+c_2)\lambda+k=0 \quad (3.36)$$

Equation (3.36) expressed in terms of c_1 is:

$$\lambda=\frac{-(c_1+c_2)\pm\sqrt{(c_1+c_2)^2-4mk}}{2m} \quad (3.37)$$

The real part of Equation (3.37) is given by:

$$\text{Real part} = \frac{-(c_1+c_2)}{2m} \quad (3.38)$$

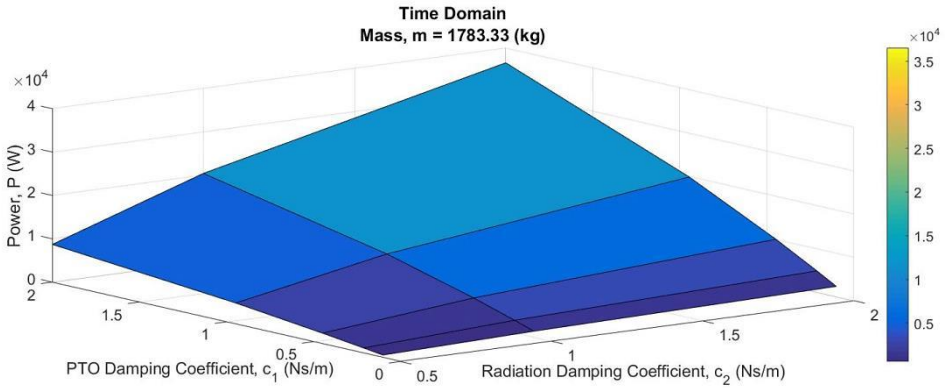
The inverse of the real part is the time constant τ which is in seconds. This term was used to make the comparison of when the models settled down from transient to steady-state behaviour.

For the time domain model, Equation (3.14) was used to calculate the buoy response and for the steady-state harmonic model, Equation (3.34) was used. The following conditions were applied in MATLAB:

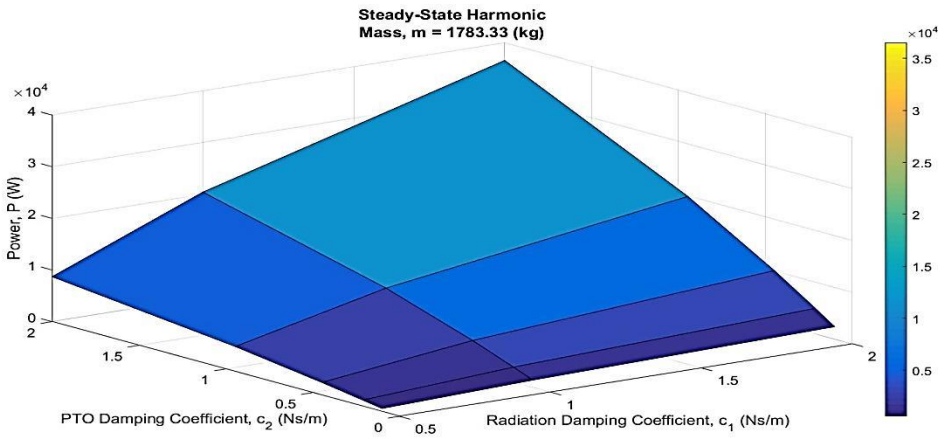
- PTO damping coefficient c_1 = constant x k/ω (Ns/m) where the value of the constant ranged from 0.1 to 2 using 5 time steps.
- Radiation damping coefficient $c_2 = c_c$ [0.5 to 2] (Ns/m). The value of c_2 was varied using 3 time steps.
- Buoy mass m varied from 4000 kg to 10 kg using 10 time steps.

3.6.2. Results and Findings

The maximum power absorptions predicted using the time domain and steady-state harmonic solutions are given in Figures 3.15a and 3.15b, respectively. The time taken for both models to reach steady state was 60 s and the maximum power absorption achieved for both models was 36.53 kW. The results from both analyses were almost identical, with a



(a) Time domain



(b) Steady-state harmonic

Fig. 3.15: Maximum power absorption vs c_1 and c_2 at $m = 1783.33$ kg

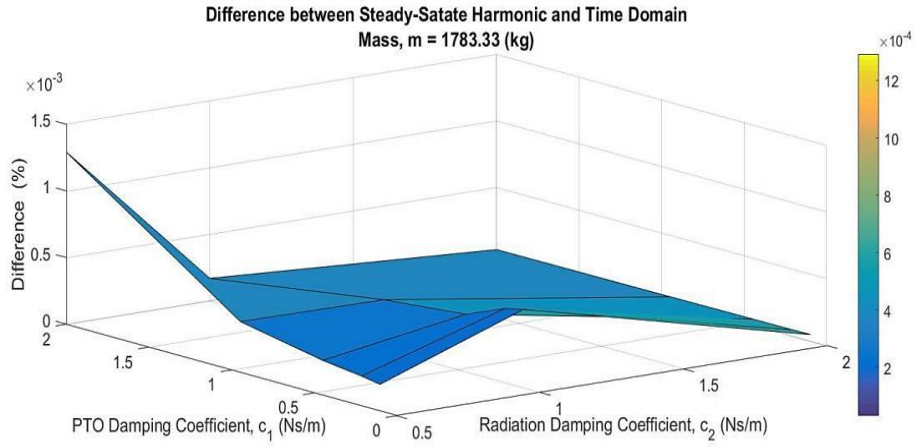


Fig. 3.16: Maximum power capture model difference (%) at $m = 1783.33$ kg

Deviation of only 0.0012% in the maximum power absorption as seen in Figure 3.16. This indicated that the steady-state harmonic model developed for analysing the steady-state conditions of the WEC system gave good predictions for buoy behaviour. The steady-state harmonic model efficiently predicts the system behaviour and reduces the required computational effort. Therefore, it was utilised for further optimisation of the system as illustrated in the following sections.

3.7. Steady-State Harmonic Model Optimisation

The objective of this section is to determine the optimal damping profile for a point absorber (buoy) using the values for c_1 and c_2 which gave the greatest power absorption. The shape of the optimal damping profile is assumed to be independent of the specific device parameters.

From Equation (3.32) the optimum performance is achieved when $c_1 = c_2$. The power response was thus maximised by using the best value for c_2 from the region driven by high c_2 for determining the best value of c_1 for a mass equal to the optimum mass.

3.7.1. Results and Findings

For the resonance condition, the best value of PTO damping coefficient c_1 for the optimal radiation damping coefficient c_2 = 6.54 × 10^5 Ns/m is illustrated in Figure 3.17. The results of the simulation in Figure 3.18 show a linear behaviour between c_1 and c_2 and confirm the validity of the linear relationship $(c_1 = c_2)$ derived in Equation (3.32).

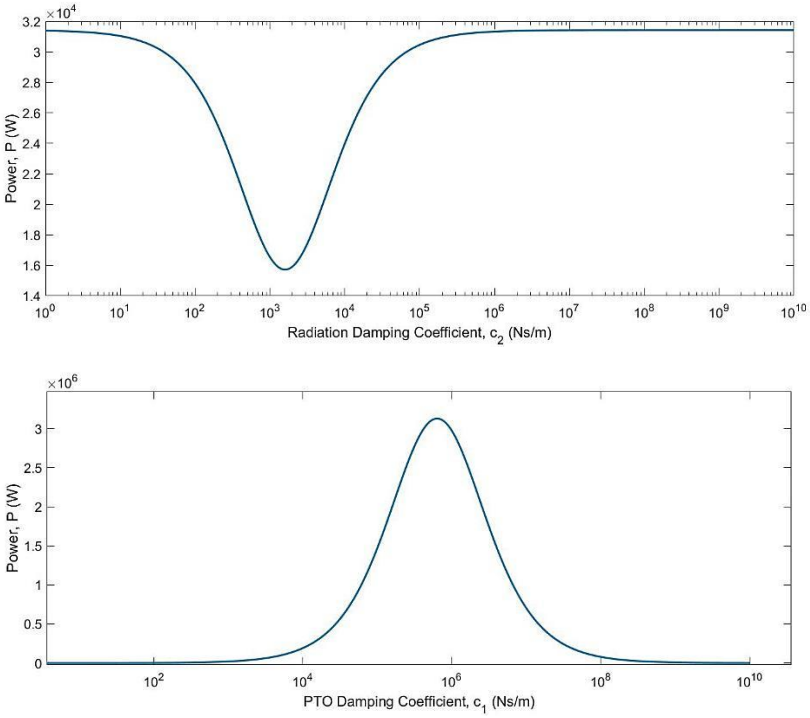


Fig. 3.17: Power capture at $c_1 = 6.54 \times 10^5$ Ns/m and $c_2 = 6.54 \times 10^5$ Ns/m

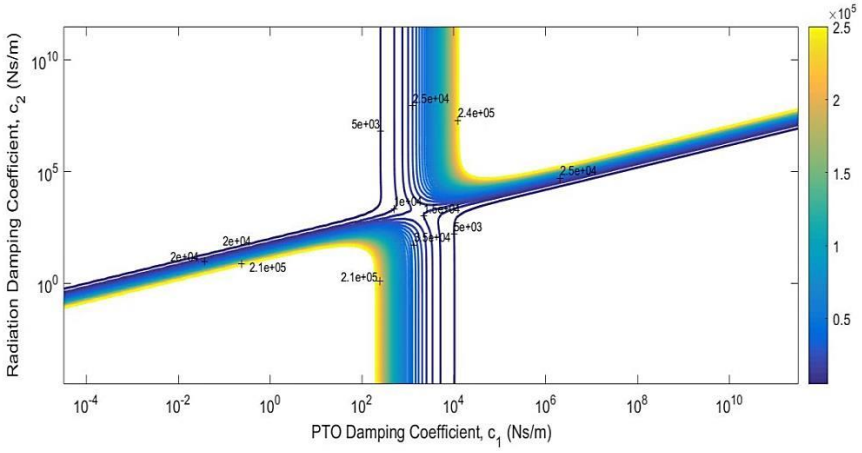


Fig. 3.18: Contour plot for the relationship between c_1 and c_2 at $\tilde{m}$

The region driven by the high radiation damping c_2 maximises the power response and determines the best value of c_1 for a mass equal to the optimum mass. Figure 3.17 shows the c_1 value at which maximum power is achieved for a given c_2 value. The lower graph also shows that the maximum power is achieved in the regions corresponding to infinite and negligible values of c_2, and the worst power absorption occurs for values of c_2 ranging from 4.00 Ns/m to 6.54 $\times$ 10^5 Ns/m. Operation with $c_2 \geq$ 6.54 $\times$ 10^5 Ns/m is therefore recommended. On the other hand, from Figure 3.17, the highest power is produced when c_1 is close to 6.54 $\times$ 10^5 Ns/m. This demonstrates that the best value for c_1 is $c_1 = c_2$ as derived in Equation (3.32).

Further investigations were conducted to examine the $c_1 = c_2$ relationship at resonance. From Figure 3.19 it can be seen that the highest power occurs at $c_1 = c_2$ with the optimum mass of 253.4549 kg. The value of c_2 is defined by the structure of the buoy and cannot be changed once the buoy has been constructed. The term c_1 is used to model the PTO damping mechanism which is a variable parameter that can be tuned to match the sea state. It is therefore recommended that buoys are constructed with large c_2 values such that the optimum c_1 value will equal c_2 and will not change when the system is not at resonance.

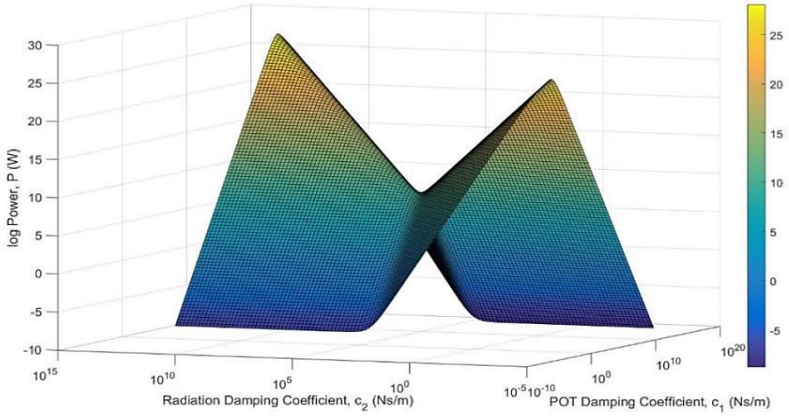
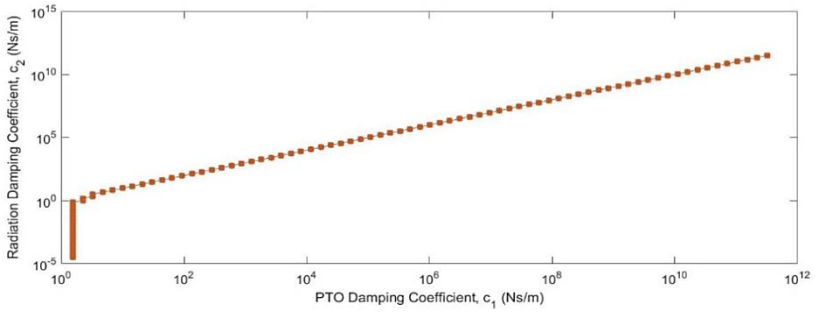
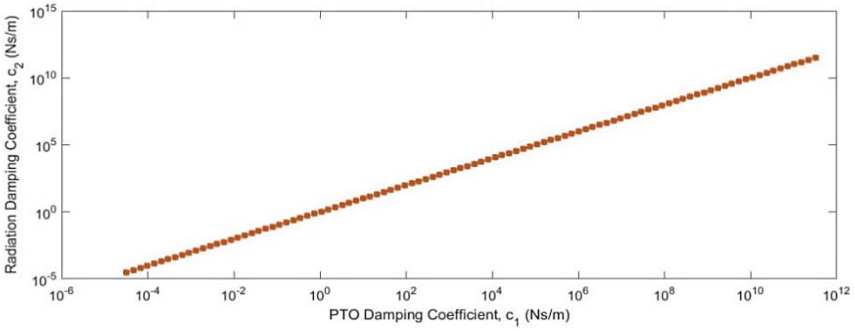


Fig. 3.19: Log power vs c_1 and c_2 at $\widetilde{m}$ = 253.4549 Kg

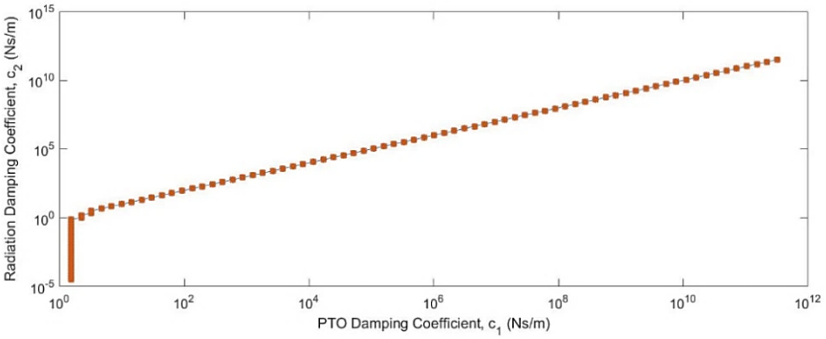
At optimum mass the system is in resonance, and in order to maximise the power absorbed, the condition of $c_1 = c_2$ must be met. Further analyses were conducted with mass values of 99.99% and 100.01% of $\tilde{m}$. The tests revealed that for a system that is not in resonance, the linear relationship between c_1 and c_2 no longer holds true. This was true even when mass deviated by only 0.01% from its optimum value as seen in Figures 3.20a and 3.20c. It was concluded that the relationship $c_1 = c_2$ is only valid if the point absorber is at its optimum mass (Figure 3.20b) and is at resonance with the peak frequency of the sea state.



(a) mass equals 99.99 % of $\tilde{m}$



(b) optimum mass $\tilde{m}$



(c) mass equals 100.01 % of $\tilde{m}$

Fig. 3.20: The relationship between c_1 and c_2 with m

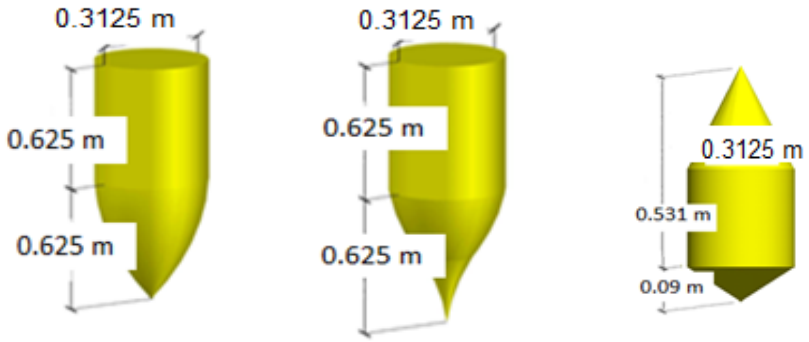
3.8. Buoy Shape Optimisation

In the previous sections, the highest power absorption for the sea states with the highest energy contribution was calculated by optimising the damping coefficients and mass for the cases of non-resonance and resonance. Validating the steady-state harmonic model against experimental data is, however, still required. Therefore, the objective of this section is to use the steady-state harmonic model to determine the optimal damping profiles for different point absorber (buoy) shapes. As already shown, wave energy extraction is a complicated procedure and every change in the geometrical or control parameters has a major impact on the system's power extraction. It was therefore decided to carry out the optimisation process by keeping the diameter of the buoys fixed and comparing the buoys purely based on their shape and draft.

Four different buoy shapes were “shortlisted” from the literature reviewed, namely egg (Blommaert, 2010), cylinder-cone (De Backer et al., 2007; De Backer, 2008; Blommaert, 2010; Nazari et al., 2013; Pastor and Liu, 2014; Khojasteh and Kamali, 2016), cylinder hemisphere (De Backer et al., 2007; De Backer, 2008; Pastor and Liu, 2014; Goggins and Finnegan, 2014; Sjökvist et al., 2014; Khojasteh and Kamali, 2016) and cylinder bi-cone ($60^o/120^o$) (Vantorre et al., 2002; Sjökvist et al., 2014). It was found by De Backer et al. (2008), that a conical buoy absorbs 4% to 8% more energy than a hemispherical buoy. A buoy with a combination of two conical surfaces with top angles of 60° and 120° (bi-cone) was felt to be the best for this study as it has the advantage of having the most wetted area located near the free surface making it more receptive to wave excitation. The lower part reduces draft and hence the probability of slamming. Furthermore, in order to reduce the effects of reflection and refraction and to increase the uniformity of the waves reaching the buoy, a cylindrical body was selected. In addition to the bi-cone ($60^o/120^o$ two intermediate shapes were also chosen for the testing pruposes of this

chapter, namely (a) bullet, and (b) spike. Details of the buoy selection criteria can be found in Table 3.2 next.

The dimensions of the buoy prototypes are illustrated in Figure 3.21. All the shapes have the same cross-sectional area (diameter = 0.3125 m) but have different mass and draft values as shown in Table 3.1 in the next section. The bullet and spike buoys had relatively longer drafts (0.755 m) than the bi-cone buoy (0.22 m).



(a) Bullet **(b)** Spike **(c)** Bi-cone

Fig. 3.21: Shapes and dimensions of prototype buoys

The damping characteristics of the three different point absorber (buoy) shapes were determined experimentally (see chapter 4 for further details) and the results were compared against the steady-state harmonic model to determine the optimum operating region for each buoy shape.

Table 3.2: Buoy Shape Selection Criteria

Buoy Shape	Bottom and breaking Wave Slamming	Absorber Power	Waterline Diameter (D) and draft (d)	Performance	Conclusions
Egg 	Severe bottom slamming loads (Blommaert, 2010).				Eliminated immediately (Blommaert, 2010).
Cylinder-Cone 	Cone with apex angle 90°/dead-rise angle 45° reduces bottom slamming (Blommaert, 2010). If buoy draft is sufficient compared to the relative motion of the buoy to the waves then slamming problems will rarely occur (De Backer, 2008). The slamming restriction only influences the power absorption in higher wave classes, especially for buoys with smaller drafts. (De Backer et al., 2007).	Absorbs 4% to 8% more energy than the hemispherical shape (De Backer, 2008). The supplemental mass and external damping forces have to be adjusted to maintain the efficiency when the sea state increases (Pastor and Liu, 2014). To maximise the power absorption, the tuning and external damping forces must be tuned for the average sea state (Pastor and Liu, 2014). Power absorption efficiency is affected by the peak wave period at a certain sea state (Pastor and Liu, 2014).	Diameter significantly influences the power absorption, whereas the impact of draft is limited (De Backer, 2008). Largest diameter allowed under economic constraints which can still be used on the offshore platform should be selected for building the buoy (Pastor and Liu, 2014). Smaller draft performs slightly better than larger drafts (Pastor and Liu, 2014). A smaller draft is associated with a larger added mass, damping coefficient and amplitude of the heave exciting force (Pastor and Liu, 2014).	Compared to flat cylinder the drag coefficient is decreased by 50%, and the average amplitude of heave motion is increased by 20% (Nazari et. al., 2013). The maximum impact pressures are significantly lower near the bottom of the cones with dead-rise angles of 20° and 45° compared to the pressures on a hemisphere (De Backer, 2008). A buoy that is smaller will be more favourable for lower damping, while a larger buoy will be more favourable if the damping is increased (Sjökvist et al., 2014; Khojasteh and Kamali, 2016).	Larger diameter and smaller drafts. (De Backer, 2008) Performs better than cylinder-hemisphere (De Backer, 2008; Pastor and Liu, 2014; De Backer et al., 2007), egg (Blommaert, 2010) and flat cylinder (Nazari et. al., 2013) The conical buoy slightly outperforms the hemispherical buoy when comparing the hydrodynamic diffraction results produced by AQWA (Pastor and Liu, 2014).

Buoy Shape	Bottom and breaking Wave Slamming	Absorber Power	Waterline Diameter (D) and draft (d)	Performance	Conclusions
Cylinder-Hemisphere 	If a sufficient buoy draft can be provided compared to the relative motion of the buoy to the waves, slamming problems will rarely occur (De Backer, 2008). The slamming restriction only influences the power absorption in higher wave classes, especially for buoys with smaller drafts (De Backer et al., 2007).	Absorbs 4% to 8% less energy than the cone shapes (De Backer, 2008).	Same as above	Impact pressures measured near the bottom of the hemisphere are significantly larger than those registered on a cone with an apex angle of 90° (De Backer, 2008). A buoy that is smaller will be more favourable for lower damping, while a larger buoy will be more favourable if the damping is increased (Sjökvist et al. 2014; Khojasteh and Kamali, 2016).	A truncated vertical cylinder with a hemisphere attached to the base is the optimum geometry for a radius of less than 10 m (Goggins and Finnegan, 2014). Eliminated since cone cylinder performance better than hemisphere in terms of power absorption, impact pressures near the bottom and hydrodynamic diffraction results (De Backer, 2008; Pastor and Liu, 2014; De Backer et al., 2007).
Cylinder-Bi-Cone (60º/120º) 	The lower part increases the draft and hence reduces the probability of slamming (Vantorre et al., 2002).	A buoy with radius = 2.5 m absorbs 5% more energy than cone/90 and 9% higher than cone/60 º. (Vantorre et al., 2002) Bi-cone (60º/120º) with radius = 2.5 m absorb 62% of the energy available in a wave		Two conical surfaces with top angles of 60° and 120° (bi-cone) gives the advantage of having the most wetted area located near the free surface making the buoy more receptive to wave excitation (Vantorre et al., 2002). An average power of 21.5 kW may	Higher energy absorption compared to cone-60 º/90 º/120 º and hemisphere. (Vantorre et al., 2002) Very good performance.

Buoy Shape	Bottom and breaking Wave Slamming	Absorber Power	Waterline Diameter (D) and draft (d)	Performance	Conclusions
Cylinder-Bi-Cone (60º/120º) 	The lower part increases the draft and hence reduces the probability of slamming (Vantorre et al., 2002).	crest width equal to the buoy diameter averaged over all H_s classes (Vantorre et al., 2002).		be captured by a point absorber unit, if both supplementary mass and external damping are controlled operationally (Vantorre et al., 2002). A buoy that is smaller will be more favourable for lower damping, while a larger buoy will be more favourable if the damping is increased (Sjökvist et al., 2014).	
Cone-Cylinder-Cone 	The shorter cylinder allows it to withstand severe bottom and breaking wave slamming loads (Blommaert, 2010).			A buoy that is smaller will be more favourable for lower damping, while a larger buoy will be more favourable if the damping is increased (Sjökvist et al., 2014).	Good performance if slamming is a major issue.

Decay tests were performed at the Kuwait Institute for Scientific Research (KISR) utilising the Coastal Management Program's wave flume tank facility. The approach for this work consisted of two parts: (a) conducting decay tests to determine the radiation damping coefficient, c_2, for each buoy shape; and (b) examining the behaviour of each buoy under different damping conditions. Only the bullet and spike buoys were used for part (b). The different damping conditions were achieved by arbitrarily adding one (damped) or two (extra damped) round discs to the lower section of the buoys. This damping approach was the best available option to provide the different damping conditions as to the discs availability at the testing facility. When two discs were used, they were attached 2 inch and 3 inch apart for the bullet and spike buoys, respectively. After testing, the values of c_2 obtained from the decay tests were verified by checking whether they were close to the worst c_2 value obtained from the optimised steady-state harmonic model or approached the best c_2 values.

In the decay tests, the buoys were released separately from a position different from their equilibrium position in still water. After approximately 10 seconds, the influence of the radiated waves reflected on the side walls of the flume became clearly visible and the natural angular frequency, ω_a , and damping ratio, ξ, were found. Details of the decay tests and how ω_a and ξ were calculated are given in chapter 4 and APPENDIX 4. No tests were conducted for the damped and extra damped bi-cone shape due to the limited time available at the testing facility.

3.8.1. Statistical Analysis

Each decay test was conducted five times and the mean value for the radiation damping coefficient was used for comparison with the model predictions. In order to determine the data distribution about the mean (i.e. to determine the error in the c_1 measurements) statistical sample variance was used as follows:

Suppose $X_1, X_2, \ldots\ldots, X_n$ are observations of a random sample of size n with a normal distribution.

The mean of the n observations is:

$$\bar{X} = \frac{1}{n}\sum_{i=1}^{n} X_i \tag{3.39}$$

The sample variance is given by:

$$s^2 = \frac{1}{n-1}\sum_{i=1}^{n}(X_i - \bar{X})^2 \tag{3.40}$$

The standard deviation on individual measurements is given by:

$$s = \sqrt{s^2} \tag{3.41}$$

The effect of adding extra damping on the value of c_2 for each buoy shape was examined using a t-test. The t-test allows testing of the hypothesis that adding round discs to the lower section of the buoys can increase the radiation damping value c_2 associated with the buoy. This was used to confirm whether the c_2 data in any set (i.e. zero damped$\rightarrow$damped, zero damped$\rightarrow$ extra damped, damped$\rightarrow$extra damped) was significantly higher than the others. The t-test is a statistical hypothesis test in which the test statistic follows a Student's t-distribution under the null hypothesis. The t-test equation is given as:

$$t = \frac{(\bar{X}_1 + \bar{X}_2)}{\sqrt{\frac{s_1^2 + s_2^2}{n}}} \tag{3.42}$$

where $\bar{X}$ is the sample mean, s^2 is the sample variance, n is sample size (n = 5), and S is the standard deviation. Statistical significance was determined by looking at the p-value which gives the probability of observing the test results under the null hypothesis ensuring approximately 95% confidence in the results.

The decay test and statistical results are summarised in Table 3.3 and the t-tests results are given in Table 3.4. Sand was added from the top

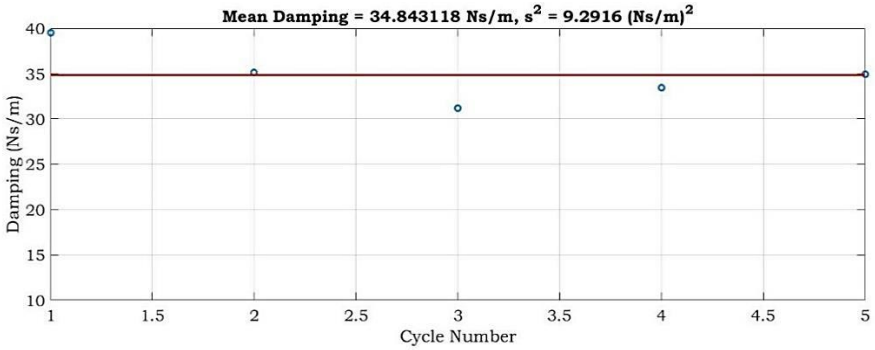
to stabilise each buoy and to adjust its draft on the cylindrical part to 0.13 m. The amount of sand added differed which resulted in a variation in the weight of the buoys of different shapes. The radiation damping profiles for the zero damped, damped and extra damped buoys are shown in Figures 3.22, 3.23 and 3.24, respectively.

Table 3.3: Bullet, spike and bi-cone decay tests and statistical results

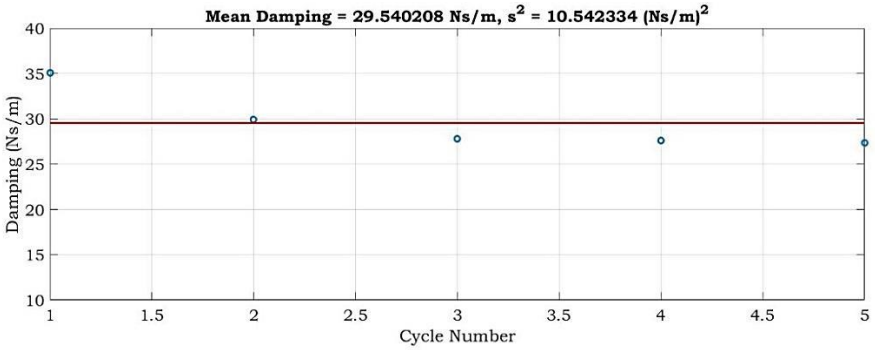
Buoy Shape	Mean Damping Ratio	Buoy Mass (kg)	Mean Draft (m)	Mean Damped Frequency (Hz)	Mean Radiation Damping Coefficient, c_2 (Ns/m)	Sample Variance s^2 $(Ns/m)^2$
Bi-cone	0.094	11.63	0.220	1.164	16.0	7.8795
Spike	0.128	27.72	0.755	0.729	32.51	3.6074
Bullet	0.124	33.44	0.755	0.667	34.84	9.2916
Damped Spike	0.114	27.30	0.755	0.727	28.51	0.8511
Damped Bullet	0.111	31.24	0.755	0.685	29.54	10.5423
Extra Damped Spike	0.099	27.58	0.755	0.715	24.55	5.3399
Extra Damped Bullet	0.095	31.01	0.755	0.693	25.55	2.37

Table 3.4: Probability of damping reduction (%) for different buoy shapes

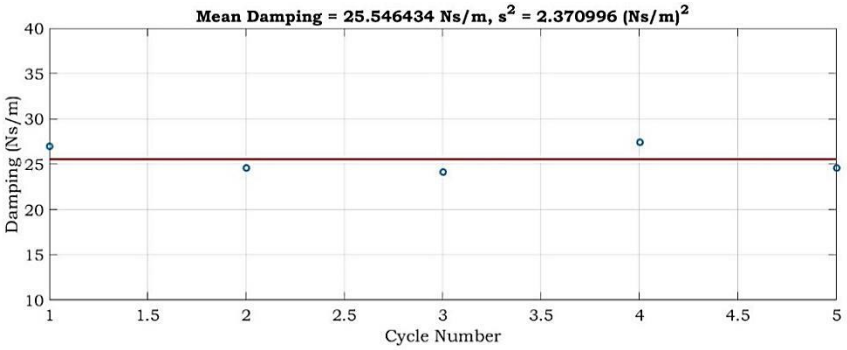
Buoy Shapes			Probability of damping reduction (%)
Bi-cone	⟶	Spike	100
Spike	⟶	Bullet	99.5
Bi-cone	⟶	Bullet	100
Spike	⟶	Damped spike	99.8
Damped spike	⟶	Extra damped spike	99.6
Bullet	⟶	Damped bullet	98.6
Damped bullet	⟶	Extra damped bullet	98.1
Spike	⟶	Extra damped spike	99.9
Bullet	⟶	Extra damped bullet	99.9



(a) Zero damped bullet buoy

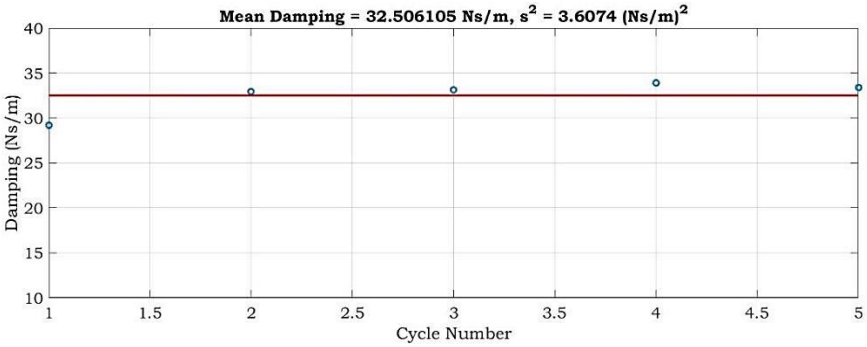


(b) Damped bullet buoy

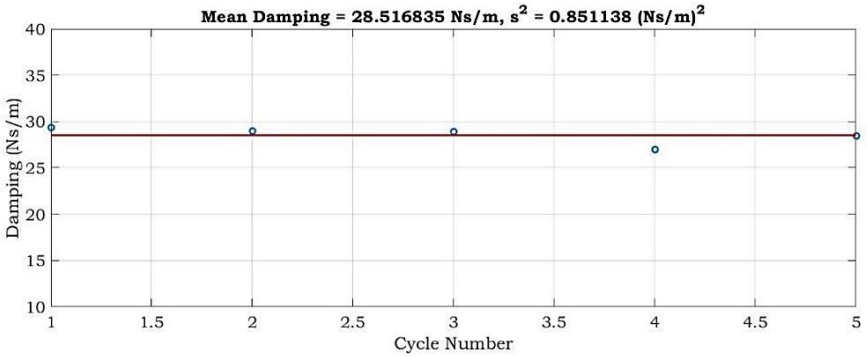


(c) Extra damped bullet buoy

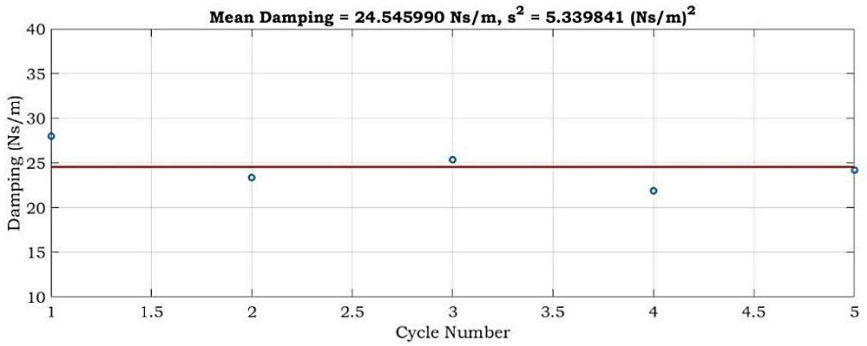
Fig. 3.22: Profiles of c_2 for the bullet buoy



(a) Zero damped spike buoy



(b) Damped spike buoy



(c) Extra damped spike buoy

Fig. 3.23: Profiles of c_2 for the spike buoy

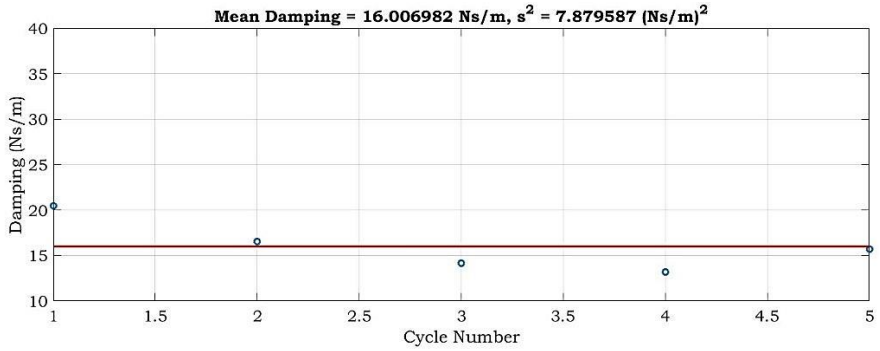


Fig. 3.24: Profiles of c_2 for the bi-cone buoy

3.8.2. Buoy Power Optimisation

In order to optimise the power absorbed by each buoy at resonance and under zero damped, damped and extra damped conditions, the steady-state harmonic model was used to determine the optimal c_2 damping profiles for each shape. The values of c_2 obtained during decay testing were verified to ensure they were not near the worst c_2 value obtained from the model. All the damping coefficient values were scaled down to match the physical models as the diameter used for the steady-state harmonic analyses was d = 1 m and the physical models had d = 0.3125 m.

The performance of the bullet, spike and bi-cone buoys was optimised using the following hydrodynamic parameters in MATLAB:

- Buoyancy-stiffness corresponding to a wetted plane cross sectional buoy area of 0.08 m^2 in sea water, k = ($\pi d^2/4$) × 9.81 × 1000 N/m.
- Wave frequency, $\omega = 2\pi$ = 6.28 rad/s.
- Resonance frequency, ω_n= $2\pi/0.9$ rad/s. This was calculated based on the experimental results which gave resonance at T= 0.9 s (see Chapter 4).
- Mass = mass of buoys used in the decay tests (see Table 3.1).

- Radiation damping coefficient c_2= damping ratio $\times c_c$ (Ns/m). Damping ratio of each buoy shape was taken from the decay tests (see Table 3.1) and used to determine c_2 value associated with it.
- Radiation damping coefficient $c_2 = c_c[(10^{-8})\ to\ (10^{8})]$ (Ns/m). The c_2 value in the model was varied using 500 time steps.

3.8.3. Results and Findings

During the experimental testing, the opportunity to vary the performance of the buoys at very little cost was utilised. Based on the steady-state harmonic model predictions, it was concluded that operating in the high damping region is recommended to maximise the power extraction rate which suggests that it is beneficial to add some form of damping. This was tested during the experimental investigation and extra damping was provided in the form of round discs mounted on the lower parts of the bullet and spike buoys. A comparison between the mean c_2 values for all the shapes was conducted and the results are illustrated in Figure 3.25. The desired effects of increasing c_2 values using the round discs were not found as the extra damped bullet and spike buoys had the lowest radiation damping values compared to the zero-damped and damped buoys. This behaviour was confirmed by the statistical t-test, where probabilities above 95% provided very high confidence in the results, see Table 3.2. Increasing damping by adding two round discs appeared to be a reasonable idea but the results were unexpected and require further investigation.

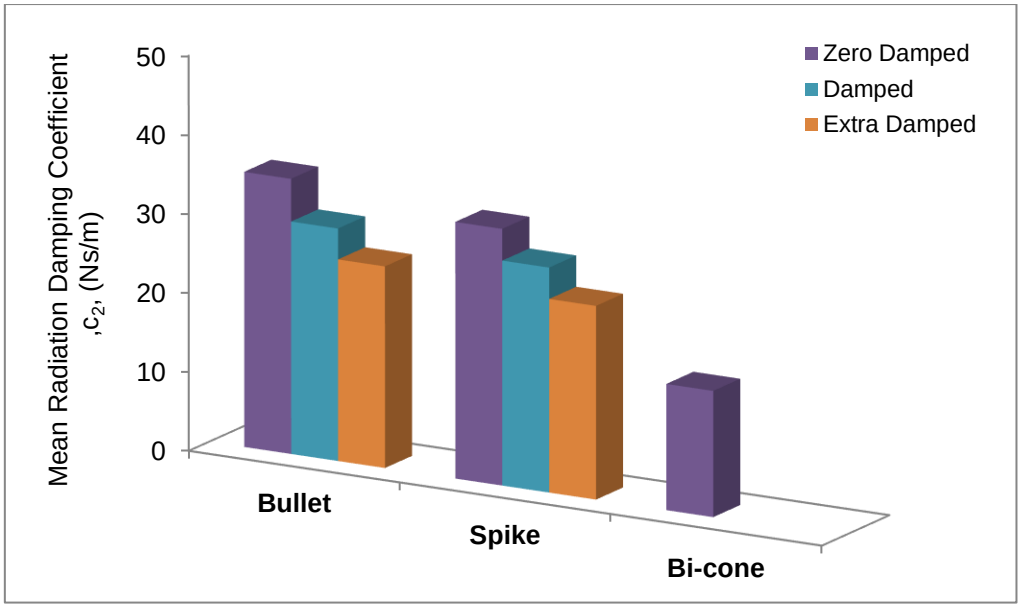
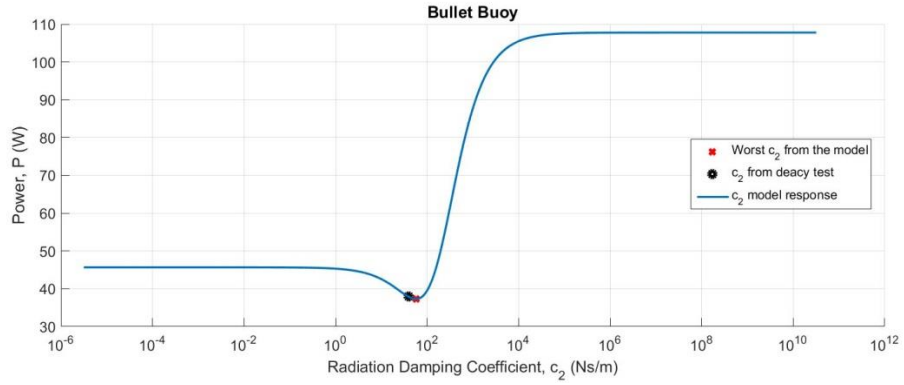


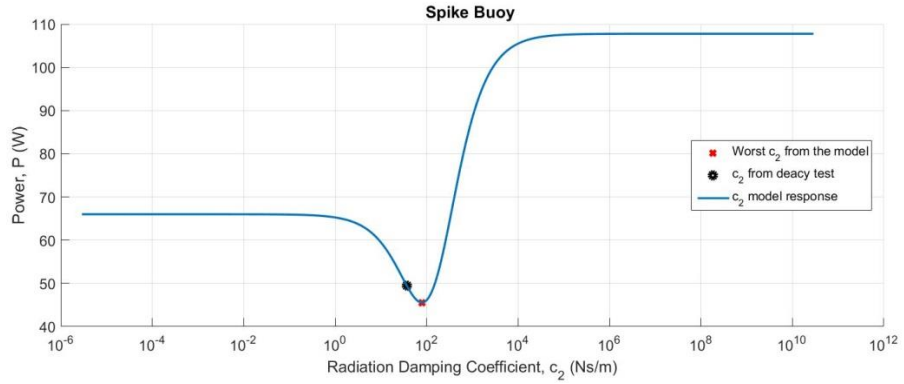
Fig. 3.25: Mean c_2 for the bullet, spike and bi-cone buoys

The variation in the power absorbed by the zero damped buoys as a function of the radiation damping values is illustrated in Figures 3.26a, 3.26b and 3.26c. In these figures, the c_2 values derived from the decay tests for each shape are marked in blue, and the worst c_2 values from the model are marked in red.

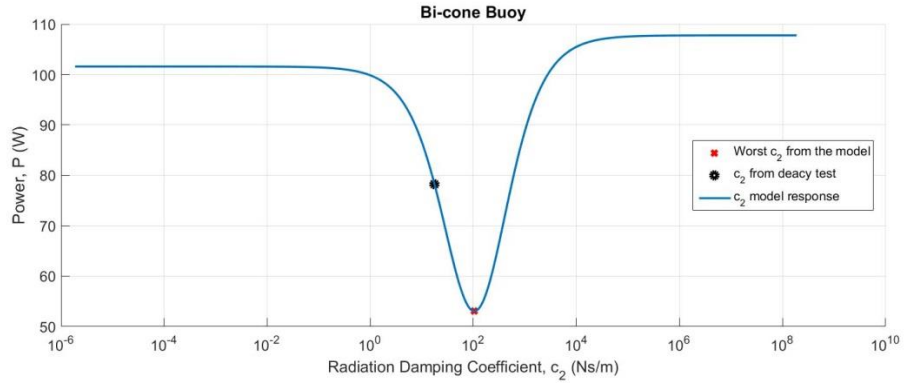
Figures 3.26a and 3.26b, for the bullet and spike buoys, respectively, show lower power capture in the left low c_2 region only. This means that their mass is far from optimum, as indicated in Figure 3.13 previously, which shows results for masses above and below optimum. The c_2 values for the bullet and spike buoy shapes are close to the worst value for c_2 predicted by the model. In Figure 3.26a for the bullet buoy, the power recorded in the highest and lowest c_2 regions was 107.78 W and 45.67 W, respectively. The worst power region for the bullet buoy occurred for c_2 between 2.41 and 1.51 $\times$ 10^4 Ns/m. In order for this buoy to achieve a power absorption of 107.78 W its c_2 value should be higher than 1.51 $\times$ 10^4 Ns/m.



(a) Bullet buoy



(b) Spike buoy



(c) Bi-cone buoy

Fig. 3.26: Maximum power capture at $\widetilde{c_2}$ for zero damped buoys

In Figure 3.26b for the spike buoy, the power recorded in the highest and lowest c_2 regions was 107.78 W and 65.0 W, respectively. The power output is measured by the buoy height variation with time. The worst power region for the spike buoy occurred for c_2 between 2.84

and 3.12 $\times$ 10^4 Ns/m. The highest absorbed power for this buoy could be achieved if its c_2 value higher than 3.12 $\times$ 10^4 Ns/m.

In contrast, the bi-cone response (Figure 3.26c) was similar to the model response at optimum mass (see Figure 3.13b) which indicates that its mass (11.63 kg) was close to optimum. It was also seen that the c_2 damping associated with the bi-cone shape was reasonably far from the worst c_2 value predicted by the model. In Figure 3.26c, it is clear that the power for the bi-cone buoy is approximately equal in the highest and lowest c_2 regions, 107.78 W and 101.60 W, respectively. The worst power region for the bullet buoy occurred for a value of c_2 in the range 2.87 to 1.89 $\times$ 10^4 Ns/m.

3.9. Conclusions

In this chapter, a point absorber was considered as a mechanical system with two sets of parameters, namely geometrical parameters and control parameters. The geometrical parameters include a linear radiation damping term c_2 which defines the geometry of the buoy. The control parameters relate to the PTO damping mechanism c_1. These are usually variable parameters that can be tuned to match a given sea state. In this respect, to increase wave device efficiency and consequently minimise energy production costs, a new approach to optimising the geometry and performance of heaving point absorbers was outlined including the development of a steady-state harmonic model. In the model the power output of a harmonically oscillating buoy was measured by varying the buoy's height with time. The power response was maximised by using the best value for c_2 from the region driven by high c_2 for determining the best value of c_1 for a mass equal to the optimum mass.

The steady-state harmonic model developed in this chapter revealed that at resonance, a buoy of any shape will have two types of behaviour: one driven by low radiation damping and the other by high

radiation damping. Successful operation in the low radiation damping region is difficult to achieve and hence operation in the high damping region is recommended for maximising power capture. This suggests that it is beneficial to add some form of external damping. The model also revealed that the optimum value for c_1 is $c_1 = c_2 = k/\omega$ when the buoy with optimum mass is at resonance with the peak frequency of the sea state at $\omega^2 = k/m$. Further examination with mass values of 99.99% and 100.01% of $\tilde{m}$ revealed that for a system that is not in resonance, the linear relationship between c_1 and c_2 no longer holds true, even when mass deviated by only 0.01% from its optimum value. In other words, at optimum mass, $\tilde{m}$, when the system is in resonance, in order to maximise the power, the $c_1 = c_2$ condition must be met. The use of the model to optimise the geometrical and damping parameters of a device could lead to major economic design benefits for any point absorber buoy of any shape.

Increasing damping c_2 by adding two round discs to the lower part of the buoy was tested experimentally and the reliability of the results was confirmed statistically. It was found that the round disc technique did not give the desired outcome as the extra damped buoys with two discs had lower c_2 values than the zero damped buoys with one disc. Although the technique appeared reasonable, the low damping outcomes were unexpected and are worthy of further investigation. Other ideas on how to alter the c_2 values emerged such as adding roughness to the buoys but could not be achieved within the scope of this work and are still worth investigating.

The mass of the bullet, spike and bi-cone buoys was 33.44 kg, 27.72 kg, and 11.63 kg, respectively. Of all the tested buoy shapes (bullet, spike and bi-cone), the bi-cone ($60^o/120^o$) response was most similar to the optimum mass response of the model which indicated that its mass of 11.63 kg was close to optimum.

It was also noted that the c_2 damping value for the bi-cone shape differed from the worst c_2 value predicted by the model. In conclusion, the results revealed that the buoy with the bi-cone buoy had the best performance and its potential integration with a parabolic concentrator will be assessed experimentally in chapter 4. In addition, the results encourage the conduction of further investigation to tune the geometrical and control parameters of different buoy shapes by optimising their c_1 and c_2 values to match a given sea state.

The PTO system has been modelled with a constant damping coefficient for regular waves. This might be considered as the model's main limitation because approaches which consider irregular waves tend to be more accurate as they better replicate real sea conditions. In reality, the constant damping coefficient approach is not valid and power losses due to the PTO will be present. The PTO system thus needs to be modelled more accurately. Cargo et al. (2012) conducted an extensive study on the modelling of a PTO system and his results could be used to further improve the steady-state harmonic model presented here. He demonstrated that simplification of the PTO system during the simulation phase of device development could lead to incorrect design decisions and subsequently to additional delay and cost.

Chapter 4: Experimental Wave Flume Tank Testing

In the comprehensive literature review presented in chapter 2 a viable solution to protect Qaru Island from wave attacks and erosion was identified. The conducted literature revealed that the wave climate around Qaru Island was suitable for the installation of a WEC device and a floating breakwater was identified as the most appropriate type to be combined with the WEC device. In addition, with the low wave power density and limited resources of good quality stone in the area of interest, chapter 2 provided the first evaluation of the potential of a parabolic concentrator to enhance wave energy conversion around the island. A parabolic concentrator was found to be the best solution as it can function as a breakwater, a WEC device and a mooring facility. The combination of a parabolic concentrator with a point absorber was assessed further in chapter 2. In chapter 3, the bi-cone ($60^o/120^o$) buoy configuration was found to have the best performance and its potential integration with a parabolic concentrator will be assessed experimentally in chapter 4.

The aim of this chapter is to describe the wave flume tank testing carried out as part of this research. The experimental work was designed to investigate the response of two parabolic structures to an ocean wave spectrum representative of the operational wave environment in Kuwait. In addition, the status of the parabolic concentrator-point absorber technology and its use as a WEC and breakwater device was evaluated. In particular, the aim was to identify the locations of the amplification zones created by the two different parabolic structures where the wave energy density is the highest, and to compare these to the locations of the parabolae's focal points. This

was done to determine the suitability of such devices for use in the Kuwaiti mild wave environment. It was fortunate for the progress of this research that it was possible to conduct testing at the Kuwait Institute for Scientific Research (KISR) using the Coastal Management Program's wave flume tank facility.

A theoretical background to aspects related to the hydrodynamics of wave energy and power is given in section 4.1 of this chapter, along with analysis of wave tank behaviour using Fourier series. In addition, aspects related to the Froude number and its use for the scaling of wave tank physical models are discussed. The following section, section 4.2, contains an outline of the testing conducted. A detailed description of the experimental setup and testing procedures of all the wave flume tank tests is presented in section 4.3. The data collected and other observations are reported in section 4.4. These are used to provide a basis for a series of recommendations for further testing to improve the design of the parabolic concentrator-point absorber WEC system and for partial validation of the numerical simulation studies.

4.1. Theoretical Background

In this section the purpose of using the Fourier series to break up the periodic signals of the power absorption function is presented. The basic idea of this representation is to break down the periodic signals into a set of simple terms that can be solved individually and then recombined to obtain the power absorbed by a heaving buoy.

4.1.1. Power Absorption

The energy in an ocean wave can be divided into two parts: kinetic and potential. The kinetic energy is due to the water fluid motion, and the potential energy is due to the wave elevation. The total energy of a plane harmonic wave on deep water is half kinetic and half potential. The total energy stored in waves per unit area of sea surface, E, is given as:

$$E = \frac{\rho g H^2}{16}\left[1 + \tanh(k_n d)\right] \tag{4.1}$$

For deep water conditions where $\tanh(k_n d) \approx 1$, the total energy stored in waves per unit area of sea surface is simplified further to give:

$$\overline{E} = \frac{1}{8}\rho g H^2 \tag{4.2}$$

where ρ is the density of the water, H is the wave height, d is the water depth, k_n is the wave number, and g is the acceleration due to gravity.

The power per unit length of waves is found by multiplying the energy intensity in the wave with the group velocity of the wave (v_g). Therefore, the power in the wave front or average incident wave power per unit crest width (P) is defined as:

$$P = v_g E \tag{4.3}$$

The power absorbed by a heaving buoy (P_a) with velocity, v, across its damper, subjected to a force, F_i, is given as:

$$P_a = \frac{1}{N\Delta t}\sum_{i=1}^{N} F_i v_i \Delta t \tag{4.4}$$

where F_i is the force in the heaving direction, v_i is the buoy velocity in the heaving direction $\left(v_i = \frac{y_i - y_{i-1}}{\Delta t}\right)$, y_i is vertical displacement at time Δt and y_{i-1} is vertical displacement at time $(i-1).\Delta t$.

The absorption width is defined as the length of wave front transporting the same amount of power as the device would absorb under the same wave conditions. The absorption width is found by dividing the power

absorbed by the heaving buoy (P_a) by the power in the wave front (P). Absorption width is given as:

$$AbsorptionWidth = \frac{P_a}{P} \tag{4.5}$$

The absorption efficiency, also referred to as the 'relative absorption width', is the ratio of the absorbed power to the available power transported by the wave front over the width of either the buoy or the flume tank. Absorption efficiency is given as:

$$AbsorptionEfficiency(\eta) = \frac{P_a}{P.L_{Tank}} \times 100 \qquad (\%) \tag{4.6}$$

where L_{Tank} is the width of the flume tank or can be taken as the buoy diameter, D , as required.

4.1.2. Fourier Series for Analysing Wave Tank Behaviour

A Fourier series takes a periodic signal and decomposes it into a sum of a number of sine and cosine expressions with different frequencies. Assume that we have a periodic signal that lasts for 0 < t_s < T_p. The approximation made by breaking the signal is represented by the following infinite series:

$$f(t_s) = a_0 + \sum_{n=1}^{\infty}\left(a_n \cos(\frac{2\pi n t_s}{T_p}) + b_n \sin(\frac{2\pi n t_s}{T_p}) \right) \tag{4.7}$$

where $f(t_s)$ is the signal in the time domain, a_n and b_n are coefficients of the series, n is an integer equal to 5, t_s is the signal time, and T_p is the periodic time of the wave.

The coefficients a_n and b_n are related by the following equation:

$$c = \sqrt{a_n{}^2 + b_n{}^2} \tag{4.8}$$

The signal magnitude at the general n^{th} integer can be determined as:

$$f(t_s) = \left(\cos(0 \times t_s 2\pi / T_p)\right)' . \frac{\underline{f}}{m} + \sum_{n=1}^{\infty} \left(\left(\cos(2\pi m t_s / T_p)\right)' . \frac{\underline{f}}{m/2} \times \cos(\frac{2\pi m t_s}{T_p}) + \left(\sin(2\pi m t_s / T_p)\right)' . \frac{\underline{f}}{m/2} \times \sin(\frac{2\pi m t_s}{T_p}) \right) \quad (4.9)$$

where $\underline{f}$ is the vector of force value, $\underline{t}$ is the vector of time value and m is the series number. The continuous periodic force exerted by the wave on the buoy and the buoy's velocity across its damper can be represented by a summation of the first, second, third, fourth and fifth harmonics. This summation is used to calculate the power absorbed by the heaving buoy (P_a) using Equation (4.4).

4.1.3. Froude Scale Ratio

For a physical scale model to be completely similar to its prototype, it needs to satisfy a set of mechanical similarity criteria as follows:

(i) **Geometrical similarity:** similarity in shape.

(ii) **Kinematic similarity:** requires geometrical similarity and similarity of motion between model and prototype particles.

(iii) **Dynamic similarity:** requires geometrical and kinematic similarity in addition to similarity of all the force ratios in the two models.

To create the most representative physical model of a full-scale device, with minimal modelling errors due to hydrodynamic and other nonlinear phenomena, the largest scale factor for the prototype has to be selected. In this study, the model size was limited by what would reasonably fit in the testing facility at KISR. Ideally, when scaling a model, two non-dimensional quantities, namely the Froude number and the Reynolds number, would be held constant. However, for wave tank testing where gravity and inertial forces are dominant, and the effect of the remaining forces such as viscous forces are assumed negligible, Froude scaling on its own is considered valid. Most water phenomena

are modelled based on the Froude method, such as free surface flows in hydraulic structures, waves and WECs. Different scale ratio formulas are used to scale Froude model parameters (Froude scale = Parameter $_{prototype}$/Parameter $_{model}$). The typical scale ratios for Froude models are given in Table 4.1.

Table 4.1: Scale ratio for Froude models (Heller, 2011)

Parameter	Dimension	Froude Scale
Geometric Similarity		
Length	[L]	λ
Area	[L^2]	λ^2
Volume	[L^3]	λ^3
Rotation	[-]	1
Kinematic Similarity		
Time	[T]	$\lambda^{1/2}$
Velocity	[LT^{-1}]	$\lambda^{1/2}$
Acceleration	[LT^{-2}]	1
Discharge	[L^3T^{-1}]	$\lambda^{5/2}$
Dynamic Similarity		
Mass	[M]	λ^3
Force	[MLT^{-2}]	λ^3
Pressure and stress	[$ML^{-1}T^{-2}$]	λ
Energy and work	[ML^2L^{-2}]	λ^4
Power	[ML^2T^{-3}]	$\lambda^{7/2}$

4.2. Outline of Experimental Work

A series of experimental wave tank tests were performed to understand the hydrodynamic and power performance of the parabolic concentrator-point absorber WEC system. Within the WEC, the PTO system is responsible for converting the force created by the motion of the heaving point absorber to useful power. The specifications for the flume tank tests are described briefly in Table 4.2.

Stage-1 of the testing examined two different parabola model configurations with a width of 2.5 m (the full width of the flume). The

configurations chosen were at either end of the potentially useful range of geometries. During this stage, the wave tank tests were carried out to examine the behaviour of regular, unidirectional, two dimensional, long crested waves. For the present analysis, in order to investigate the focusing effects at the amplification zone, a range of very low discrete wave states representing Kuwaiti sea conditions were considered. Video image analysis of the water surface was used to visualise the effect of the two model configurations on wave behaviour in addition to finding the location of the amplification zone and the level of amplification at the zone.

In stage-2, tests were conducted in two phases. In phase I, a zero damped point absorber (heave motion only) was tested to analyse its dynamic response and to record displacements. Phase II involved testing a damped point absorber (fully damped and half damped) so that deflections, forces and maximum power outputs could be measured.

The stage-1 and stage-2 wave tank tests were aimed at evaluating the hydrodynamics and power output of the system in an operational wave environment similar to that in Kuwait. The results and findings from these tests were used to form recommendations for the final (stage-3) testing in which the performance of an optimum configuration for the following systems was evaluated: (i) parabolic concentrator-heave only zero damped point absorber, and (ii) parabolic concentrator-heave only damped point absorber to evaluate the hydrodynamics and power output of this novel technology.

Table 4.2: Experimental wave tank tests outline. All experiments were carried out at the Kuwait Institute for Scientific Research

Test Number		Type	Model Scale	Date	Note
STAGE-1		Parabolic Concentrator	1/16	June-August 2015	Test 2 different concentrator shapes. Analyse their wave focusing effects using video image analysis. Find the level of amplification at the amplification zone.
STAGE-2	Phase I	Heave-only Zero Damped Point Absorber	1/16	May 2016	Test zero damped point absorber in heave motion only. Analyse the dynamic response of the system and measure PA displacement.
	Phase II	Heave-only Damped Point Absorber	1/16	May 2016	Test damped point absorber in heave motion only. Measure deflection, forces and maximum power output.
STAGE-3		Parabolic Concentrator-Point Absorber	1/16	July 2016	Test optimum configuration: (i) Free PA and concentrator. (ii) Damped PA and concentrator. Measure upward forces and find the best configuration to give maximum power absorption.

The flume tank, instrumentation, and buoy and parabola geometries and dimensions, from the initial conceptual design stage through assembly, installation, data acquisition, measurement, and data interpretation are detailed in the following sections.

4.3. Experimental Setup and Measurement

4.3.1. Wave Flume Tank

The concrete flume tank at KISR is of the following dimensions: length 40 m, width 2.5 m and depth 2.5 m. Within the mechanical, geometric and hydraulic limitations of the system, the installed active absorption type (Danish Hydraulic Institute (DHI)) wave maker is capable of generating waves of heights up to 40 cm with wave periods in the range 1.0 to 5.0 s and lower. The wave maker setting includes damping to stop reflected waves at the wave maker end of the flume. The system can be used to generate different kinds of two dimensional regular and random wave sequences or sea states. It has wave synthesiser software to control wave generation, data acquisition and analysis. The maximum water depth in the flume is 2.5 m. The water depth near the wave maker is 1.5 m, and a constant water depth of 1.5 m was chosen for all the tests to represent a deep water situation. The slope of the beach begins at a distance of 30.5 to 38.8 m from the wave generator. The flume tank tests were carried out with regular, unidirectional, two dimensional, long crested waves. A range of very low discrete wave states which represent Kuwaiti sea conditions were considered. The range of wave states chosen also took into account the minimum operating range of the wave maker. A spectrum of wave components was generated at the same time so testing times could be reduced. The propagation and reflection of the waves as well as the wave focusing effects of the concentrators were analysed.

The parabolic concentrators and the point absorber (buoy) were designed according to Froude number and fabricated at the Coastal Management Program at KISR. A detailed description of the model scaling is given in section 4.3.2. A schematic top view of the experimental setup is shown in Figure 4.1.

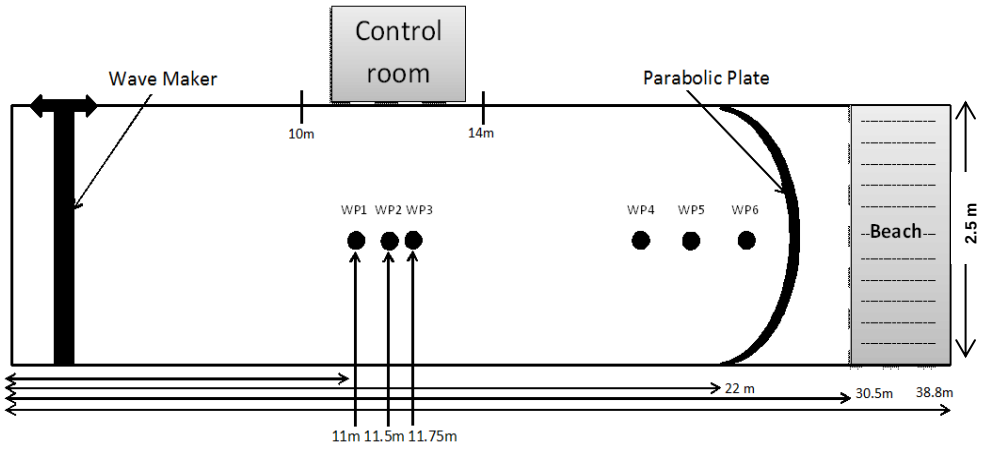
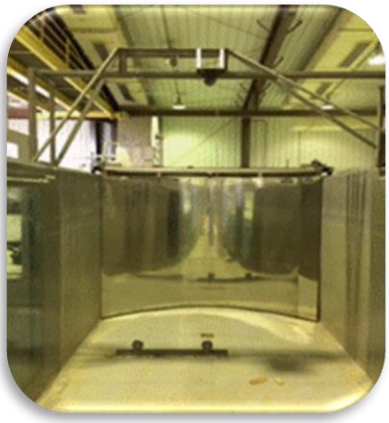


Fig. 4.1: Schematic of wave flume tank and position of parabola

The various stages of the flume tank testing are illustrated next in Figure 4.2. During stage-1 wave tank tests two different parabola model configurations with a width of 2.5 m (the full width of the flume) were tested to identify the amplification zones created by each parabola where wave energy density was the highest. In addition, the level of amplification in the amplification zone arising from various wave heights will also be studied. The parabola configurations will be used to provide a basis for the buoy design and final shape selection. In addition, the design will be optimised for the wave conditions at which the highest amplification factors are recorded with parabola-1 and parabola-2 during stage-1 testing. Based on the outcomes of stage-1, stage-2 tests of heaving point absorber will be conducted in two phases. The results and findings from these test will determine the optimum parabolic concentrator–point absorber configuration which will be tested during stage-3. The experimental testing facility and data acquisition setup at KISR are illustrated in Figure 4.3.



Parabolic Concentrator Testing

Parabola model-1

width (2.5 m) & focal length (0.313 m)

Parabola model-2

width (2.5 m) & focal length (0.625 m)



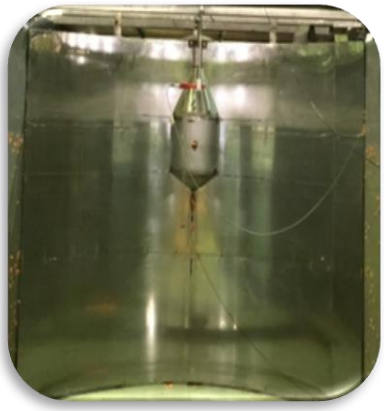
Point Absorber Testing

Phase I

Zero damped heaving point absorber

Phase II

Damped heaving point absorber



Parabolic Concentrator- Point Absorber Testing

Best Configuration to give maximum power absorption

Fig. 4.2: Stages of wave flume tank testing

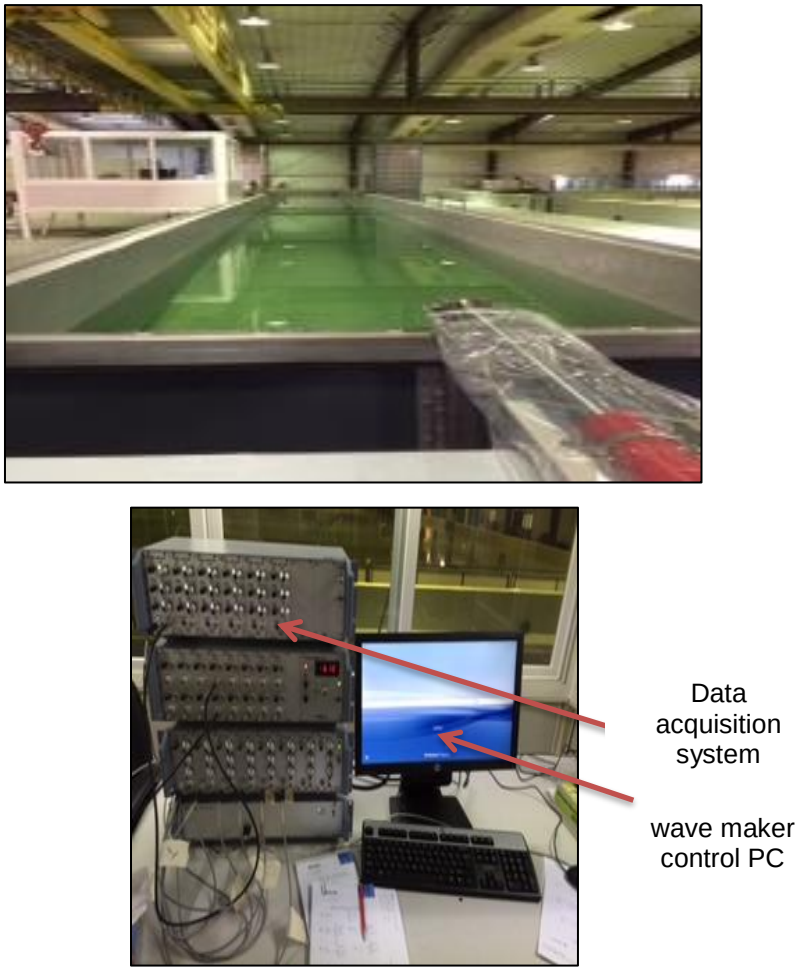


Fig. 4.3: Wave flume tank facility and data acquisition setup at KISR

4.3.2. Wave Conditions Generated

Although the area of the Kuwaiti territorial water is only about 7611 km^2, the wave climate varies significantly from one location to another. Wave energy potential and wave spectrum were predicted for 19 different locations based on 12 and 15 years' worth of wave data. The wave data was hindcasted using the wave prediction model (WAM) for the total period. The WAM model results were in the form of the significant wave height and mean wave period for every one hour. The data was hindcasted for all the Kuwaiti territorial waters based on a grid size of $0.1^o \times 0.1^o$ (Neelamani et al., 2007).

From the joint distribution of significant wave height and mean wave period presented in Table 4.3 for location 1 around Qaru Island in the

Kuwaiti territorial waters (number of occurrences over 12 years), the device operating conditions were found to be: incident wave period, T_i = 2.6 – 4.5 s and significant wave height, H_g = 0.25 –1.5 m). These conditions were chosen to ensure the safe and economic design of the structure (Neelamani et al., 2007). In order to achieve the experimental objectives and investigate the focusing effects at the amplification zone(s), a range of very low discrete regular wave states (wave periods, T = 3.2, 3.4, 3.6, 4.0 and 4.8 s and wave amplitudes, H = 0.48, 0.96 and 1.44 m) representing Kuwait sea conditions were considered.

Table 4.3: Joint distribution of significant wave height and mean wave period for location 1 in Kuwaiti territorial waters (number of occurrences over 12 years) (Neelamani et al., 2007)

H_s (m)	Mean wave period, T_{mean} (s)										
	0–1.0	1.01–2.0	2.01–3.0	3.01–4.0	4.01–5.0	5.01–6.0	6.01–7.0	7.01–8.0	8.01–9.0	Total no. of occurrences	Mean value (S)
0–0.25	0	2893	24,148	6839	542	24	2	0	0	34,448	2.648
0.251–0.5	0	139	11,392	25,189	1547	146	0	0	0	38,407	3.244
0.51–0.75	0	0	52	16,347	1238	354	0	0	0	17,991	3.605
0.751–1.0	0	0	0	3647	961	146	8	0	0	4762	3.768
1.01–1.25	0	0	0	1914	1707	120	20	0	0	3761	4.034
1.251–1.5	0	0	0	358	3402	194	37	0	0	3991	4.477
1.51–1.75	0	0	0	5	1085	118	28	2	0	1238	4.641
1.751–2.0	0	0	0	0	222	113	16	0	0	351	4.913
2.01–2.25	0	0	0	0	33	94	14	0	0	141	5.365
2.251-2.5	0	0	0	0	1	47	4	0	0	52	5.558
2.51–2.75	0	0	0	0	0	14	14	0	0	28	6.0
2.751–3.0	0	0	0	0	0	1	18	0	0	19	6.447
3.01–3.25	0	0	0	0	0	0	3	0	0	3	6.5
3.251–3.5	0	0	0	0	0	0	0	0	0	0	

A Froude scaling of 1:16 was used to obtain the values of the scale model parameters. From Table 4.1 the scale factor for the wave height is λ and for the wave period is $\sqrt{\lambda}$. The wave height and wave period scale ratio formulas used for the model and prototype scaling were:

$$\lambda = \frac{H_{prototype}}{H_{model}} \tag{4.10}$$

$$\sqrt{\lambda} = \frac{T_{prototype}}{T_{model}} \tag{4.11}$$

The regular wave testing conditions at the prototype and model scales are summarised in Table 4.4.

Table 4.4: Regular wave testing conditions at prototype and model scales

	Prototype Scale		Model Scale	
	H (m)	T (s)	H (cm)	T (s)
Stage-1	0.48, 0.96, 1.44	3.2	3, 6, 9	0.80
		4.0	3, 6, 9	1.0
		4.8	3, 6, 9	1.2
Stage-2	0.48, 0.96, 1.44	3.2	3, 6, 9	0.80
		3.4	3, 6, 9	0.85
		3.6	3, 6, 9	0.90
		3.8	3, 6, 9	0.95
		4.0	3, 6, 9	1.0
Stage-3	0.48, 0.96, 1.44	3.2	3, 6, 9	0.80
		3.4	3, 6, 9	0.85
		3.6	3, 6, 9	0.90
		3.8	3, 6, 9	0.95
		4.0	3, 6, 9	1.0
		4.8	3, 6, 9	1.2

The accuracy of the wave profiles generated by the wave maker was evaluated for the majority of the point absorber test conditions conducted in the flume with and without the parabola. The damping associated with the wave maker was included to stop reflected waves at the wave maker end of the flume tank. The generated surface elevations measured by the wave probes at specific locations were compared to the target conditions. As the incident wave power is highly dependent on wave height, it is important to ensure that the generated wave heights are acceptably close to the required values and the wave period is correct. Representative wave heights and periods were extracted from the measured data for the fully developed, regular, unidirectional, two dimensional, long crested waves. It was found that the generated wave heights were mostly within 10% of the input wave heights. The results also showed that the higher wave heights diverged further from the input values due to the increased non-linearity

associated with these conditions. All wave periods generated in the flume compared reasonably well with the input wave periods (approximately in the range -3% to +4%).

4.3.3. Measurement Instrumentation

The experimental setup is equipped with a large number of sensors, supplied by KISR, which are able to continuously monitor the performance of the parabolic concentrator-point absorber device. In this research, only the data from the wave probes were utilised:

Conductive Type Wave Probe, WP (s): The wave probes used consisted of two thin parallel stainless steel electrodes. The resistance between the plates is measured when the probe is immersed. The conductivity is proportional to the variation in the water surface elevation. A set of compensation electrodes is mounted at the bottom end of the wave gauge to balance the effects of changes in temperature and salinity. Six conductive type wave probes (supplied by DHI, Denmark) were calibrated and arranged at two locations within the flume tank.

In order to establish wave reflection within the tank and ensure steady state conditions, the distance between the wave maker and probe WP1 was chosen to be 11 m. To complete the cluster, probes WP2 and WP3 were placed at distances of 11.5 and 11.75 m from the wave maker, respectively. WP1, WP2 and WP3 were used to measure the incident waves. In general, two stationary wave probes are needed for extracting wave reflection information. However, in this study, three probes were used since in some cases when there are only two probes, they may measure the same wave height, which makes it impossible to extract reflected wave information. Probes WP4, WP5 and WP6 were used for measuring the wave focusing effects created by each parabola. These were placed within close proximity to the parabola plate so that wave heights in the amplification zone could be monitored closely. Probes WP1, WP2 and WP3 are shown in situ in the photograph in Figure 4.4. The probes were hung from a bar that was

mounted on top of the tank; the same mounting arrangement was used for WP4, WP5 and WP6.

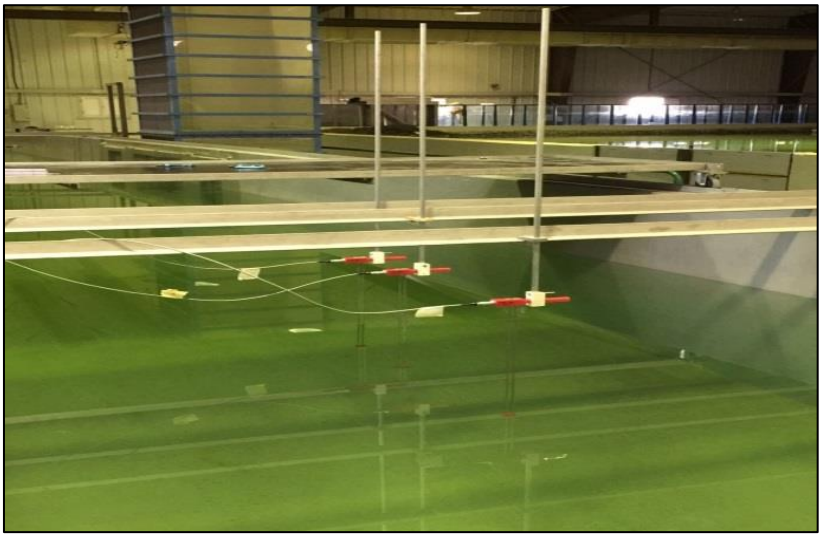


Fig. 4.4: Wave probes in the concrete flume tank measuring regular waves for wave characterization

Potentiometer: The relative heave motion of the point absorber was registered by a linear potentiometer. The potentiometer was mounted on a frame and attached to the side of the buoy (Figure 4.5). In order to ensure the accuracy of the potentiometer measurements, a camera tracking system was also used. In the potentiometer, an electrically conductive wiper slides across a fixed resistive element and a voltage is applied across the element forming a voltage divider circuit. The output voltage (V_{out}) is measured and is proportional to the distance moved by the buoy.



Fig. 4.5: Potentiometer mounted on the frame at the concrete flume tank

Load Cell(s) (Force Transducer): Force measurements were needed to evaluate the power generation performance of the buoy shown in Figure 4.6a. These were obtained by using two calibrated load cells. In order to measure the tension in the cable and the net upward forces acting on the buoy, one load cell was attached to the top between the buoy and the cable (Figure 4.6b) and the other was attached below the buoy using the configuration shown in Figure 4.6c. The tension in the cable was calculated by adding the two measured load cell signals and the net upward force acting on the buoy was calculated from the difference between the signals.

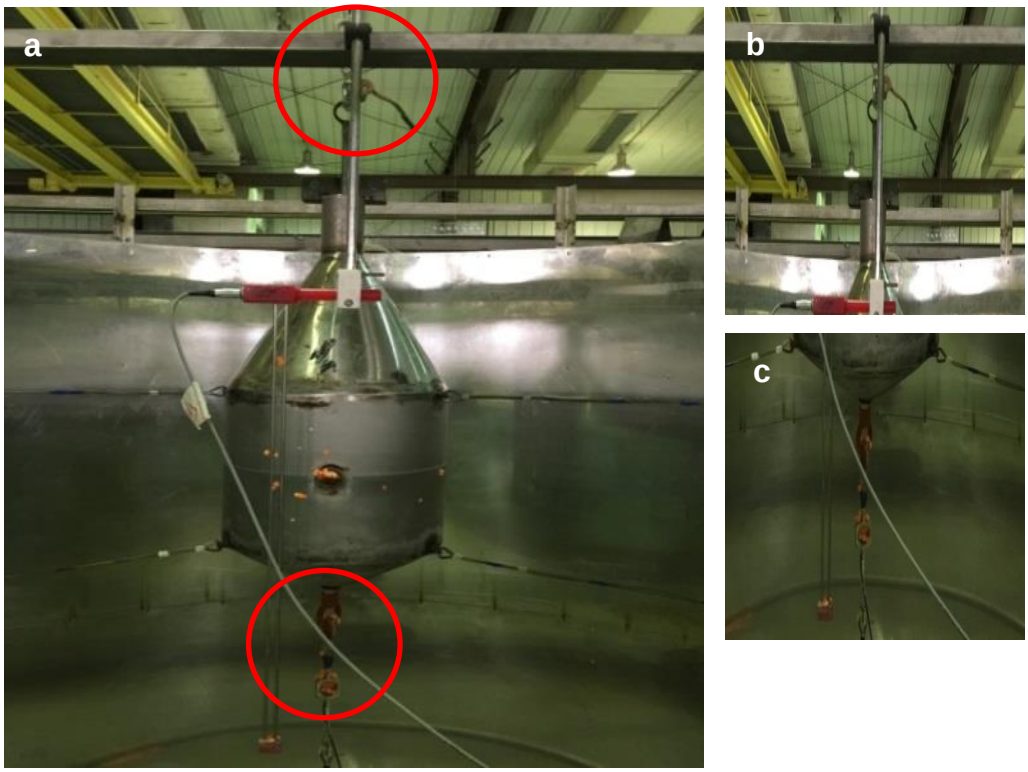


Fig. 4.6: Load cells to measure forces acting on the buoy

PTO Motor: A motor was connected to the buoy to provide damping to represent a power take-off (PTO) mechanism. The motor was connected to an “open-circuit” (i.e. nothing was connected to its terminals) or to one of two “short-circuits” (i.e. one where all the terminals were connected together and the other where only two terminals were connected together). The difference between these tests provided information about how much of the total torque resistance was caused by the electric current. The airgap torque of the short circuit caused the motor to behave like a pure damper. During motor calibration with the complete short-circuit, the translational and optimal damping values were calculated by dividing the force by the velocity. The optimum translational damping for power capture was calculated to correspond to a maximum wave amplitude of 0.09 m (peak-to-peak) for the buoy with diameter 0.312 m. Using the buoyancy force and velocity values, this optimal damping value was found to be approximately 60 Ns/m. A translational damping of 4172 Ns/m was calculated for the case of a force being exerted on the motor by allowing a weight of

0.751 kg attached to the motor to drop freely at a speed of 0.0018 m/s. (Details of these calculations can be found in Appendix 4.) Based on these damping values, the radius of the pulley used in the experimental setup was approximately 8.33 [i.e. √(4172/60)] times larger than the radius of the motor shaft]. A translational damping of 15 Ns/m was calculated provided that the resistance across the motor terminals remained unchanged. To reduce the translational damping from 15 Ns/m, either the cable was wrapped around a pulley with a diameter larger than the motor shaft or the resistance across the terminals was increased. Figure 4.7 shows photographs of the PTO mechanism.

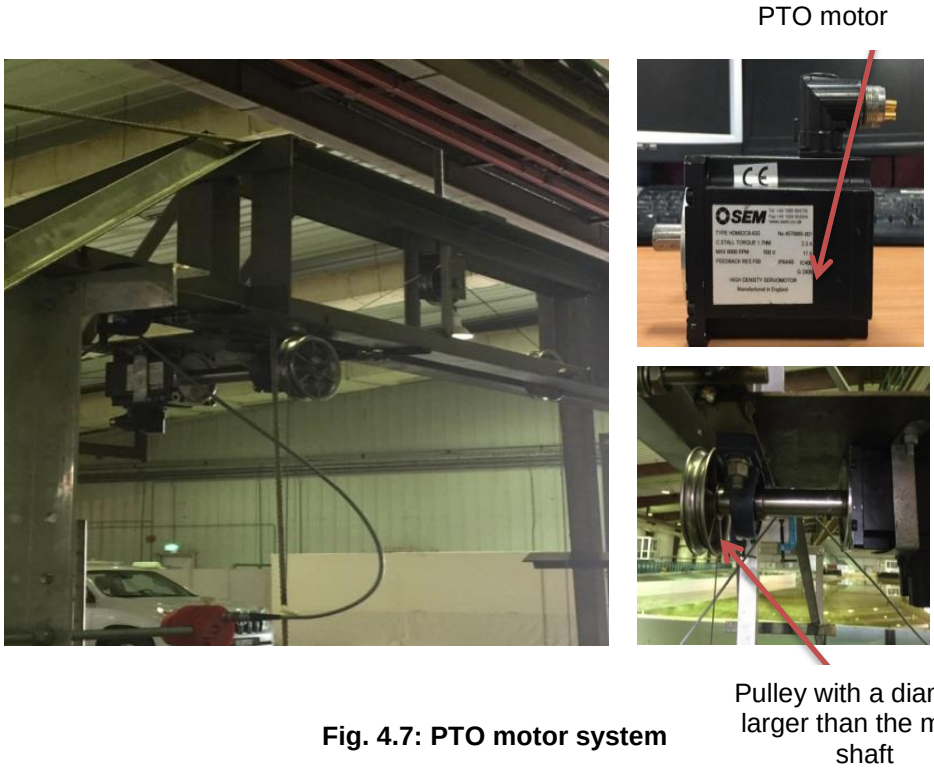


Fig. 4.7: PTO motor system

Camera Tracking System: Video image analysis of the water surface was used to visualise the focusing and amplification effects at the maximum amplification zone(s). Cameras were used to capture and visualise buoy response and wave behaviour both around the device and in the vicinity of the parabola models for various wave states. The system consisted of two cameras, one mounted on top of the tank around the amplification zone(s) to measure horizontal movements at the top, and a second mounted on the side of the flume tank.

Polystyrene Beads: Water surface movement and wave elevations were detected using orange polystyrene beads scattered around the area of interest and at various locations within the tank (Figure 4.8). The motion of the beads was tracked with carefully positioned cameras which allowed the motion of the marked beads to be mapped and translated into x-y-z coordinates for motion analysis. Time and movement histories for the waves were recorded and analysed. It would have been possible to analyse the motion of the beads in more detail, but for the purposes of the research presented in this chapter, visualisation of the beads motion was a sufficient technique to track the wave motion.

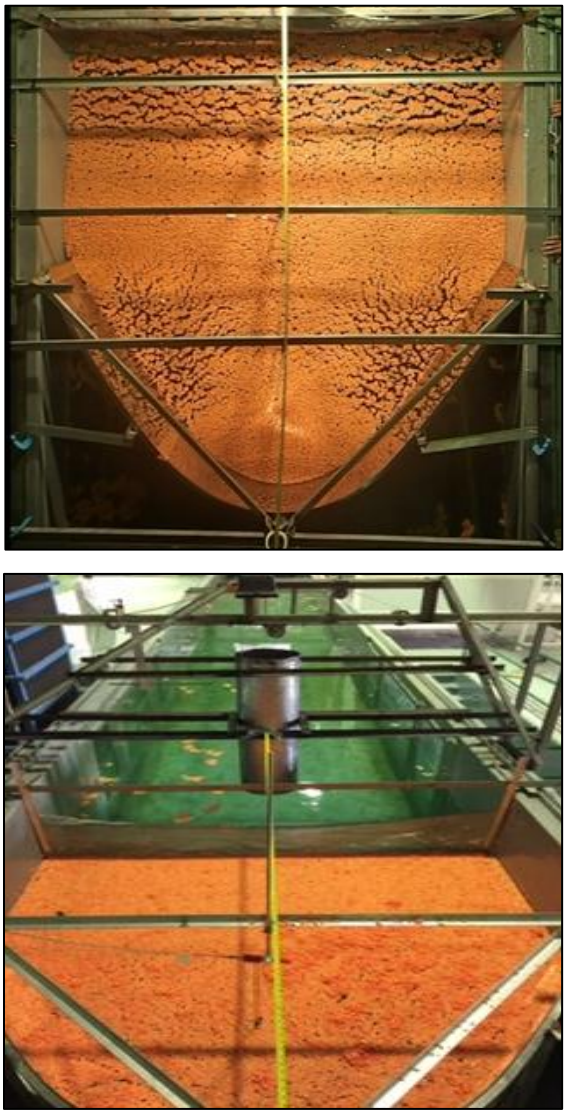


Fig. 4.8: Polystyrene beads scattered around the area of interest

4.3.4. Calibration

The six conductive type wave probes were calibrated as recommended in the user manual. Incident wave heights of up to 9 cm were generated for the experimental testing. Since with partial reflection and focusing effects wave heights of up to 40 cm could be expected at the amplification zone(s), the gain was selected such that for a 20 cm wave amplitude, the signal output was 10 V (maximum possible outputs were +/- 10V). The wave flume was initially filled with up to 70 cm of fresh water. Each wave probe wire was 60 cm long. The six probes were immersed such that 30 cm of the wire was under the water and 30 cm was above and the offset in the wave amplifier was adjusted to zero. The wave probe wire was then immersed in the water to a depth of 10 cm and the gain setting adjusted such that the output was 5 V. The wave probe was immersed by an additional 10 cm and it was verified that the output was 10 V. Similarly, the wave probes were raised by 5 cm and 10 cm and the corresponding changes in voltage were recorded. The data collected was plotted and the slope of the graph was obtained from which the calibration constant was calculated.

The wave probe calibration constant has units of cm/V and with the arrangement used, its value was approximately 2 cm/V. However, a more accurate value of the calibration constant for each wave probe was obtained by using the method of least squares to fit a straight line to the data for the wave probes individually. The calibration data and graphs can be found in Appendix 4, and the calibration constants are summarized in Table 4.5.

Table 4.5: Wave probe calibration constants

Wave Probe	Calibration constant
1	1.98
2	1.97
3	1.89
4	1.96
5	2.02
6	2.00

4.3.5. Data Acquisition and Collection

Regular wave tests were conducted for a range of very low discrete wave states (wave periods T = 0.8, 0.85, 0.9, 0.95, 1.0 and 1.2 s and wave heights H = 3, 6 and 9 cm). Data for each regular wave test was collected for a total duration of 90 s at a sampling frequency of 40 samples per second (Δt = 1/40 s). Waves were generated for a total duration of 90 s. Data collection was initiated at 0 s in order to record the wave buildup at the location of each wave probe. The wave height in the maximum amplification zone(s), incident wave height, and wave reflection coefficient were measured. Detailed analysis of the data collected by the wave probes was essential to obtain these measurements. The data analysis was carried out using the wave analysis tools within the MIKE021 software package developed and maintained by DHI. Wave Synthesiser (WS) Reflection Analysis and WS Crossing Analysis were both utilised for calculating the desired data as detailed below.

Data window Selection: The waves were generated for 90 s and data was captured over the full 90 s. It was necessary to select an appropriate window in the data for the different types of analyses and the time series window was used for cases without any reflection from the parabola and for waves with the same repetition of heights. The wave propagation speed (celerity) and the distance to the measuring point can be used to calculate the time the wave will take to reach the measurement point. For example, if C is the wave speed ($C = L/T$, where L is the wave length and T is the wave period) and l is the distance from the wave maker to WP1, then theoretically, the time required for the wave to reach WP1 is $1/C$. The wave energy propagates at group speed which is the speed at which the overall shape of waves' amplitudes propagates through space. This speed is slower than the phase speed of a wave which is the rate at which the phase of the wave propagates in space. Hence in reality, the waves take longer to reach the probe.

A theoretical estimate of the time required for the wave to reach the test section, reflect from the parabola and return to the wave maker is crucial for the selection of a suitable window for the wave analysis. The time series shown in Figure 4.9 is typical of the data obtained. It can be divided into the following sections:

1. Initially, there are no waves in the wave probe location but the wave maker is generating waves (time from 0 to 15 s).

2. The wave reaches the wave probe and continues to grow (time from 15 to 25 s).

3. The wave reaches a steady state and continues with the same height (time from 25 to 57 s). During this time, the wave moves towards the parabola and reflects back to the wave probe. Hence, the window from 25 to 57 s is purely associated with the incident wave and is suitable for extracting incident wave and incident wave energy data.

4. At 57 s, the probe begins to be affected by wave reflection and hence there is a change in wave height. From 57 to 70 s, the wave probe is affected by both incident and reflected waves. A suitable section within this window needs to be selected for the reflection analysis.

5. The parabola creates two types of wave reflection: longitudinal and cross waves, as illustrated in Figure 4.10. The longitudinal reflection reaches the wave probe location faster (straight route) than the cross waves reflection (long route). The wave history after 70 s reflects the combined effect of the longitudinal and cross waves reflections and this data is not needed for any analysis.

The time series data without any reflection effects (time from 25 to 57 s in the example plot shown) are appropriate for analysing incident wave conditions whereas the data for the period with longitudinal but not cross waves wave reflections (time from 57 to 70 s in the example plot).

are required to assess reflection wave effects. This principle was followed for all the wave data collected.

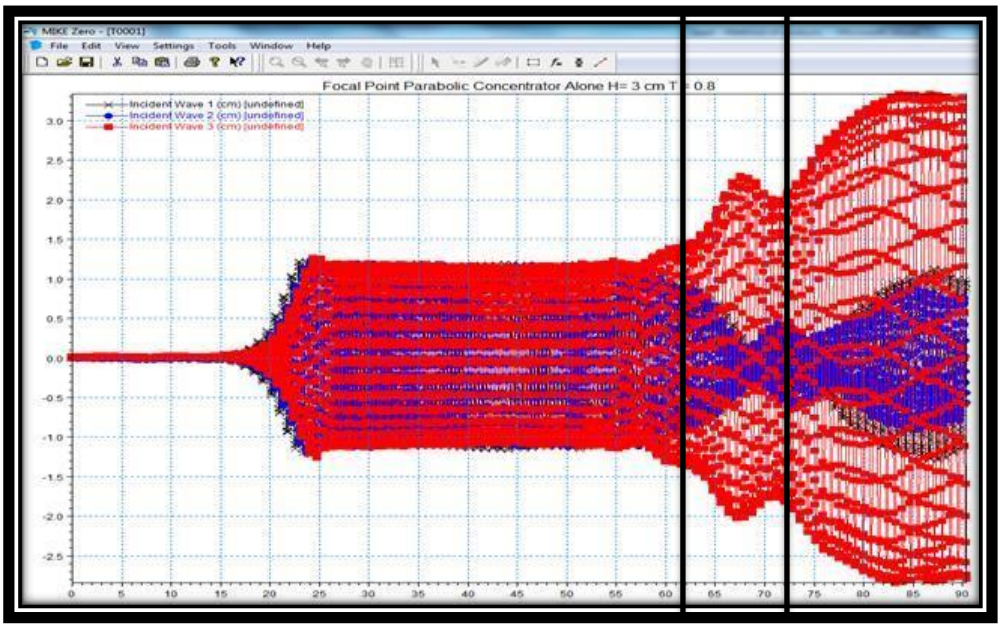


Fig. 4.9: Reflection analysis: data acquisition time selection of a suitable window for the wave analysis

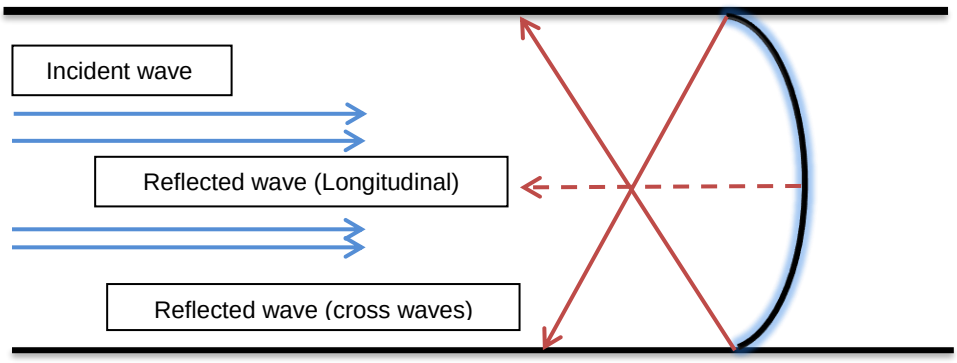


Fig. 4.10: Types of wave reflection: longitudinal and cross waves

Reflection Coefficient, R_c: The WS Reflection Analysis employed is based on the 3-point method developed by Mansard and Funke (1980). This method separates the incident and reflected spectra from the measured co-existing spectra by using a least squares analysis. It requires simultaneous measurements of the wave height at three positions inside the flume tank which are on a line parallel to the wave

propagation direction and are also in reasonable proximity to each other. The wave time series from the first three wave probes (WP1, WP2 and WP3) were used for the reflection analysis. The distances of both WP2 and WP3 from WP1 were defined in addition to the water depth used in the tests. The analysis software then separates the incident and reflected wave components from the recorded responses of these three probes and gives the average reflection coefficient, R_c, defined as the ratio of the reflected wave height H_r to the incident wave height H_i (i.e. $Rc = H_r / H_i$).

Prior to the analysis, the times series file (Figure 4.9) was checked to identify the data to be used. After 55 s, the wave probes started reading the reflected waves indicating the starting point for data acquisition. The effect of the re-reflected waves was taken into consideration from the point at which the wave amplitude increased towards the end of data acquisition. No data was used from after this point. The time to reach this point differed slightly from one probe to another. The starting and ending times for the data acquisition for the reflection analysis of the test with H = 3 cm and T = 0.8 s were 64 s and 71 s, respectively, as illustrated in Figure 4.9. If the reflection coefficient was found to be larger than 1, the analysis was repeated.

Crossing Analysis: The WS Crossing Analysis method is based on the zero-crossing analysis method where the input time series is divided into events. Each event is defined by when the time series value crosses the zero level either in the upwards (called zero-up-crossing) or downwards direction (called zero-down-crossing). For the regular wave data, WS Crossing Analysis was used to extract the peak-to-peak values for the generated incident wave height (H_i) from the time series data collected by the wave probes. In this research, the incident wave height for each test was estimated by the average incident wave height from probes WP1, WP2, and WP3 from the peak-to-peak value output. The heights in the amplification zone(s) were estimated from the data from WP4, WP5, and WP6. The results were used interchangeably

depending on the location of the area of interest and the parabola configuration.

Incident Wave Height, H_i: Before the start of the incident wave height analysis, the time series file was checked for wave probes WP1, WP2 and WP3. The steady state for the generated waves (constant window of waves) is shown in Figure 4.11 for the test with H = 3 cm and T = 0.8 s. This may have differed slightly from one probe to another. The starting and ending times for the data acquisition for the incident wave analysis could have been selected as 26 and 55 s. However, the window from 33 to 48 s was deemed sufficient. Theoretically speaking, for regular waves, a single wave is enough. However, it is usual practice to select 10 to 15 or more waves to obtain an average wave height. Hence, the average wave height of all the waves from 33 to 48 s was calculated.

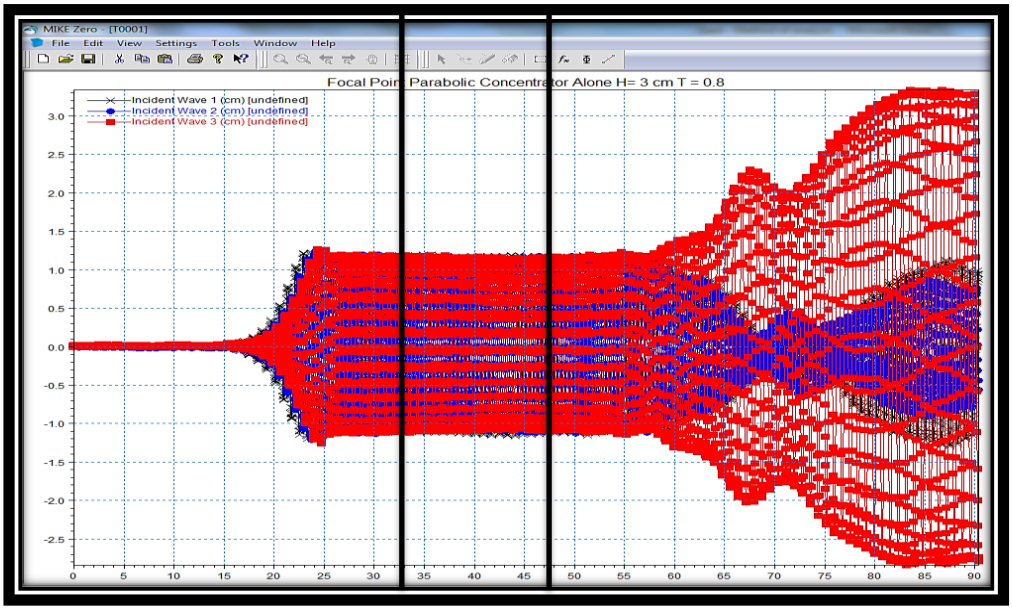


Fig. 4.11: Incident wave height: data acquisition time selection of a suitable window for the wave analysis with wave probes WP1, WP2 & WP3

Wave height at amplification zone(s), H_f: Before the start of the analysis, the times series file was checked for wave probes WP4, WP5 and WP6. After seeing the amplification effects at the amplication zone, the three wave probes were placed at the zone and the wave heights

were recorded. The data from the wave probe with the highest water surface elevation was chosen for the analysis. Probe WP5 had the highest wave elevation and hence was used throughout. The starting and ending time for the data acquisition for the reflection analysis for the case of H = 3 cm and T = 0.8 s were 56 s and 70 s, respectively, (as shown in Figure 4.12), since the waves in this region had repeatedly similar heights.

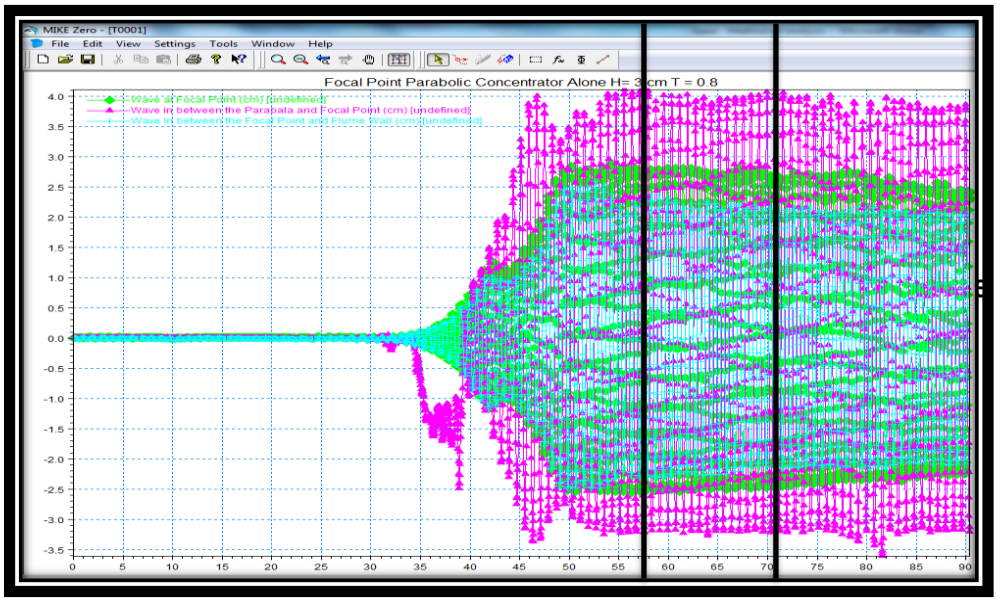


Fig. 4.12: Incident wave height: data acquisition time selection of a suitable window for the wave analysis with wave probes WP4, WP5 & WP6

4.4. Stage-1: Experimental Wave Tank Tests

4.4.1. Parabolic Concentrator

The first set of tests was used to examine two different parabola model configurations designed as part of this research and fabricated at the Coastal Management Program at KISR. The parabola configuration relies on constructive interference that occurs within the parabola structure where interfering waves have a displacement in the same direction equal to the sum of the amplitudes of the individual waves which gives the desired amplification effects. In addition, both parabolae create both longitudinal and cross waves reflections, hence it was necessary to keep the effect of the cross waves oscillations in mind

throughout the experimental investigations. The objective of the stage-1 testing was to identify the amplification zones created by each parabola where wave energy density was the highest. In addition, the location of the amplification zone was compared to the focal points of the parabola for the very low discrete wave states representing the Kuwaiti sea conditions. The level of amplification in the amplification zone arising from various wave heights was also studied.

4.4.2. Stage-1 Test Setup

In order to attenuate the waves, the parabolic concentrator must have a dimension extending in the direction of waves, typically on an order of the wave length. The parabola structure must have a reasonably deep draft to extend to depths equal if not greater than the amplitude of the waves. From Table 4.3 for location 1-3 around Qaru Island, the device operating conditions were found to be: incident wave period, T_i = 2.6 – 4.5 s and significant wave height, H_g = 0.25 –1.5 m). The mean wave period design condition for the prototype of a parabolic concentrator suitable for locations 1–3 around Qaru Island was chosen to be T = 6.5 s (highest mean wave period for locations 1–3) with a wavelength = 66 m. The parabolae focal lengths were chosen such that the focal length of parabola-1 was double that of parabola-2. The shape of a parabola in the xy-plane is described by $y^2 = -2px$, and the focal point is at $x = -p/2$ and y = 0. Therefore, the focal lengths of the parabola-1 and parabola-2 prototypes were chosen to be 5 m and 10 m based on 7.5% and 15% of the design wavelength, respectively. Tests were carried out on two parabola model configurations at a Froude scale of 1:16:

- **Model 1:** Focal point was exactly in line with the edges of the parabola and the focal length was 0.625 m.
- **Model 2:** Focal point was further away from the parabola edges and the focal length was 0.3125 m.

The parabola-1 and parabola-2 model configurations were fabricated with a width of 2.5 m to match the width of the flume tank. In addition, both parabolae were designed to bound the potentially useful range of

geometries in that the one shown in Figure 4.13 is shallow and the focal point is in line with the edges of the parabola whereas the one in Figure 4.14 is deep and the focal point is far inside the zone bounded by the parabola.

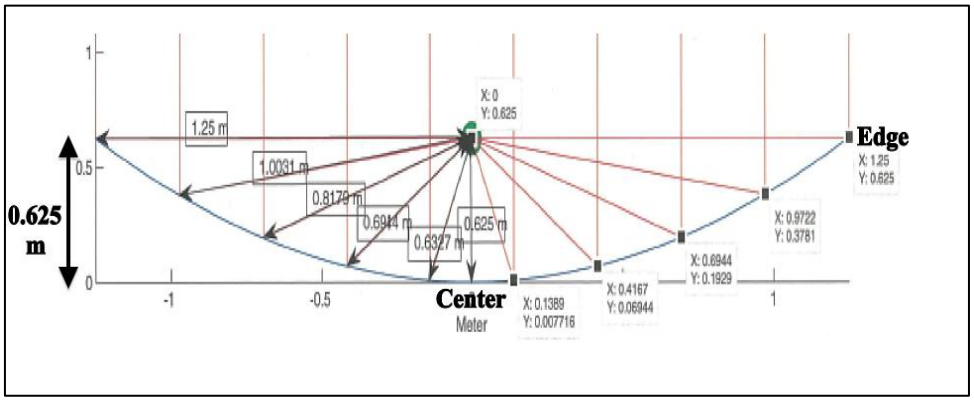


Fig. 4.13: Proposed design for shallow parabolic concentrator (Model 1)

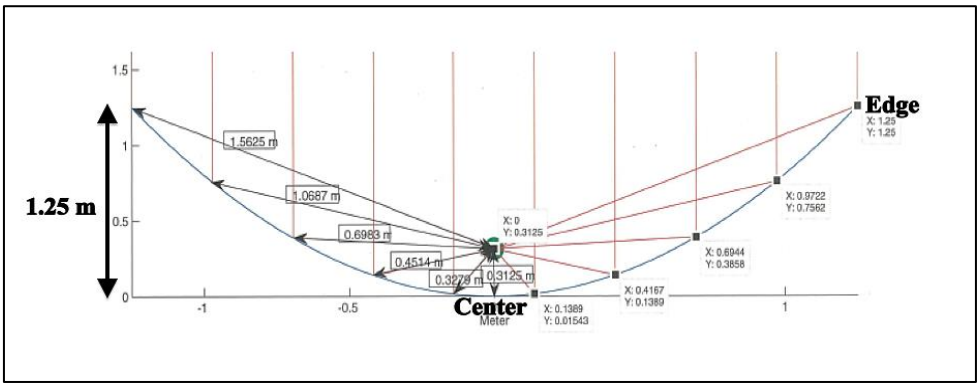


Fig. 4.14: Proposed design for deep parabolic concentrator (Model 2)

In addition, in reality it is not necessary to construct the concentrator to extend up from the sea floor, as wave action is typically confined to the upper strata of the water. Accordingly, it has been found that the proposed floating concentrator can also provide the desired attenuation of wave action, when provided with the proper characteristic and anchored in appropriate locations using heave plates. The heave plates installed at the bottom of the parabola can enhance stability of the structure.

During stage-1 experiments, the parabola plates were fabricated from stainless steel beams and sheets to extend up from the flume wave tank floor. In total, six horizontal beams were bent using a wooden

design template and three vertical beams were added for support. Sheets were then placed on the beams facing the incoming wave direction as shown in Figure 4.15. During testing, each parabola was placed at a distance of approximately 22 m from the wave maker.

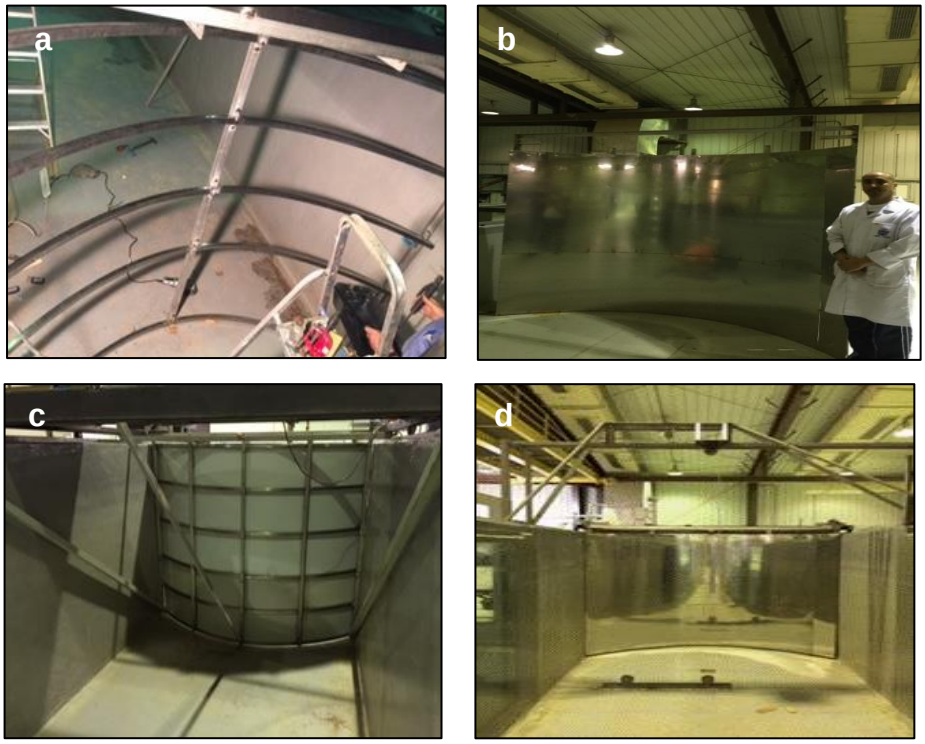


Fig. 4.15: Fabrication and installation stages of parabola models at KISR: a) fabrication of stainless steel beams structure b) Fabrication of parabola stainless steel sheet c-d) Installation of parabola structure

4.4.3. Stage-1 Results

Results for the incident wave height, H_i, maximum amplification zone wave height, H_f, maximum amplification zone diameter, D_{ij}, maximum amplification zone length, L_{fe}, amplification factor $AF = H_f/H_i$ and water depth to wave length ratio, d/L, were collected. The wavelength is related to the wave period by Equation (4.16) and the results in this chapter are presented graphically against wavelength. A ratio of d/L greater than 0.5 was obtained for all tests which indicates the tests reflected the deep water conditions found around Qaru Island, Kuwait. A summary of the data collected for parabola-1 and parabola-2 can be found in Table 4.6.

Table 4.6: Experimental data from parabola-1 and parabola-2 tests

Flume Tank Wave Spectrum			Parabola-1						Parabola-2					
T^* (s)	L^* (m)	H^* (m)	$H_i{}^*$ (cm)	$H_f{}^*$ (m)	d/L^*	AF^*	$L_{fc}{}^*$ (m)	$D_{ij}{}^*$ (m)	$H_i{}^*$ (m)	$H_f{}^*$ (m)	d/L^*	AF^*	$L_{fc}{}^*$ (m)	$D_{ij}{}^*$ (m)
0.8	1.00	0.03	2.28	0.072	1.50	3.16	0.59	0.721	0.021	0.065	1.50	3.10	0.54	0.800
0.8	1.00	0.06	4.77	0.142	1.50	2.97	0.59	0.668	0.044	0.185	1.50	4.20	0.55	0.705
0.8	1.00	0.09	6.73	0.230	1.50	3.42	0.59	0.703	0.065	0.258	1.50	3.95	0.55	0.632
1.0	.156	0.03	2.38	0.049	0.96	2.06	0.91	0.919	0.022	0.036	0.96	1.63	1.51	0.996
1.0	1.56	0.06	4.94	0.126	0.96	2.54	0.91	1.098	0.046	0.077	0.96	1.66	1.51	0.953
1.0	1.56	0.09	7.16	0.179	0.96	2.51	0.91	0.985	0.070	0.161	0.96	2.3	1.51	0.843
1.2	2.25	0.03	2.52	0.064	0.67	2.54	1.23	-	0.027	0.047	0.67	1.77	2.09	1.510
1.2	2.25	0.06	5.12	0.123	0.67	2.40	1.23	-	0.046	0.099	0.67	2.15	2.09	1.493
1.2	2.25	0.09	7.44	0.175	0.67	2.36	1.23	-	0.073	0.169	0.67	2.33	2.09	1.469

***The nomenclature of the parameters and the equation used to calculate the tabulated data are given next.**

NOMENCLATURE

T	=	Wave period (s)
H	=	Wave height selected for wave generation (m)
H_i	=	Incident wave height (m)
H_f	=	Wave height at maximum amplification point (m)
C_r	=	Coefficient of reflection
Hr	=	Reflected wave height (m)
D_{ij}	=	Diameter of maximum amplification zone (m)
L_{fe}	=	Length from edge of parabola to centre of maximum amplification zone (m)
L_{fc}	=	Length from center of parabola to centre of maximum amplification zone (m)
d	=	Water depth (m)
L	=	Wave length (m)
L_o	=	Deep water wave length (m)

Wave length, $L = \frac{gT^2}{2\pi} \times \tanh(\frac{2\pi d}{L})$ (4.12)

Amplification factor, $AF = \frac{H_f}{H_i}$ (4.13)

Reflected wave height, $H_r = R_c.H_i$ (4.14)

Length from centre parabola to centre maximum amplification zone, $L_{fc} = \left(\frac{L_{fe} + 62.5}{100}\right)$ (4.15)

Deep water wave length, $L_o = \frac{gT^2}{2\pi} = \frac{9.81 \times (T)^2}{2 \times \pi}$ (4.16)

The amplification factors and wave motion responses for both parabolae are shown in Figure 4.16.

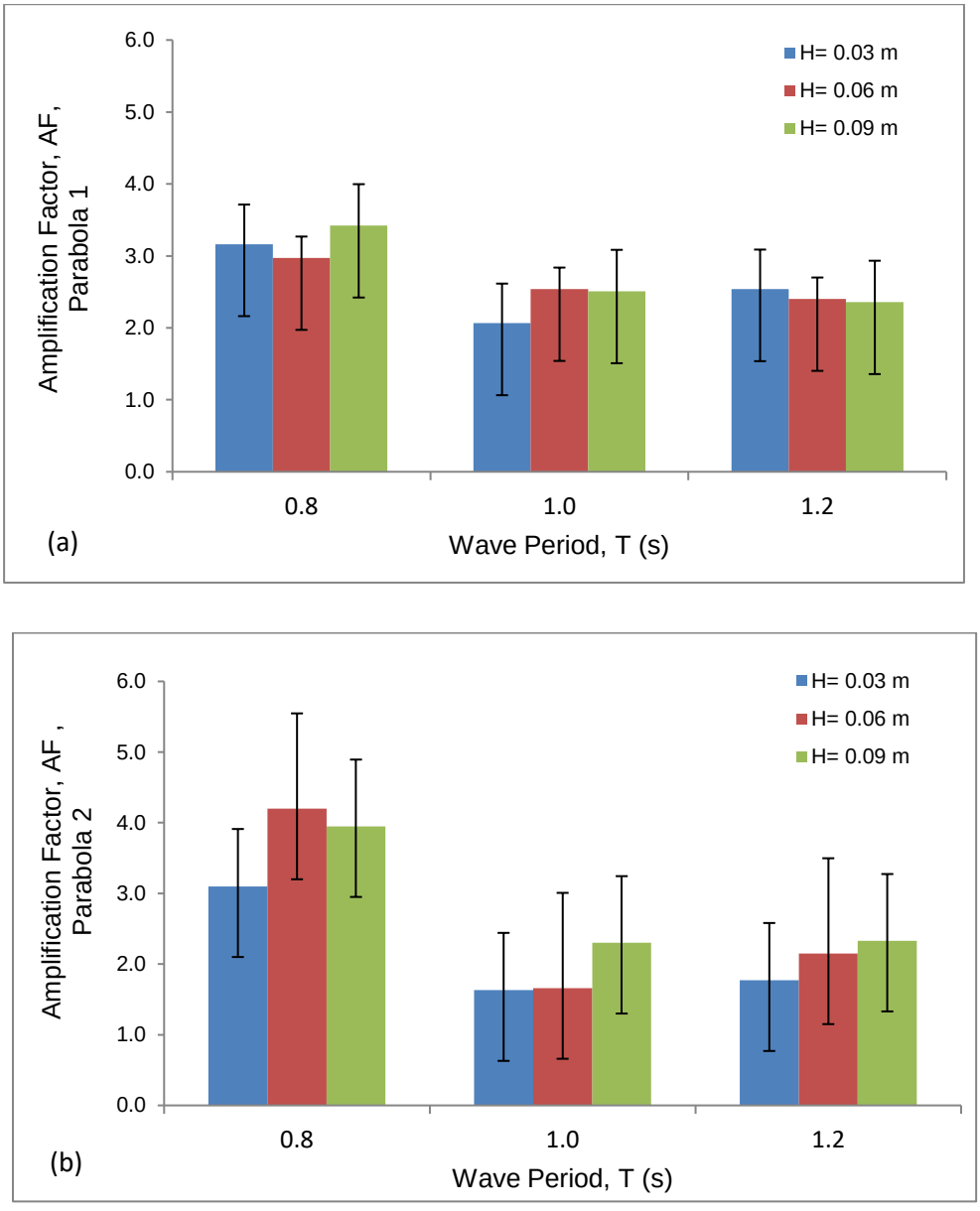
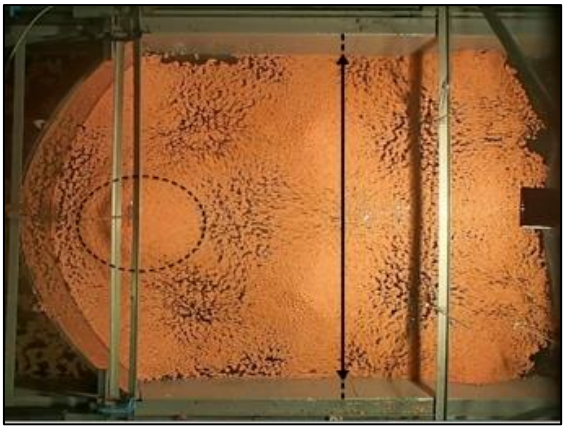
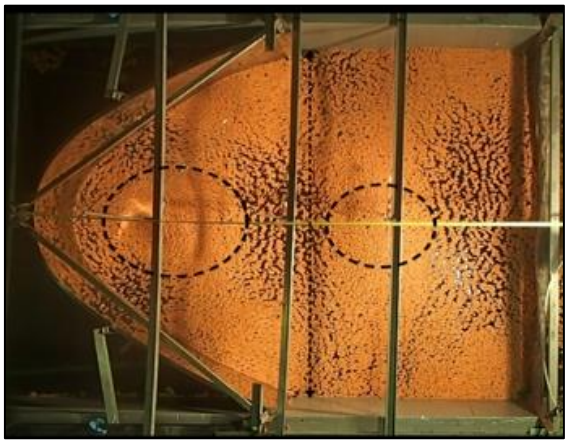


Fig. 4.16: (a) Parabola-1 response and (b) Parabola-2 response

Images of the maximum amplification zone dimensions and diameters are shown in Figure 4.17.



(a) Parabola-1 at T, H (0.8 s, 0.09 m)



(b) Parabola-2 at T, H (0.8 s, 0.06 m)

Fig. 4.17: Photographs of the maximum wave amplification zones for parabola models 1&2

4.4.4. Stage-1 Discussion

Parabola-1

The test results revealed that lower wave periods (T = 0.8 s) and wavelengths (L = 1 m) resulted in higher amplification factors compared to those achieved with higher wave periods as shown in Figure 4.16. Amplification factors ranged between 2.06 and 3.42. The highest factor recorded for parabola-1 was 3.42 corresponding to a wave period of 0.8 s and wave height of 9 cm.

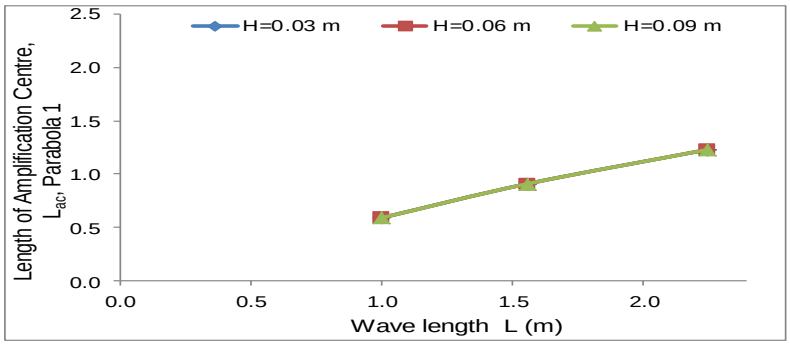
It is possible that even higher amplification could have occurred with higher frequency waves. However due to the capability of the wave maker, a wave period lower than 0.8 s was not possible for the experimental work. The amplification zone for parabola 1 was always present and was seen to move further away from the structure as the wave period increased. In general, for parabola-1, the area of interest was easy to detect; a typical image is shown in Figure 4.17a where the zone of maximum amplification is clearly visible.

Parabola-2

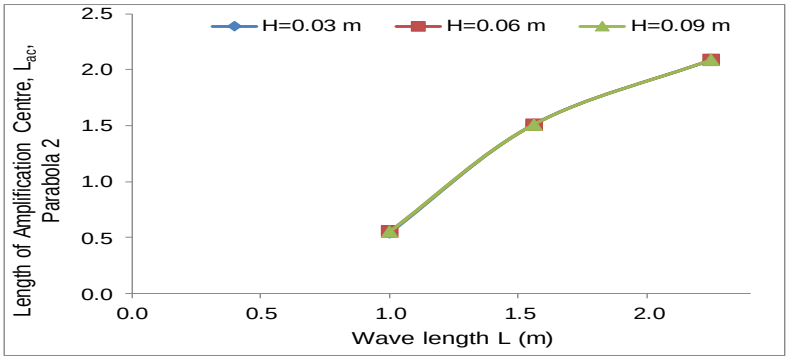
Similar results for the amplification factor for parabola-2 were observed (Figure 4.16b). The amplification factors ranged between 1.63 and 4.20. The highest factor recorded for parabola-2 was 4.20 corresponding to a wave period and wave height of 0.8 s and 6 cm, respectively. Unlike with parabola-1, wave build up was detected at several points around the point of maximum amplification. It was also noticed that the diameter of the amplification zone becomes larger at higher wave periods, and difficult to detect due to the reflection of the waves from the side walls. This type of multiple reflection and hence multiple amplification zone behaviour would not occur in field conditions. The first amplification zone, closest to parabola-2, was therefore considered to be the most important.

Parabola-1 and Parabola-2

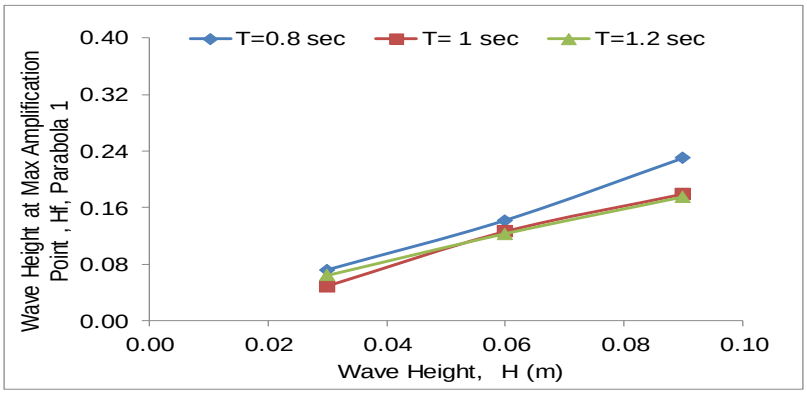
From Table 4.6 it can be seen that the diameter of the amplification zone D_{ij} increases as the wave period increases for both parabolae. Similarly, as the wave length L increased, the length from the centre of the parabola to the centre of the maximum L_{ac} also increased (Figures 4.18a & 4.18b). As expected, the wave height recorded at the maximum amplification point was found to increase as the generated wave height increased for both parabolae (Figures 4.18c & 4.18d).



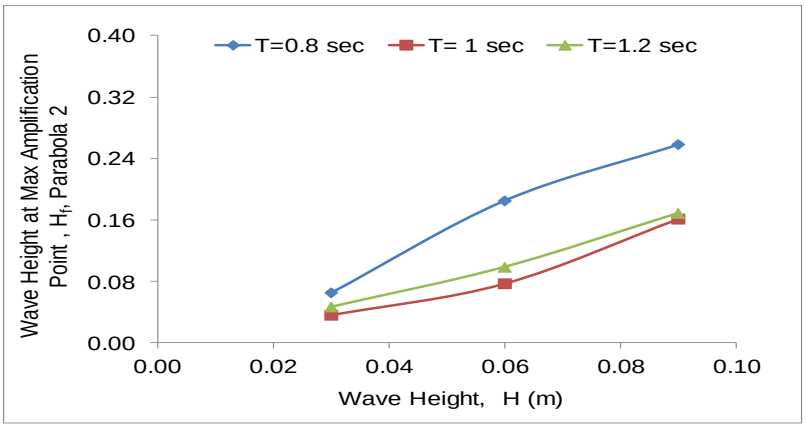
(a)



(b)



(c)



(d)

Fig. 4.18: Parabola-1 and parabola-2 model responses-(a, b, c, d)

The characteristics of the area of interest were found to be greatly influenced by the wave length; i.e. they were greatly affected by wave period but not wave height.

It is clear that both parabolae work very well within a small range of wave periods and each one had a threshold wave period beyond which no focusing was apparent. The threshold wave periods for parabola-1 and parabola-2 were found to be 1.5 s and 1.2 s, respectively. In addition, the reflected waves tended to involve a combination of both longitudinal and cross waves motions which can affect the distance from the parabola to the centre of its amplification zone. The reflection from the parabolic focusing wall has two components: longitudinal and cross waves. With the longitudinal component, the wave travels up to the wave maker and is almost absorbed by the wave maker since the wave maker functions in an 'active absorption' mode. With the cross wave, the wave travels perpendicular to the flume direction, and the side walls of the wave flume, which are 2.5 m apart, act as reflecting surfaces. The pure reflection from the side wall results in node and antinode behaviour. Wave magnification is the highest at the antinode point. Since a reflected longitudinal wave is also present, it results in a node and an antinode along the length of the flume. The antinode closest to the parabola is the first one developed. Therefore, reflections of cross waves create a focusing effect that is closer to the parabola structure than that created by the longitudinal wave reflections.

Based on the predominant wave period conditions for a particular site, the most appropriate type of parabola needs to be selected. The results for both parabolae showed their suitability when regular narrow banded waves are dominant in mild wave climates similar to that found in Kuwait. For a broadband spectrum with a wide range of frequencies, the area of maximum amplification will move back and forth and no amplification will be detected. In addition, no correlation was identified between this area and the focal point of a geometric parabolic curve.

4.4.5. Stage-1 Findings

Both parabolae are found to be good wave focusing devices. The amplification and focusing of waves was seen to increase not only around the geometrical focal point but also at a series of locations around the parabolae's amplification zones. It was found that the parabolae tested can amplify incident waves by up to 3.0 to 4.0 times. This indicates that using a parabolic element as part of a WEC could amplify and focus wave energy and thus significantly increase yield.

Both parabolae work efficiently within a small range of wave periods. With very small wave periods, the amplification centre tends to be located closer to the parabola. With increasing wave period, the amplification centre moves away from the parabola. The diameter of the amplification zone is smaller with low wave periods and wave lengths and increases with increased wave periods. For wave periods greater than 1.2 s, the amplification effect is difficult to detect. The focusing length is found to be independent of the incident wave height. To benefit from this concept, wavelengths must be short relative to the physical dimensions of the device. However, a wave energy device such as a point absorber (buoy) can produce more power if waves are amplified since power is proportional to the square of the wave amplitude according to linear wave theory. These experimental results were validated against the findings of the 3D numerical modelling conducted by Yang and Ertekin (1991). Similar to the results of the stage-1 testing, the 3D model also revealed that the energy density of waves increases not only at the amplification zone but also at a series of locations within the parabolic step. The modelling also showed that the magnitude of wave amplification was dependent on the focal length, the location of the side walls, and the incoming wave length which agreed with the experimental results for parabola-2.

The potential increase in energy capture was tested during stage-2 experiments where the best location for the buoy with respect to the parabolic concentrator was examined. Both parabolae worked very well

within a small range of wave periods and showed their suitability when regular narrow banded waves were dominant. Therefore, the potential of both parabolae to be used in conjunction with a WEC was tested. However, for the selected wave spectrum, the amplification zone for parabola-1 was easier to detect, and hence testing with this model formed the basis for the stage-2 experimental data analysis. Moreover, the threshold wave periods for parabola-1 and parabola-2 (1.5 s and 1.2 s, respectively) needed to be taken into account during stage-2 testing because beyond these limits, the parabolae act as vertical walls and no amplification occurs.

4.5. Stage-2: Point Absorber (Buoy)

The test setup for the point absorber testing consisted of three main components: the floating point absorber (buoy), the cable/pulley arrangement to restrict the buoy motion to heave only, and the power take-off system modelled by a motor where the torque due to the electrical current behaves like a pure damper. During the phase I testing of a heaving buoy, the dynamic response of the system and its displacements were recorded. During phase II experiments a damped buoy was tested to measure deflections, forces and maximum power outputs.

4.5.1. Stage-2 Buoy Geometry

The selection of buoy design was made on the basis of the literature review presented in Chapter 2 and published work regarding shape, dimensions (waterline diameter, D, and buoy draft, B_d), absorbed power, performance and response to slamming loads. A successful point absorber device for the sea conditions around Kuwait should fulfil the following conditions:

- Wave energy should be extracted efficiently over an appropriately selected frequency and amplitude range to match the Kuwaiti sea conditions.

- The natural frequency of the buoy in heave should be within the peak range of the incident wave spectrum.
- The buoy should perform efficiently regardless of wave direction.
- The waterline diameter, D, and draft, B_d, of the buoy should be designed with consideration given to the dimensions of the amplification zone.
- The probability of wave slamming should be limited as much as possible.

A buoy with a combination of two conical surfaces with top angles of 60º and 120º (bi-cone) was felt to be the best for this study as it has the advantage of having the most wetted area located near the free surface making it more receptive to wave excitation (Vantorre et al., 2002; Sjökvist et al., 2014). The lower part reduces draft and hence the probability of slamming. Furthermore, in order to reduce the effects of reflection and refraction and to increase the uniformity of the waves reaching the buoy, a cylindrical body was selected. Detailed buoy selection criteria can be found in chapter 3.

The wave parameters of the Kuwaiti sea and the parabola configurations were used to provide a basis for the buoy design. In addition, the design was optimised for the wave conditions at which the highest amplification factors were recorded with parabola-1 and parabola-2 during stage-1 testing. Therefore, the design wave period was chosen to be 0.8 s for which the wavelength is 1 m and the amplification zone diameter is approximately 0.7 m. Before selecting the buoy diameter, it was important to note that a buoy with a large diameter is not capable of absorbing the maximum energy with short wavelengths and correspondingly, a buoy with a small diameter will absorb less energy with long wavelengths (Bozzi, 2013). Therefore, the design diameter, D, was chosen to be approximately one third of the wavelength (or D = 0.3125 m corresponding to D = 5 m for a prototype based on a scale of 1:16). The choice of diameter selected was supported by the results of a study on wave energy absorption of a

heaving buoy in the Iranian seas (Khojasteh and Kamali, 2016). It that study, the effects of buoy draft and diameter on the maximum power absorption of cone-cylinder and hemisphere cylinder buoys were studied using the boundary element solver package ANSYS AQWA. Buoys with diameters of 5 m were found to be the most appropriately sized point absorbers for Iranian coastlines which are close to Kuwait. The same prototype diameter (D = 5 m) was tested by De Backer, (2008) for conical and hemispherical buoys using three different buoy drafts B_d = 0.189 m, 0.221 m and 0.284 m corresponding to drafts of 3 m, 3.5 m and 4.5 m in a prototype, respectively. It was found that a smaller draft resulted in an increased power absorption value. However, the draft of the buoy needs to be sufficiently large to avoid the issue of bottom slamming.

In order to select the final buoy shape and draft value, it was decided to test and optimise the bi-cone (60º/120º), along with two intermediate shapes with longer drafts, using the steady-state harmonic model developed in chapter 3. Three buoy shapes were selected: (a) bullet, (b) spike and (c) bi-cone (60º/120º). The buoys' shapes selection criteria is given in chapter 3. Their prototype dimensions are illustrated in chapter 3 in section 3.8. All the shapes had the same cross-sectional area (D = 0.3125 m) but had different masses and drafts. The bullet and spike buoys had relatively longer drafts (0.755 m) than the bi-cone buoy (0.22 m). The steady-state harmonic model detailed in chapter 3 was used to estimate the optimum power absorption for the best buoy shape. As described in chapter 3, for the modelling purpose different damping conditions were tested experimentally. The different damping conditions were achieved by arbitrarily one round disc (damped) and two round discs (extra damped) to the lower sections of the bullet and spike buoys only. This damping approach was the best available option to provide the different damping conditions as to the discs availablity at the testing facility. When two round discs were used, they were fixed at a distance of 2 inch and 3 inch apart for the bullet and spike buoys, respectively. Finally, the values for the damping coefficient, c_2,

obtained during decay tests were verified by checking if they landed near the worst c_2 value obtained from the steady-state harmonic model or towards the best c_2 regions.

The bi-cone (60º/120º) buoy model dimensions corresponding to a scale of 1:16 (D = 0.3125 m and B_d = 0.22 m) are illustrated in Figure 4.19. The buoy was fabricated at the Coastal Management Program in KISR. The maximum allowable design weight was 10 kg, and the actual weight measured after fabrication was 9 kg. The low weight was achieved by fabricating the buoy from 1.5 mm stainless steel sheet. Sand was added to the buoy from the top for stabilisation and to adjust its draft giving a final total mass of approximately 11.63 kg. The bi-cone (60º/120º) buoy dimensions for the prototype and model are summarised in Table 4.7. The bullet and spike buoys are illustrated in Figures 4.20 and 4.21, respectively.

Table 4.7 Bi-cone (60º/120º) buoy dimensions (prototype and model)

Dimension	Prototype m	Model (scale 1:16) mm	Model (scale 1:16) m
Buoy diameter, D	5.0	321.50	0.3215
Buoy radius, r	2.5	156.25	0.1560
Total cylinder height, H_T	4.0	260.00	0.2600
Cylinder wetted height, H	2.0	130.00	0.1300
Cone wetted height, h	1.4	90.20	0.0902

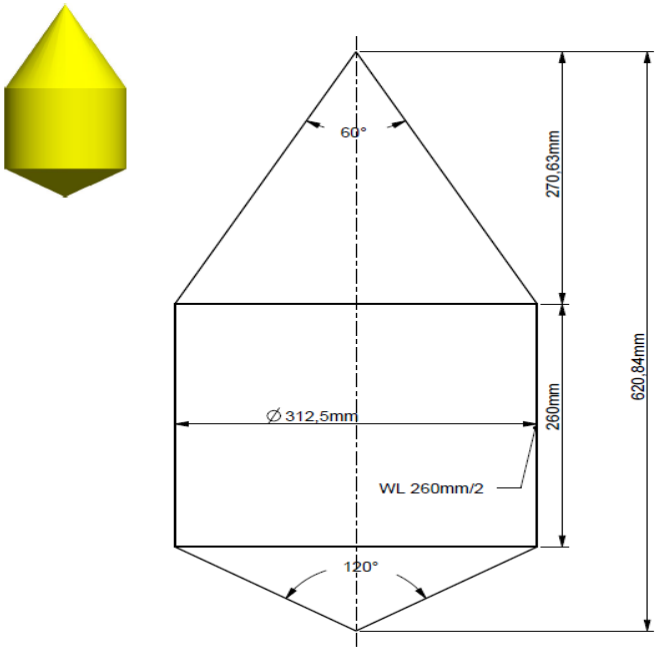




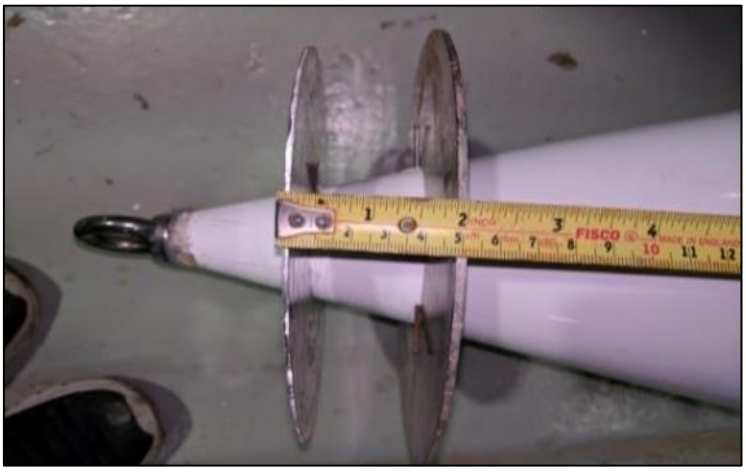
Fig. 4.19: Bi-cone (60°/120°) buoy shape (model scale in mm)



(a) Zero damped



(b) Damped

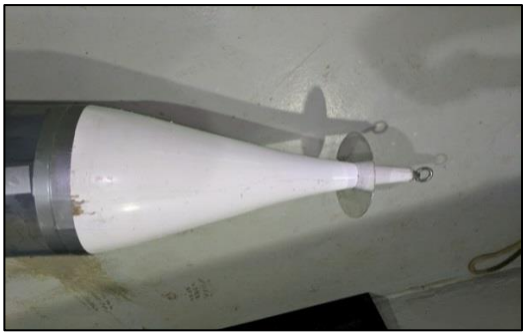


(c) Extra damped

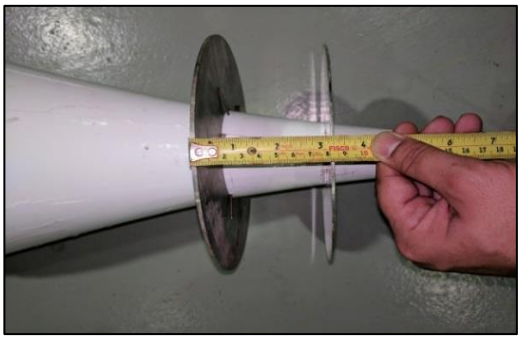
Fig. 4.20: Zero damped, damped and extra damped bullet buoy



(a) Zero damped



(b) Damped



(c) Extra damped

Fig. 4.21: Zero damped, damped and extra damped spike buoy

It was concluded in Chapter 3 that out of all the buoy shapes (bullet, spike and bi-cone), the bi-cone (60º/120º) buoy's response was most similar to the optimum mass response predicted by the steady-state harmonic model. It was also found that the c_2 damping associated with the bi-cone shape was reasonably far from the worst c_2 value predicted by the model. Moreover, the results revealed that the bi-cone

buoy gave the best performance, and therefore its potential integration with a parabolic concentrator will be assessed in the upcoming sections.

Only the decay tests conducted for the bi-cone buoy are detailed in section 4.5.3; the bullet and spike buoy decay tests are discussed in chapter 3 and further details on frequency profiles and damping ratios for each shape can be found in chapter 3.

4.5.2. Stage-2 Test Setup

The test setup for all the buoy shapes consisted of a buoy, a cable/pulley arrangement and a PTO at a fixed distance from the wave maker and connected to the flume tank by an arrangement of four stainless steel wire cables and one elastic wire cable as shown in Figure 4.22. The use of wire cables enabled the construction of a system with a high mechanical strength which allowed for a high degree of movement. This resulted in a significant improvement in the survivability of the buoy in larger waves.

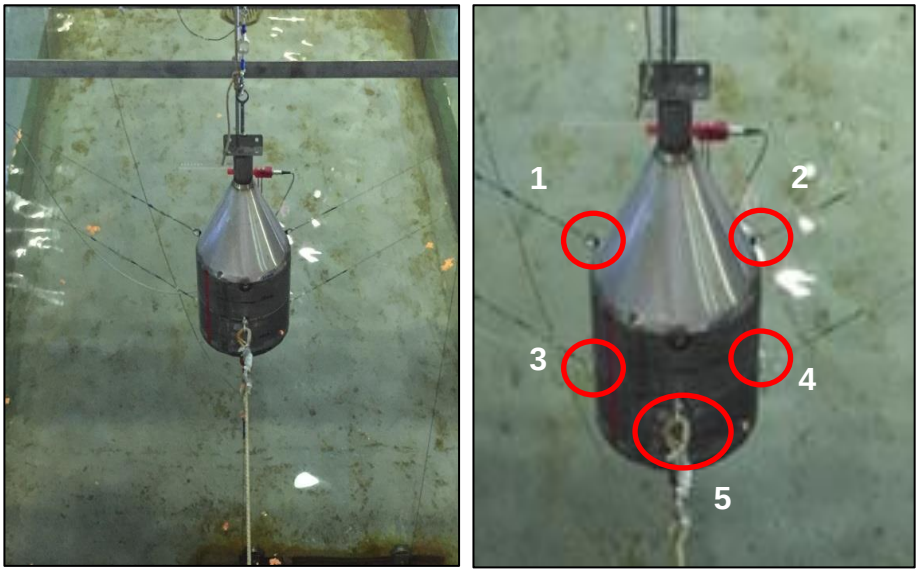


Fig. 4.22: Test Setup for point absorber (buoy) and the heaving mechanism

Two important design parameters for the system are the buoyancy and the weight of the buoy, because these factors determine the maximum damping force achievable. For improved efficiency, the damping force needs to be carefully chosen to match the buoyancy and weight of the buoy as well as the wave environment. The buoyancy force for the buoy was calculated to be 67 N and the optimum translational damping for power capture was approximately 60 Ns/m as explained in section 4.3.3 (see Appendix 4 for calculation details). The stainless steel wire rope attached to the bottom of the buoy passed around two pulleys with bearings (pulley diameter = 84.87 mm) fixed to the flume tank floor to reduce cable friction. The top of the buoy was connected to the mounting frame by means of three pulleys of the same diameter. Out of these three pulleys, the middle pulley is used as a pre-tensioner (adjusted using a screw) and a second pulley is attached to the motor only during damped buoy tests. This latter pulley had no bearing and the cable was wrapped around the pulley twice to prevent it from slipping. The pulley with bearing was used for the zero damped system. A schematic of the cable and pulley arrangement can be seen in Figure 4.23 and the experimental setup is shown in Figure 4.24.

The frequency of the damped motion induced in the buoy could easily be changed by changing the resistance across the motor's terminals. The buoy was intended to follow the wave motion, whereas the cable and pulley arrangements were not intended to be as sensitive to this motion.

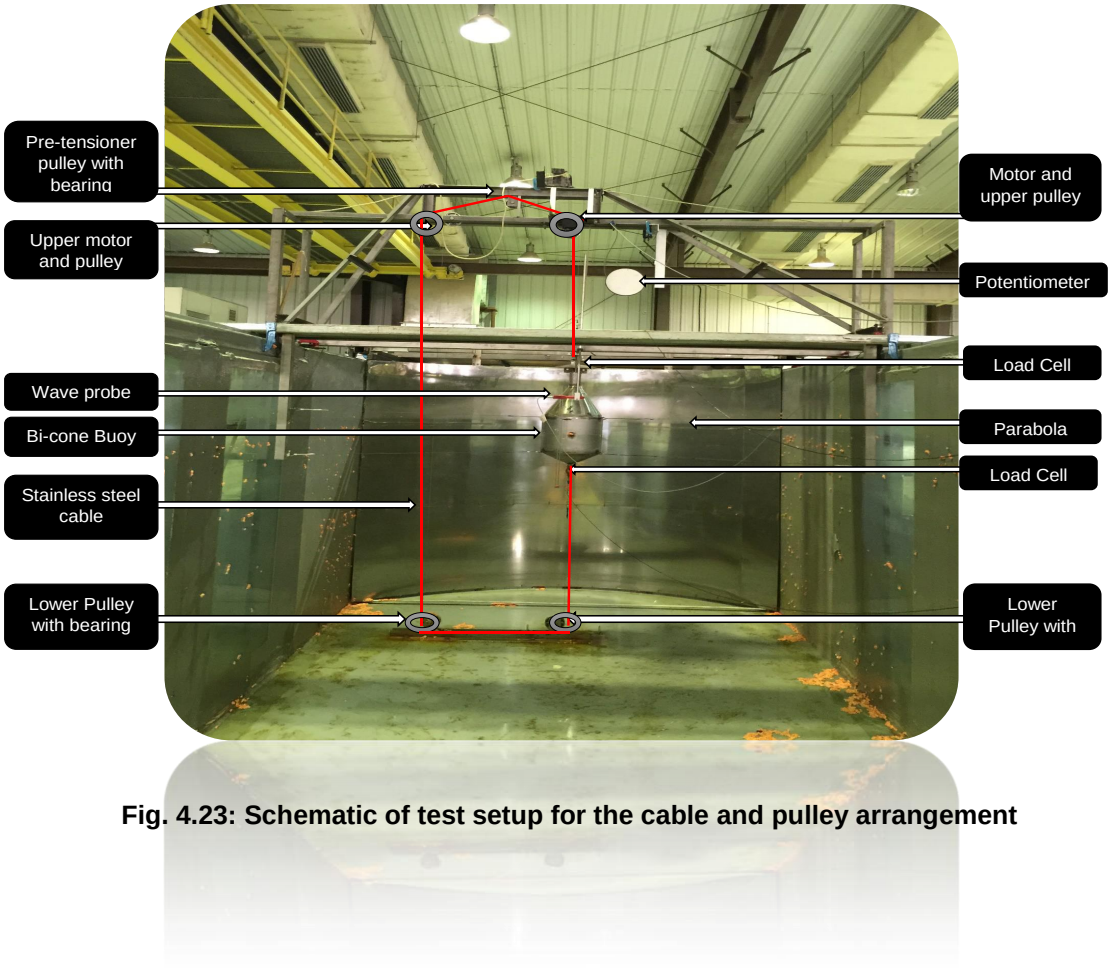


Fig. 4.23: Schematic of test setup for the cable and pulley arrangement



Fig. 4.24: Experimental setup of cable and pulley arrangement

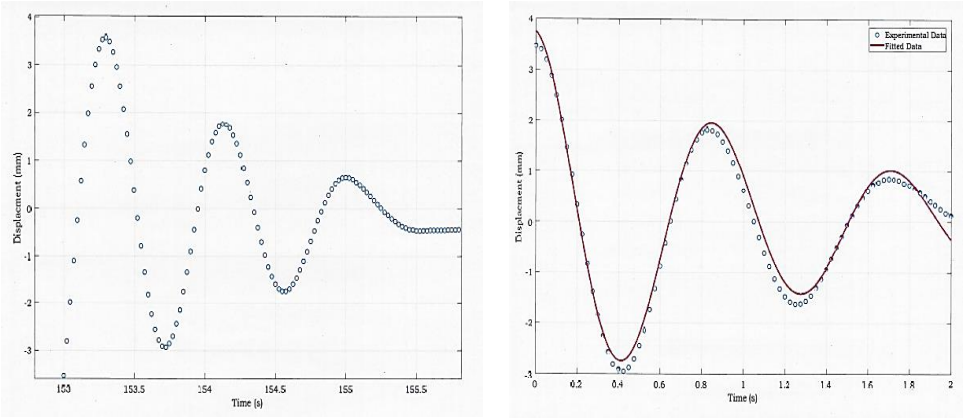
4.5.3. Stage-2 Decay Test

The aim of the decay tests was to observe the transient decay of the buoy and derive its hydrodynamic damping coefficient. In the decay

tests, the bi-cone (60º/120º) buoy was released from an initial position different from its equilibrium position in still water. After approximately 10s, the influence of the radiated waves reflected on the side walls of the flume became clearly visible and the buoy underwent damped free oscillation. The natural angular frequency, ω_a, and the damping ratio, ζ, can be derived from the results of the decay tests. Decay tests were performed for the zero damped buoy, half damped buoy and fully damped buoy. The buoy motion corresponds to a damped oscillation, which can be mathematically expressed as:

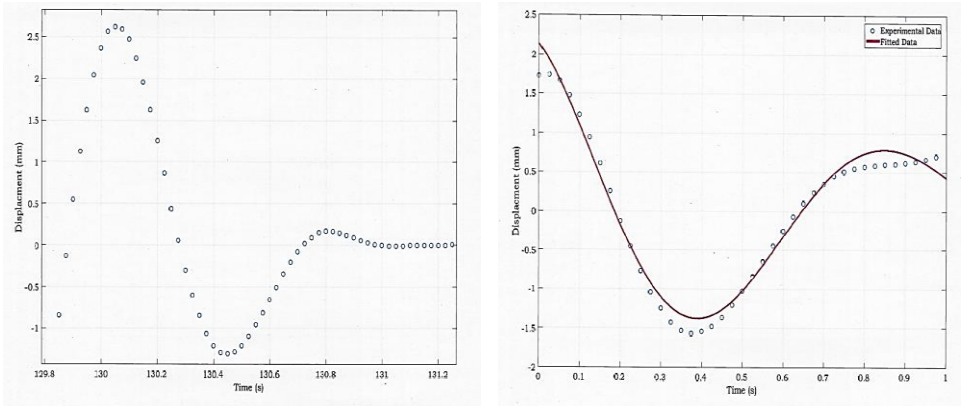
$$z(t) = a\exp(-\zeta\omega_a t)\sin(\omega_d t + \Phi) \tag{4.17}$$

Equation (4.17) was fitted (red line) to the measured position of the bi-cone buoy, as shown in Figures 4.25b, 4.26b and 4.27b. The initial part of the curve was omitted to avoid the influence of static friction and the last part was excluded to avoid the influence of reflected waves.



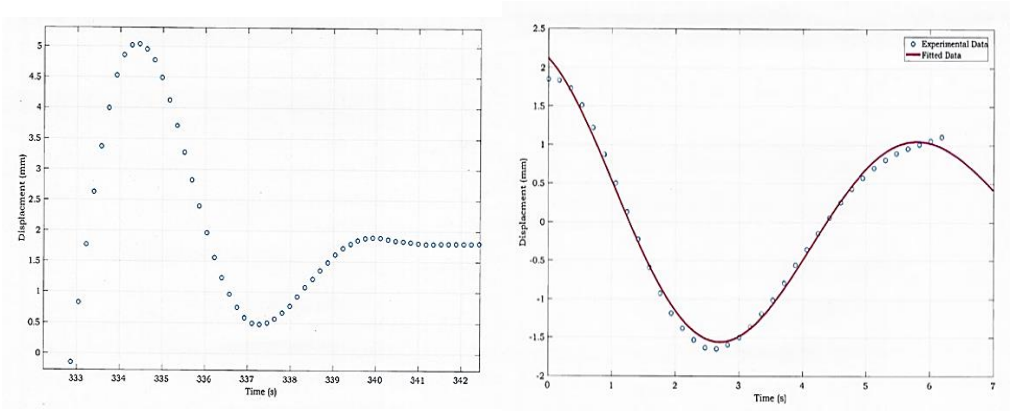
(a) Decay test results **(b)** Curve fit

Fig. 4.25: Measured zero damped buoy position during decay test and curve fit



(a) Decay test results **(b)** Curve fit

Fig. 4.26: Measured half damped buoy position during decay test and curve fit



(b) Decay test results **(b)** Curve fit

Fig. 4.27: Measured fully damped buoy position during decay test and curve fit

From the decay tests of the bi-cone (60º/120º) buoy, the natural angular frequency, ω_a, and the damping factor, ζ, were derived for the different buoy configurations. The derived values are:

- **Zero damped buoy:** natural frequency: 1.16 Hz and damping factor: 0.11.
- **Half damped buoy:** natural frequency: 1.09 Hz and damping factor: 0.18.
- **Fully damped buoy:** natural frequency: 0.16 Hz and damping factor: 0.12.

4.5.4. Stage-2 Results

The behaviours of the zero damped buoy (very low damping), half damped buoy and fully damped buoy were tested in regular waves of different heights and periods. More specifically, wave periods of 0.8, 0.85, 0.9, 0.95 and 1.0 s and wave heights of 0.03 m, 0.06 m and 0.09 m were used. The overall power absorption efficiencies (η) were calculated using Equation (4.6) from section 4.1.1. Power absorption efficiency is defined as the ratio between the power absorbed by the buoy and the available power transported by the wave front over the width of the buoy. This reflects the fact that the buoy is permitted to absorb power from the total wave front incident on the buoy, not just the portion of the wave front with the same width as the buoy. The power absorption efficiency (η) is a commonly used performance index for wave conversion technologies.

The efficiency of power absorption for all the buoy configurations is plotted as a function of wave period for significant wave heights of H = 0.03, 0.06, 0.09 m in Figures 4.28a, 4.28b and 4.28c, respectively. The power absorption is plotted similarly in Figures 4.29a, 4.29b, and 4.29c.

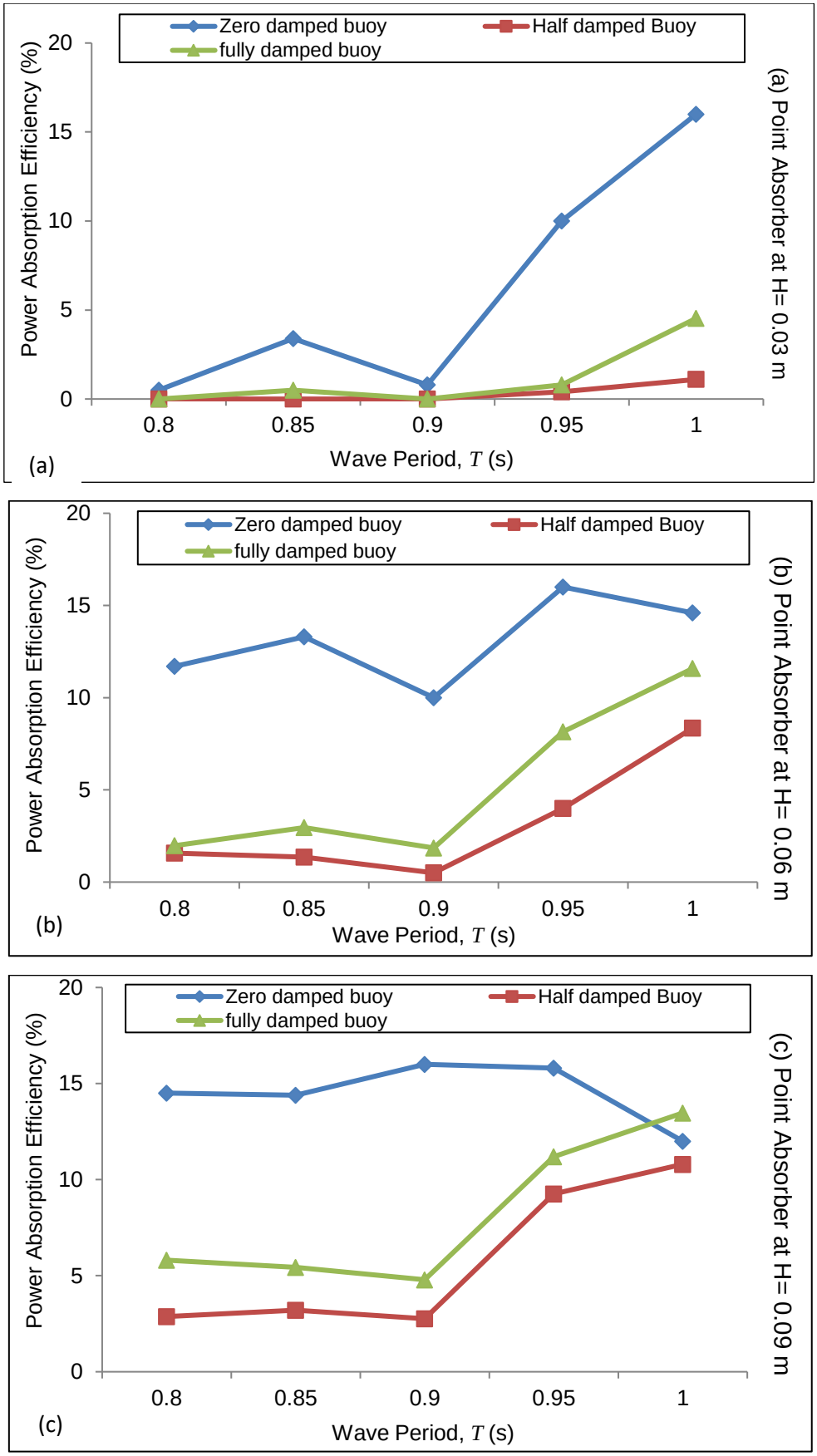


Fig. 4.28: Efficiency of power absorption, η, (%) as a function of wave period (a, b and c)

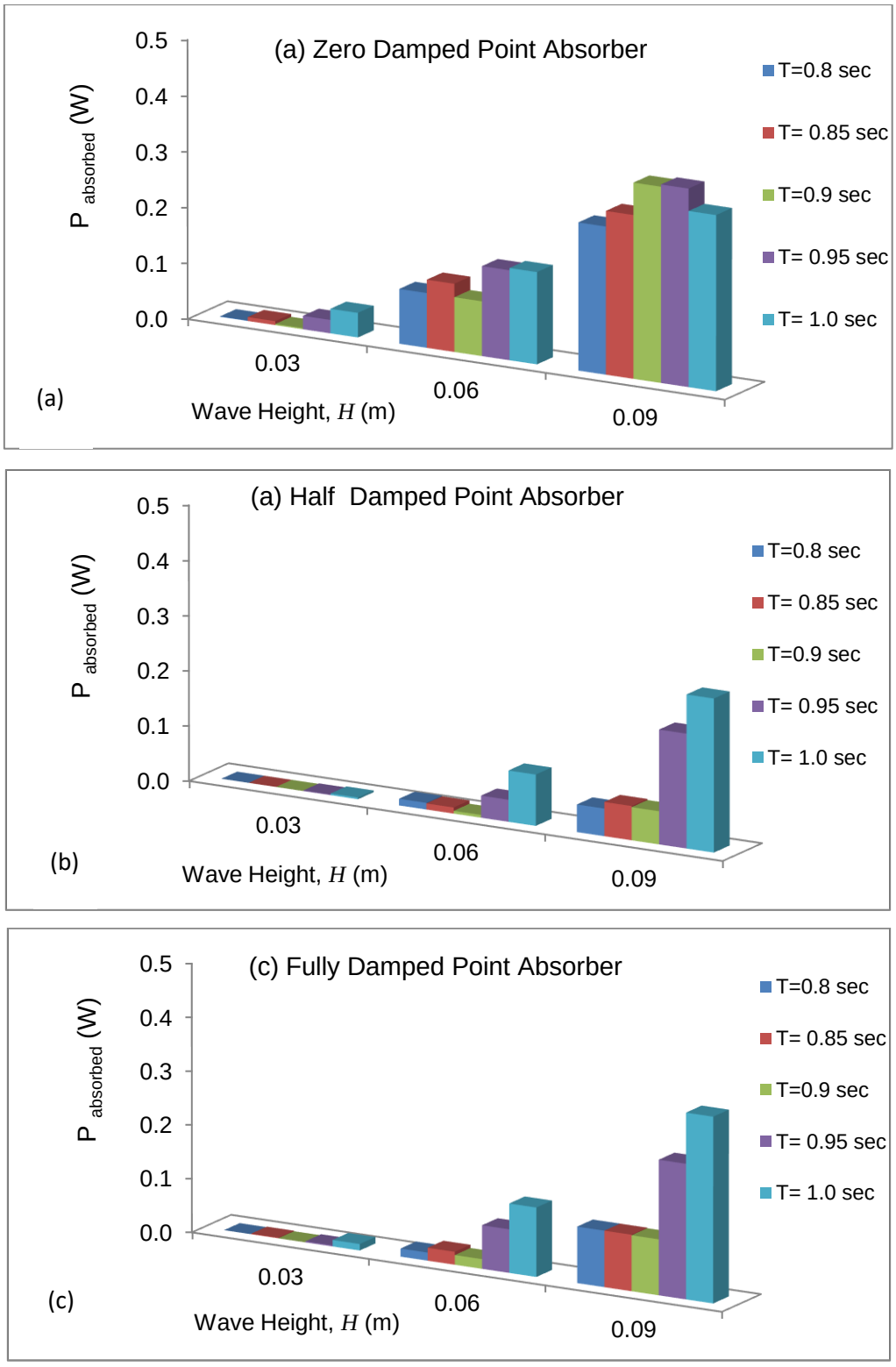


Fig. 4.29: Power absorbed by the buoy (W) as a function of wave height (a, b, c)

4.5.5. Stage-2 Discussion

Zero Damped Point Absorber (Buoy): The buoy's performance was found to improve with increasing wave height for 0.03 m < H < 0.09 m as shown in Figures 4.28-(a,b,c). On the other hand, for longer wave periods, in particular longer than 0.95 s, the performance decreased quite rapidly for wave heights of 0.06 and 0.09 m. A decrease in performance at longer wave periods was also noticed by Bozzi et al., (2013). The maximum efficiencies (16%) recorded corresponded to the following sea states: (H: 0.03 m, T: 1.0 s), (H: 0.06 m, T: 0.95 s) and (H: 0.09 m, T: 0.9 s). The results indicate that efficiency is relatively sensitive to wave period and higher efficiencies were recorded at T = 1.0 s. It also depends on wave height and higher efficiencies were recorded at H = 0.09 m compared to H = 0.03 m and 0.06 m when T was between 0.8 and 0.95 s. Moreover, unexpectedly, the so-called zero damped buoy was found to perform much better than the half and fully damped buoys. This was noted in Chapter 3 as the c_2 damping value for the bi-cone shape was in the low c_2 region predicted by steady-state harmonic model but far from its predicted worst c_2 value.

From Figure 4.29a, it can be seen that the maximum buoy power absorption was achieved with a wave height of 0.09 m for all sea states tested. This was expected and confirms that the buoy will have a greater energy conversion capacity at more energetic deployment locations in the Kuwaiti sea. The maximum absorption of the incoming wave energy (0.36 W) occurred with a wave height and wave period of 0.09 m and 0.95 s, respectively (Figure 4.29a). When the waves had a period around 0.95 s, the buoy was in resonance. The maximum power absorption at H = 0.09 m was seen to occur with T values of 0.95 s, followed by 0.9 s, 1.0 s, 0.85 s and 0.8 s. Similar to device efficiency, absorbed power was also found to be dependent on wave height and wave period.

Fully Damped Point Absorber (Buoy): The applied external damping was found to greatly influence the efficiency of the buoy. When the

buoy was subjected to high levels of damping, its performance was seen to increase rapidly with increasing wave period and wave height (Figures 4.28-(a,b,c)) for wave periods greater than 0.9 s. In general, it was observed that the fully damped buoy had a better efficiency in higher wave classes (H = 0.06 – 0.09 m and T = 0.9 – 1.0 s). The maximum efficiency (13.5%) recorded corresponded to the sea state with H = 0.09 m and T = 1.0 s. The maximum efficiencies for all wave periods occurred when H = 0.09 m. This confirms that the buoy will have a greater energy conversion capacity in more energetic deployment locations in the Kuwaiti sea. The maximum efficiencies were recorded with wave periods of 1.0 s, followed by 0.95 s, 0.8 s, 0.85 s and 0.9 s. The results indicate that the efficiency of the damped system is relatively sensitive to wave height and the performance of the fully damped buoy is also highly dependent on wave period with peak efficiencies at 1.0 s for all wave heights.

Much lower power absorption values (almost threefold) were recorded at wave periods lower than 0.9 s with the damped buoy compared to the zero damped buoy. The maximum absorption of the incoming wave energy (0.35 W) occurred with a wave height and wave period of 0.09 m and 1.0 s, respectively, as seen in Figure 4.29c. The maximum power absorption was achieved for waves with a period of 1.0 s as the buoy was in resonance. This period is almost 6 times smaller than the system's natural wave period (6.25 s). The absorbed power was also found to be dependent on the wave height and wave period.

Half Damped Point Absorber (Buoy): Applying a small amount of damping to the buoy was found to influence the efficiency of the buoy. In the low damped system, the maximum efficiency occurred with wave periods higher than 0.95 s and the buoy's performance was seen to improve with increasing wave period (Figures 4.28-(a, b, c)). The half damped buoy behaved similarly to the fully damped buoy where the highest power absorption was achieved in higher wave classes (H = 0.06 – 0.09 m and T = 0.95 – 1.0 s)). However, a lower maximum efficiency (10.8%) was recorded for the half damped buoy compared to

the fully damped buoy when H = 0.09 m and T = 1.0 s as this was the condition in which the maximum efficiency was recorded for the fully damped buoy. The maximum efficiency at H = 0.09 m was seen to occur with a wave period of 1.0 s, followed by 0.95 s, 0.85 s, 0.8 s and 0.9 s. The efficiency comparison shows that the efficiency of the half damped system is also dependent on wave height and wave period.

Lower power absorption values were recorded for the half damped buoy in all sea states compared to the fully damped and zero damped buoy. The maximum absorption of the incoming waves (0.28 W) occurred when the sea state had a wave height and wave period of 0.09 m and 1.0 s (Figure 4.29b), respectively, similar to with the fully damped buoy. This means that the buoys subjected to external damping came into resonance at the same wave period as the zero damped buoy (i.e. at T = 1.0 s). This period is close to the system's natural wave period (0.9 s) which was derived during the decay test. The absorbed power was also found to be dependent on the wave height and wave period.

4.5.6. Stage-2 Findings

The results of the stage-2 testing proved that the bi-cone ($60^o/120^o$) buoy is a promising wave energy device which is likely to have greater energy conversion capacity at more energetic deployment locations in the Kuwaiti sea. These results are encouraging for the stage-3 testing as the buoy will benefit from the wave amplification provided by a parabolic structure and produce more power as the power available for capture is proportional to the square of the wave amplitude according to linear wave theory (Yang and Ertekin, 1991).

The performance of the zero damped buoy, fully damped buoy and half damped buoy was seen to increase with increasing wave height and wave period. The zero damped buoy recorded the highest efficiency of 16%. The lowest maximum efficiency (10.8%) recorded for the half damped buoy and maximum efficiency for the fully damped buoy (13.5%) both corresponded to sea states of H = 0.09 m and T = 1.0 s.

For the half damped buoy, lower power absorption was recorded for all sea states compared to fully damped and zero damped buoys. For all buoys, the maximum power absorption was achieved at a wave period of approximately 1.0 s at which the buoys were brought into resonance. The maximum power absorption (0.36 W) was recorded for the zero damped buoy indicating a power absorption of almost 6 kW could be achievable at prototype scale. The Power was scaled using the Froude scaling factor of $\lambda^{7/2}$ explained in section 4.1.3. The power absorption efficiencies and absorbed powers of all buoys tested were found to be dependent on the wave height and wave period.

Further investigation of the high efficiency values achieved for the zero damped buoy are required. In addition, its damping needs to be evaluated as it may help to explain its performance. Recommendations and findings from stage-1 and stage-2 including the locations of amplification zones, the threshold wave periods beyond which no focusing was apparent, and the wave period at which the buoys were brought into resonance were used to assess the potential of the proposed parabolic concentrator-point absorber technology for stage-3 testing. These will also be used to determine the best location for the buoy with both parabolae and the optimum wave spectrum at which maximum power absorption is expected to occur.

4.6. Stage-3: Parabolic Concentrator-Point Absorber (Buoy)

The test setup for the parabolic concentrator-point absorber consisted of the following components: floating buoy, parabola, five cable/pulley arrangement and PTO system. Prior testing had identified that wave amplification could be achieved through using a parabola to focus wave energy and that the selected design of buoy performed well. In stage-3, the two were combined.

4.6.1. Stage-3 Test Setup

In stage-1 testing, the amplification zones for parabola-1 and parabola-2 were identified. The location chosen for the floating bi-cone buoy was

based on the results from stage-1. Visual inspection was conducted during testing to identify the best distance from each parabola for the buoy to be located. The parabola structures were moved until the buoy was in the optimal location at which testing was initiated. The parabolic-concentrator setup can be seen in Figure 4.30.



Fig. 4.30: Test setup for parabolic concentrator-point absorber and motion tracking using orange polystyrene beads

4.6.2. Stage-3 Results

The behaviours of the zero damped buoy (very low damping), half damped buoy and fully damped buoy with parabola-1 and parabola-2 were tested in regular waves of different heights and periods. More specifically, with parabola-1, wave periods of 0.8, 0.85, 0.9, 0.95, 1.0 and 1.2 s and wave heights of 0.03 m, 0.06 m and 0.09 m were used and with parabola-2, only wave periods of 0.85, 0.9 and 0.95 s were examined with the same range of wave heights.

The parabola-buoy device's overall power absorption efficiency ,η, was calculated using Equation (4.6) from section 4.1.2 with L_{tank} taken as the flume tank width. The efficiency values were calculated using the

average incident wave power per unit flume tank width instead of unit buoy width to account for the presence of the parabola. This is because the buoy is permitted to absorb power from the total wave front focused by the parabola not just the wave front with the same width as the buoy. The efficiency of the power absorption for all the parabola-buoy configurations as a function of wave period for wave heights H = 0.03, 0.06 and 0.09 m are shown in Figures 4.31-(a,b,c, and d). The power absorbed by all the buoys as a function of wave height is shown in Figures 4.32-(a, b, c, d and e).

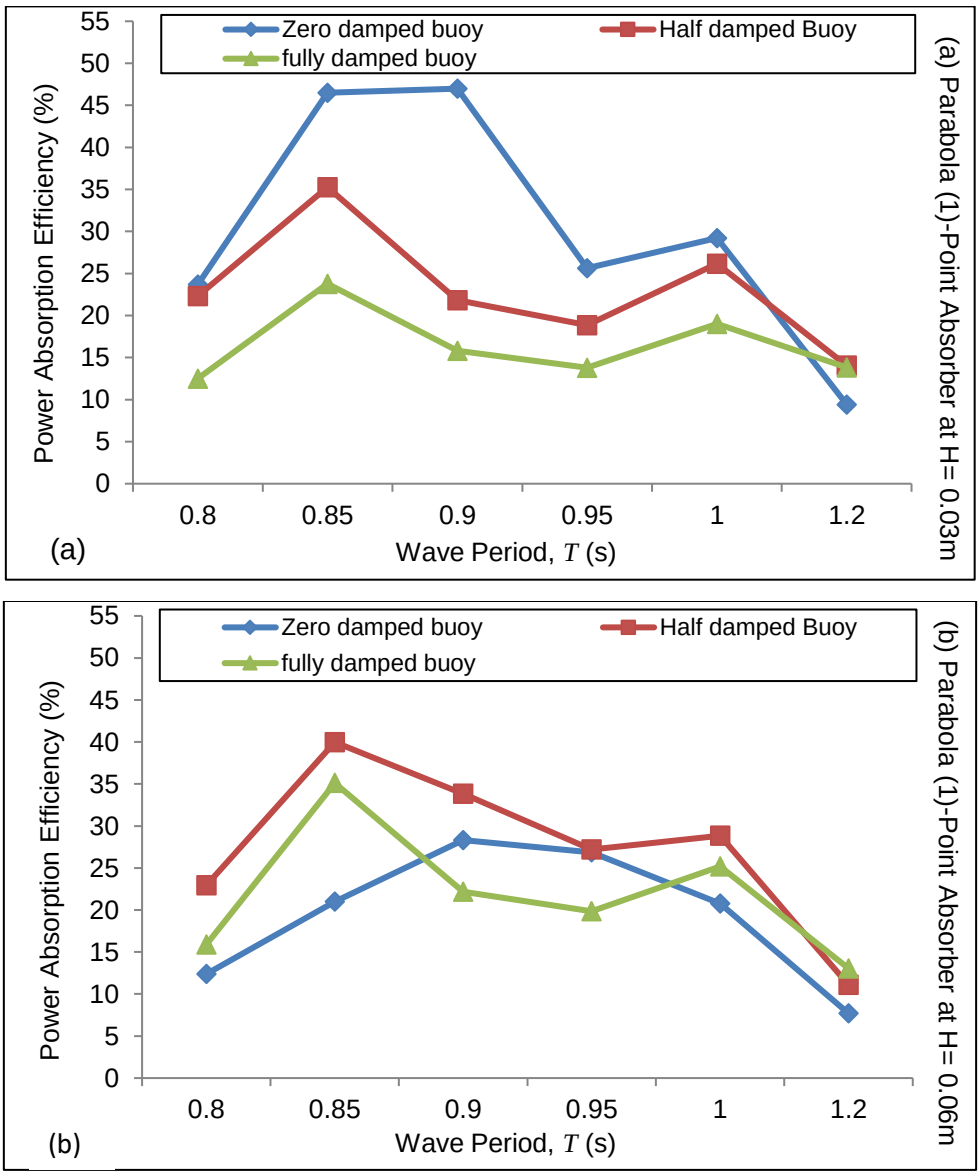
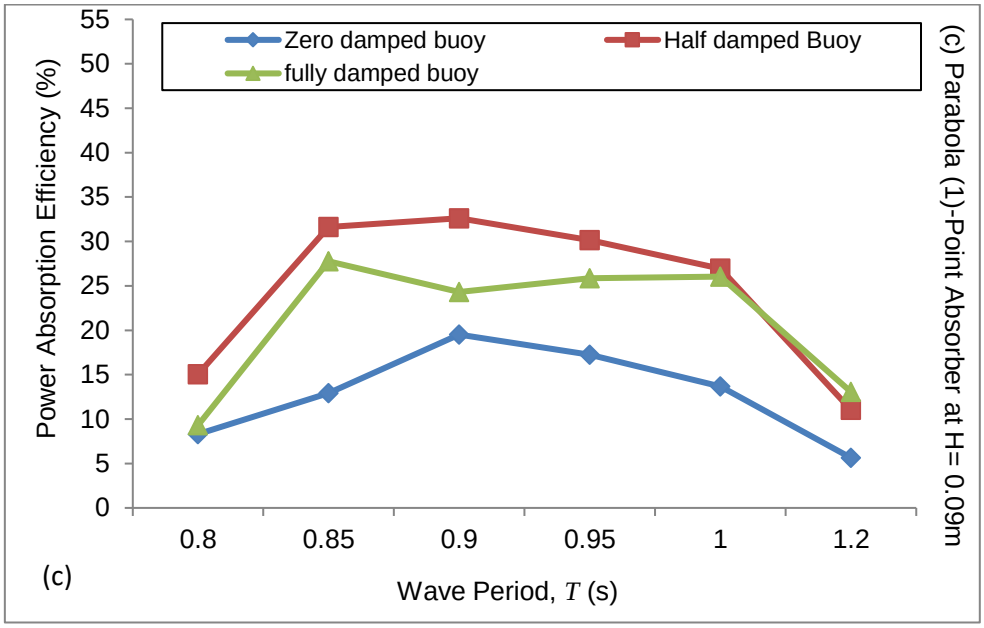


Fig. 4.31: Efficiency of power absorption, η, (%) as a function of wave period for parabolic concentrator-point absorber (a, b, c, and d)



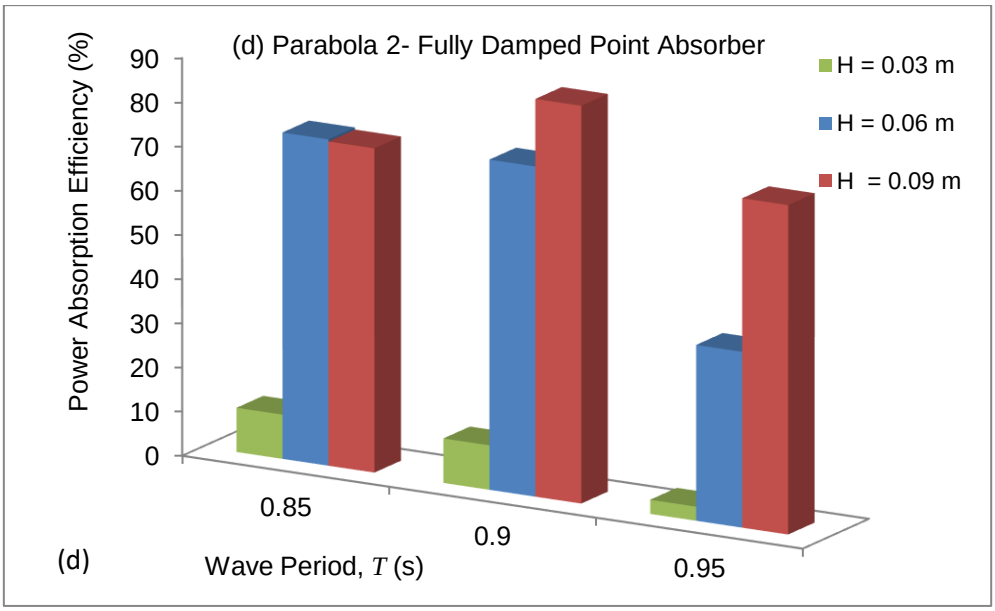


Fig. 4.31: Efficiency of power absorption, η, (%) as a function of wave period for parabolic concentrator-point absorber (a, b, c, and d)

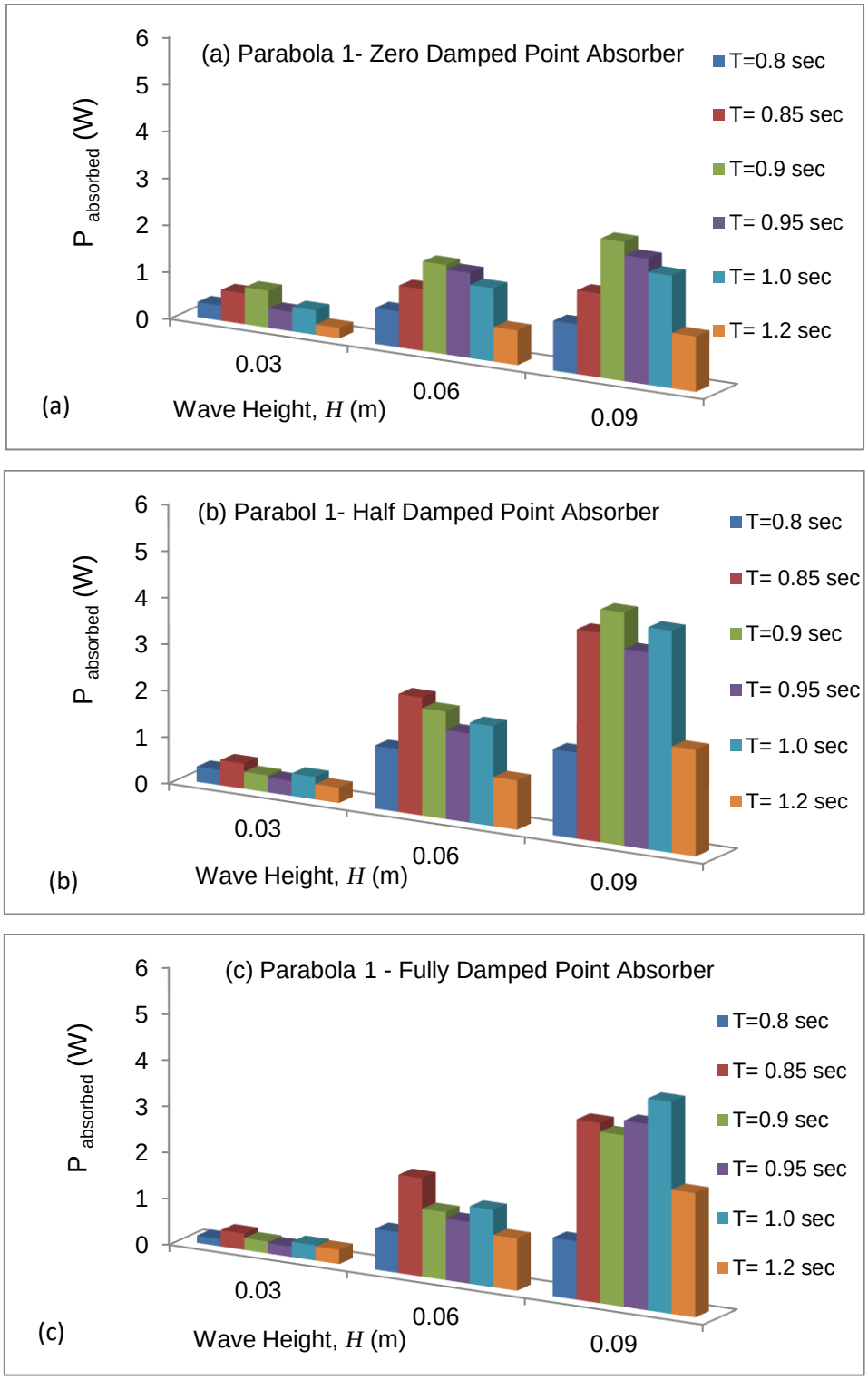


Fig. 4.32: Power absorbed by the buoy (W) as a function of wave height for parabolic concentrator-point absorber-(a, b, c)

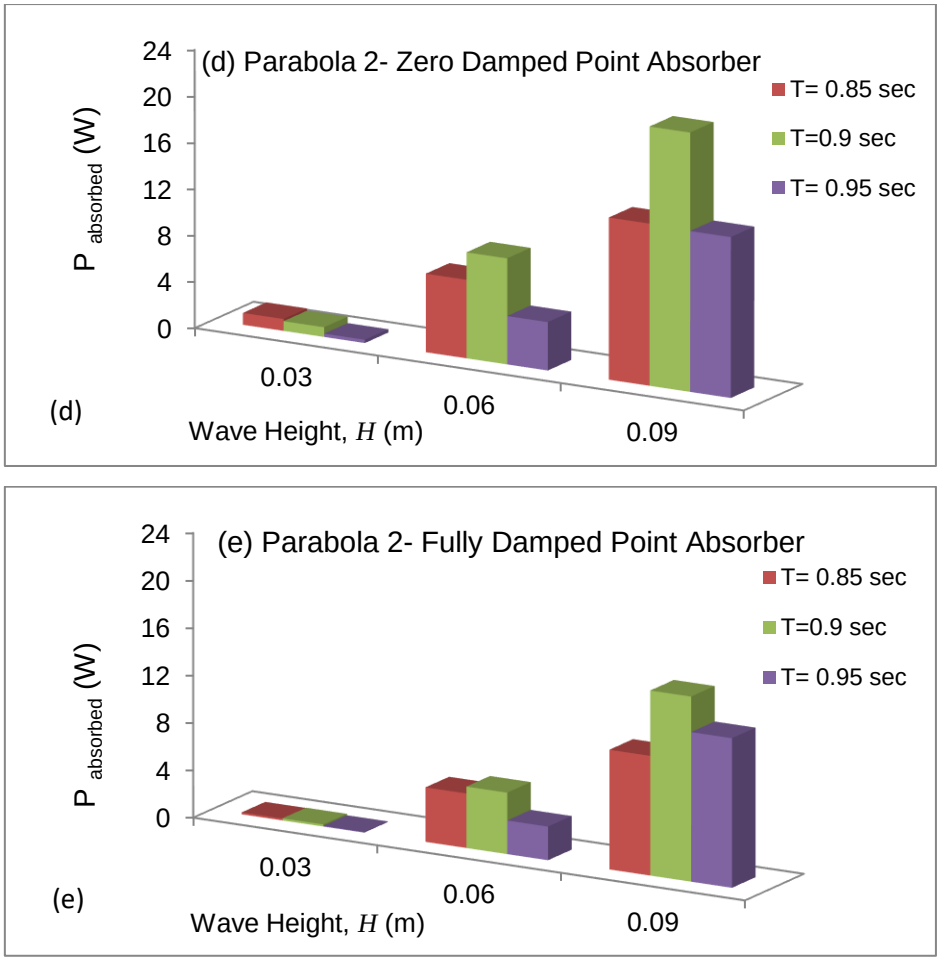


Fig. 4.32-(d, e): Power absorbed by the buoy (W) as a function of wave height for parabolic concentrator-point absorber

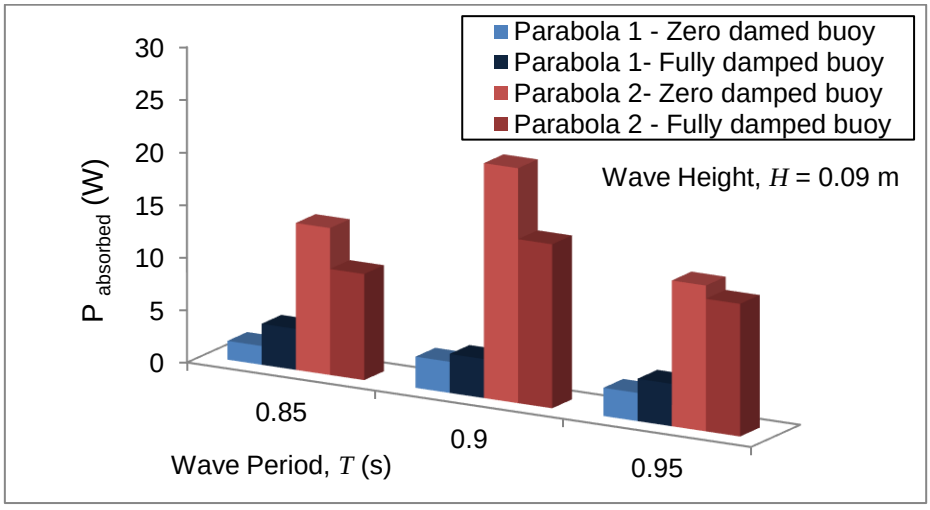


Fig. 4.33: Comparison of power absorbed by the buoy (W) as a function of wave height (H = 0.09 m) for parabola 1 and 2 for the same location

4.6.3. Stage-3 Discussion

Parabola-1–Zero Damped Point Absorber (Buoy): The device's performance in terms of its power absorption efficiency (Figures 4.31-(a, b, c)) was found to decrease with increasing wave height, for H = 0.03, 0.06 and 0.09 m. For longer wave periods, particularly those longer than 0.9 s, the efficiency was decreased for all wave heights. This behaviour is similar to that observed when the zero damped buoys were operating alone at wave heights larger than 0.03 m. However, the presence of the parabola affected the buoy's power absorption tremendously. Maximum power absorption of approximately 3.0 W was achieved when parabola-1 was used compared to 0.4 W when the buoy was used alone which means the power absorbed was almost 8 times higher. As expected, the buoy's maximum power absorption was achieved with the highest wave height (0.09 m) for all sea states tested. The maximum absorption of the incoming wave occurred when the sea state had a wave height and wave period of 0.09 m and 0.9 s, respectively, as seen in Figure 4.32a. The maximum power absorption with H = 0.09 m occurred with a wave period of 0.9 s, followed by 0.95 s, 1.0 s, 0.85 s, 1.2 s and 0.8 s. This clearly shows that at the two extreme wave periods, i.e. T = 0.8 s and T = 1.2 s, the buoy absorbed the least power (as seen in Figure 4.32a). The highest wave energy absorption occurred at wave periods ranging between 0.85 and 1.0 s for all wave heights and no clear trend can be observed in this range. However, there appears to be a "sweet-spot" or a good wave spectrum operational range where T = 0.85 – 1.0 s for the parabola-1–zero damped point absorber. For all the tests, the absorbed power was found to be dependent on the wave period and wave height. The maximum efficiency (47%) was achieved with a sea state of (H: 0.03 m, T: 0.9 s). The highest efficiencies for H = 0.06 m (28%) and H = 0.09 m (19%) were also seen to occur with T = 0.9 s. The system's efficiency decreased with increasing wave height. In addition, it is clear that the efficiency of the system is relatively sensitive to wave period and wave height. Higher efficiencies were recorded at lower wave heights and

lower efficiencies were recorded at the two extremes of the wave period range. The “sweet-spot” or good wave spectrum operational range was only observed with H = 0.06 m and H = 0.09 m. The system was in resonance at T = 0.9 s at which both maximum power and absorption efficiency was observed.

Parabola-1–Half Damped Point Absorber (Buoy): Applying a small amount of external damping to the parabola-1–buoy system was found to influence efficiency. When the system was subjected to a small degree of damping, the efficiency was highest around the same “sweet-spot” detected for the undammed system. A maximum efficiency of 39% was recorded which corresponded to the sea state with H = 0.06 m and T = 0.85 s. The highest efficiency values for H = 0.06 m (40%) and H = 0.09 m (33%) were observed with T = 0.85 s. It was found that the efficiency of the half damped system is relatively insensitive to wave height. On the other hand, the efficiency of the system was found to be relatively sensitive to wave period where highest efficiencies were recorded with T = 0.85. The “sweet-spot” was only observed at H = 0.09 m. Maximum power absorption for the system was achieved at the highest wave height (0.09 m) for all sea states. Much higher power absorption values (almost 17 times higher) were recorded (5.0 W) for parabola-1–half damped buoy system compared to the half damped buoy alone (0.3 W). The maximum absorption of the incoming wave energy occurred when the sea state had a wave height and wave period of 0.09 m and 0.9 s (Figure 4.32b), respectively. No clear trend can be observed from the data, but in general the highest absorbed powers were recorded at the “sweet-spot”. For all the tests, the absorbed power was found to be dependent on both the wave period and wave height.

Parabola-1–Fully Damped Point Absorber (Buoy): The maximum efficiency (35%) recorded with this arrangement corresponded to the sea state with H = 0.06 m and T = 0.85 s. The highest efficiency values for H = 0.03 m (24%) and H = 0.09 m (28%) were also seen to occur with T = 0.85 s. In general, it was observed that the highest efficiencies

were recorded at T = 0.85 s and the device performance were found to increase with increasing wave height. The maximum power was achieved at the highest wave height (0.09 m) for all sea states. Much higher power absorption values (4.6 W) were recorded for the system compared to the fully damped buoy alone (0.35 W). The maximum absorption of the incoming wave energy occurred when the sea state had a wave height and wave period of 0.09 m and 1.0 s (Figure 4.32c), respectively, similar to with the fully damped buoy alone. Again, the highest absorbed powers were recorded at the "sweet-spot" with no clear trend in the data. For all the tests, the absorbed power was found to be dependent on both wave period and wave height.

Parabola-2–Zero damped Point Absorber (Buoy): The power absorption efficiency measured for this device recorded was very high (greater than 100%). A maximum efficiency of approximately 137% was recorded with H = 0.09 m and T = 0.9 s which cannot be explained at this stage and might be due to experimental error or slamming effects. For this reason, only the power absorption measurements will be evaluated. As expected, the buoy maximum power absorption was achieved at the highest wave height (0.09 m) for all sea states. The maximum power absorption at H = 0.09 m was seen to occur with a wave period of 0.9 s, similar to parabola-1. The power absorbed by the buoy with parabola-2 (22 W) was much higher than that absorbed with parabola-1 (3.0 W) as seen in Figure 4.33. The power absorbed was also found to be dependent on the wave period and wave height.

Parabola-2–Fully Damped Point Absorber (Buoy): A maximum efficiency of 97% was achieved compared to 35% achieved with parabola-1 (Figure 4.33). The maximum efficiency (97%) recorded corresponded to the sea state with H = 0.09 m and T = 0.9 s as shown in Figure 4.31d. The device's performance at T = 0.85 s was found to be as good as its performance at T = 0.9 s. The efficiency of the system was found to be relatively sensitive to wave height and wave period. The maximum absorption (16 W) of the incoming wave energy occurred when the sea state had a wave height and wave period of 0.09 m and

0.9 s (Figure 4.32e), respectively. Much higher power absorption values were recorded for the system compared when parabola-1 was used (4 W). The system was brought into resonance at a wave period of T = 0.9 s. The absorbed power was found to be dependent on the wave period and wave height.

4.6.4. Stage-3 Findings

The proposed parabolic concentrator-point absorber combination has proven to be very successful. The presence of the parabola affected the buoys' power absorption tremendously. This is more important than the efficiency because the energy source (waves) is freely available. The findings from the stage-3 testing are:

- More of the available wave energy was seen to be absorbed with the parabola-buoy structure than with the buoy alone. The parabolic concentrator technology and its use as a WEC and breakwater device proved to be very successful.
- The lowest absorbed powers were recorded at the two extremes of the wave period range. The highest wave absorption occurred at wave periods ranging between 0.85 and 1.0 s for all wave heights. This appears to be the "sweet-spot" or good wave spectrum operational range (i.e. T = 0.85 – 1.0 s) for parabola 1. A "sweet-spot" was not detected for parabola-2 as only a small range of wave periods was tested (i.e. T = 0.85 – 0.95 s). The absorbed power was found to be dependent on the wave period and wave height.

- External damping was clearly found to affect the power absorbed by the parabola-buoy structure. With parabola-1, applying a small amount of damping to the buoy (i.e. half damped) was seen to be better than applying full damping (Figure 4.31c). When the buoy was subjected to low damping, a maximum power absorption of 5 W was recorded, which means that this buoy would be capable of absorbing almost 82 kW at prototype scale.

- The chosen parabola designs were both effective. The two structures were at either end of the potentially useful range of geometries in that parabola-1 was shallow whereas parabola-2 was deep. Higher efficiencies were recorded with parabola-2 compared to parabola-1. There were uncertainties in some of the calculated efficiencies for the device with parabola-2 and a zero damped buoy that might have been due to second reflections from the parabola-2 wall or due to the fact that the buoy extracted more power at the start and reached levels above steady-state before its power dropped back again. The performance of the parabola-2–buoy combination is worthy of further investigation.

- The results for the parabola-buoy systems showed their suitability when regular narrow banded waves are dominant in mild wave climates similar to that found in Kuwait. The good wave spectrum operational range with parabola-1 in Kuwaiti sea conditions was found to be T = 3.4 – 4.0 s (prototype scale) for all tested wave heights. The type of parabola to be used needs to be selected based on the predominant wave period conditions for the implementation site. In general, the parabola-buoy combination is a promising wave energy device which can have greater energy conversion capacity at more energetic deployment locations in the Kuwaiti sea.

4.7. Conclusions

The physical model and the experimental results showed that there is a substantial benefit for power absorption through using a combined parabolic concentrator-point absorber device. This is an encouraging step towards making wave energy more attractive in Kuwait as it will allow waves to be focused and amplified and thus enable more electrical power to be produced.

The experimental investigation also showed that placing a buoy at the amplification zone of a parabola can cause the absorption efficiency to

increase tremendously compared to a buoy on its own. There are fascinating scientific challenges and possible solutions for improving the efficiency and performance of the system.

The shape of the parabola was found to affect power absorption significantly. The differences in power absorption efficiency and total absorbed power between the two parabola shapes evaluated were very large. A maximum efficiency of 97% was achieved with parabola-2 compared to only 35% achieved with parabola-1 for the fully damped buoy. Much higher (16 W) power absorption values were recorded for the parabola-2 system compared to the parabola-1 system (4 W). This means that the parabola-2–buoy system would be capable of absorbing almost 260 kW power at prototype scale when the sea state have a wave height and wave period of 1.44 m and 3.6 s. In general, the results for both parabola structures showed their suitability when regular narrow banded waves are dominant in mild wave climates similar to that found in Kuwait. The final choice between a parabola-1, parabola-2 or intermediate shape for the wave energy focusing device will probably be more influenced by aspects other than its hydrodynamic performance, e.g. by material costs, fabrication costs and the ability of the structure to withstand the predominant wave period conditions at a particular site. The optimal buoy size is case specific and will be determined by wave climate, damping and cost considerations.

The wave climate around Qaru Island would benefit greatly from the installation of a parabolic concentrator-point absorber device and the extracted power may be sufficient for the utility services on Qaru Island for a year. The model developed in this study could easily be scaled up to a full size prototype by following the scaling laws. The first step would be to scale up the size of the buoy. Based on the buoyancy force and power output, the size of the cylinder and hydraulic motor could be calculated.

The main error in the experimental testing was in the pulley arrangement described in section 4.5.2. Of the three pulleys located above the buoy, the middle pulley was used as a pre-tensioner and adjusted using a screw. Further improvements could be made by using a spring pre-tensioner to reduce vibration and noise in the vertical force readings. It was also noted that the cable arrangement restricted the buoy's motion at high wave heights which needs to be addressed.

The following recommendations are proposed for future work with the physical model:

- Testing of different parabola shapes for use with a broadband wave spectrum with a wide range of frequencies.
- Testing to determine the optimum level of damping for the buoy.
- Testing at the good wave spectrum operational range found for parabola-1 to tune the device towards resonance.
- Testing with different buoy diameters and drafts.
- Testing to examine the buoy's mooring design and its influence on power extraction.

Chapter 5: Computational Fluid Dynamics (CFD) Modelling

This chapter describes the numerical investigation carried out as part of this research. The numerical analysis focused on modelling elements of the wave tank and buoy system used in the experimental investigation presented in Chapter 4.

Conventional computational fluid dynamics was identified as the best modelling approach considering the constraints of this project. The numerical simulations of the wave generation were performed through the commercial CFD code ANSYS-FLUENT package using the Volume of Fluid (VOF) multiphase model to reproduce the the wave generation in the tank. This chapter gives a brief introduction to the governing equations for fluid flow, spatial and temporal discretisation, pressure-velocity coupling, and boundary conditions followed by a detailed description of how FLUENT was used to model the regular wave propagation inside the tank at KISR. The chapter also includes a brief summary of the methods that were initially considered and developed but were ultimately rejected for the final analysis.

The chapter focuses on the CFD study and includes a description of the mesh generation, geometry, physical setup and boundary conditions along with details of the mesh sensitivity study undertaken. In the latter part of the chapter, the results of the CFD predictions for fluid motion in a wave tank with a parabolic concentrator are presented and compared to the available experimental data. The final part of the chapter presents data from the CFD analysis of a wave tank containing a static buoy.

5.1. Computational Fluid Dynamics (CFD)

This section is focused on using a conventional CFD method that could ultimately be developed to analyse the dynamic behaviour of a floating buoy under wave forces in 3D. This method was found to be the most appropriate for this work and the method development and application forms the remainder of this chapter.

5.1.1. Computational Fluid Dynamics (CFD) Development

Computational Fluid Dynamics (CFD) can be used to perform numerical experiments and to analyse problems when physical experiments would be difficult or dangerous resulting in significant reductions in time and cost (Violeau, 2012). CFD modelling also provides additional information that cannot be obtained from direct experimental observation as it not only describes flow variables, but it provides an insight into the physical processes controlling a phenomenon (Violeau, 2012). Typical applications of CFD include the modelling of floating structures in deep water and the investigation of the physics of ocean waves.

The most common CFD model used for modelling Wave Energy Converters (WECs) is based on an incompressible representation of the Navier–Stokes (NS) equations. A relatively large number of Oscillating Water Column (OWC) CFD models have been developed (see for example Qian et al., 2005). Zhang et al., (2012) and Luo et al., (2014a) developed a 2D OWC model and obtained better agreement with experimental results than were achieved with calculations based on linear potential flow theory. Luo et al., (2014b) developed a 2D, fully nonlinear CFD model with a dynamic mesh for analysing the performance of a heave-only floating OWC device. The model was validated against previous experimental, analytical and numerical results for wave–air–structure interactions from the literature. The results showed that both the turbine pneumatic damping coefficient and mooring spring elasticity coefficient have a significant effect on power capture efficiency. Vyzikasa et al., (2017) demonstrated the strength of

CFD modelling for obtaining better insight into the hydrodynamics of OWCs. The OWCs examined were fixed to the sea bed and had a slit opening on the seaward side.

Li and Lin, (2012) developed a 2D fully nonlinear CFD numerical wave tank model for examining wave–body interactions for a stationary floating structure under regular and irregular waves with different water depths, wave heights and periods. The tank model was based on the RANS equations and the RNG $k-\varepsilon$ model, and the equations were discretised based on the FVM. The simulations for regular and irregular waves and wave impacts showed good agreement with analytical solutions and experimental data. Another fully nonlinear 2D CFD model based on the RANS equations but using the VOF surface capturing scheme was implemented by Elhanafi et al., (2017) to carry out wave energy balance analyses for an offshore OWC. The CFD model was validated using published experimental measurements for: chamber differential air pressure, chamber water level oscillation and vertical velocity, overall wave energy extraction efficiency, reflected and transmitted waves, and velocity and vorticity fields.

CFD has also been used for modelling a moving WEC. An early example is the work of Agamloh et al., (2008), who modelled an isolated and a pair of heaving buoys in 3D using CFD. The response and power capture were calculated from the motion of the buoys. Despite the fact that the results were not compared with experimental data or other theoretical predictions, they did show an expected decrease in conversion efficiency with wave amplitude. Other moving WEC CFD models have considered a cylindrical WE device (Agamloh et al., 2008), the SEAREV WEC (Babarit et al., 2009), an oscillating wave surge converter (Schmitt et al., 2012; Henry et al., 2014), a moored heaving WEC (Palm et al., 2013), a two-body heaving WEC (Yu and Li, 2013), a heaving/surging horizontal cylinder (Anbarsooz et al., 2014), and a tetrapod breakwater (Dentale et al., 2014). In addition, Lal and Elangovan, (2008) attempted to establish guidelines for using CFD to simulate a flap type wave-maker. The CFD results in Lal and

Elangovan's (2008) study were in good agreement with other theoretical results.

Similar to the case with OWCs, CFD models of WECs have been found to produce better estimates of hydrodynamic forces than linear potential flow models. However, CFD model predictions are still often different to the measured responses of wave-tank models. A comparison was made of the results from several commercial and non-commercial CFD codes including SPH models for modelling the Pelamis and Manchester Bobber WECs (Westphalen et al., 2009). Westphalen et al., (2014) also investigated of wave–structure interaction using state of the art CFD techniques. The commercial CFD code Flow-3D was also used for the numerical modelling of two different surging point absorber WEC to achieve an optimised shape and to predict power output at a higher or full scale (Bhinder et al., 2009a). The results were found to be in good agreement with experimentally measured data. In addition, a review of the CFD modelling of WECs has been provided by Wolgamot and Fitzgerald, (2015). Details of the application of the incompressible surface capturing method for WEC simulation can be found in Qian et al., (2005). In addition, the numerical simulation of both linear deep water waves and linear waves with a finite depth using CFD was carried out by Finnegan and Goggins, (2012).

Instead of detailing all the various competing CFD codes, it is more useful to understand the desirable features of the different codes. A first important feature for a CFD code to be used for simulating WECs is that it must be able to consider two fluids, namely air and water. In addition, it must be able to allow for waves breaking in shallow water or in stormy conditions. One approach which has been employed in WEC simulations is to use a single fluid CFD solver where the numerical solution is computed only in the water component and the air/water interface (free surface) is defined by a surface boundary condition. Solutions using this approach either broke down or gave incorrect results (Folly, 2016). Two-fluid solvers have been found to be more useful where the underlying fluid equations are solved simultaneously

in both the air and water components. This approach is numerically challenging because of the large discontinuity in density across the air/water interface (water is one thousand times denser than air). The volume of fluid (VOF) method (Ubbink, 1997) is one way of creating the air/water interface. Although the VOF method can be used to model breaking waves, reconstruction of the interface becomes complicated in 3D.

A second important feature required of a CFD code for simulating WECs is its ability to deal with the motion of the device. As described in Chapter 3, the motion of WECs has 6 degrees of freedom. Hadzic et al., (2005) explored the motion of a floating rigid body with up to 6 degrees of freedom subjected to large amplitude waves. In this type of analysis, grid generation is a critical step and it accounts for most of the time needed for modelling. When using the gridding approach, the grid is stretched and compressed in the vicinity of the WEC as it moves to ensure that the grid remains fitted to the body at all times (Bhinder et al., 2009b; 2011). This approach is efficient for the small amplitude oscillatory motion of a WEC. At large wave amplitudes when the device motion becomes large and grid cells become highly skewed; the model either breaks down or needs frequent re-meshing. Another approach is to include the WEC in its own interior body. With this method, a fitted sub-grid moves with the WEC within a fixed external grid and its structure does not change (Schmitt and Elsaesser, 2015). At each time step, the data is interpolated at the intersection of the sub-grid and the fixed external grid. Although this gridding approach can cope with random WEC motion, it does have some problems. In particular, care must be taken over the generation of the body fitted internal grid and the interpolation of the data between the interior and exterior grid boundaries.

There are a large number of CFD modelling tools available for modelling WECs. Generally speaking, the commercial packages are well documented and are easier to use than the open source CFD models. They are therefore considered to be the best option for WEC

engineering applications. Some of the commercial CFD packages that have been used previously for WEC simulation are: FLUENT, CFX and FLOW-3D.

Due to its availability and stated capabilities, ANSYS-FLUENT was chosen for this project. It has plenty of flexibility including the capability to introduce custom code segments to expand a simulation. CFD modelling considerations and a description of the model development are given in section 5.3. For further details on any of the aspects discussed in section 5.3, refer to the ANSYS Fluent User's Guide, (2011).

5.2. Computational Fluid Dynamics (CFD) Methodology

CFD is a computer-based simulation technique which is considered a useful tool for solving fluid flow problems. In CFD, fluid flow equations are solved to calculate the values of flow variables such as pressure and velocity. The commercial CFD code FLUENT version 17.1 was used for this study. FLUENT uses the finite volume method to divide the domain into control cells or volumes. The definition of flow properties at the domain boundaries allows flow variables to be calculated within these control volumes using iterative finite differencing methods which upon convergence, give a solution to the flow field problem.

5.2.1. Convergence

In CFD, the numerical model is not only discretised in space but also in time because it is impossible to use infinitely small time steps. The largest time step possible is used to reduce the simulation time while still achieving an acceptable level of accuracy.

For transient solutions within FLUENT, the solver iterates to convergence at each time step such that the residuals defined by the user are achieved and then advanced automatically. The time step is the incremental change in time for which the governing equations are being solved. It must be set small enough to resolve the time dependence and ensure convergence within the maximum number of

iterations defined by the user. CFD convergence uses residual values as it quantifies the errors in the solution of each conserved variable in each control volume. Every cell in the model has its won residual value for each equation being solved. The residuals can never go to zero where low residuals mean more an accurate solution. In this study the residuals used for the continuity equation was 0.001 s and 1×10^{-6} s for the other equations. The maximum iterations per time step reporting interval were 10 and typically converges occurred within 600,000 iterations. This convergence in FLUENT was deemed sufficient for this study.

5.2.2. Boundary Conditions

Defining the conditions at the domain boundaries is a crucial part of the setup of the computational domain as the boundary conditions direct the motion of the flow and specify fluxes into the computational domain e.g. mass, momentum and energy. Appropriate initial conditions and boundary conditions are required for solving both the NS equation and continuity equation. There are several types of boundary conditions possible and those used in the analyses are described in the relevant section. The mathematical principles underlying these different types of boundary conditions are given below.

Wall: All the wall boundaries including the parabola wall were modelled as stationary solid walls where no-slip shear boundary conditions apply. The no-slip condition means that the fluid velocity is either zero or equal to the velocity of the wall.

Pressure Boundaries: Pressure boundaries are applied when the pressure at the location in the domain is known and the velocity flow rate is unknown. FLUENT requires that the total pressure is prescribed and the temperature also must be specified as the energy equation is used. The total pressure (p_{total}) for an incompressible fluid is given as:

$$P_{total} = P_s + \frac{1}{2}\rho v_a^{\,2} \tag{5.1}$$

where P_s is the static pressure, v_a is the absolute dynamic fluid viscosity and ρ is the density of the fluid.

In all the cases within this work, the gauge pressure at the top boundary surface was set at 0 Pa relative to a specified operating pressure of 101,325 Pa.

5.2.3. Turbulence

Turbulent flows are typically characterised as irregular and chaotic and are thus a challenge to model. Modelling turbulent flow directly is possible but requires very small mesh sizes and time steps. This is computationally expensive. A comparison was made between a laminar and a turbence $k-\varepsilon$ model for 3D wave tank with a wave generator. It was found that there was no difference in the generated wave elevation between the two models (Lal and Elangovan, 2008; Finnnegan and Goggins, 2012). Therefore, for simplicity the numerical wave tank in this chapter was built for a flat plate boundary layer laminar flow (Schlichting, 1960). The Reynolds number is given as:

$$\mathrm{Re} = \frac{\rho \nu \, L_c}{v_a} \tag{5.2}$$

where ν is the velocity, L_c is the characteristic length, v_a is the absolute dynamic fluid viscosity and ρ is the density of the fluid. For the flow a Reynolds number of $\mathrm{Re} = 5 \times 10^5$ was computed.

5.3. The Volume of Fluid (VOF) Model

Conservation equations for each phase are derived such that a set of equations which have a similar structure for all phases are obtained. Within FLUENT, the volume of fluid (VOF) model used. The model is designed for two (or more) immiscible fluids where the position of the interface between the fluid phases is related to the volume fraction. It allows the fluids to be solved using one set of momentum equations and the volume fraction of each of the fluids in each cell is tracked

throughout the domain. Applications of the VOF model include: stratified flows, free-surface flows, the motion of large bubbles in a liquid and the steady or transient tracking of liquid-gas interfaces. This model is the appropriate one for the free-surface simulations in this chapter.

The VOF method is the least computationally intensive multiphase model available as it solves only one set of momentum equations. The model is particularly effective when modelling phases with significant differences in density and a clear interface. The VOF formulation relies on the fact that the two (or more) phases are not interpenetrating and in each control volume, the volume fractions of all phases sum to unity. The fields for all variables and properties are shared by the phases and represent volume-averaged values provided that the volume fraction of each of the phases is known at each location. Thus the variables and properties in any given cell either represent one of the phases or a mixture of the phases, depending on the volume fraction.

With the VOF method, a single momentum equation is solved and the resulting velocity field is shared among the phases. The momentum equation is dependent on the volume fractions of all phases through the properties ρ and μ as follows:

$$\frac{\partial}{\partial t}(\rho \vec{v}) + \nabla.(\rho \vec{v}\vec{v}) = -\nabla p + \nabla.\left[\mu(\nabla \vec{v} + \nabla \vec{v}^{T})\right] + \rho \vec{g} + \vec{F} \tag{5.3}$$

The tracking of the interface between the phases is accomplished by the solution of a continuity equation for the volume fraction of one (or more) of the phases. The volume fraction, α, is tracked by:

$$\frac{1}{\rho_p}\left[\frac{\partial}{\partial t}(\alpha_q \rho_q) + \nabla.(\alpha_q \rho_q v_q) = s_{\alpha q} + \sum_{p=1}^{\vec{n}}\left(\dot{m}_{pq} - \dot{m}_{qp}\right)\right] \tag{5.4}$$

where the subscripts p and q refer to the two different phases, $\dot{m}_{pq}$ is the mass transfer from phase p to phase q, and $s_{\alpha q}$ is a source term.

The volume fraction equation is solved for each phase separately. For the primary phase, the volume fraction is computed based on the following constraint:

$$\sum_{q=1}^{n} \alpha_q = 1 \tag{5.5}$$

In this chapter, the air is the primary phase and the water is the secondary phase. The waves are linear Airy waves (described in chapter 2) with a large wave-length to depth ratio and low interface shear, hence any nonlinear breaking and splashing effects have been ignored.The volume of fluid (VOF) model is not available within the FLUENT code with the density-based solver. Therefore, the pressure-based solver was used for this work. Moreover, the pressure-based solver can handle a wide range of incompressible and compressible flow regimes. For incompressible flow calculations with a low Reynolds number, the use of a pressure-based solver is recommended. Several models are available to achieve this coupling, of which the Semi-Implicit Method for Pressure-Linked Equations (SIMPLE) algorithm was used in this study (ANSYS Fluent User's Guide, 2011).

Time Discretisation

Two time discretisation methods exist for solving the volume fraction equation, namely the Euler explicit scheme and the implicit scheme. In the Euler explicit scheme, volume fraction data from both the current and the previous time steps are required and the FLUENT finite-difference interpolation scheme is applied as follows:

$$\frac{\alpha_q^{n+1}\rho_q^{n+1} - \alpha_q^{n}\rho_q^{n}}{\Delta t} V_{cell} + \sum_f (\rho_p U_f^n \alpha_{q,f}^n) = \left[\sum_{p=1}^{n} (\dot{m}_{pq} - \dot{m}_{qp}) + S_{\alpha q} \right] V_{cell} \tag{5.6}$$

where $n+1$ is the index for the new time step, n is the index for the previous time step, $\alpha_{q,f}$ is the face value of the qth volume fraction, V_{cell} is the cell volume and U_f is the volume flux through the face. In

contrast to the implicit scheme, the explicit scheme does not require iterative solution of the transport equation during each time step.

In the implicit scheme, volume fraction values at the current time step are required thus a standard transport equation can be solved iteratively for each phase (other than the primary phase). In this case, the FLUENT finite-difference interpolation scheme is applied to obtain the face fluxes for all cells, including those near the interface as follows:

$$\frac{\alpha_q^{n+1} - \alpha_q^n}{\Delta t} V_{cell} + \sum_f (U_f^{n+1} \alpha_{q,f}^{n+1}) = 0 \quad (5.7)$$

The implicit VOF scheme can be used for both time-dependent and steady state calculations. This approach is generally preferred as it allows larger time steps to be used than can be used with the explicit formulation and convergence is achieved more quickly. However, for the modelling work here, it proved impossible to achieve convergence with the implicit scheme hence the explicit approach was selected. For the VOF analyses described in this chapter, a fixed time step was specified based on the transient frequency of the wave.

For a laminar flow that is aligned with the hexahedral grid, the numerical diffusion will be naturally low, so the simpler 1st order scheme can generally be used without any significant loss of accuracy. 1nd order discretisation was therefore used for this work. Transient simulations use a steady state solution to define the initial conditions and transient parameters vary depending on the mesh. Each time step is limited to a maximum of 0.001 s and the number of time steps is 60,000.

Interface Interpolation

In FLUENT the convection and diffusion fluxes through the control volume faces at the interface between phases must be computed and balanced in order to maintain the control volume formulation. In standard discretisation schemes, such as the 1st order upwind or the modified high resolution interface capturing (HRIC) schemes (ANSYS

Fluent User's Guide, 2011), the interpolation at the boundary is treated in the same ways as interpolation within a cell which is completely filled with one phase.

Central differencing schemes and upwind schemes are overly diffusive and hence are not suitable when modelling VOF simulations as they may give erroneous results. The modified HRIC scheme in FLUENT is a good alternative as it blends upwind and downwind differencing non-linearly. It also offers a cost effective means of improving accuracy over 2nd order schemes and was found to be more accurate than the 3rd order QUICK scheme for VOF formulations. A better alternative is to use a special interface interpolation treatment called the Geometric Reconstruction scheme. This scheme uses a linear piecewise approach which assumes that the interface in each cell has a linear slope. This is then used for the calculation of advection through the cell face.

The Geometric Reconstruction scheme was chosen for the VOF simulations described in this chapter. The steps of this scheme are:

1. The position of the linear interface is calculated based on volume fraction and its derivatives.
2. The fluid advection through the face is calculated based on the computed linear interface and the normal and tangential velocity values.
3. The volume fraction in the cell is calculated using the balance of fluxes from step 2.

A volume fraction of water equal to 0.5 was selected. The intersection of the interphase with the plane $z = 0$ gave a curve segment which was used to capture the interphase for different cases.

Surface Tension

The VOF model can also include the effects of surface tension at the interface. Surface tension arises as a result of attractive forces between molecules in a fluid. In this chapter the continuum surface force (CSF)

model within FLUENT, as proposed by Brackbill et al., (1992), was used. The CSF model represents the surface tension by a pressure jump across the surface which is included by adding a volume force into the momentum equation as a source term. When two different phases are present this force is defined as:

$$F_{vol} = \sigma_{ij} \frac{\rho k_i \nabla \alpha_i}{0.5(\rho_i + \rho_j)} \tag{5.8}$$

where σ_{ij} is the surface tension coefficient, k_i is the curvature from the surface normal, α is the volume fraction and ρ is the volume-average density. From Equation (5.8) it can be seen that the surface tension source term is proportional to the average density in the cell.

5.3.1. Wave generation

Waves were generated in this work using an open channel wave boundary condition which allows specific wave parameters to be set at open channel wave inlet boundaries. This is available when the VOF multiphase model is selected. The method, developed by Horko, (2007).

For incoming surface gravity waves, FLUENT allows the use of the 1st order Airy wave theory, which is applicable to small amplitude waves in shallow to deep liquids, and is linear in nature. Short gravity wave expressions for each wave are based on infinite liquid height, whereas shallow or intermediate wave expressions are based on finite liquid heights.

The wave height specified by the user is defined as follows:

$$H = 2A = A_t + A_c \tag{5.9}$$

where A is the wave amplitude, A_t is the wave amplitude at the trough, and A_c is the wave amplitude at the crest. For linear wave theory $A_t = A_c$.

The wave number k_n is defined as:

$$k_n = \frac{2\pi}{L} \tag{5.10}$$

where L is the wave length supplied as a user input.

The vector form for the wave number k_n is:

$$\vec{K} = k_x \hat{x} + k_y \hat{y} \tag{5.11}$$

where $\hat{x}$ is the reference wave propagation direction, $\hat{y}$ is the direction opposite to gravity and $\hat{z}$ is the direction normal to $\hat{x}$ and $\hat{y}$.

The wave numbers in the $\hat{x}$ and $\hat{y}$ directions are defined as:

$$k_x = k_n \cos\theta \tag{5.12}$$

$$k_y = k_n \sin\theta \tag{5.13}$$

where θ is the wave heading angle, which is defined as the angle between the wave front and the reference wave propagation direction in the $\hat{x} - \hat{y}$ plane.

The effective wave frequency , ω_e, is defined as:

$$\omega_e = \omega + \vec{K}.\vec{U} \tag{5.14}$$

where ω is the wave angular frequency and $\vec{U}$ is the averaged velocity of the flow current. The effects of a moving object can be incorporated through the flow current by setting the flow as relative to the motion of the moving object.

The wave speed , C , is defined as:

$$C = \frac{k_n}{\omega} \tag{5.15}$$

The final velocity vector for incoming waves obtained by superposing all the velocity components is:

$$\vec{V} = \vec{U} + u\hat{x} + v\hat{y} + w\hat{z} \tag{5.16}$$

where u, v and w are the velocity components of the surface gravity wave in the $\hat{x}$, $\hat{y}$, and $\hat{z}$ directions, respectively.

Airy Wave Theory

The wave profile for a linear wave is given as:

$$\zeta(X,t) = A\cos\alpha \tag{5.17}$$

The term α is defined as follows:

$$\alpha = k_x x + k_y y - \omega_e t + \varepsilon \tag{5.18}$$

where x and y are the space coordinates in the $\hat{x}$ and $\hat{y}$ directions, respectively, ε is the phase difference, and t is the time.

The wave frequency, ω, for short gravity waves is:

$$\omega = \sqrt{gk_n} \tag{5.19}$$

where k_n is the wave number, and g is the acceleration due to gravity.

The velocity components for the incident wave boundary condition are described in terms of short gravity waves as follows:

$$\begin{pmatrix} u \\ v \end{pmatrix} = \frac{gk_n A}{\omega} e^{kz} \begin{bmatrix} \cos\theta \\ \sin\theta \end{bmatrix} \cos\alpha \tag{5.20}$$

$$w = \frac{gk_n A}{\omega} e^{kz} \sin\alpha \tag{5.21}$$

where z is the height from the free surface level in the direction $\hat{z}$, which is opposite to the direction of the gravitational force.

At the velocity inlet in the model, the horizontal and vertical velocity components are applied together with the volume fraction of air and water. The velocities are only applied to the water fraction only. The velocity of the air fraction at the inlet boundary is set to zero. The values used for wave height, wavelength and phase difference were 0.06 m, 1.5613 m and 0, respectively, for the cases in this study. Modelling the wave generation at the inlet numerically provides greater flexibility and improves the capability of the model.

5.3.2. Mesh Selection

There are different geometries of cell available, namely triangle, quadrilateral, hexahedral, prism, tetrahedral and pyramid. Hexahedral cells have eight nodes and six quadrilateral faces, tetrahedral cells have four nodes and four faces, and prism cells have six nodes and five faces. Hexahedral cells can provide better solution accuracy and a superior rate of convergence as opposed to tetrahedral cells in the case where the flow and cell directions are aligned (Bakker, 2002). Three types of grid are available in FLUENT namely:

- Structured grid,
- Unstructured grid, and
- Hybrid grid.

A hexahedral mesh is a structured grid in which the cells and nodes are placed regularly. When the cells are placed in an irregular manner, the grid is known as unstructured and it is normally constructed from tetrahedral cells. A hybrid grid is comprised of a combination of either hexahedral and tetrahedral cells (simple domain) or tetrahedral and prism cells (complicated domain). A hexahedral mesh is good for capturing flow features because with hexahedral grids the predominant flow direction is aligned with the grid nodes (Bakker, 2002). In this research, a hexahedral structured mesh was used for the parabola

wave tank model and a tetrahedral unstructured mesh was used around the buoy.

5.4. CFD Wave Tank Model

In this section, the CFD model of the parabolic concentrator wave tank created is described. The model was constructed so that its predictions would be directly comparable to the data captured in the wave tank, providing a route for validation of the model. Once the wave tank model was validated, it was used for further work which included the modelling of the buoy. Based on the NS equations for incompressible fluids and the VOF method, a 3D numerical wave tank was established. A dynamic meshing method was used to simulate the wave generation, and the Geometric Reconstruct scheme was used to capture the free surface.

Wall and pressure inlet boundaries were used to construct the computational domain. Linear regular waves were simulated using the numerical model and the results were compared with experimental data. When defining a computational domain in FLUENT, a number of assumptions are required as follows:

- Density of water 998.2 kg/m^3 and density of air 1.22 kg/m^3
- Viscosity of water 0.001003 kg/ms and viscosity of air 1.7894×10^{-5} kg/ms (assumed to be constant)

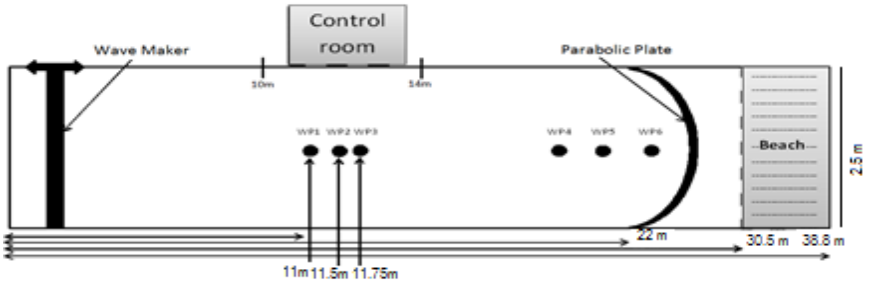
5.4.1. Geometry Setup

The wave flume tank has a length of 40 m, a width of 2.5 m and a depth of 2.5 m. Within the mechanical, geometrical and hydraulic limitations of the system, the active absorption type (Danish Hydraulic Institute (DHI)) wave maker is capable of generating regular waves of amplitudes of up to 40 cm and wave periods in the range 1.0 – 4.0 s. In order to establish wave reflection within the tank and ensure steady state was reached, the distance between the wave maker and probe WP1, used to measure incident waves, was chosen to be 11 m. Probes WP4, WP5 and WP6 were used for measuring the wave focusing effects created

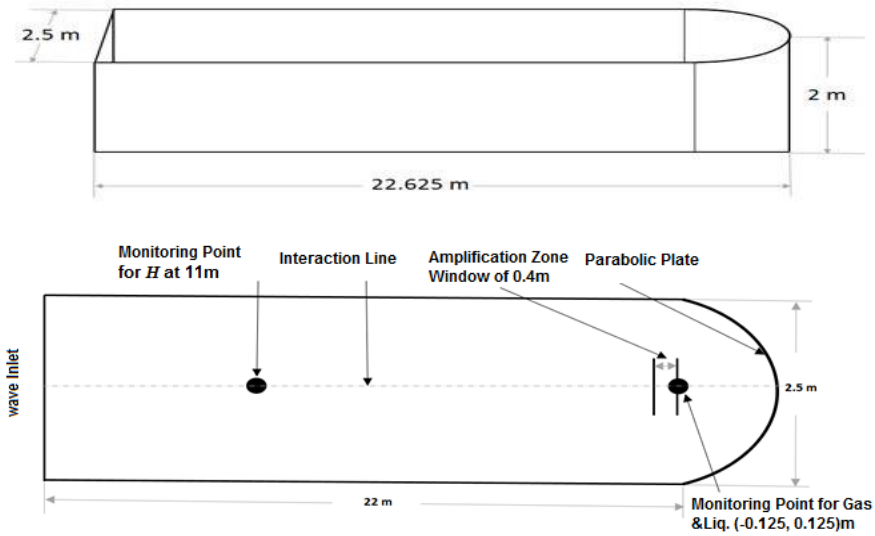
by the parabolic concentrator being tested. The distance between the wave maker and the start of the parabola was approximately 22 m. The dimensions of the physical tank are illustrated in Figure 5.1a. Orange polystyrene beads were used to track the wave motion and identify the amplification zone. Carefully positioned cameras allowed the motion of the marked beads to be mapped and translated into x-y-z coordinates for motion analysis.

The geometry of the computational domain used for the mesh study was a rectangular cuboid with length 22.625 m, width 2.5 m and depth 2 m as seen in the side and top views shown in Figure 5.1b. Although the tank length in the CFD model was shortened to 22.625 m to reduce the computational cost, it still reflected the real scenario. The selection of the height of the model depended on a number of factors, namely the still water level, the maximum height of the waves, and the response amplitude and height of the buoy. In this study, the wave tank was designed for deep water wave theory, and the height of the CFD tank was chosen to be 2 m to replicate the real scenario in the KISR wave tank. The water depth was taken to be 1.5 m which left sufficient room at the top (opening boundary) of the tank for the static buoy to interact with the incoming wave. The parabolic concentrator wall was installed at a distance of 22.625 m from the front inlet. Two monitoring points were used in the model, one at a distance of 11 m from the wave inlet and the other at the amplification zone, to replicate those in the physical model. The location of the amplification zone was identified in the experiments and this was replicated in the CFD model within a 0.4 m window taken at the focal point.

The wave data was extracted along an interaction line located in the middle of the domain as shown in Figure 5.1b. Any properties of the flow along the line may be extracted for a particular time. Wave height measurements within this window were taken at a vertical distance of -0.125 m from the line for the liquid and 0.125 m for the gas at the focal point of the parabola. The dimensions of the tank in the CFD model are illustrated in Figure 5.1b.



(a) Physical model



(b) CFD model

Fig. 5.1: Schematic of wave tank dimensions

One set of wave parameters used in the testing was selected for the modelling: wave period T = 1.0 sec and wave height H = 6 cm. This set was chosen as it was in the middle of the wave spectrum tested. The characteristics of the generated waves are summarised in Table 5.1. The wave tank model was allowed to run for a set period of time before data was taken to allow equilibrium conditions to be reached, i.e. when there was an unchanging progressive wave.

Table 5.1: Characteristics of generated waves

Parameters	Values
Wave period (T)	1.0 sec
Wave height (h)	0.06 m
Wave length (L)	1.56 m
Depth (d)	1.5 m

5.4.2. Boundary Conditions

The top of the wave tank model had an opening boundary condition which only allowed air to pass through and leave the domain, see Figure 5.2. This acted as a pressure outlet and the boundary condition of atmospheric pressure was applied. At the wall boundary, the velocity was set to zero.

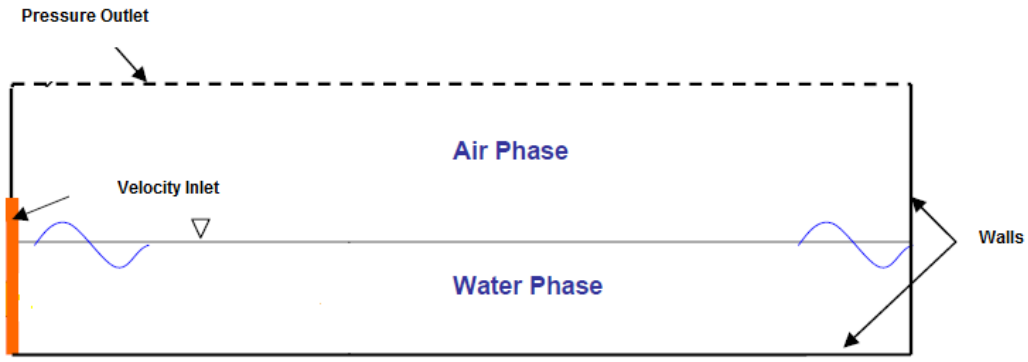


Fig. 5.2: Wave tank schematic representation

All model boundaries were handled in a consistent manner. The right and left boundaries of the solution domain were solid walls with no-slip boundary conditions. Static wall boundary conditions were chosen for the adjacent sides. The open top of the tank was modelled as a pressure outlet boundary, with the pressure set to be equal to atmospheric pressure. The bottom was modelled as a no-slip wall, similar to the right and left boundaries. The parabola wall was simply modelled as a curved wall boundary. The stationary walls including the parabola were set to be no-slip walls as this more accurately reflected the test arrangement.

5.4.3. Mesh

The hexahedral structured 3D mesh shown in Figure 5.3 was constructed in three main blocks. The total size of the domain was 22.625 m × 2.5 m × 2 m. The ‘‘stationary’’ mesh comprised cells of varying size with larger sizes towards the wall boundaries to provide the

damping effect of the waves. Top and isometric views of the mesh are shown in Figure 5.4. In order to capture the wave motion at the interface accurately, a finer mesh was used in this area.

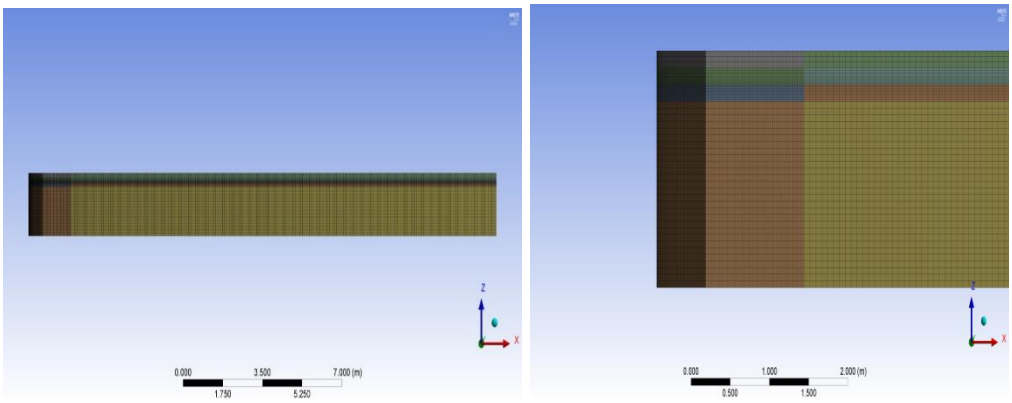


Fig. 5.3: 3D hexahedral structured mesh for wave tank model

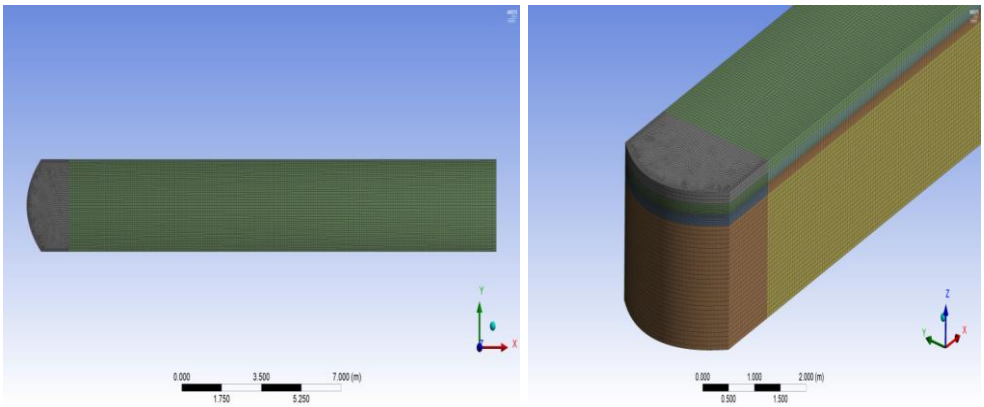


Fig. 5.4: Plan and isometric views of the 3D hexahedral structured mesh grid

The vertical coordinates where the water volume fraction was equal to 0.5 were taken to be the coordinates of the free surface. Values for the gas (air) and liquid (water) pressure and velocity were extracted at two positions: 0.125 m above and 0.125 m below the geometrical focal point of the reflection wall (parabola) for each time step.

5.4.4. Mesh Sensitivity Study

Grid generation is a critical step for any numerical approach as it is important to establish that the numerical solution is not dependent on the mesh used. The numerical solution can be affected by the grid quality which involves more than just the number of elements but also parameters such as aspect ratio, skewness and mesh size relative to adjacent cells. Moreover, CFD codes behave more robustly and have a higher efficiency when the mesh is well constructed and the mesh size is optimised. In this study, one of the important factors is the sensitivity of the wave elevation to the mesh refinement. Therefore, it was essential to optimise the mesh for the height and period of the waves being created.

5.4.4.1. Mesh Generation

A mesh dependency study was conducted and Table 5.2 gives the data for the various cases considered. Meshes containing 6900, 4300, 3300 and 1800 thousand cells were generated and the resulting data was compared to identify the optimum mesh size. The resolution of the finest and coarsest cells was 2 mm and 50 mm, respectively. The difference in the meshes was mainly in the fine mesh region surrounding the interface as illustrated in Figure 5.5. The generated wave spectrum used for the comparison had a wave period T = 1.0 s and wave height H = 6 cm.

As mentioned previously, the mesh sensitivity study focused on the fine grid region which was located within +/- 0.125 m of the interface, see Figure 5.8. A number of successively denser meshes were created by increasing the number of mesh layers near the interface (wave region) to improve the peak to trough resolution of the waves. The number of layers near the interface for each mesh is given in Table 5.2. The grid cell sizes used were either specified at the edges or for the body as a whole; these are also included in Table 5.2. In addition, to ensure mesh uniformity, the mesh was graded from coarse to fine as it approached

the interface region. The grading factors for each case are given in Table 5.2. The coarser grid used to represent the surrounding air and water regions is illustrated in Figure 5.6 and was the same for all cases.

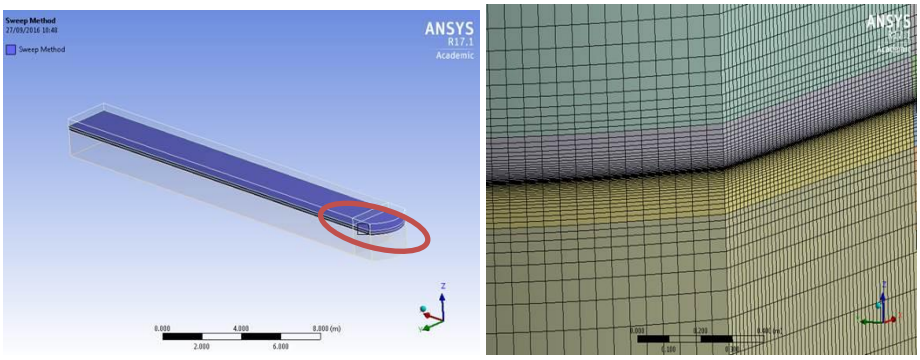


Fig. 5.5: Meshing in the interface region

Table 5.2: Outline of all input parameters in the mesh sensitivity study for the wave tank parabola model

Number of elements	Number of mesh layers near interface region	Body grid cell size (m)	Edge grid cell size (m)	Mesh to cell size ratio
6900 k	40	0.025	0.02	5
4300 k	30	0.025	0.025	5
3300 k	20	0.025	0.025	10
1800 k	10	0.03	0.03	10

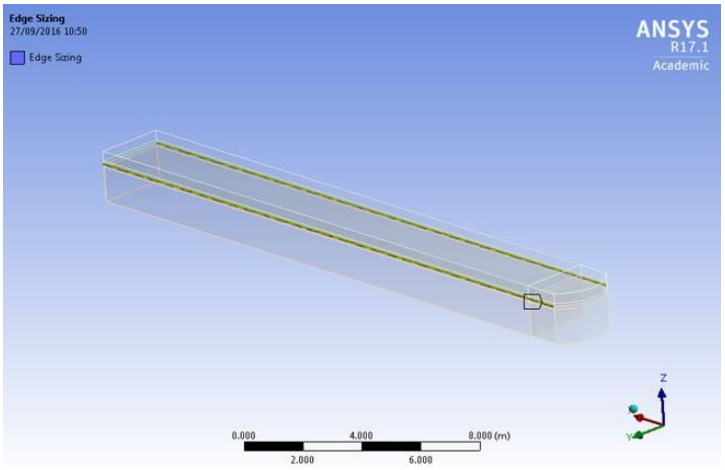


Fig. 5.6: Surrounding rough grid for air and water regions

The mesh size was controlled in the vicinity of the amplification zone to guarantee the quality of the results as illustrated in Figure 5.7. This was the main constraint to the cross-stream mesh gradation in the y-direction.

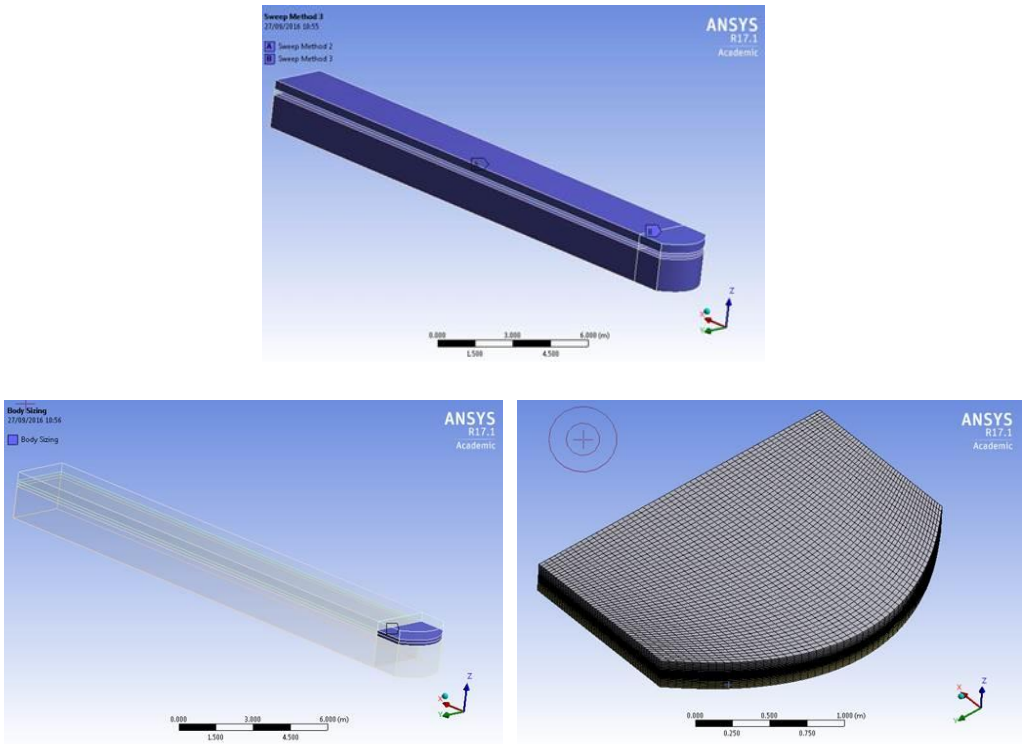


Fig. 5.7: Meshing in the vicinity of the parabola-1 amplification zone

5.4.4.2. Results for Parabola Model Mesh Sensitivity Study

Data for the air (gas) velocity profiles at 0.125 m above the interface in line with the geometric focal point for all the meshes considered are given in the surface elevation time history plots shown in Figures 5.8. The velocity and pressure profiles in the liquid in line with the geometric focal point at -0.125 m are given in Figures 5.9a and 5.9b, respectively. In all cases, the data was extracted between 0 and 60 s. The portion from 45 to 60 s was sufficient for the mesh sensitivity analysis since in this region, the waves have repeatedly similar heights and steady state has been reached. The variations in velocity and pressure time histories for all mesh cases were compared and showed good agreement with the finest mesh case considered.

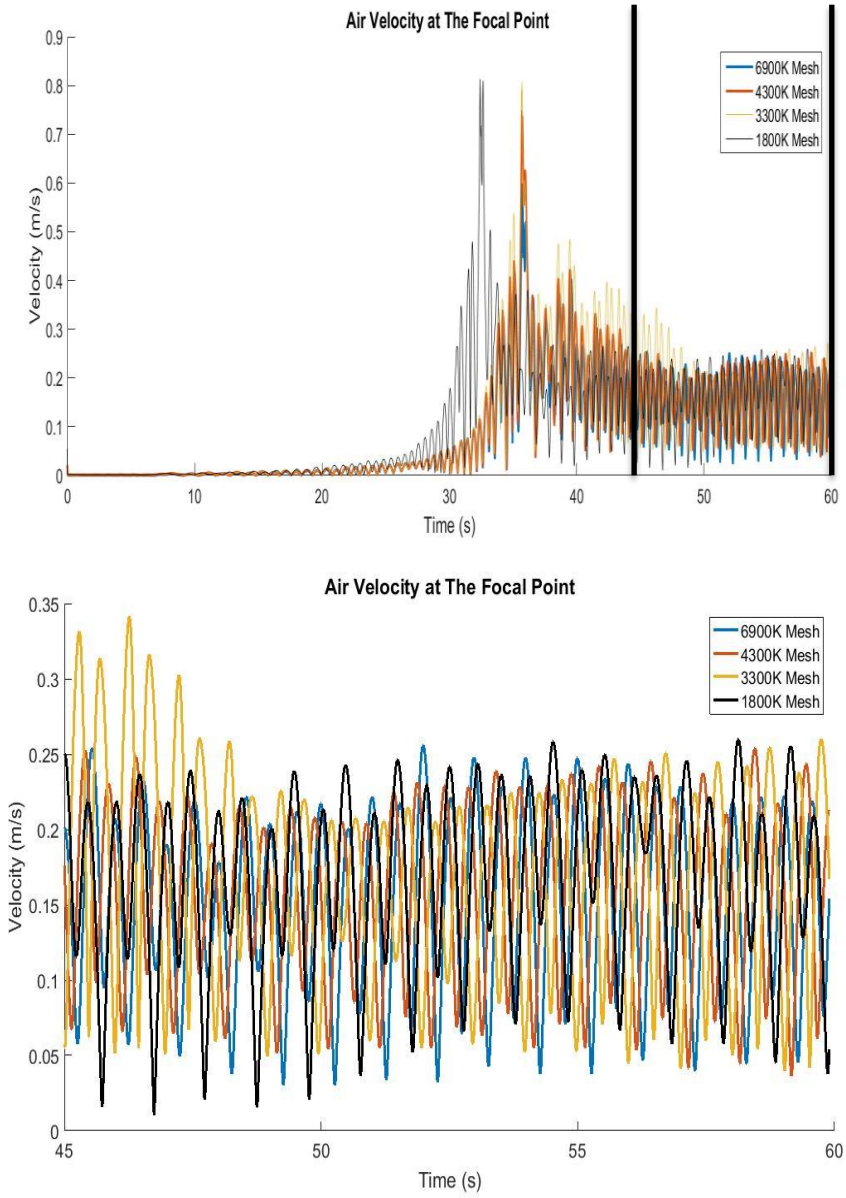


Fig. 5.8: Calculated air velocity time histories at the focal point from mesh sensitivity study

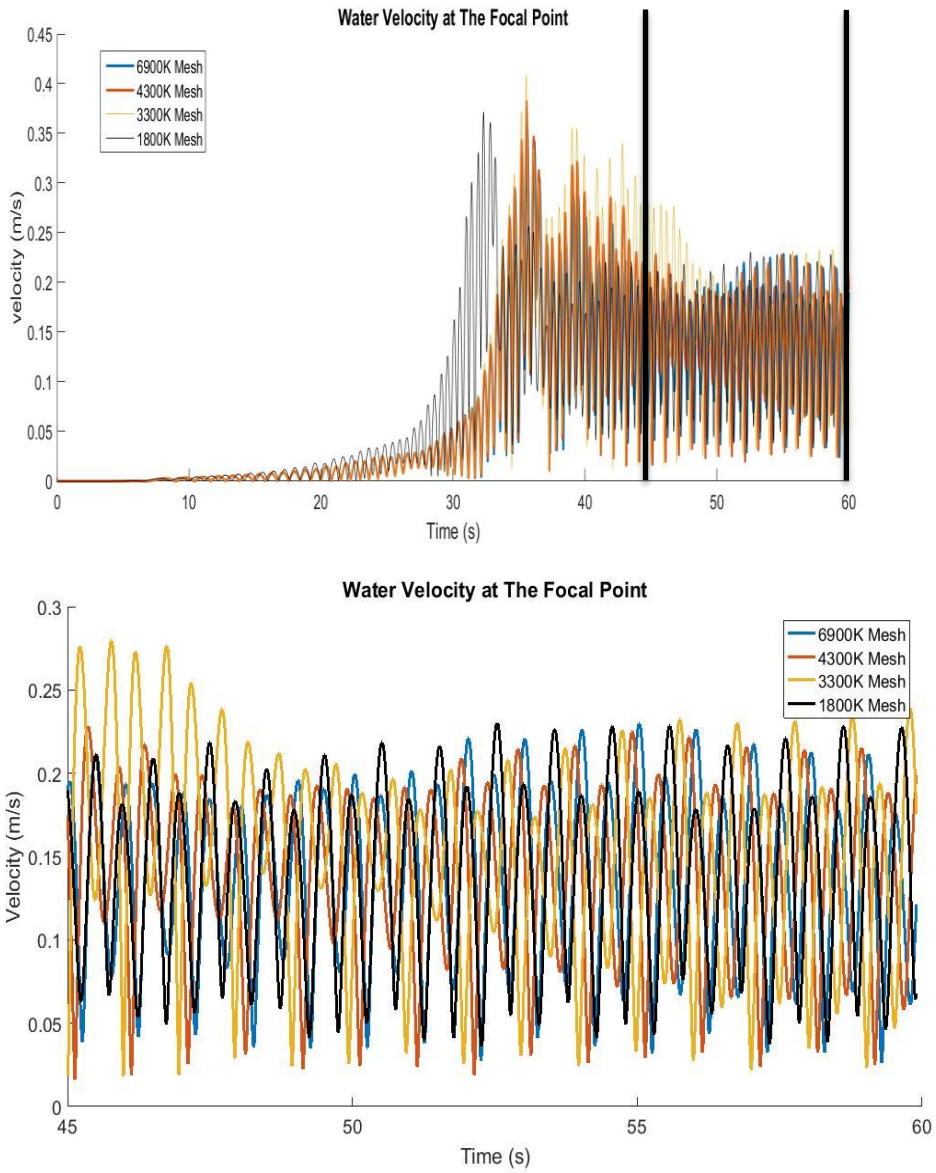


Fig. 5.9a: Calculated water velocity time histories at the focal point from mesh sensitivity study

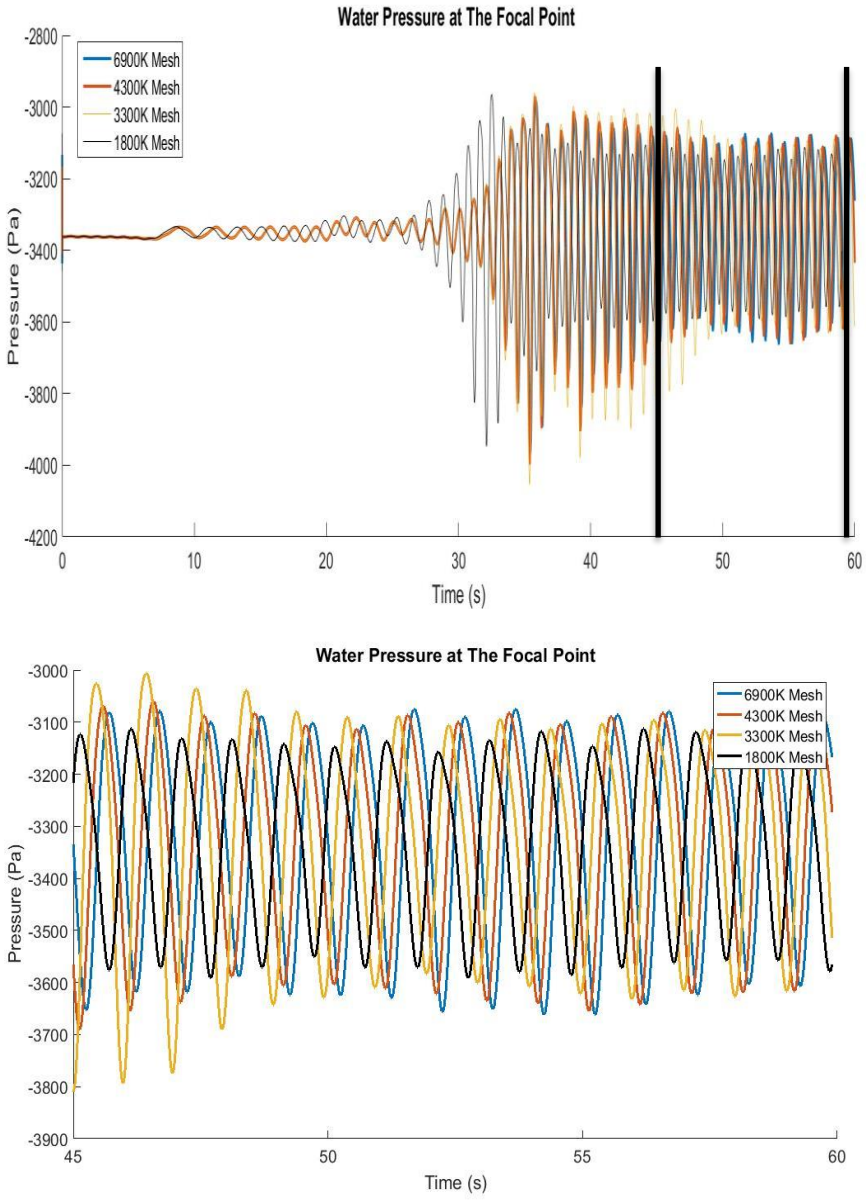


Fig. 5.9b: Calculated water pressure time histories at the focal point from mesh sensitivity study

The variables considered in the mesh sensitivity study for the parabola-1 model were: incident wave height, location of the amplification zone, wave height at the amplification zone, amplification factor and pressure and velocity components. A comparison of the predicted and experimental results is given in Table 5.3.

Table 5.3: Mesh sensitivity study results (P = pressure, V = velocity)

Number of elements	Incident wave height at 11 m (m)	Wave height at amp. zone (m)	Location of amp. zone (m)	Amp. factor	Root mean square for liquid at -0.125 m		Root mean square for gas at 0.125 m		Type of mesh and flow
					P RMS (Pa)	V RMS (m/s)	P RMS (Pa)	V RMS (m/s)	
Experiment	0.049	0.126	0.910	2.55	-	-	-	-	-
6900 k	0.052	0.121	0.807	2.32	3336.87	0.146	2762.50	0.164	Hexahedral structured / Laminar
4300 k	0.051	0.121	0.807	2.40	3335.70	0.149	2762.51	0.167	Hexahedral structured / Laminar
3300 k	0.050	0.129	0.807	2.56	3335.92	0.163	2762.53	0.183	Hexahedral structured / Laminar
1800 k	0.045	0.123	0.882	2.72	3331.18	0.148	2762.43	0.176	Hexahedral structured / Laminar

The full domain wave heights at 11 m and at the amplification zone for all the meshing cases are given in Figures 5.10 and 5.11, respectively. In all cases, the data was collected from 0 to 60 s. However, a window from 25 to 40 s was used for the sensitivity analysis of the wave heights at 11 m and a window from 40 to 60 s was used for the wave heights in the amplification zone as these were considered to represent steady state behaviour.

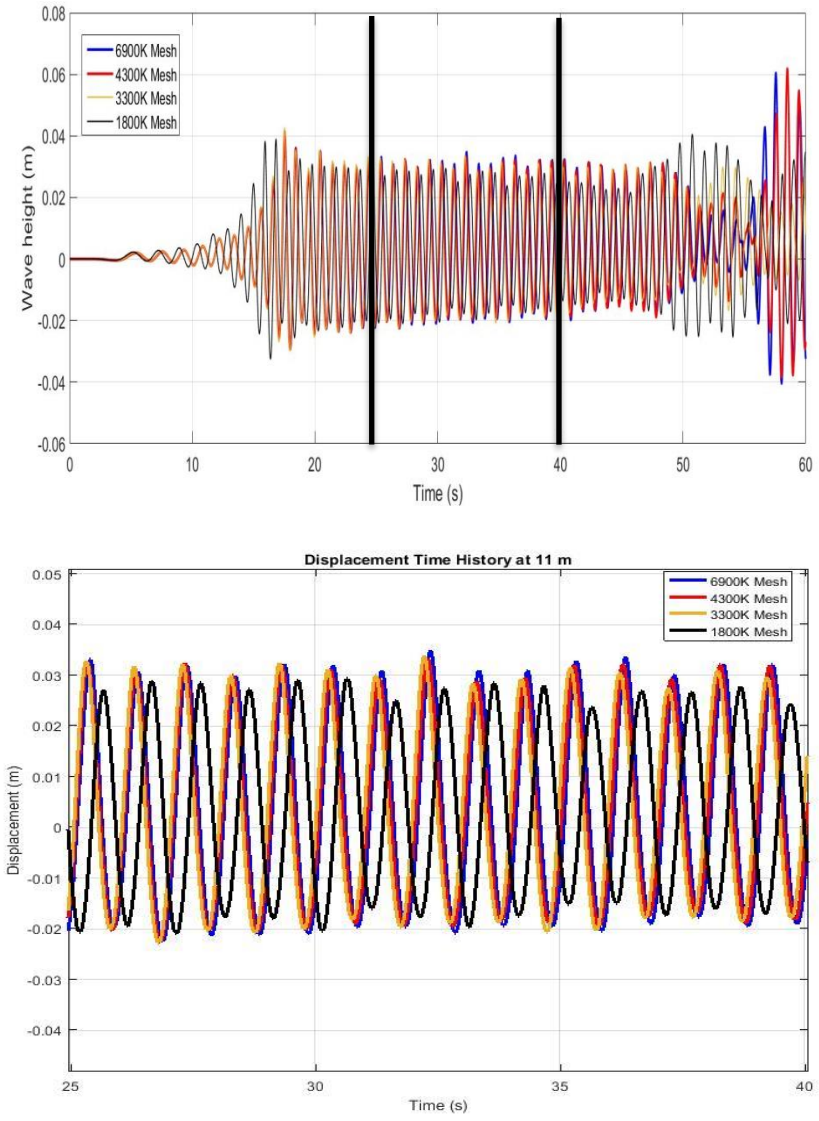


Fig. 5.10: Predictions of wave height at 11 m from mesh sensitivity study

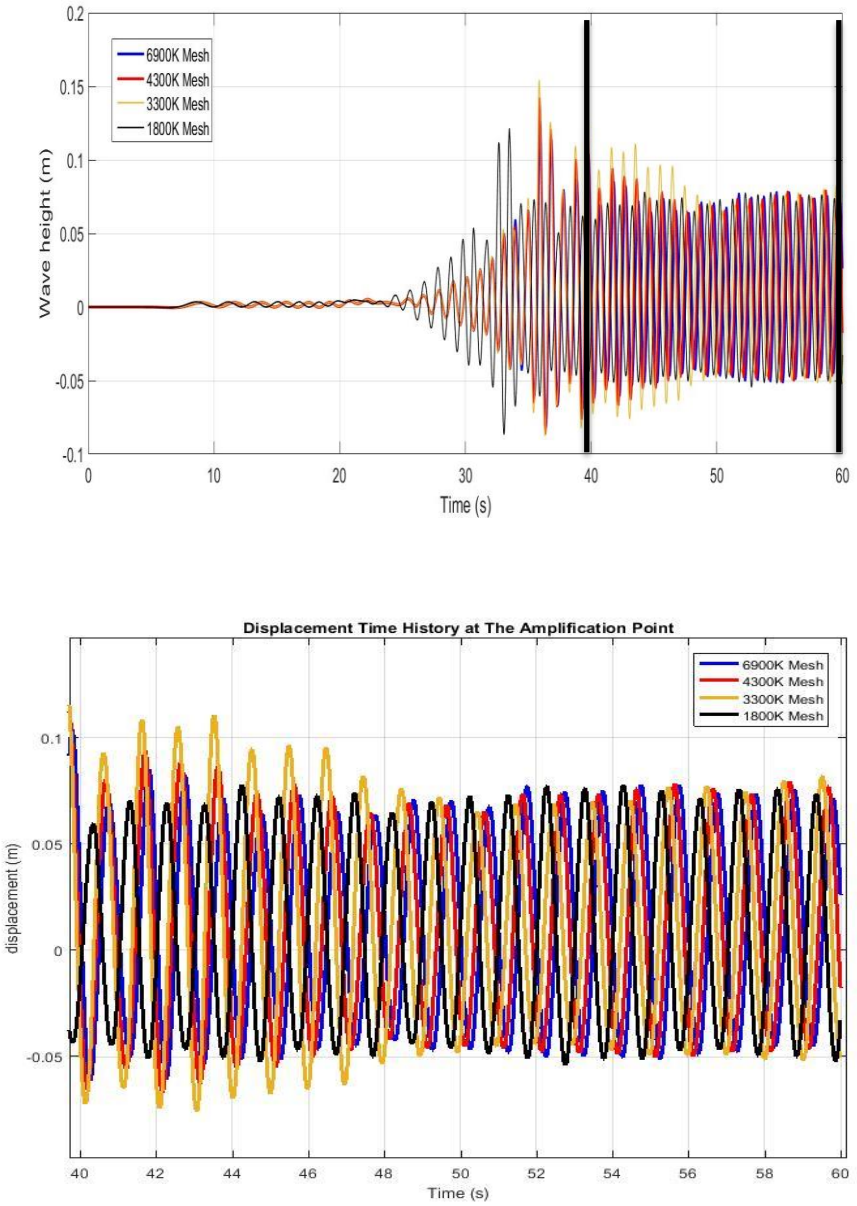


Fig. 5.11: Calculated wave height at amplification zone from mesh sensitivity study

The results of the CFD model indicated that at different time intervals, the wave amplification not only occurred at the geometric focal point but also at a series of locations along the parabola wall. The amplification zone was thus located within a 0.4 m window at different distances from the focal point. The peak wave height at each location was recorded and the average was taken to represent the wave height in the amplification zone. The locations of the amplification zones for each

mesh case are given in Table 5.3. The results were compared to the 6900 k mesh results to determine the percentage difference in the predictions for the key parameters of wave height at the amplification zone and incident wave height at 11m (see Table 5.4).

From Table 5.4, it is clear that the mesh with 4300 k cells gives the closest results to the 6900 k mesh in terms of wave heights at 11 m and in the amplification zone. The percentage differences were considered very small with respect to computational effort (see Table 5.2). The wave height time histories from the 4300 k mesh also showed very good agreement with the results from the 6900 k mesh, see Figures 5.13 and 5.14. Therefore, the 4300 k mesh was selected for further modelling and was utilised for validating the model against the experimental data.

Table 5.4: Percentage difference in wave height calculated during the mesh sensitivity study from the 6900 k mesh case

Number of Elements	Difference in Incident Wave Height (%)	Difference in Wave Height at the Amplification Zone (%)
6900 k	-	-
4300 k	2.62	6.55
3300 k	3.31	22.09
1800 k	13.85	7.41

5.4.5. Parabola CFD Model Validation

Data from the wave tank model with 4300 k cells was compared to the equivalent experimental data. The location and characteristics of the amplification zone within the parabola-1 structure were considered to be particularly important. Figures 5.12 and 5.13 show data for the wave heights at 11 m and in the amplification zone from the experiment and the CFD model, respectively. In both cases, the waves reached both

the probe at 11 m and the amplification zone probe at the same time (15 s and 35 s, respectively).

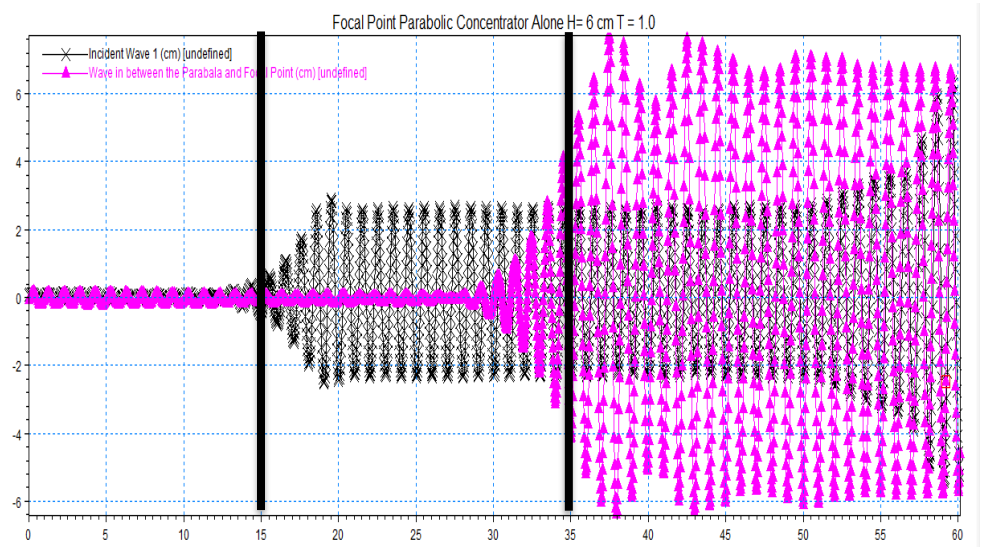


Fig. 5.12: Physical model wave height at 11m (black) and at amplification zone (pink)

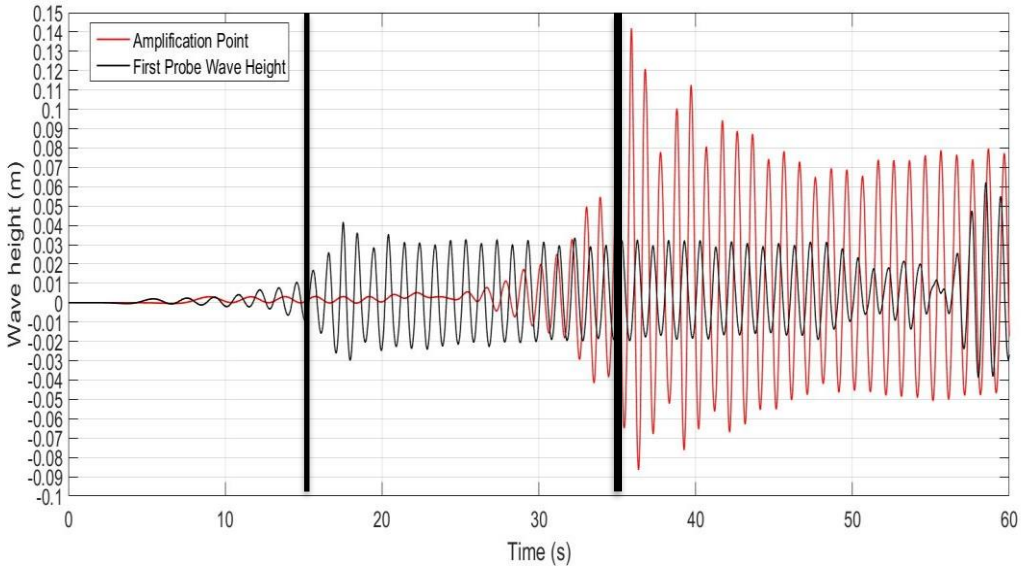


Fig. 5.13: 4300 k CFD model wave height at 11m (black) and at amplification zone (red)

During the experiments the surface water movement and wave elevations were detected using orange polystyrene beads scattered

around the area of interest and at various locations within the tank. The measured pressure at amplification zone in the CFD model can be translated to the height of the water level and so it can be translated to wave height. The comparison was conducted to highlight the location of the maximum amplification zone around the parabola. The beads were seen to rare fact in the region where wave heights are low and compress in the region where wave heights are high. As the wave height increases the pressure due to hydrostatic pressure increases. Therefore, validation of the CFD model was done by comparing top views of the pressure contours with photographs taken during the experimental testing of the wave tank surface seeded with the orange beads.

The CFD pressure contours are illustrated in Figure 5.14 for times between 45.0 and 45.9 s. The photographs in the same Figure were also taken during testing at time intervals between 45.0 and 45.9 s with H = 0.06 m and T = 1 s. It is clear from Figure 5.14 that the CFD predictions for the location of the maximum wave amplification zone (approximately in line with the ends of the parabola) is in good agreement with the experimental results. Looking at the photograph of the wave tank surface at t = 45.0 s, the beads are spread out in the regions where wave heights are low. This corresponds with the low pressure regions in the pressure contour plots in Figure 5.14 at t = 45.0 s. In addition, at t = 45.0 s the high pressure regions in red match the locations at which the wave heights are highest and where the beads are more closely spaced. Similar agreement was observed for almost all the time intervals from 45.0 to 45.9 s.

Furthermore, as seen in Table 5.3, the predicted wave height in the maximum amplification zone for T = 1.0 sec and H = 0.06 m was found to be equal to 0.121 m which is in good agreement with the value obtained experimentally i.e. 0.126 m (see Chapter 4). It was therefore concluded that the CFD model was capable of reproducing the salient flow features for the waves in a wave tank with a parabolic concentrator.

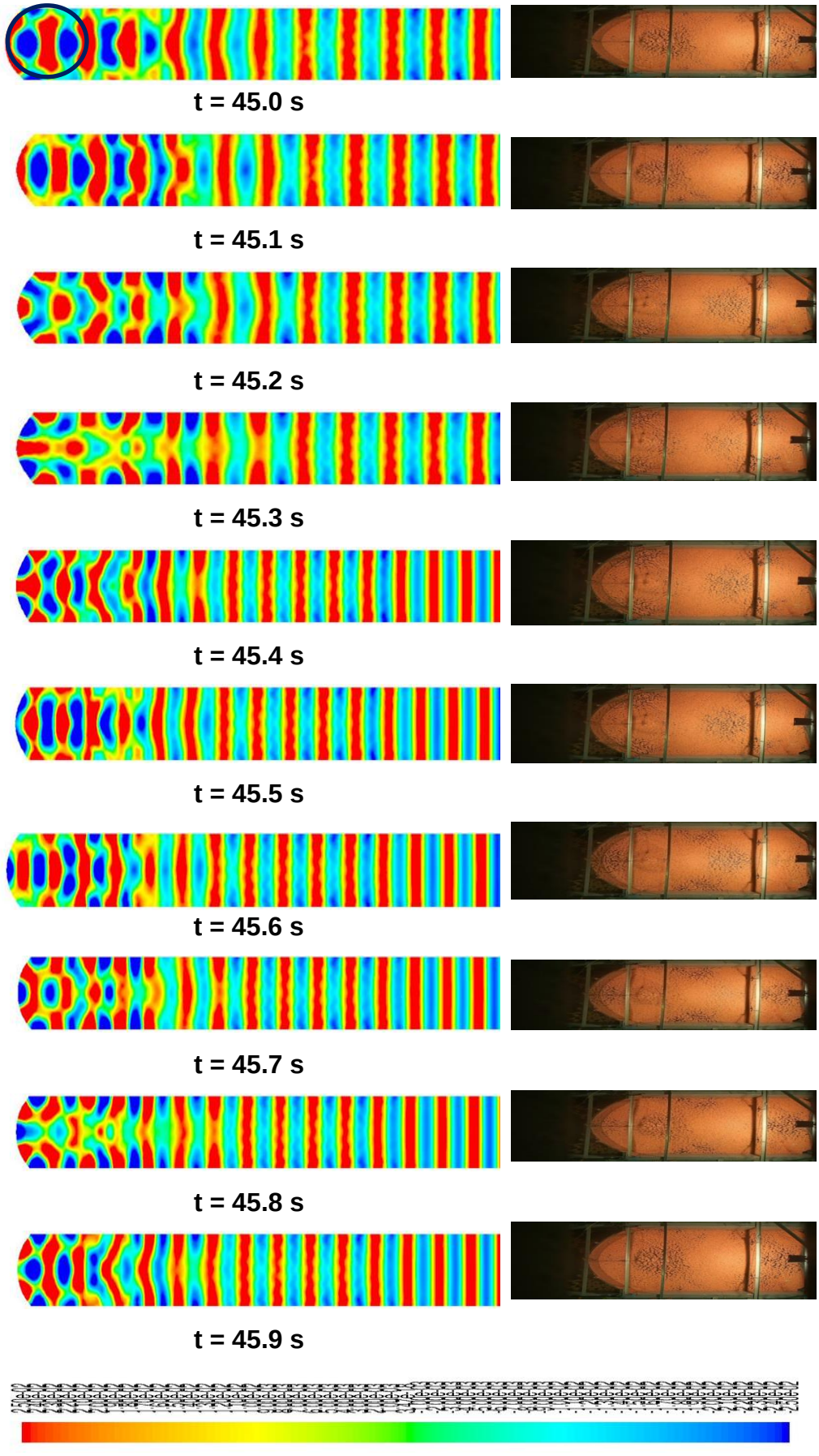


Fig. 5.14: CFD predictions for pressure contours in the wave tank

5.5. CFD Wave Tank Model with Buoy

The aim of the work presented in this section was to create a CFD model that would accurately represent the experimental setup with a parabolic concentrator and a buoy in a wave tank. The model was designed to calculate the forces acting on a stationary buoy.

This CFD model follows on logically from the model presented in the previous section and is based on the 4300 k cell mesh. In the model, a stationary buoy is placed in the amplification zone of the parabolic concentrator. This models the experimental condition where the buoy is not free to move but is present in the flume. Wall boundaries and a pressure inlet boundary were used to construct the computational domain.

The interaction between a linear wave and a tethered buoy placed in the amplification zone of the parabolic concentrator was investigated. The buoy structure was held in a fixed position to calculate the forces acting on it. In addition, the model was designed to represent deep water conditions; a water depth of 1.5 m was deemed sufficient as the buoy was stationary and no fluid velocities would be created beneath it.

5.5.1. Geometry Setup

The dimensions of a bi-cone ($60^o/120^o$) buoy with diameter 0.3125 m and draft 0.22 m are illustrated in Figure 5.15. The buoy was fixed in the CFD model at the location illustrated in the volume fraction contour plot in Figure 5.16.

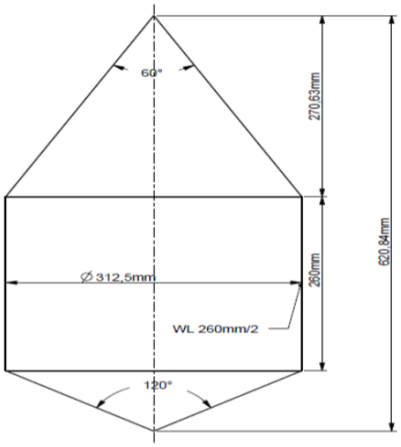


Fig. 5.15: Physical model bi-cone (60º/120º) buoy dimensions

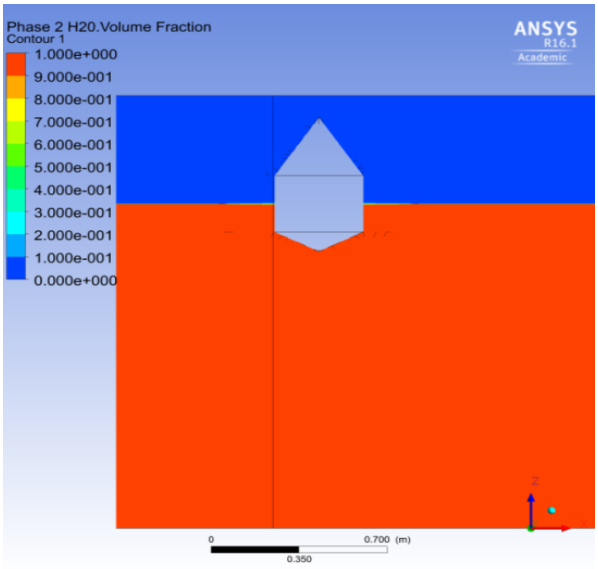


Fig. 5.16: CFD model bi-cone (60º/120º) buoy volume fraction contour plot

5.5.2. Boundary Conditions

At the buoy surface, a no-slip condition was used to ensure that the fluid velocity remained fixed at zero as the buoy was not moving.

5.5.3. Forces

A buoy placed in a fluid flow is subjected to forces from the surrounding fluid. The lift, drag and side forces were computed using the model for

the stationary buoy by integrating the pressure over the surface of the buoy with respect to the area. The results can be positive or negative, indicating the direction of the force. The lift force is related to the water lifting the buoy and acts in a direction that is perpendicular to the relative flow and in the direction of gravity (F_L in z-direction).The drag force quantifies the drag or resistance of the buoy and acts in the direction opposite to the relative flow (F_D in x-direction). The side force quantifies the forces acting on the buoy in a direction perpendicular to the flow direction (F_γ in y-direction) and assumed negligible for the static buoy.

5.5.4. Mesh

The 4300 k mesh for the air and water described in section 5.4.3 was used for this model. In order to incorporate the static buoy into the 4300 k model, it was necessary to add cells in the region around the buoy. An arbitrary tetrahedral mesh was added around the buoy to resolve the curvature of the buoy without the need for any high aspect ratio cells giving a total mesh size of 8 M cells. The new model is comprised of three main blocks where the middle block is the area with the buoy which contains a finer mesh with very large number of cells. Side and plan views of the wave tank with buoy mesh are shown in Figure 5.17.

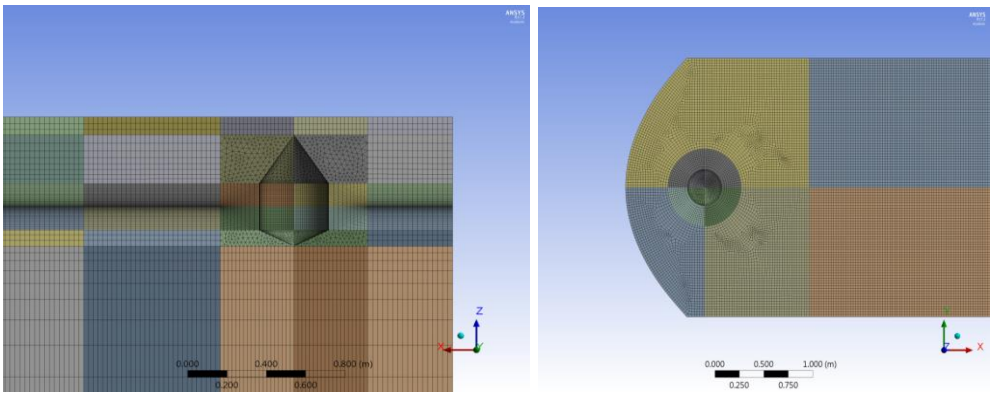


Fig. 5.17: Plan and side views of the wave tank with buoy mesh

A mesh sensitivity study was also conducted for the wave tank with buoy model. The aim was to obtain a fine enough grid to capture the geometry as the background mesh was already fine enough to capture the flow. Details of the two meshing cases considered containing 10 M and 8 M elements are compared in Table 5.5. The generated wave spectrum used for the comparison had a wave period of T = 1.0 sec and a wave height of H = 6 cm. The grid cell sizes used were either specified at the edges or for the body as a whole and are tabulated in Table 5.5. In addition, to ensure mesh uniformity, the mesh was graded between the coarse and fine areas. These grading factor for each mesh sensitivity case are also included in Table 5.5.

5.5.5. Results for Parabola-Static Buoy Mesh Sensitivity Study

The input parameters for the meshing cases containing 10 M and 8 M cells are given in Table 5.5. The variables considered in the mesh sensitivity study of the wave tank with buoy were the lift and drag forces.

Table 5.5: Outline of all input parameters in the mesh sensitivity study for the wave tank model with buoy

Number of elements	Number of mesh layers near interface region	Body grid cell size (m)	Edge grid cell size (m)	Mesh to cell size ratio
8 M	30	0.025	0.02	5
10 M	40	0.025	0.025	5

The results from the mesh sensitivity cases for the key outputs of lift and drag force are compared in Figures 5.18a and 5.18b, respectively. The graphs show that there is very good agreement between the data from the two models. The starting and ending times for data acquisition were 0 and 60s, respectively, and a window from 40 to 60 s was deemed sufficient for the comparison of the two models as the

magnitude of the forces over this period were reasonably regular. The drag and lift force magnitudes for the 8 M and 10 M mesh cases are given in Table 5.6. An explanation of the negative drag forces is given in section 5.6. In both cases, the difference in the results is approximately 1% and thus the mesh with 8 M cells was judged to be acceptable and was selected for further modelling and to validate the CFD parabola-buoy model against experimental data.

Table 5.6: Drag and lift forces in the mesh sensitivity study for the wave tank model with buoy

Number of elements	Mean drag force (N)	Mean lift force (N)	Difference in drag force (%)	Difference in lift force (%)
8M	-2.564	158.030	0.97	1
10M	-2.633	158.016	-	-

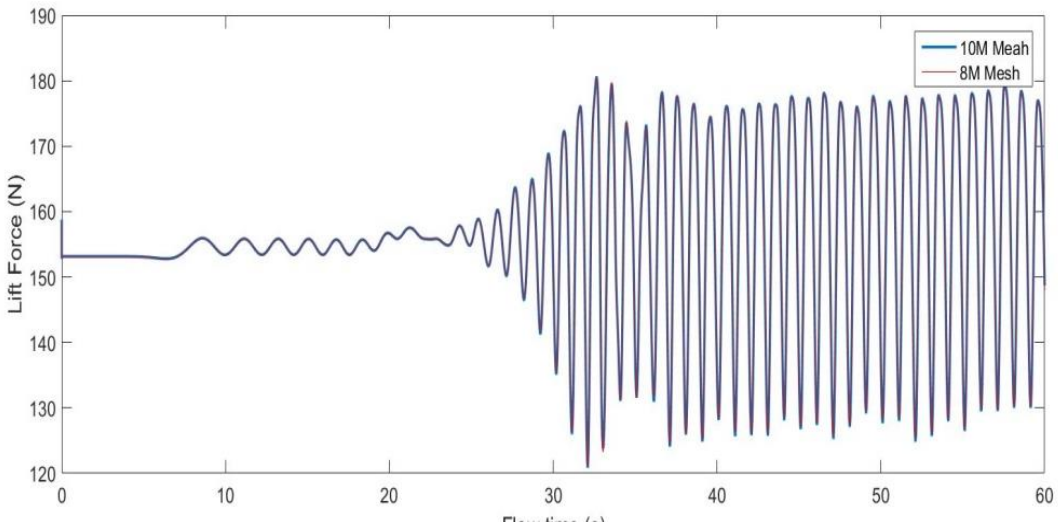


Fig. 5.18a: Calculated lift force from models with 8 M and 10 M cells

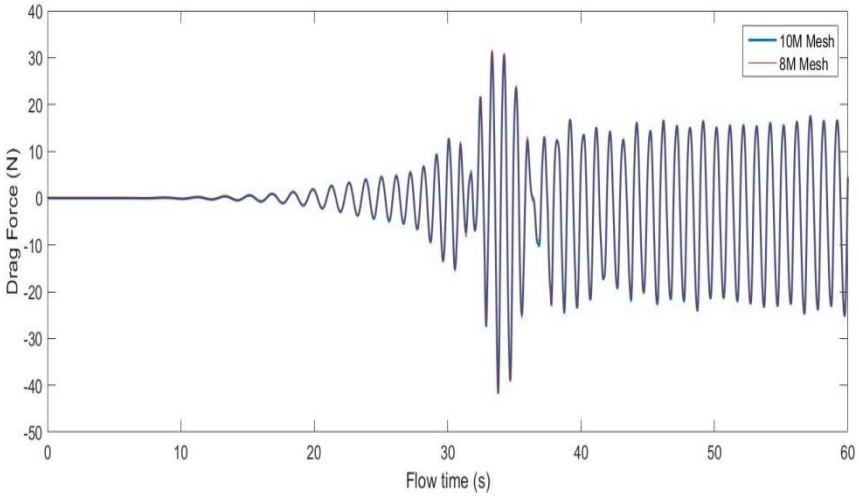


Fig. 5.18b: Calculated drag force from models with 8 M and 10 M cells

5.6. CFD Results for Static Buoy

Data from the static buoy model with 8 M cells was used to analyse the dynamic response of the waves and to investigate the wave-buoy interaction. The full time histories for the wave height around the buoy in the amplification zone and the forces acting on the buoy are given in Figures 5.19a and 5.19b, respectively. During the experiments in chapter 4 there were no waves at the wave probe location but the wave maker was generating waves at time from 0 to 15 s. The waves reached the wave probe and continued to grow at time from 15 to 25 s. To analyse the data, a window from 48 to 52 s was used as this corresponded to steady state response, see Figures 5.23a and 5.23b for the wave height and force data, respectively. A full wave cycle was also taken from Figures 5.20a and 5.20b for more detailed analysis.

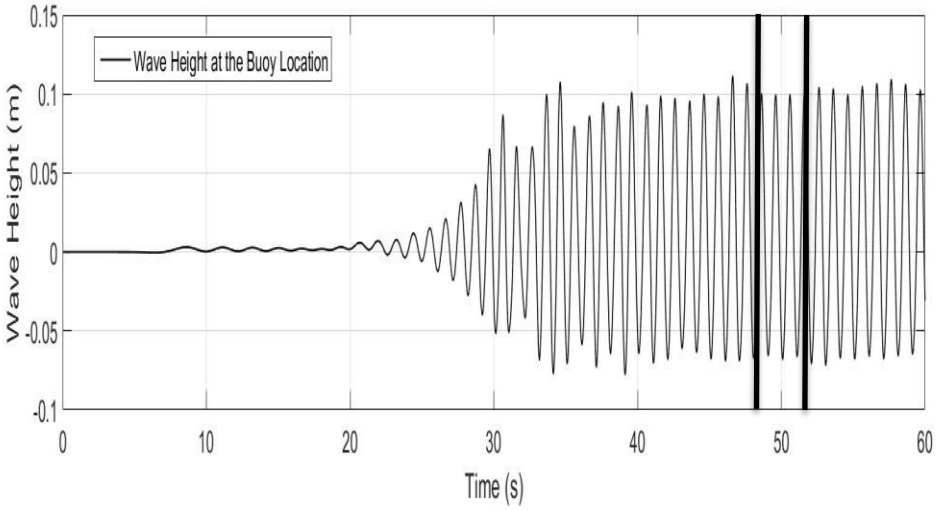


Fig. 5.19a: CFD predictions for wave height at amplification zone

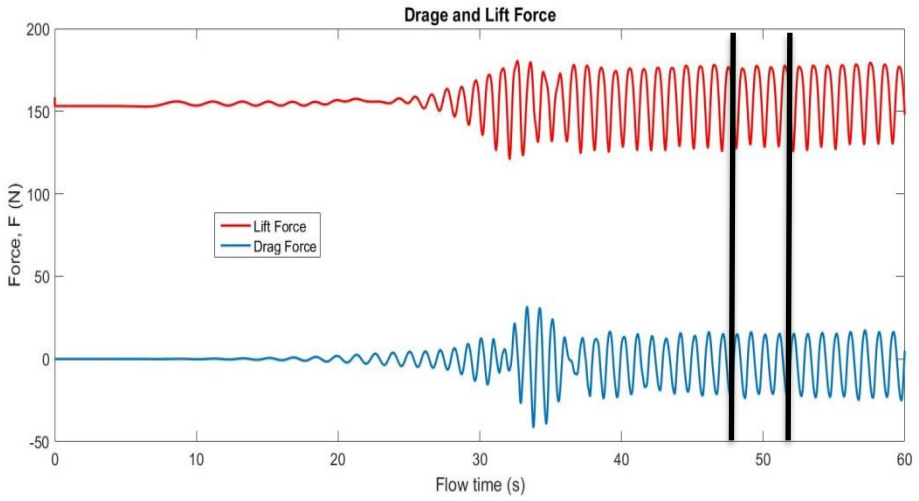


Fig. 5.19b: CFD predictions for lift and drag forces

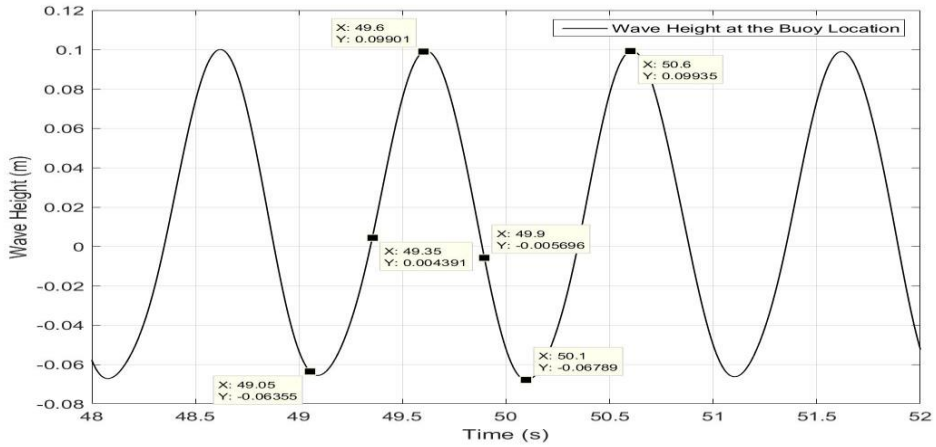


Fig. 5.20a: Wave height at amplification zone from t = 48 to t = 52 s

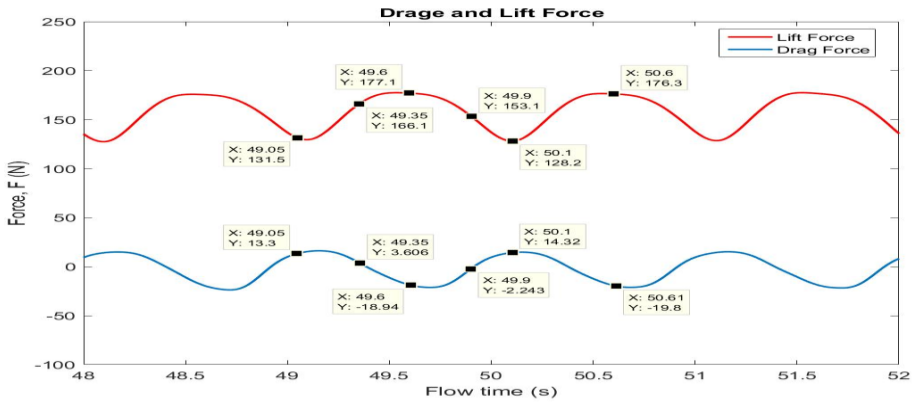


Fig. 5.20b: Lift and drag force from t = 48 to t = 52 s

A comparison of the wave height in the vicinity of the buoy and the forces acting on the buoy was conducted by looking at the data corresponding to times of t = 49.05, 49.35, 49.60, 49.90, 50.10, and 50.61 s. It can be seen in Figures 5.20a and 5.20b, that at the wave trough, the lift force is at its minimum and the drag force is at its maximum. In contrast, at the wave peak, the lift force is at its maximum and the drag force is at its minimum. The same behaviour is repeated during each full wave cycle. The wave dynamics around the buoy are investigated further in section 5.6.

The model results for the pressure and shear stress on the surface of the buoy are illustrated in the contour plots in Figure 5.21. It can be seen that the shear stress on the surface is negligible compared to the pressure. Therefore, the drag and lift effects on the buoy are caused largely by the pressure on the buoy surface in the wave–buoy interaction analysis.

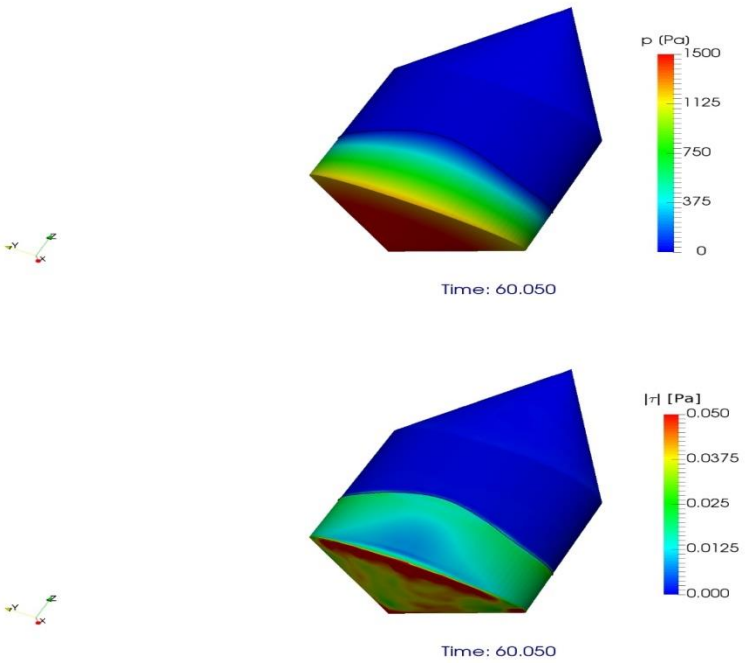


Fig. 5.21: Pressure and shear stress contours for the static bi-cone (60º/120º) buoy

In order to gain a thorough understanding of the wave–static buoy interactions, the wave behaviour around the buoy and the pressure on the buoy's surface were examined over a period of one full wave cycle for the locations highlighted in Figure 5.20a. The responses at times of t = 49.05, 49.35, 49.60, 49.90 and 50.10 s and the three dimensional (3D) contours of the wave tank are given in Figures 5.22a-b, 5.23a-b, 5.24a-b, 5.25a-b and 5.26a-b, respectively. In each figure, the lift and drag forces acting on the buoy are illustrated by the pressure arrows where the right side of the buoy faces the waves coming from the inlet side (wave maker) and the left side of the buoy faces the waves coming from the parabola side. In addition, interface and plane surface visualisation of the velocity field is generated by a technique known as Line integral convolution (LIC) (Cabral and Leedom, 1993). LIC represents a method for imaging 2D and 3D vector fields. The algorithm filters an input image along local stream lines defined by an input vector field and generates an output image. The one dimensional filter shape

is independent of either input and can be arbitrary. To indicate directional flow of the vector field a whole family of continuous motion filters is used to give apparent motion in the direction of the vector field. LIC together with instantaneous vector plots show the nature of the flow field and flow structures like re-circulations. These are given in Figures 5.22c, 5.23c, 5.24c, 5.25c, and 5.26c for the same time points.

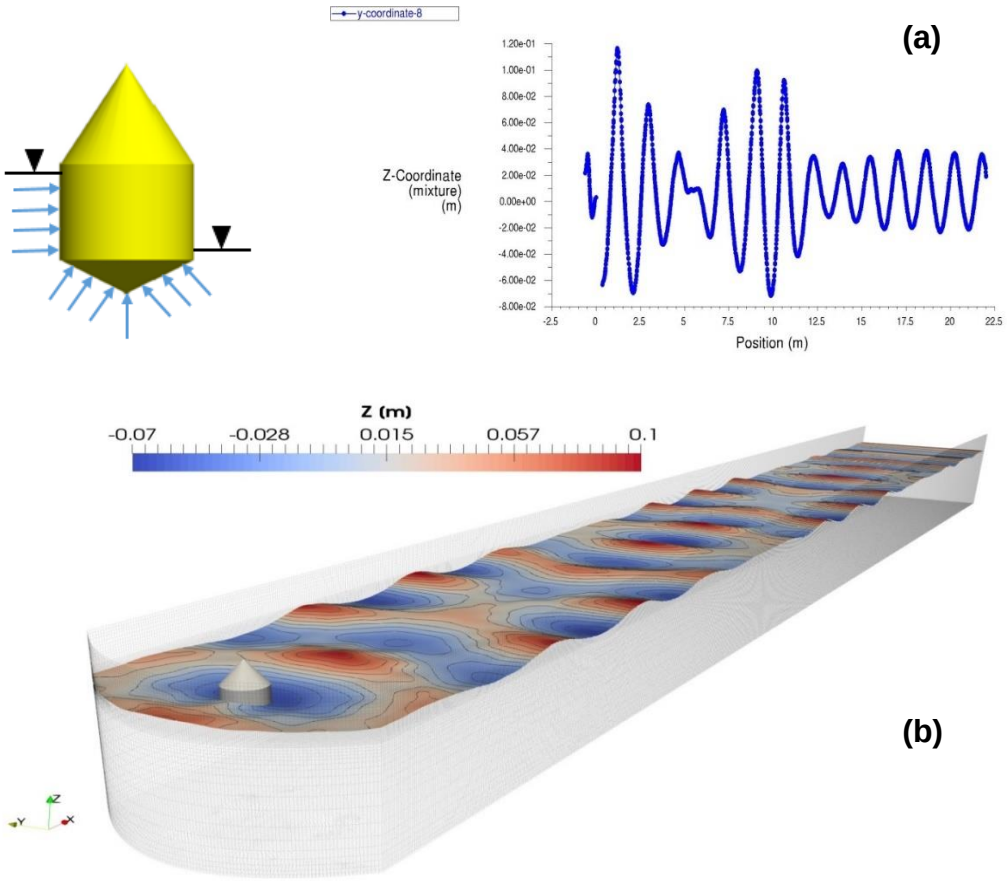


Fig. 5.22a-b: (a) Wave-buoy interaction response (b) 3D wave tank contours at t = 49.05 s

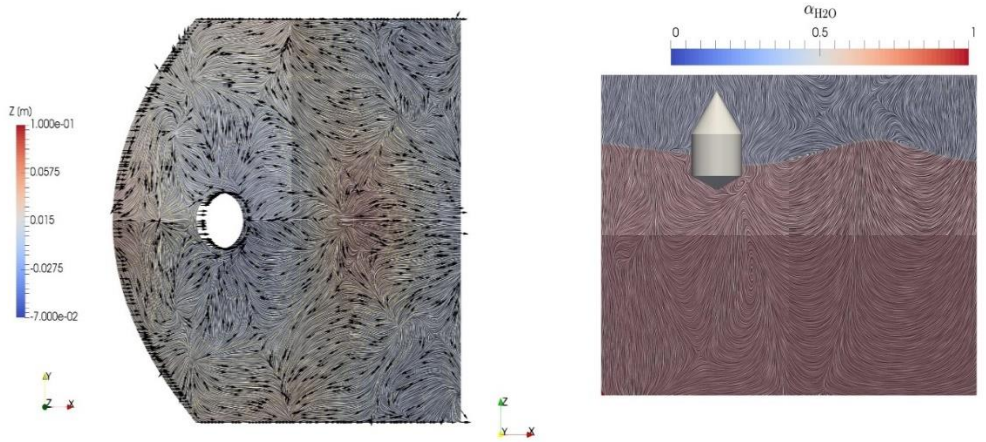


Fig. 5.22c: Wave- buoy vectors of interface velocity field (left). LIC visualization of the velocity field, coloured by the volume fraction of water on a vertical plane in the middle of the domain (right) at t=49.05 s

In Figure 5.22a-b at t = 49.05 s, the wave heights on the z-coordinate (mixture) in Figure 5.22a from the concentrator side are much larger than the wave heights from the inlet side. The large drag force on the buoy acts in the direction opposite to the wave flow. The lift force is controlled by the wave height in the amplification zone. When the wave height is at its maximum, the pressure is also at its maximum giving the highest lift force. At t = 49.05 s the wave height is very low and hence a very low lift force is generated by the water at this time. Furthermore, the 3D wave tank contours in the same Figure show the wave motion along the length of the wave tank and the different wave heights around the parabola-buoy system.

The interface LIC vector contours in Figure 5.22c show the wave motions around the buoy and their interaction with the buoy.

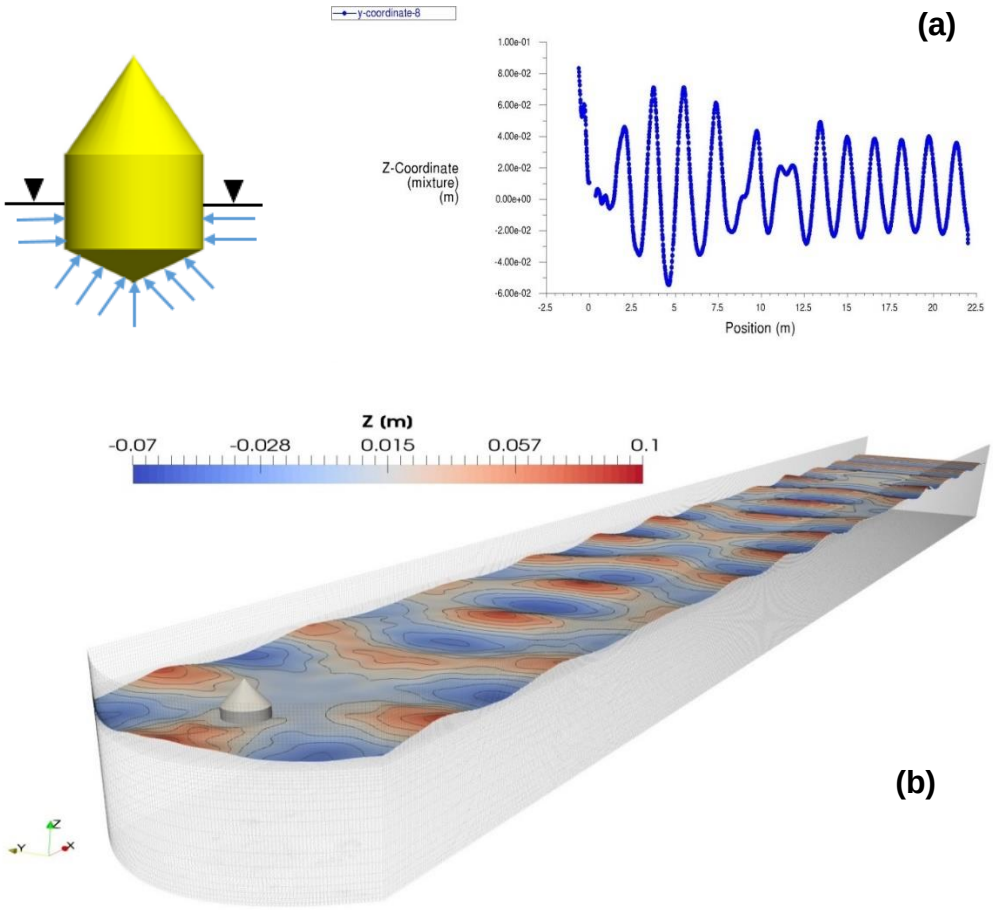


Fig. 5.23a-b: (a) Wave-buoy interaction response (b) 3D wave tank contours at t = 49.35 s

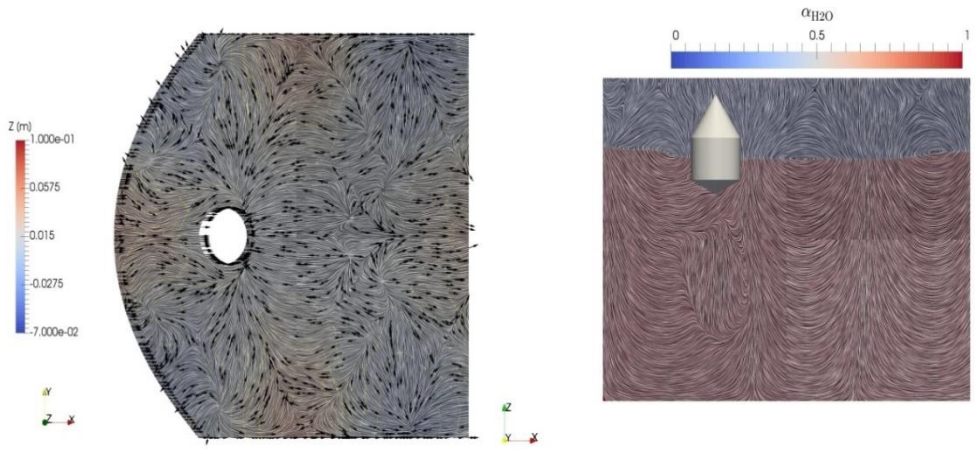
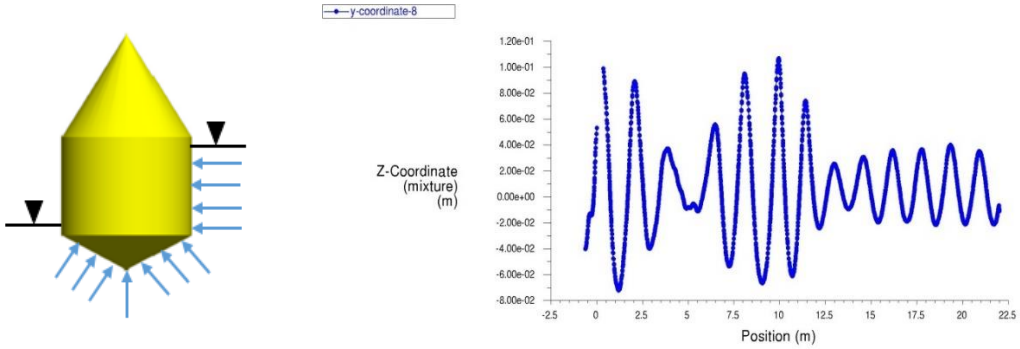


Fig. 5.23c: Wave- buoy vectors of interface velocity field (left). LIC visualization of the velocity field, coloured by the volume fraction of water on a vertical plane in the middle of the domain (right) at t = 49.35 s

In Figure 5.23a-b at t = 49.35 s, the wave heights from the concentrator side are equal to the wave heights from the inlet side. Therefore, the drag or resistance forces on the buoy cancel giving a net drag of zero. No lift is generated on the buoy as it is at the equilibrium position. The 3D wave tank contour plot in the same Figure shows the wave motion along the wave tank and the different wave heights around the parabola-buoy system. The interface LIC vector contours in Figure 5.23c show the wave motion as it interacts with the buoy at t = 49.35 s.

(a)



(b)

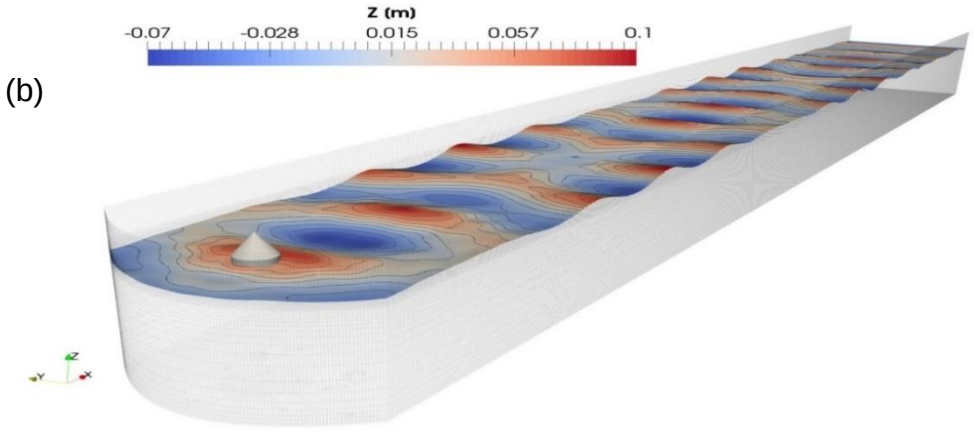


Fig. 5.24a-b: (a) Wave-buoy interaction response (b) 3D wave tank contours at t = 49.60 s

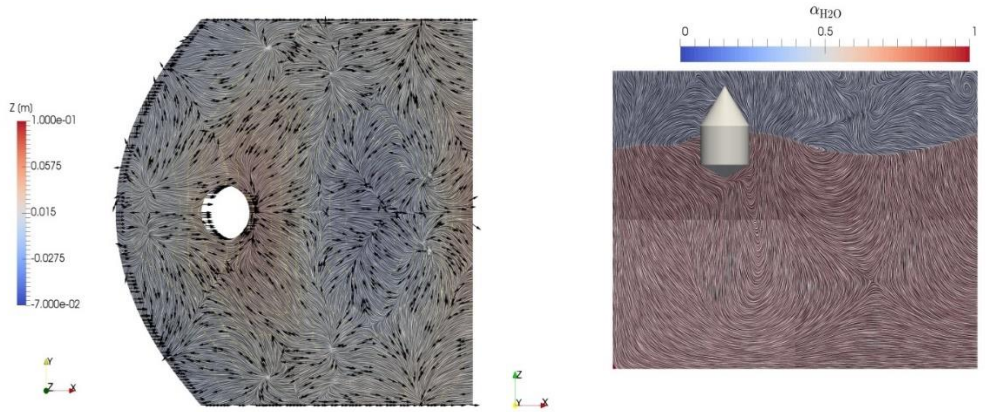


Fig. 5.24c: Wave- buoy interface vectors of interface velocity field (left). LIC visualization of the velocity field, coloured by the volume fraction of water on a vertical plane in the middle of the domain (right) at = 49.60 s

In Figure 5.24a-b at t = 49.60s, the opposite behaviour to that at t = 49.05 s is observed. The wave heights from the concentrator side are much lower than the wave heights from the inlet side. As the drag or resistance of the buoy acts in a direction that is opposite to the wave flow, the drag value is negative as seen in Figure 5.22b. At this point, the lift force is at its maximum as the wave height is at its maximum due to the waves coming from the wave maker. Furthermore, the 3D wave tank contour in Figure 5.24a-b shows the wave motion along the length of the wave tank and the different wave heights around the parabola-buoy system.

The interface LIC vector contours in Figure 5.24c show the wave motions around the buoy and their interaction with the buoy.The wave-buoy interactions at time points t = 49.05 s, and t = 49.35 s are the same as at t = 49.90 s and t = 50.10 s, respectively, and hence the same concepts discussed above apply to Figures 5.25-a, b, c and 5.26-a, b, c.

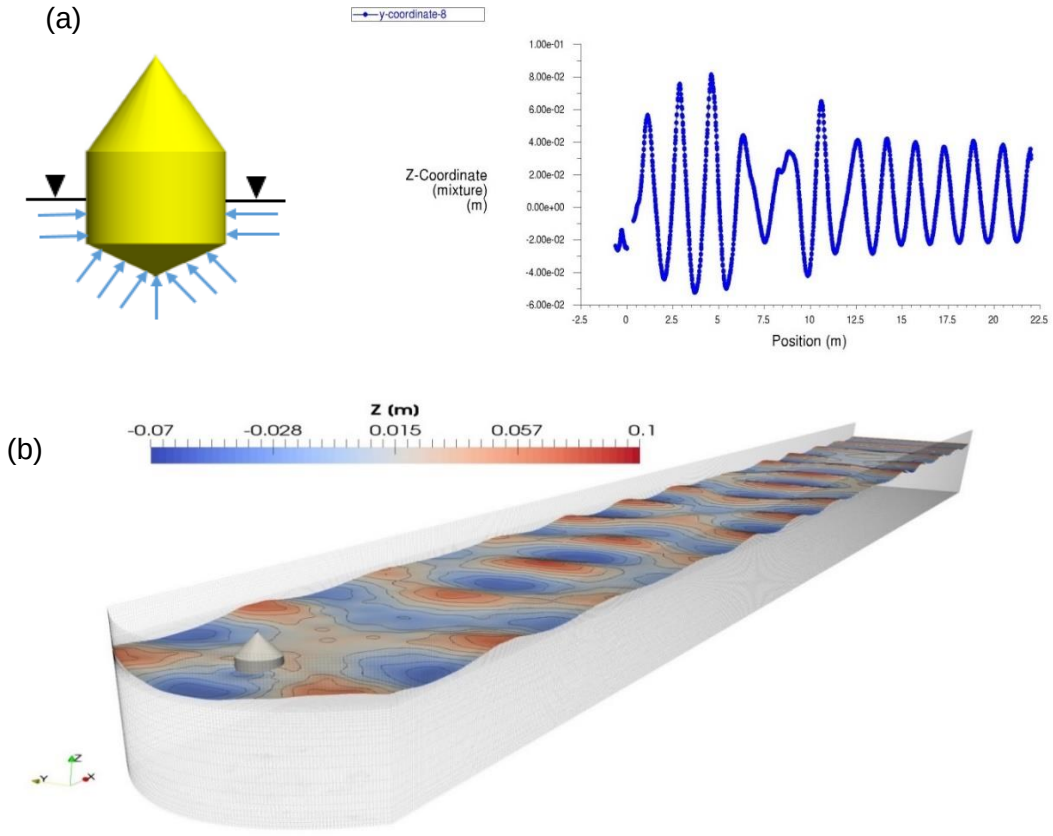


Fig. 5.25a-b: (a) Wave-buoy interaction response (b) 3D wave tank contours at t = 49.90 s

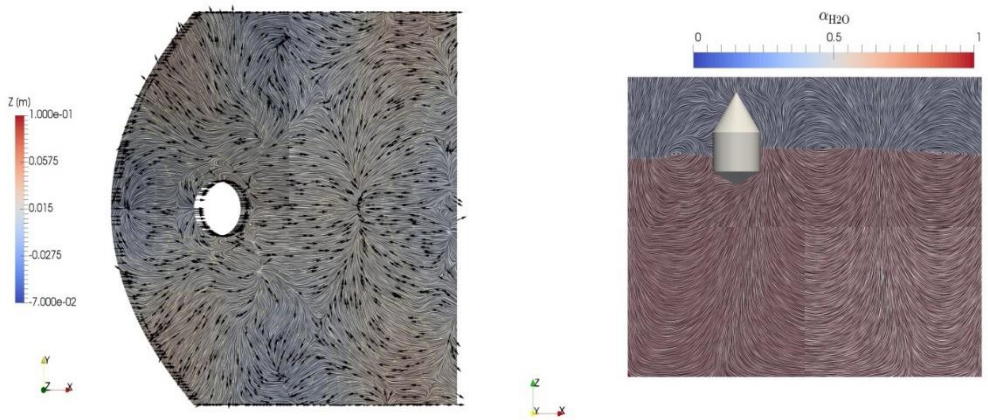


Fig. 5.25c: Wave- buoy interface vectors of interface velocity field (left). LIC visualization of the velocity field, coloured by the volume fraction of water on a vertical plane in the middle of the domain (right) at = 49.90 s

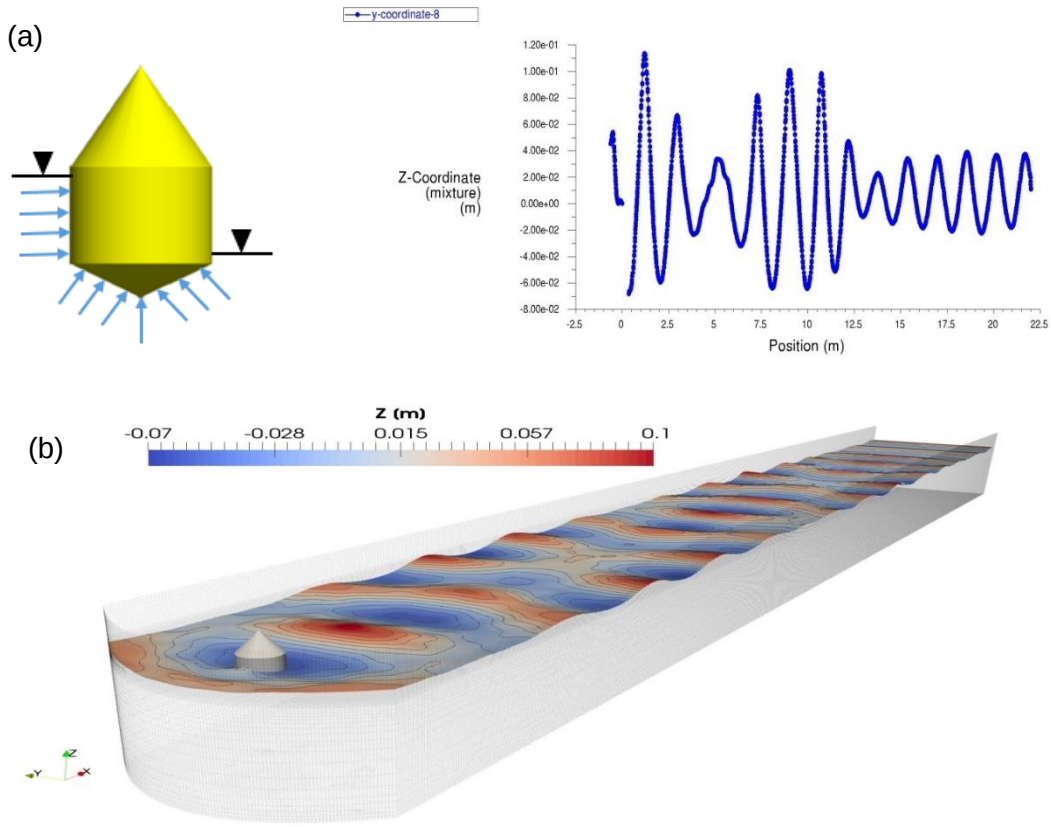


Fig. 5.26a-b: (a) Wave-buoy interaction response (b) 3D wave tank contours at t = 50.1 s

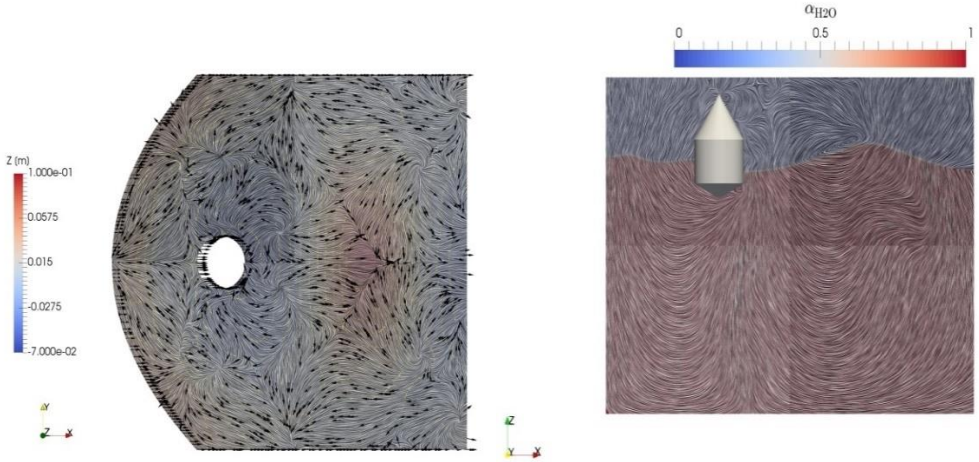


Fig. 5.26c: Wave- buoy interface vectors of interface velocity field (left). LIC visualization of the velocity field, coloured by the volume fraction of water on a vertical plane in the middle of the domain (right) at t = 50.1 s

The side view velocity contour plot of the wave tank in Figure 5.27 shows the wave velocity around the buoy which was impossible to visualise during the experimental testing. This type of data reveals the benefits of using CFD to develop a detailed understanding of the wave behaviour around a buoy.

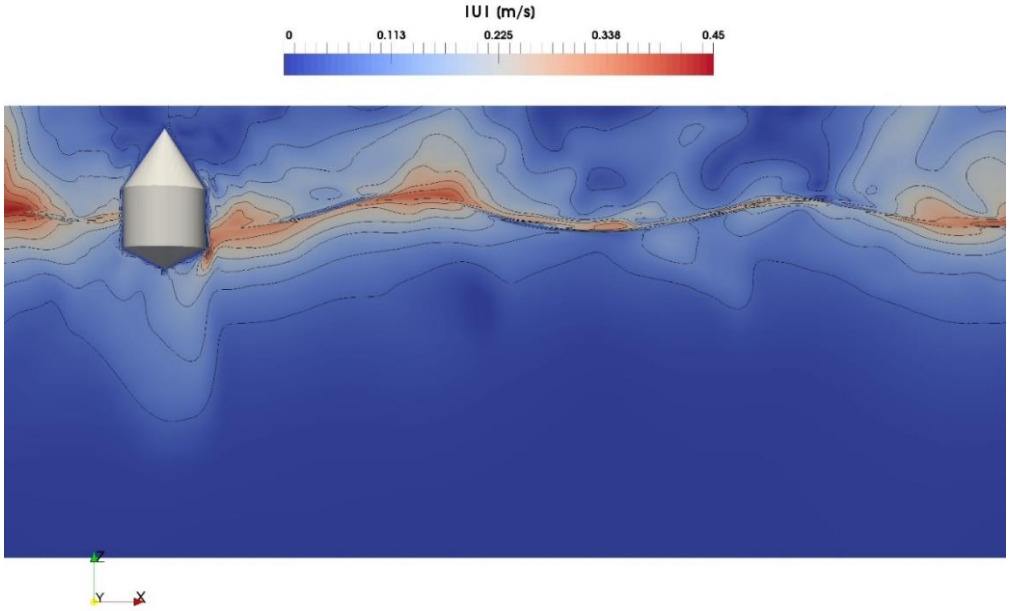


Fig. 5.27: velocity contour of y-plane wave tank with buoy

5.7. Future CFD Modelling

The CFD model of the static buoy in the wave tank offered a very good understanding of the wave dynamics in the tank and the interaction of the waves with the static buoy. It also provided a means of determining the lift and drag forces acting on the buoy as a function of time. The next challenge would be to develop a CFD model with a buoy in heave motion to understand the dynamic behaviour of the buoy. In order to achieve this, a separate dynamic model of the buoy needs to be developed that can be used to calculate the buoy's displacement in response to the forces predicted by the CFD model.

The main challenges lie in the mesh development and the re-meshing required once the buoy is moving. The snapshots obtained during the

experimental testing of the buoy in heave motion could be used as a basis for the model development. These are shown in Figure 5.28.

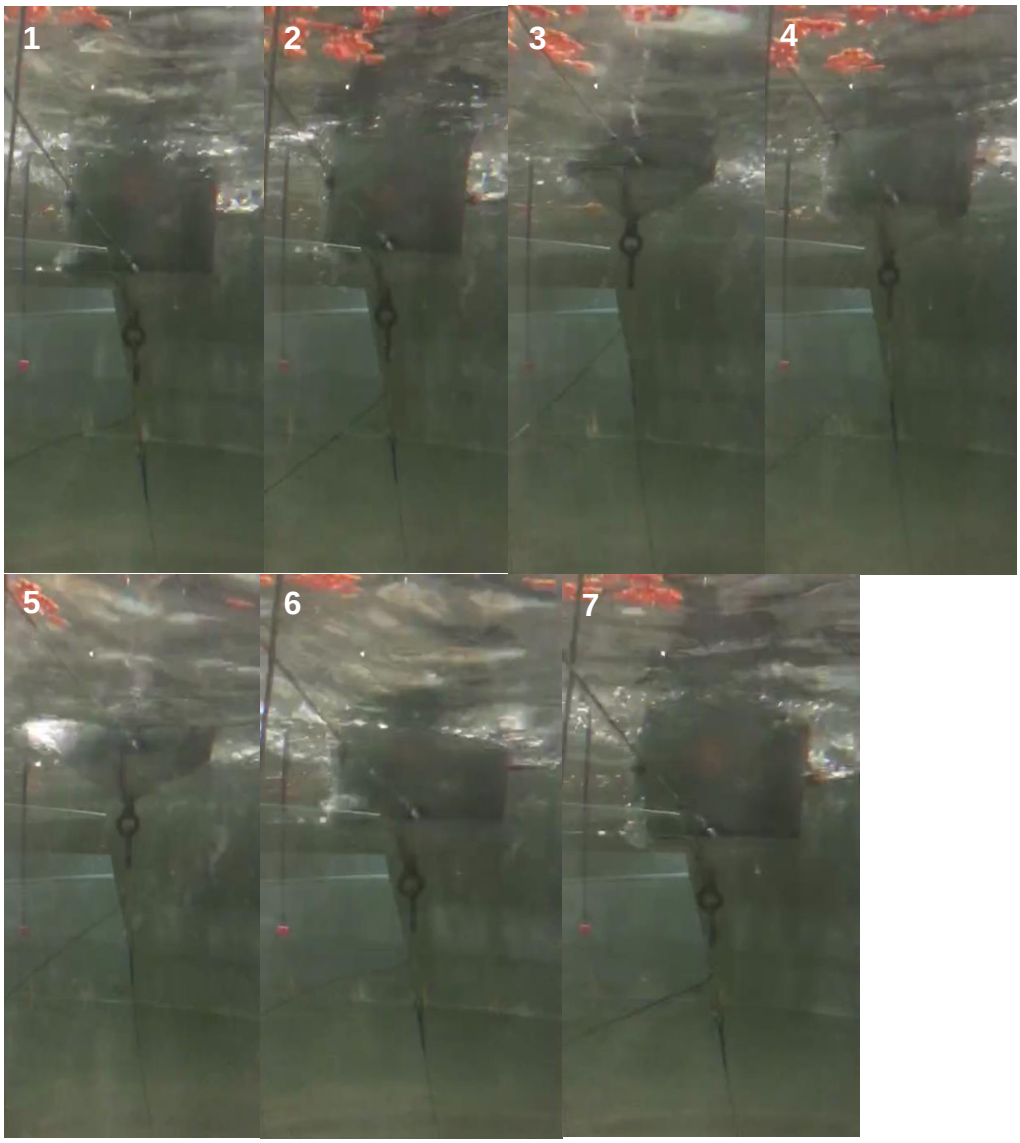


Fig. 5.28: Buoy motion in heave during stage-2 experimental testing

Moving body simulations using an overset mesh CFD framework together with a rigid body dynamics model are becoming commonplace in marine dynamics applications. The overset composite grid consists of several overlapping grids that form a complete mesh system (Koomullil et al., 2008). This makes the grid generation less labour-intensive, and

the grid movements can be independently modelled for the individual mesh. Appropriate algorithms are used to remove the mesh points outside the domain of interest and to find the regions where the flow variables need to be interpolated from other meshes. During the time integration of the governing equations, appropriate information is transferred between different meshes for an accurate simulation. As one or more of the components move relative to each other, the meshes associated with them also move rigidly along with the body. The use of overset meshes makes the flow simulation process more efficient and allows mesh motion without deformation or re-meshing. The overset framework and the six degree of freedom rigid body dynamics simulators were developed by Koomullil et al., (2008) in a library form for easy incorporation into existing flow solvers. These methods offer a possible approach to the CFD modelling of wave-buoy interactions and are recommended as an area of future research.

5.8. Conclusions

The CFD study in this chapter identified how an acceptable CFD model should be formulated and highlighted the sensitivity of the results to meshing and modelling parameters. Conventional CFD using the VOF method has been shown to be an effective approach for modelling the behaviour of a static buoy in a wave tank. The CFD model offered a very good understanding of the wave dynamics in the tank and the interaction of the waves with the static buoy. It also provided means of determining the lift and drag forces acting on the buoy as a function of time.

The CFD study identified how an acceptable CFD model should be formulated and highlighted the sensitivity of the results to meshing and modelling parameters.

As it is necessary to resolve the interface region using a fine mesh, the transient computations are not particularly rapid. However, the results obtained from the model of the wave tank without the buoy compared

well with the available experimental data, replicating the behaviour of the waves in KISR's parabolic concentrator wave tank well.

There is potential for the future application of CFD to model a moving buoy in waves. However, utilising the model to examine vertical heave motion and simulating wave-buoy interactions would require the addition of fluid-structure interactions in the model which was behind the scope of this study. With such a model, it would be possible to predict the forces acting on the buoy and expand the results to examine the buoy's heave motion response in different wave conditions.

A thorough understanding of buoy response within a wave tank could be achieved using CFD which could help lead design modifications to improve the performance of WEC devices.

Chapter 6: Conclusions and Further Research

In this thesis, several design aspects of a parabolic concentrator breakwater and a single heaving point absorber (buoy) have been investigated. The performance of the point absorber device was optimised, taking into account geometrical parameters that define the structure of the buoy and control parameters related to the PTO damping mechanism. In this chapter, the most important findings are emphasised and areas for possible future research are suggested.

6.1. Main Achievements

A comprehensive review of the historical development and current state of the art regarding breakwater technology has been conducted. The results indicated that a floating breakwater would be appropriate for combining with wave energy conversion technology for use in the Kuwaiti near shore marine environment. A point absorber device was identified as being the most suitable and a bi-cone ($60^o/120^o$) buoy shape was proposed. The need for increasing the energy density was highlighted and a parabolic concentrator for use in combination with the point absorber was designed for this purpose. This is the first time such a combination has been suggested.

To increase wave device efficiency while minimising energy production costs, a new approach for optimising the geometry and performance of a point absorber was proposed. A steady-state harmonic model was developed to simulate the motion of a single buoy with one degree of freedom (heave) along the vertical axis to optimise its geometrical and control parameters and maximise its power absorption from incident waves. The steady-state harmonic model was verified against a time domain model by comparing the predictions of the models for steady state response. The geometrical and control parameters of the heaving

buoy were optimised to achieve a cost-effective buoy design which maximised power absorption from incident waves. The buoy behaviour was simulated for the case of regular waves. The approach used was numerical and the dynamic equations were formulated and results calculated in the time domain using the software MATLAB. The PTO damper c_1 was assumed to be a constant damping coefficient for simplicity and the radiation force was decomposed into a linear radiation damping term c_2 which reflected the system geometry (Figure 3.10). Further analyses were carried out to determine the damping profiles of different buoy shapes namely: bullet, spike and bi-cone ($60^o/120^o$).

The steady-state model revealed that at resonance, maximum power absorption of the buoy occurred in two regions values with either low or high range of values of radiation damping coefficient. Operation in the low c_2 region is difficult to achieve in practice and hence it is recommended that devices should be designed to operate in the high c_2 region to maximise power capture. This suggests that some sort of external damping should be added to the buoy structure. The results also indicated that for each buoy shape, there was an optimum operating range for the PTO driven generator where wave energy capture and thus electrical power would be greatest. The model revealed that the best value for c_1 is $c_1 = c_2 = k/\omega$ when the buoy is at resonance with the peak frequency of the sea state and its mass is optimum. The PTO device size can therefore be manufactured accordingly to maximise power absorption. Out of all the tested buoy shapes (bullet, spike and bi-cone), the bi-cone ($60^o/120^o$) buoy's response was most similar to the optimum mass response predicted by the model which indicated that its mass of 11.63 kg was closest to optimum. It was also noted that the c_2 damping associated with the tested bi-cone shape was quite different from the c_2 value predicted by the model to give the worst performance. The optimisation approach developed could be used to realise major economic design benefits for

any point absorber buoy shape. The model presented in this work provides an analytical framework for improved understanding of point absorber PTO devices.

The experimental results showed that there was a substantial benefit for power absorption from using a combined parabolic concentrator-point absorber technology. This was encouraging for making wave energy an attractive renewable energy source for Kuwait, as waves can be focused and amplified to increase electrical power output. The experimental investigation also showed that placing a buoy at the amplification zone of a parabola can significantly increase absorption efficiency in comparison to that achieved with a buoy on its own. The shape of the parabola was found to affect power absorption significantly. The focal lengths of the parabolae in this study were chosen such that the focal length of parabola-1 was double that of parabola-2. The differences in power absorption efficiency and total absorbed power for the two parabola shapes examined were very large. A maximum efficiency of 97% was achieved with parabola-2 compared to 35% achieved with parabola-1 for the case of a fully damped buoy connected to a motor that provided the PTO mechanism. Much higher power absorption values were also recorded for the parabola-2 system (16 W) compared to the parabola-1 system (4 W). The results indicate that a parabola-2 buoy system would be capable of absorbing almost 260 kW of power at prototype scale (1:16). In general, the results for both parabolae showed their suitability for use in regular narrow banded waves in mild wave climates similar to that found in Kuwait. In practice, the final shape of a real parabola structure will probably be more strongly influenced by aspects other than its hydrodynamic performance, e.g. material costs, fabrication costs and its ability to withstand the predominant wave period conditions for the particular site in question. The optimal buoy size will be determined by wave climate, damping and cost considerations. This research has highlighted the potential of parabolic concentrators for enhancing the

efficiency of wave energy conversion. It has also shown the need for optimisation.

The computational modelling carried out as part of this study has shown that a volume of fluid (VOF) approach within a conventional computational fluid dynamics (CFD) code can provide a valid route for future investigation of wave energy concentration. The CFD model offered a very good understanding of the wave dynamics in the tank and the interaction of the waves with the static buoy. It also provided means of determining the lift and drag forces acting on the buoy as a function of time. Although fine meshes with a large number of cells are needed, CFD data compared well with the experimental data for the wave tank simulations. Adding a buoy to the model which moved in response to the wave motion was beyond the achievable scope of this thesis, but would be an important area for future research. It is clear that CFD modelling in conjunction with wave tank testing provides a viable route for future optimisation work.

6.2. Contributions to Knowledge

The work presented in this thesis contributes to the body of knowledge in the literature in three respects. Firstly, the analytical study extends current understanding of the role of damping to the response of an idealised point absorber device. Secondly, the wave tank testing demonstrated how a parabolic concentrator element could act to increase potential wave energy harvesting and generated a wealth of data that could be used to support CFD model development. Finally, the CFD study identified how an acceptable CFD model should be formulated and highlighted the sensitivity of the results to meshing and modelling parameters. The conventional CFD using the VOF method was an effective approach for modelling the behaviour of a static buoy in a wave tank. In all three areas, new data and new understandings have been generated.

6.3. Project Cost

The main objective of this section is to calculate the cost of a parabolic concentrator-heaving buoy device for Qaru Island. It is beyond the scope of this study to present a detailed cost for the location because many of the costs are sensitive to the site environment which defines infrastructure and resource capacity. Instead, the cost presented here takes into account cost uncertainties and is presented to promote the wave energy focusing technology. For Qaru Island, there are many cost uncertainties because no similar projects have been undertaken to date. In addition, information on resource and infrastructure for marine energy projects is too sparse in the area to undertake such assessments. A full cost calculation will need to be done for the site as part of a detailed feasibility study. The cost estimates used in this study are applicable to the many wave energy devices that exist in Kuwait's marine energy industry and are discussed below in relation to the parabolic concentrator-heaving buoy concept.

6.3.1. Capital Cost

The capital cost breakdown adapted for this study is similar to that provided by Dalton et al. (2010a). The capital cost of the project includes the WEC device (materials, components and labour), shipping, mooring/foundations, deployment and installation. The structure and mechanical components represent the largest share of the cost. The cost of power conversion equipment such as PTO system, electrical components and grid connection needed for device functionality have been neglected. Summary of the parabolic concentrator-buoy device capital cost is given in Table 6.1.

Device

The structure of the parabola forms the largest cost component, as it has to interact with the waves and support power conversion by the buoy. The parabolic concentrator design allowed for the structure to be built locally in Kuwait from off-the-shelf materials, whilst the complex

design of the bi-cone buoy required the whole device to be manufactured overseas in Turkey which is near Kuwait. In this case, the cost of shipping the buoy to Kuwait was included.

Gulf Dredging and General Contracting Co., pioneer and leaders in the field of offshore contracting and engineering in Kuwait provided cost estimates for the fabrication, transport to the site location and installation of parabolic precast concrete blocks structure (Length: 40m, Height: 8m, Width: 3m) in the range of £1,898,089. The cost estimation included carrying out bathymetric survey at site location, fabrication of Precast concrete blocks structure as per the detailed design, transporting of structure from fabrication yard to work location (Qaru Island), preparation of concrete block foundation by rock materials, preparation of bedding layer by aggregates and placing of precast concrete blocks structure at site.

Asakua Su Urunleri Ltd provided cost estimates for the Bi-cone buoy device (Diameter: 5m, Draft: 2.4m, Total Height: 9.4m) in the range of £59,099. The buoy is manufactured from Epoxy painted steel and the cost estimates included manhole, bulkhead, ladder (inside), mooring and lifting eyebolts. Cost excluded installation and supervising services.

Mooring

The mooring comprises all the parts necessary to hold the buoy in place and allow it to move independently while preventing it from drifting from its location at the amplification zone. Furthermore, the design has to incorporate the extreme loads placed on it by hydrodynamic forces at sea. Asakua Su Urunleri Ltd designed the mooring arrangement based on sea conditions around Qaru Island. Factors considered were buoy survival conditions, significant wave height and period, seafloor soil conditions and water depth. The heaving bi-cone buoy employed a mooring system using a combination of tarred steel chains, Galvanized bow shackle, galvanized eye-to-eye swivel, 9.5 ton steel anchors and Steel made mooring connector. The

cost of mooring provided by Asakua Su Urunleri Ltd is in the range of £64,104.

6.3.2. Shipping

The shipping of the buoy parts and mooring components are cost factors that are dependent on the location of the project. The technical expertise and the process of manufacturing steel sections of the buoy are too complex to be achieved locally, and manufacturing was done in Turkey. Qaru Island lacks information on the cost of shipping marine energy devices for deployment purposes, so this needs further investigation in the future. A comprehensive study on shipping costs would entail identifying the nearest facility to fabricate the buoy and the most cost-effective route to ship the device to the site. The shipping cost estimate for the buoy and mooring system provided by Asakua Su Urunleri Ltd is in the range of £11,405.

6.3.3. Installation

Installation methods are dependent on the nature of the structure and are the most demanding part of the project. Gulf Dredging and General Contracting Co. included transportation and installation cost of the parabolic structure in their estimates. In total, the cost of installation amounts to £499,819. For the buoy/mooring system a specialised vessel with adequate lifting capacity is required for transporting and installation of the system on site. Such vessels are often used to install ship moorings and are available locally. The cost of deployment can be estimated using vessel charter rates and location. There would be cost savings if vessels were hired from within Kuwait. However, the cost of hiring such vessel is not included in the capital cost.

Table 6.1: Parabolic concentrator-buoy device capital cost summary

	Description	Amount
Parabolic Structure	Fabrication of Precast Concrete Blocks	**£ 917,372**
	Transportation of Precast Concrete Blocks & Rock Materials for Foundation	**£ 480,897**
	Placing of Precast Concrete Blocks including Rubble Base	**£ 499,819**
	Sub Total	**£ 1,898,089**
Buoy	Diameter : 5m, Total Height : 9.4m Material : Epoxy painted steel Including manhole, bulkhead, ladder(inside), mooring	**£ 59,099**
Anchor	9.5 tonnes Steel Anchor (3 pcs.)	**£ 38,887**
Chain – 25m	Dimensions: Ø76mm L: 25m, Material: Tarred steel (1pcs.)	**£ 5,331**
Chain – 75m	Dimensions: Ø76mm L: 75m, Material: Tarred steel (3 pcs.)	**£ 4,924**
Chain – 10m	Dimensions: Ø76mm L: 10m, Material: Tarred steel (1 pcs.)	**£ 2129**
Shackle	Galvanized bow shackle with safety pin, Size: 76mm (11 pcs.)	**£ 7,087**
Swivel	Galvanized eye-to-eye swivel, Size: 84mm (1 pcs.)	**£ 3,377**
Connector	Steel made mooring connector (1 pcs.)	**£ 2369**
Shipping	Buoy and mooring system	**£ 11,405**
	Sub Total	**£ 134,608**
***Grand Total**		**£ 2,032,697**

*Exclusions: Obtaining necessary permits from Local Authorities/ Ministries, and obtaining necessary access to the site (if any).

6.3.4. Operation and Maintenance Cost

The operation and maintenance cost includes costs related to planned and unplanned maintenance during its service life, and monitoring throughout the operational life of the facility (Table 6.2). Planned maintenance includes cost of parts replacement and regular servicing components. Unplanned maintenance includes of stocking spares in case of failure; servicing and labour requirements. All elements of the parabolic concentrator-buoy system, including underwater components,

need to undergo thorough inspection to ensure the continued operation of the device. Major maintenance activities will be carried out in the summer months during calm weather conditions for safety purposes. After storms, some unplanned maintenance may need to be carried out on failures requiring immediate attention. Removal of the device is required only to repair structural damage.

The WAVEPLAM study (2009) reported and calculated the cost of operation and maintenance as 3% of the total project initial cost (i.e. the capital cost), while the Wave power feasibility study report (2009) undertaken for the city of San Francisco, USA, reported annualised operations and maintenance, ranging from 3% to 5% of total capital cost. Dalton et al. (2010b) assessed these costs to be in the range 1% to 5% of capital cost. For the scope of this study the operation and maintenance costs are calculated as 5% of the capital cost. These yielded annual operation and maintenance costs of £101,635.

6.3.5. Mid-life Overhaul

During the lifetime of the device an overhaul and refit of major components may be required. This should take place mid-way in the device's operational lifetime to ensure that it was able to withstand the extreme marine environment around Qaru Island. The buoy has to be taken onshore for a complete overhaul and refit every ten years. The cost of the refit will depend on the severity of wear and tear that the device has undergone under operational conditions. Dalton et al. (2010b) accounted 10% of the capital cost for overhaul which would result in an expenditure of £203,270 half-way through the operation lifetime.

6.3.6. Decommissioning

The device has to be removed from Qaru Island and disassembled towards the end of the project life (20–25 years). Similar procedures used in installation activities will be used for decommissioning. Prediction of decommissioning is difficult as it may not be practical to

remove some elements, such as the 40m long precast concrete blocks structure and heavy anchors, so they can be left in place, as they may provide a habitat and shelter for marine life (Previsic 2010). In addition, at the end of the life of the moorings the device may be sunk or sold for scrap. Dalton et al. (2010b) accounted 10% of the capital cost for decommissioning which would result in an expenditure of £203,270. However, the cost of decommission needs to be done for the site as part of a detailed feasibility study.

6.3.7. Total Lifetime Cost

The total lifetime cost of the device was calculated based on the above estimates. It was calculated to be £ 2,540,872 as shown in Table 6.2.

Table 6.2: Total lifetime cost of parabolic concentrator-buoy device

Description	Amount
Capital Cost (parabolic structure + buoy)	**£ 2,032,697**
Lifetime Operation and Maintenance for 25 years	**£ 101,635**
Mid-life Overhaul	**£ 203,270**
Decommissioning	**£ 203,270**
Grand Total	**£ 2,540,872**

6.4. Future Work

In this thesis the PTO system was modelled with a constant damping coefficient for regular waves. This method is standard practice when modelling the hydrodynamic action of a point absorber WEC and hence it was a natural starting point for the work. This might be considered as the model's main limitation, because approaches with irregular wave inputs tend to be more accurate as they replicate real sea conditions. In reality, a PTO does not have a linear response and power losses due to the PTO will always occur. The PTO system therefore needs to be modelled more accurately. Cargo (2012) carried out an extensive study

on the modelling of a PTO system and his results could be used to further improve the steady-state harmonic model in this work. Cargo (2012) demonstrated that over-simplification of the PTO during the simulation phase of WEC development could lead to incorrect design decisions and subsequent delays and costs. Furthermore, economic considerations need to be taken into account during the design process. Optimal design parameters such as buoy shape, dimensions and structure are driven by the radiation damping c_2 which in turn is dependent on the costs involved.

The parabolic concentrator-point absorber scale model developed in this work could easily be scaled up to a full-scale prototype (1:16) model using the appropriate scaling laws. If this were to be done, the size of the buoy need to be scaled first. Given the buoyancy force and power output required, the size of the cylinder and hydraulic motor can then be calculated.

The factor in the experimental work which contributed most to uncertainties in the results was the pulley arrangement. Of the three pulleys located at the top of the buoy, the middle pulley was used as a pre-tensioner and adjusted using a screw. Further improvements to the test set-up would include the addition of a spring pre-tensioner to reduce device vibration and noise in the vertical force readings. It was also noted that the cable arrangement restricted the buoy's motion at high incident wave heights which needs to be addressed. Increasing the c_2 damping by adding two round discs to the lower part of the buoy appeared to be a sensible approach to increase the external damping on the buoy, but the outcomes gave lower damping, which were unexpected and are worthy of further investigation.

Regarding design aspects, further testing could be carried out with different parabola shapes that would be suitable for a broadband spectrum of waves with a wide range of frequencies. Testing could also be done with different buoy diameters, drafts and damping values to find cost effective buoy designs. The optimum wave spectrum operation

range found for parabola-1 could be utilised to tune the device towards resonance and increase understanding of buoy behaviour near resonance. Furthermore, investigation of the buoy's mooring design and its influence on power extraction is needed.

A CFD model was developed using the commercial software FLUENT to model the behaviour of waves in KISR's parabolic concentrator-point absorber wave tank testing facility as part of this study. The CFD model offered a very good understanding of the wave dynamics in the tank and the interaction of the waves with the static buoy. It also provided a means of determining the lift and drag forces acting on the buoy as a function of time. Using the model for examining buoy vertical heave motion and simulating wave-buoy interactions would require fluid-structure interaction modelling, which was beyond the scope of this work. However, this is clearly an area for future research. If funding were to become available, it would be of benefit to conduct full-scale testing using an off-the-shelf point absorber device in combination with a parabolic concentrator to validate the predictions for performance improvements. This work would serve as a platform for predicting the forces acting on a buoy, and could be used to develop simulations of buoy motion in different wave conditions.

Moving body simulations using an overset mesh CFD framework together with a rigid body dynamics model are becoming commonplace in marine dynamics applications (Koomullil et. al., 2008). These methods offer a possible approach to the CFD modelling of wave-buoy interactions and are recommended as an area of future research.

The total lifetime cost of a parabolic concentrator-heaving buoy device for Qaru Islandthe device was calculated to be £ 2,540,872. A full cost calculation will need to be done for the site as part of a detailed feasibility study.

References

A. R. ANSYS®, *Release 14.0, ANSYS Fluent User's Guide*, 2011, ANSYS, Inc.

ABP. 2008. *Atlas of UK marine renewable energy resources: Technical report*. ABP Marine Environmental Research Ltd, Department for Business, Enterprise & Regulatory Reform.

Abul-Azm, A.G. 1996. Wave diffraction through submerged flexible breakwaters. *Ocean Engineering,* 23(5). pp.403-422.

Agamloh, E.B., Wallace, A.K. and Von Jouanne, A., 2008. Application of fluid-structure interaction simulation of an ocean wave energy extraction device. *Renewable Energy*, 33(4). pp.748-757.

Airy, G.B. 1841. *Tides and waves*. Encyclopaedia Metropolitana. pp.396.

Alamian, R., Shafaghat, R., Miri, S.J., Yazdanshenas, N., and Shakeri, M. 2014. Evaluation of technologies for harvesting wave energy in Caspian Sea. *Renewable Sustainable Energy Review*, 32. pp.468-476.

Ali, A. 2006. Floating Transhipment Container Terminal. M.Sc thesis, Delft University of Technology, Delft, the Netherlands.

Anbarsooz, M., Passandideh-Fard, M., and Moghiman, M. 2014. Numerical simulation of a submerged cylindrical wave energy converter. *Renewable Energy,* 64:132-143.

Anon. 1984. *Shore Protection Manual Volume I*. 4th ed. US Army Engineer Waterways Experiment Station, Coastal Engineering Research Center, US Government Printing Office, Washington, DC.

Arena, F., Romolo, A., Malara, G., and Ascanelli, A. 2013. On design and building of a UOWC wave energy converter in the Mediterranean Sea: A case study. In: *Proceedings of the 32nd international conference on ocean, offshore and arctic engineering*. Nantes.

Asakua Su Urunleri Ltd, Turkey. *Last accessed on December 2017*, www.asakua.com.

Babarit A., Hals J., Muliawan, M.J., Kurniawan, A., Moan, T., and Krokstad, J. 2012. Numerical benchmarking study of a selection of wave energy converters. *Renewable Energy,* 41: 44-63.

Babarit, A., and Clement, A.H. 2006. Optimal latching control of a wave energy device in regular and irregular waves. *Applied Ocean Research*, 28(2):77-91.

Babarit, A., Duclos, G., and Clement, A.H. 2004. Comparison of latching control strategies for a heaving wave energy device in random sea. *Applied Ocean Research*, 26(5):227-238.

Babarit, A., Guglielmi, M., and Clement, A.H. 2009. Declutching control of a wave energy converter. *Ocean Engineering*, 36:1015-24.

Babarit, A., Mouslim, H., Clement, A. 2009. On the numerical modelling of the nonlinear behaviour of a wave energy converter. In: ASME, *Proceedings of the 28th international conference on ocean, offshore and arctic engineering*. Honolulu, Hawaii. pp.1045-1053.

Baby, S. 2011. Information research on coastal morphological environment of Kuwait: Organisations, role and coastal legislations. *Emirates Journal for Engineering Research*, 16(2): 7-25.

Bachynski, E.E., Young, Y.L., and Yeung, R.W. 2012. Analysis and optimization of a tethered wave energy converter in irregular waves. *Renewable Energy*, 48: 133-145.

Bahaj, A.S. 2011. Generating electricity from the oceans, *Renewable and Sustainable Energy Reviews,* 15(7): 3399–3416.

Bakker A. 2002. Lecture 7 - Meshing Applied Computational Fluid Dynamics Instructor: http://www.bakker.org © André Bakker (2002-2006) © Fluent Inc. (2002).

Bhinder, M.A., Babarit, A., and Gentaz, L. 2011. Assessment of viscous damping via 3D-CFD modelling of a floating wave energy device. In: *Proceedings of the 9th European wave and tidal energy conference (EWTEC)*. Southampton, UK.

Bhinder, M.A., Mingham, C.G., and Causon, D.M. 2009b. Numerical and experimental study of a point absorbing wave energy converter in regular waves. In: IEEE, *2009 international conference on clean electrical power*. Capri, Italy,.pp.599-603.

Blommaert, C. 2010. *Composite floating 'point absorbers' for wave energy converters: Survivability, design, production method and large-scale testing*. PhD. Ghent University.

Boccotti, P. 2007. Comparison between a U-OWC and a conventional OWC. Ocean Engineering, 34(5): 799-805.

Bozzi, S., Moreno Miquel, A., Antonini, A., Passoni ,G., and Archetti, R. 2013. Modeling of a Point Absorber for Energy Conversion in Italian Seas, *Energies*, 6: 3033-3051. doi:10.3390/en6063033.

Brackbill, J.U., Kothe, D.B., and Zemach, C. 1992. A continuum method for modelling surface tension. *Journal of Computational Physics*, 100: 335-354.

Brekken T.K.A., Von Jouanne A., and Hai Y.H. 2009. Ocean wave energy overview and research at oregon state university (Lincoln, NE: IEEE Power Electronics *and Machines in Wind Applications).*

Briggs, M., Ye, W., Demirbilek, Z., and Zhang, J. 2002. 'Field and numerical comparison of the RIBS floating breakwater'. Journal of Hydraulic Research, 40(3).

Brooke, J. 2003. *Wave Energy Conversion*. New York: Elsevier Ocean Engineering.

Budal, K., and Falnes, J. 1975. A resonant point absorber of ocean waves. *Nature*, 256: 478-479.

Budal, K., and Falnes, J. 1980. Interacting point absorbers with controlled motion. In: B. Count. *Power from sea waves*. Academic Press.

Burcharth, H. F. 2009. Choice of Breakwater Type and Optimum Safety Levels. In A. S. Arcilla, & G. R.Tomasicchio (Eds.), 4th SCACR International Short Conference on Applied Coastal Research: 15-17 June Nuova Editoriale Bios.

Cabral B., Leedom, L.C. 1993. Imaging Vector Fields Using Line Integral Convolution. Proceeding SIGGRAPH '93 Proceedings of the 20th Annual Conference on Computer Graphics and Interactive Techniques, pp.263-270, ISBN:0-89791-601-8 doi>10.1145/166117.166151.

Cargo, C.J., Hillis, A.J., and Plummer, A.R. 2016. Strategies for active tuning of wave energy converter hydraulic power take-off mechanisms. *Renewable Energy,* 94: 32-47.

Cargo, C.J., Plummer, A.R., Hillis, A.J., and Schlotter, M. 2012. Determination of optimal parameters for a hydraulic power take-off unit of a wave energy converter in regular waves. *Proceedings of the Institute of Mechanical Engineers, Part A: Journal of Power Energy*, 226(1): 98-111.

Cheung, K.F., Lee, J.W., and Isaacson, M. 1995. Wave diffraction around a three-dimensional body is a current. In: *Proceedings of the conference on offshore mechanical and arctic engineering.* Copenhagen. 1A: 395-402.

Clément, A., McCullen, P., Falc˘ao, A., Fiorentino, A., Gardner, F., Hammarlund, K., Lemonis, G., Lewis, T., Nielsen, K., Petroncini, S., Pontes, M.-T., and Schild, B. O. 2002. Wave energy in Europe: current status and perspectives. *Renewable and Sustainable Energy Reviews*, 6(5): 405-431.

Craik, A.D. 2004. The origins of water wave theory. *Annual Review of Fluid Mechanics,* 36: 1-28.

Cruz J. 2008. Ocean wave energy: Current status and future perspectives*.* ISBN 978-540-74894-6.

D'Angremond, K., and van Roode, F.C. 2001. Breakwaters and closure dams. Delft: Delft University Press.

Dalton, G.J., Alcorn, R., and Lewis, T. 2010a. Case study feasibility analysis of the Pelamis wave energy convertor in Ireland, Portugal and North America. *Renewable Energy,* 35(2): 443–455.

Dalton, G.J., Alcorn, R., andLewis, T. 2010b. Operational expenditure costs for wave energy projects; O/M, insurance and site rent*. In Proceedings of the 3rdInternational Conference on Ocean Energy (ICOE)*, 6-8, October, Bilbao, Spain.

De Backer, G. 2008. *Hydrodynamic design optimisation of wave energy converters consisting of heaving point absorbers*. PhD. Ghent University, Ghent, Belgium.

De Backer, G., Vantorre, M., Banasiak, R., Beels, C., and De Rouck, J. 2007. Numerical modelling of wave energy absorption by a floating point absorber system. In: *Proceedings of the Seventeenth International Offshore and Polar Engineering Conference*, July 1-6 ,Lisbon, Portugal, ISBN 978-1-880653-68-5; ISBN 1-880653-68-0 (Set); ISSN 1098-6189 (Set) 374.

Denniss, T. 2007. *Ocean wave energy extraction*, CA 2271021 C. Energetech Australia Pty. Limited.

Dentale, F., Donnarumma, G., and Carratelli E. P. 2014. Numerical wave interaction with tetrapods breakwater. International Journal of Naval Architecture and Ocean Engineering 6(4): 800-812.

Drieman, R. 2011.Feasibility study on the use of a floating breakwater to protect a new artificial beach in Balchik, Bulgaria. Masters Thesis. Delft University of Technology. uuid:90105712-9aed-48f5-a5ac-33f60bde9211.

Drimer, N., Agnon, Y., and Stiassnie, M. 1992. A simplified analytical model for a floating breakwater in water of finite depth. *Applied Ocean Research* 14(1): 33-41.

Duncan, J.H., and Brown, C.E. 1982. Development of a numerical method for the calculation of power absorption by arrays of similar arbitrarily shaped bodies in a seaway. *Journal of Ship Research*, 26(1): 38-44.

Elchahal, G., Younes, R., and Lafon, P. 2008. The effects of reflec-tion coefficient of the harbour sidewall on the performance of floating breakwaters. Ocean Engineering, 35(11,12): 1102–1112. doi:. 10.1016/j.oceaneng.2008.04.015.

Elhanafi, A., Fleming, A., Macfarlane, G., and Leong, Z. 2017. Numerical hydrodynamic analysis of an offshore stationary floating oscillating water column wave energy converter using CFD. *International Journal of Naval Architecture and Ocean Engineering,* 9: 77-99.

EMEC (The European Marine Energy Centre Ltd.). 2014. “Wave Devices”, *Last accessed on March 2017* www.emec.org.uk/marine-energy/wave-devices.

Engström, J., Kurupath, V., Isberg, J., and Leijon, M. 2011. A resonant two body system for a point absorbing wave energy converter with direct-driven linear generator. *Journal of Applied Physics*, 110: 124904:1-124904.

Ertekin, R.C., and Monopolis, G.M. 1985. Investigation of wave focusing over a parabolic step. *Hydrodynamics of ocean wave-energy utilisation conference*. Part of the series: *International union of theoretical and applied mechanics*, pp.433-443.

Evans, D. 1976. A theory for wave-power absorption by oscillating bodies. *Journal of Fluid Mechanics*, 77:1-25.

Evans, D. 1980. Some analytic results for two- and three-dimensional wave energy absorbers. In: B. Count. *Power from sea waves.* Academic Press.

Falcao, A. 2008. Phase control through load control of oscillating-body wave energy converters with hydraulic PTO system. *Ocean Engineering*, 35: 358-366.

Falcão, A. 2009. The development of wave energy utilization. In: 2008 Annual Report, A. Brito-Melo and G. Bhuyan (eds.), International Energy Agency Implementing Agreement on Ocean Energy Systems, Lisboa, Portugal, pp. 30-37.

Falcao, A.F. 2007. Modelling and control of oscillating-body wave energy converters with hydraulic power take-off and gas accumulator. *Ocean Engineering*, 34: 2021-2032.

Falcao, A.F.O. 2010. Wave energy utilization: A review of the technologies. *Renewable and Sustainable Energy Reviews*, 14: 899-918.

Falnes J. 2002, *Ocean Waves and oscillating systems, linear interactions including wave-energy extraction.* Cambridge University Press, Cambridge.

Falnes, J. 2006. Discussion. International Journal of Offshore and Polar Engineering,16.

Falnes, J. and Lillebekken, P.M., 2003. Budals latching-controlled-buoy type wave power plant. In: *Proceedings of the 5th European Wave Energy Conference.* Cork. pp.17-20.

Finnegan, W., and Goggins, J. 2012. Numerical simulation of linear water waves and wave–structure interaction. *Ocean Engineering,* 43: 23-31.

Folley, M., and Whittaker, T. 2009. The control of wave energy converters using active bipolar damping. *Proceedings of the Institute of Mechanical Engineers Part M Journal of Engineering for the Maritime Environment*, 223(4): 479-487.

Folly, M. 2016. *Numerical Modelling of Wave Energy Converters: State-of-the-Art Techniques for single devices and arrays*. Elsevier Science & Technology Books.

Fousert, M.W. 2006. *Floating breakwater: A theoretical study of a dynamic wave attenuating system*. MSc. Delft University of Technology.

Garvey, S.D. 2010. Structural capacity and the 20MW wind turbine. *Proceedings of the Institution of Mechanical Engineers, Part A: Journal of Power and Energy*. Volume: 224 issue: 8, page(s): 1083-1115.

Goggins, J., and Finnegan, W. 2014. Shape optimisation of floating wave energy converters for a specified wave energy spectrum. *Renewable Energy,* 71: 208-220.

Gozo, T., Kazuya, O., Fumihiko, Y., Tetsuya, K., Masatoshi, Y., Takaaki, E., Itaru, I., and Satoru, T. 2009. A study on an estimation of horizontal wave fields around double barrier floating breakwater. *Journal of Japan Society of Civil Engineers*, *Ser. B2 (Coastal Engineering)*, 65(1): 761-765.

Greenhow, M. 1982. Approximation of models of a heaving sphere with linear and non-linear power take-off mechanisms. *Journal of Applied Ocean Research*, 4(3): 160.

Greenhow, M., and White, S.P. 1997. Optimal heave motion of some axisymmetric wave energy devices in sinusoidal waves. *Applied Ocean Research*, 19: 141-59.

Grinyer, A.W. 1995. Fixed and floating breakwaters for small craft harbours: Experience at Town Quay Southampton, Haslar Marina, Portsmouth and Parkstone Yacht Haven, Poole. *Transactions on The Built Environment* (8), www.witpress.com, ISSN 1743-3509.

Gulf Dredging and General Contracting Co. (KSC) (GD), Kuwait, *Last accessed on December 2017* , www.gulfdredging.com.

Hadzic, I., Hennig, J., Peric, M., and Xing-Kaeding, Y. 2005. Computation of flow-induced motion of floating bodies. Applied Mathematical Modelling, 29: 1196-1210.

Hagerman, G. 1995. A standard economic assessment methodology for renewable ocean energy projects. *Proceedings of the international symposium on coastal ocean space utilization*. COSU, Yokohama, Japan, pp.129-138.

Hales, L.Z. 1981. *Floating breakwater: State-of-the-art, literature review*. TR 81-1. Fort Belvoir, Virginia: U.S. Army Coastal Engineering Research Center.

He, F., and Huang, Z. 2014. Hydrodynamic performance of pile-supported OWC-type structures as breakwaters: an experimental study. *Ocean Engineering,* 88: 618-626.

He, F., Huang, Z., and Law, A.W.K. 2012. Hydrodynamic performance of a rectangular floating breakwater with and without pneumatic chambers: An experimental study. *Ocean Engineering*, 51: 16-27.

He, F., Huang, Z., and Law, A.W.K. 2013. An experimental study of a floating breakwater with asymmetric pneumatic chambers for wave energy extraction. *Applied Energy*, 106: 222-231.

Heller, V. 2011. Scale effects in physical hydraulic engineering models. *Journal of Hydraulic Research,* 49(3): 293-306.

Helstad, J. 1980. Power production based on focused ocean swell, submerged crescent plate. *Coastal Engineering Japan*, 31(2): 231-243.

Henry, A., Rafiee, A., Schmitt, P., Dias, F. and Whittaker, T. 2014. The characteristics of wave impacts on an oscillating wave surge converter. *Journal of Ocean and Wind Energy* (ISSN 2310-3604), 1(2): 101-110.

Hong D.C., Hong, S.Y., and Hong S.W. 2006. Reduction of hydroelastic responses of a very-long floating structure by a floating oscillating-water-column breakwater system, *Ocean Engineering,* 33(5–6): 610–634.

Horko, M. 2007. *CFD optimization of an oscillating water column wave energy converter*. MEngSci. The University of Western Australia.

http://www.ccell.co.uk *Last accessed on February 2017.*

http://www.oceanlinx.com. *Last accessed on March 2017.*

http://www.physicsclassroom.com. *Last accessed on February 2017.*

International Renewable Energy Agency. 2014. *Wave energy technology brief 2014.* Ocean energy technology brief 4. IRENA.

Ito, Y. 1969. A treatise on historical development of breakwater design, Technical Note of Port and Harbour Research Institute,69: 78 . (In Japanese).

Ji, C.-Y., Chen, X., Cui, J., Gaidai, O., and Incecik, A. 2015. Experimental study of a new type of floating breakwater. *Ocean Engineering*, 105: 295-303.

Ji, C.-Y., Chen, X., Cui, J., Gaidai, O., and Incecik, A. 2016. Experimental study on configuration optimization of floating breakwaters. *Ocean Engineering*, 117: 302-310.

Joly, J. 1905. On Floating Breakwaters. Scientific Proceedings of the Royal Dublin Society, 10: 378-383.

Journée, J.M.J., and Massie, W.W. 2001. *Offshore hydromechanics*. 1st ed. Delft University of Technology.

Khojasteh, D., and Kamali, R. 2016. Evaluation of wave energy absorption by heaving point absorbers at various hot spots in Iran seas. *Energy,* 109: *629-640.*

Koo, W.C. 2009. Nonlinear time-domain analysis of motion-restrained pneumatic floating breakwater Ocean Engineering, 36 (9-10): 723-731.

Koomullil R., Gary Chenga, G., Soni, B., Noack R., and Prewitt N. 2008. Moving-body simulations using overset framework with rigid body dynamics, *Mathematics and Computers in Simulation* 78: 618–626.

Koraima, A.S., and Rageh, O.S. 2013. Effect of under connected plates on the hydro-dynamic efficiency of the floating breakwater. *China Ocean Engineering*, 28(3): 349-362.

Korde, U.A. 2002. Latching control of deep water wave energy devices using an active reference. *Ocean Engineering*, 29(11):1343-55.

Koutandos, E.V., and Prinos, P.E. 2011. Hydrodynamic characteristics of semi-immersed breakwater with an attached porous plate. *Ocean Engineering*, 38(1): 34-48.

Krupp, F., and Horn, M. 2008. *Earth: The sequel. The race to reinvent energy and stop global warming.* New York: Norton and Company. pp.288.

Kudo, K., Tsuzuku, T., Imai, K. and Akiyama, Y. 1987. A wave focusing phenomenon by a submerged plate. *Journal of the Society of Naval Architecture Japan*, 106: 35-43.

Lal, A. and Elangovan, M. 2008. CFD simulation and validation of flap type wave maker. *World Academy of Science, Engineering and Technology,* 46(7).

Lamberti A., and Franco L. 1994.Italian experience on upright breakwater. Pro Int workshop on wave Barriers in deepwaters, PHRI

Leishman, J.M., and Scobie, G. 1976. *The development of wave power - a techno-economic study*. East Kilbridge Glasgow, Scotland: Economic Assessment Unit, National Engineering Laboratory.

Li, Y., and Lin, M. 2012. Regular and irregular wave impacts on floating body. *Ocean Engineering*, 42: 93-101.

Lighthill, M.J. 1979. Two-dimensional analysis related to wave-energy extraction by submerged resonant ducts. *Journal of Fluid Mechanics*, 91(2): 253-317.

Liu, Z., Shi, H., Cui, Y. and Kim, K. 2017. Experimental study on overtopping performance of a circular ramp wave energy converter. *Renewable Energy,* 104: 163-176.

Luo, Y., Nader, J.-R., Cooper, P., and Zhu, S.-P. 2014a. Nonlinear 2D analysis of the efficiency of fixed Oscillating Water Column wave energy converters. *Renewable Energy,* 64: 255–265.

Luo, Y., Wang, Z., Peng, G., Xiao, Y., Zhai, L., Liu, X. and Zhang, Q. 2014b. Numerical simulation of a heave-only floating OWC (oscillating water column) device. *Energy*, 76: 799-806.

MacCormick, M., Kastner, R., and Glover, L. 1980. *Water wave focusing by submerged lens-shaped structures.* U.S. Naval Academy report EW-14-80.

Mamun, M.A.H, Nagata, Sh., Toyota, K., and Imai, Y. 2010. Wave energy utilization: Recent trend. In: *Proceedings of the 13th Asian congress of fluid mechanics.*, 17-21 December, Dhaka, Bangladesh

Mansard, E. P., and Funke, E. 1980. The measurement of incident and reflected spectra using a least squares method. *Coastal Engineering Proceedings*, 1(17): 154-172.

Martin, D., F. Bertasi, M.A., Colangelo, M. de Vries,, Frost, M., S.J. Hawkins, Macpherson, E., Moschella, P.S., Satta, M.P., Thompson, R.C., Ceccherelli, V.U. 2005. Ecological impact of coastal defence structures on sediment and mobile fauna: evaluating and forecasting consequences of unavoidable modifications of native habitats Coastal Engineering, 52: 1027-1051

MATLAB: www.mathworks.com

McCartney, B.L 1985. Floating breakwater design. *Journal of Waterway, Port, Coastal and Ocean Engineering,* 111(2): 304-318.

Mehlum, E. and Stamnes, J. 1980. Power production based on focusing of ocean swells. In: *Proceedings of the 1st symposium on wave energy utilization*. Gothenburg: Chalmers University of Technology. pp.29-35.

Michailides, C., and Angelides, D.C. 2012. Modelling of energy extraction and behavior of a flexible floating breakwater. *Applied*

Monopolis, G.M., Ansari, G.R., and Ertekin, R.C. 1980. *Wave energy focusing. Ocean engineering: The future*. IDS Report No. 80-3. College of Engineering, University of California, Berkeley, pp.183-238.

Morey, B. J. 1998. Floating breakwaters: pred icting their performance. Memorial University of Newfoundland: Master's Thesis.

Mork, G., Barstow, S., Kabuth, A. and Pontes, M.T. 2010. Assessing the global wave energy potential. In: ASME, *Proceedings of the OMAE 2010, 29th international conference on ocean, offshore mechanics and arctic engineering*. Shanghai, China, 6-11 June New York: ASME.

Murashige, S. and Kinoshita, T. 1992. An ideal ocean wave focusing lens and its shape. *Applied Ocean Research*, 14(4): 275-290.

Naty, S., Viviano, A., and Foti, E. 2016. Wave energy exploitation system integrated in the coastal structure of a Mediterranean port. *Sustainability* 8:1342. doi:10.3390/su8121342.

Nazari, M., Ghassemi, H., Ghiasi, M., and Sayehbani, M. 2013. Design of the resonant wave energy absorber buoy. Iranica Journal of Energy & Environment, 4(2): 130-135. ISSN 2079-2115.

Neelamani, S., 2009. Challenges in commercialising the ocean wave energy technology. *Engineering congress on alternative energy applications*, 2- 6 November, Kuwait.

Neelamani, S., Al-Salem, K., and Rakha, K. 2007. Extreme waves for Kuwaiti territorial waters. *Ocean Engineering*, 34: 1496-1504.

Neelamani, S., and Al-Banna, K. 2005. Environment friendly floating breakwaters for protecting the islands and coats against erosion. *The gulf conference on environment and sustainability*. 3-5 December.

Neelamani, S., and Al-Banna, K. 2017. *The innovation in wave breakwaters forum 2017*. Kuwait: Kuwait Institute for Scientific Research.

Newman, J.N. 1976. The interaction of stationary vessels with regular waves. In: *Proceedings, llth symposium on naval hydrodynamics*, London. pp.491-501.

Ning, D., Zhao, X., Goteman, M., and Kang, H. 2016. Hydrodynamic performance of a pile-restrained WEC-type floating breakwater: An experimental study. *Renewable Energy,* 95: 531-541.

Nolan, G.A., Ringwood, J.V., Leithead W.E., and Bulter, S. 2005. Optimal damping profiles for a heaving buoy wave energy converter. In: *Proceedings of the 15th international offshore and polar engineering conference*. Seoul, Korea.

Ocean Power Technologies, 2012. Oregon state University, *Last accessed on March 2017,* http://www.oregonstate.edu/

Orer, G., and Ozdamar, A. 2007. An experimental study on the efficiency of the submerged plate wave energy converter. *Renewable Energy*, 32(8): 1317-1327.

Ozeren Y., Wren, D. G., Altinakar, M., and Work, P. A. 2011. Experimental investigation of cylindrical floating breakwater performance with various mooring configurations. *Journal of Waterway, Port, Coastal and Ocean Engineering*, 137(6): 300-309.

Palm, J., Eskilsson, C., Moura Paredes, G., and Bergdahl, L. 2013. CFD simulation of a moored floating wave energy converter. In: *Proceedings of the 10th European wave and tidal energy conference (EWTEC).* Aalborg, Denmark.

Panicker, N.N. 1976. Power resource estimate of ocean surface waves. *Ocean Engineering*, 3: 429-439.

Papaioannou, I. 2011. Marine Energy: Technology Map of the EuropeanStrategic Technology Plan (SET-Plan), Technology Descriptions Chapter 6, European Commission, JRC, Institute for Energy and Transport.

Pastor, J., and Liu, Y. 2014. Power absorption modeling and optimization of a point absorbing wave energy converter using numerical method. *Journal of Energy Resources Technology*, 136 / 021207-1.

Pelc, R., and Fujita, R.M. 2002. Renewable energy from the ocean. *Marine Policy*, 26, pp.471-479.

Peña, E., Ferreras, J., and Sanchez-Tembleque, F. 2011. Experimental study on wave transmission coefficient, mooring lines and module connector forces with different designs of floating breakwaters. *Ocean Engineering*, 38: 1150–1160.

Permanent International Association of Navigation Congress (PIANC). 1994. Floating breakwaters: A practical guide for design and

construction. Report of working group no. 13 of the permanent technical committee II. Brussels: PIANC. ISBN 2-87223-052.

Piscopo, V., Benassai, G., Cozzolino, L., Della Morte, R., and Scamardella, A. 2016. A new optimization procedure of heaving point absorber hydrodynamic performances, *Ocean Engineering*, 116: 242-259.

PND Engineers, Inc., 2015. *Breakwaters including partial penetrating wave barriers*, *Last accessed on March 2017,*

www.pndengineers.com/home/showdocument?id=413.

Previsic, M. 2010. RE Vision DE-001: Deployment effects of marine renewable energy technologies. Wave energy scenarios. Advanced Waterpower Program. U.S. Department of Energy, US.

Price, A.A.E. 2009. *New perspectives on wave energy converter control*. PhD. The University of Edinburgh.

Qian, L., Mingham, C., Causon, D., Ingram, D., Folley, M., and Whittaker, T. 2005. Numerical simulation of wave power devices using a two-fluid free surface solver. *Modern Physics Letters B,* 19, pp.1479-1482.

Raju, V.S., and Neelamani, S. 1992. “Concrete caisson for a 150 KW wave energy pilot plant: design, construction, and installation aspects,” Proc of 2nd Int. Offshore Polar Eng Conf, San Francisco, 584–591.

Richey, E.P., and Nece, R.E, 1974. Floating breakwaters: State-of-the-art. In: *Proceedings of the floating breakwaters conference*. University of Rhode Island, Kingston, RI. pp.1-20.

Salter, S.H., Taylor, J.R.M., and Caldwell, N.J. 2002. Power conversion mechanisms for wave energy. *Proceedings of the Institute of Mechanical Engineers, Part M: Journal of Engineering for the Maritime Environment,* 216: 1-27.

San Francisco Public Utilities Commission. 2009. Wave power feasibility study report. The City and County of San Francisco, San Francisco.

Schlichting, H., 1960, Boundary Layer Theory: New York, McGraw-Hill, p 647.

Schmitt, P., and Elsaesser, B. 2015. On the use of OpenFOAM to model oscillating wave surge converter. *Ocean Engineering*, 108: 98-104.

Schmitt, P., Bourdier, S., Sarkar, D., Renzi, E., Dias, F., Doherty, K., Whittaker, T., and van't Hoff, J. 2012. Hydrodynamic loading on a bottom hinged oscillating wave surge converter. In: ISOPE (International Society of Offshore and Polar Engineers), *Proceedings of the 22nd international offshore and polar engineering conference*. June 17-*22,* Rhodes, Greece. pp. 550-557.

Shih, R.S. 2012. Experimental study on wave attenuation of porous pipe breakwater. *Applied Mechanics and Materials*, 105-107, pp.1349-1352.

SI Ocean (Strategic Initiative for Ocean Energy). 2012. "Ocean Energy: State of the Art", December, http://si-ocean.eu/en/upload/docs/WP3/Technology%20Status%20Report_FV.pdf.

SI Ocean (Strategic Initiative for Ocean Energy). 2012. "Ocean Energy: State of the Art", December, https://elearning.umj.ac.id/pluginfile.php?file=%2F10144%2Fcourse%2Foverviewfiles%2FMateri_MKE%20gelombang%20laut.pdf&amp%3Bforcedownload=1.

Sjökvist, L., Krishna, R., Rahm, M., Castellucci, V., Hagnestål, A., and Leijon, M. 2014. On the optimization of point absorber buoys. *Marine Science and Engineering,* ISSN 2077-1312.

Stiassnie, M. 1980. A simple mathematical model of a floating breakwater. *Applied Ocean Research* 2(3):107-111.

Stiassnie, M., and Drimer, N. 2003. A freely floating porous box in shallow water waves. *Applied Ocean Research,* 25(5): 263-268.

Stokes, G.G. 1847. “On the Theory of Oscillatory Waves,” *Transactions, Cambridge Philosophical Society*, 8: 441–455.

Takahashi, S. 2002. Design of vertical breakwaters. Japan: Port and Airport Research Institute.

Takahashi, S., Nakada, H., Ohneda, H., and Shikamori, M. 1992. Wave power conversion by a prototype wave power extracting caisson in Sakata port. In: *Proceedings of international conference on coastal engineering.*4-9 October, Venice, Italy. pp:3440-3453.

Tanimoto, K., Takahashi,S., and Kimura, K.1987. Structures and hydraulic characteristics of breakwaters-The State of art of breakwater design in Japan-, Rept. of Port and Harbour Res. Inst., 26: (5).

Teillant, B., Gilloteaux, J.C., and Ringwood, J.V. 2010. Optimal damping profile for a heaving buoy wave energy converter. In: *8th IFAC conference on control applications in marine systems.*, 15-17 September, Rostock-Warnemünde, Germany.

The Queen’s University of Belfast. 2002, Islay Limpet Wave Power Plant. Technical Report. (s.l.):(s.n.).

Tsinker Gregory P. 1995. *Marine structures engineering: Specialised application.* New York: An International Thomson Publishing Company. Floating Breakwater pp.360-410. Published by Springer, ISBN 10: 0412985713 ISBN 13: 9780412985713.

Twidell, J. and Weir, T. 2006. *Renewable energy resources*. London: Taylor & Francis.

Ubbink, O. 1997. *Numerical prediction of two fluid systems with sharp interfaces*. PhD. Imperial College of Science, Technology and Medicine.

Uzaki, K.I., Ikehata, Y., and Matsunaga, N. 2011. Performance of the wave energy dissipation of a floating breakwater with truss structures and the quantification of transmission coefficients. *Journal of Coastal Research*, 27(4): 687-697.

Vantorre, M., Banasiak, R. and Verhoeven, R. 2004. Modelling of hydraulic performance and wave energy extraction by a point absorber in heave. *Applied Ocean Research,* 26: 61-72.

Vantorre, R., Banasiak, R., and Verhoeven, R. 2002., Extraction of sea wave energy: a mathematical evaluation of a point absorber in heave. In. Advances in Fluid Mechanics IV. Edited by Rahman, M., Verhoeven, R., and Brebbia, C.A. WIT Press, Ashurst Lodge, Southampton, SO40 7AA, UK.

Verhagen, H.J., d'Angremond, K., and Van Roode F.2009. Breakwaters and Closure dams. VSSD.

Vicinanza, D., Contestabile, P., Quvang Harck Nørgaard, J., and Lykke Andersen T. 2014. Innovative rubble mound breakwaters for overtopping wave energy conversion. *Coastal Engineering*, 88: 154-170.

Violeau, D. 2012. *Fluid mechanics and the SPH method: Theory and applications*. Oxford: Oxford University Press. ISBN: 0199655529.

Vyzikasa, T., Deshoulièresb, S., Girouxc, O., Bartona, M.. and Greavesa, D. 2017. Numerical study of fixed oscillating water column with RANS-type two-phase CFD model. *Renewable Energy*, 102(B): 294-305.

Wang, G., Ren, B., and Wang, Y. 2016. Experimental study on hydrodynamic performance of arc plate breakwaters. *Ocean Energy,* Vol:3. doi:10.1016/j.oceaneng.2015.11.016.

Wang, H.Y., and Sun, Z.C. 2010. Experimental study of a porous breakwater. *Ocean Engineering*. Article in press.

Waters, R., Rahm, M., Eriksson, M., Svensson, O., Strömstedt, E., Boström, C., Sundberg, J., and Leijon, M. 2011. Ocean wave energy absorption in response to wave period and amplitude – Offshore experiments on a wave energy converter. *IET Renewable Power Generation*, 5: 465-469.

Waveplam. 2009. D3.3 Wave Energy Pre-feasibility studies, European Union.

Wei, P., Lee, K.H., Shin, S.H., and Mizutani, N. 2013. Numerical simulation of interations between water waves and inclined-moored submerged floating breakwaters. Coastal Engineering. 82: 76-87.

Westphalen, J., Greaves, D.M., Hunt-Raby, A., Williams, C.J.K., Taylor, P.H., Hu, Z.Z., Causon, D.M., Mingham, C.G., Stansby, P.K., Rogers, B.D., and Omidvar, P. 2009. Numerical simulation of wave energy converters using Eulerian and Lagrangian CFD methods. *International Society of Offshore and Polar Engineers*, ISOPE-1-10-522.

Westphalen, J., Greaves, D.M., Raby, A., Hu., Z. Z., Causon, D. M., Mingham,C. G., Omidvar, P.,Stansby P. K., and Roger B. D. 2014. Investigation of wave-structure interaction using state of the art CFD techniques. *Open Journal of Fluid Dynamics*, 4: 18.

White, F.M.. 1999. Fluid mechanics, 4th edn. McGraw-Hill Singapore,

Williams, A.N., and Abul-Azm, A.G., 1997. Dual pontoon floating breakwater. *Ocean Engineering,* 24(5): 465-478.

Williams, A.N., Lee. H.S., and Huang, Z. 2000. Floating pontoon breakwaters. *Ocean Engineering,* 27(3): 221-240.

Wolgamot, H.A., and Fitzgerald, C.J. 2015. Nonlinear hydrodynamic and real fluid effects on wave energy converters. *Proceedings of the Institute of Mechanical Engineers Part A: Journal of Power and Energy,* 0(0): 1-23.

Wright, A., Beattie, W.C., Thompson, A., Mavrakos, S.A., Lemonis, G., Nielsen, K., Holmes B., and Stasinopoulos A. 2003. Performance considerations in a power take off unit based on a non-linear load. In: *Proceedings of the 5th European Wave Energy Conference.* Cork.

Yamamoto, T. 1981. Moored floating breakwater response to regular and irregular waves. *Applied Ocean Research*, 3(1): 27-36.

Yang, C., and Ertekin, R.C. 1991. Numerical simulation of wave energy focusing. In: *Proceedings of OCEANS '91: Ocean technologies and opportunities in the Pacific for the 90's.* 1, 10.1109 / OCEANS.1991.614024, Honolulu, Hawaii, USA.

Yavuz, H., McCabe, A., Aggidis, G., and Widden, M.B. 2006. Calculation of the performance of resonant wave energy converters in real seas. *Proceedings of the Institute of Mechanical Engineers, Part M: Journal of Engineering for the Maritime Environment*, 220(3): 117-128.

Yavuz, H., Stallard, T., McCabe, A., and Aggidis, G. 2007. Time series analysis-based adaptive tuning techniques for a heaving wave energy converter in irregular seas. *Proceedings of the Institution of Mechanical Engineers, Part A: Journal of Power and Energy*, 221(1): 77-90.

Yu, Y.H., and Li, Y. 2013. Reynolds-averaged Navier–Stokes simulation of the heave performance of a two-body floating-point absorber wave energy system. *Computational Fluids*, 73: 104-114.

Zanuttigh, B., and Angelelli, E. 2013. Experimental investigation of floating wave energy converters for coastal protection purpose. *Coastal Engineering*, 80: 148-159.

Zanuttigh, B., Martinelli, L., Castagnetti, M., Ruol, P., Kofoed, J.P., and Frigaard, P. 2010. Integration of wave energy converters into coastal protection schemes. In: *Proceedings of the 3rd international conference on ocean energy.* Bilbao, Spain.

Zhang, Y., Zou, Q.P., and Greaves, D. 2012. Air-water two phase flow modelling of hydrodynamic performance of an oscillating water column device. *Renewable Energy*, 41: 159-170.

Zhao, F. F., Kinoshita, T., Bao, W. G., Huang, L.Y., Liang, Z.L., and Wan, R. 2012. Interaction between waves and an array of floating porous circular cylinders. *China Ocean Engineering*, 26(3): 397-412.

Zhou, L., Chen, K., Zhai, S., Niu, Z., and Hu, X. 2014. Experimental study of the effects of different floating breakwater on wave absorbing. In: ASME, *Proceedings of the ASME 33rd international conference on ocean, offshore and arctic engineering*. ASME. V08BT06A047-V08BT06A047.

Appendices

Appendix 3A

A3.1 Time Domain Model

```
clc
clear
close all
%
==================================================
==================
%                   ---Mass Spring Damper System---
% Creates a structure (param) and values that correspond to properties
of
% (w=angular Frequency(rad/sec), m=mass(kg),c=dumping coefficient,
%             k=spring constant(N/m)and A=consrant )
%
==================================================
==================
% Angular frequency of waves, omega, in rad/sec (we will run the wave
at 1 Hz) (6.28 rad/sec)
param.wave_freq = (2*pi);
% Spring constant k, in N/m--rho*g*A = bouyncy stiffness 1020*9.81.1
param.buoy_stiff = 10006;
% Wave amplitude, A
param.wave_amp = 1;
matsize = 100;        % step size

%% First input
% Define n (fraction of natural frequency we're operating at)
resonance_fraction_vary = logspace(log10(0.25),log10(4),matsize);
% Work out omega from n
nat_freq_vary = param.wave_freq * resonance_fraction_vary;
% Work out mass m from natural freq and k
mass_vary = param.buoy_stiff ./ (nat_freq_vary.^2);

%% Second input
% damping ratio values between 0.01 to 5
damping_fraction_vary = logspace(-2,1,matsize+1);
% of the (critical damping=2*sqrt(k*m)( with 50 step size)
% wave hight
```

```
%% old
% m_vary = logspace(log10(16),log10(4e3),matsize);        % mass (kg) values between 16kg to 4000kg with 50 step size
% % for max mass resonance frequency (w) = 1/4 *6.28 =1.6 rad/sec---->...
% % at this frequency the mass calculate (w^2=k*m)--->m=k/w2 10006/1.6^2=4000 kg
% % for min mass resonance frequency (w) = 4 *6.28 =25 rad/sec---->...
% % at this frequency the mass calculate (w^2=k*m)--->m=k/w2 10006/25^2=16 kg

%% Initial conditions
y_0     = 0;                    % Initial displacement y(t)
y_dot_0 = 0;                    % Initial Velocity y_dot(t)
E_dot_0 = 0;                    % Initial E, E_dot(t)
Y_0 = [y_0,y_dot_0,E_dot_0];      % from vector(array)of initial

%% Initialise variables
Power                                                                   = zeros(length(resonance_fraction_vary),length(damping_fraction_vary));
% Create an array



trange = [0,60];

%% Do the loops
for L1 = 1:length(resonance_fraction_vary)

    % Get the value of omega_n and m we're using in this loop
    param.nat_freq = nat_freq_vary(L1);
    param.mass = mass_vary(L1);

    for L2 = 1:length(damping_fraction_vary)
        damping_frac = damping_fraction_vary(L2);

        critical_damping = 2*sqrt(param.buoy_stiff*param.mass);

        % C1 * critical damping (*2*sqrt*param.k*param*m)
        param.c_1 = damping_frac*critical_damping;
        % radiation damping (c_2* critical damping) - We going
        % to use 4 different values for c_2 (0.01, 0.1, 0.5, 1)
        param.c_2 = 0.05*critical_damping;


        %% Run ODE

        fprintf('Calculating %i of %i, %i of %i\n',...
```

```
        L2,length(damping_fraction_vary),...
        L1,length(resonance_fraction_vary));

    [T,y]=ode45(@(t,y)spring_v8(t,y,param),trange,Y_0,...
        odeset('Refine',10) );

    x = param.wave_amp*cos(param.wave_freq*T);          % reference
point  motion  (given)
    f = (param.buoy_stiff)*(y(:,1) - x);           % restoring Force = (k)
*displacement ( y – x )
    z =     y(:,1);                  % displacement y(t)
    z_dot = y(:,2);                    % Velocity y_dot(t)
    E_dot = y(:,3);                    % Energy in system (Joules)

    Power(L1,L2)=max(E_dot);


  end
end
%% Plot graphs


figure(1);                      % reference point-displacemet (t)
plot(T,x,'r',T,z,'b')
xlabel('time')
ylabel('Displacement-reference point')
legend({'ref. point motion','Buoy y-position'})
hold all
%
% figure(2)
% plot(T,z_dot)
% xlabel('time')
% ylabel('Velocity')
%
figure(2);                      % plot force (t)
plot(T,f); ylabel('Force (N)')
hold all
grid on
%
% figure(3);                      % plot power (t)
% plot(T,E_dot); ylabel('power in system (W)')
% hold all
% grid on
% %
% [m_plot,c_plot] = meshgrid(mass_vary,damping_fraction_vary);     %
create the grid for the 3-D plot

figure('Name','Mass vs crit frac')
surf(mass_vary,damping_fraction_vary,Power','FaceColor','interp','Face
Lighting','phong')
```

```
xlabel('Mass (Kg)'); set(gca,'XScale','log');
ylabel('Fraction of critical damping coefficient');  set(gca,'YScale','log');
zlabel('Power(W)');
grid on

figure('Name','Resonance frac vs crit frac')
surf(resonance_fraction_vary,damping_fraction_vary,Power','FaceColor
','interp','FaceLighting','phong')
xlabel('Fraction of natural frequency'); set(gca,'XScale','log');
ylabel('Fraction of critical damping coefficient');  set(gca,'YScale','log');
zlabel('Power(W)');
grid on

figure('Name','Contour');
[C,h]                                                                    =
contour3(resonance_fraction_vary,damping_fraction_vary,Power',...
    (0:0.25:2.5)*1e5);
set(h,'linewidth',2); clabel(C);
xlabel('Fraction of natural frequency'); set(gca,'XScale','log');
ylabel('Fraction of critical damping coefficient');  set(gca,'YScale','log');
zlabel('Power(W)');
grid on; view([0,90]);

% figure(5); clf; hold on;
%
mesh(m_plot,c_plot,Power,'EdgeColor',[0.5,0.5,0.5],'FaceColor','none')
% [conts,h] = contour3(m_plot,c_plot,Power);
% set(h,'LineWidth',2); clabel(conts);
% xlabel('Mass (N/m)'); set(gca,'XScale','log');
% ylabel('Damping coefficient(Ns/m)');  set(gca,'YScale','log');
% zlabel('Average Power(W)');
% grid on
%
%
```

A3.2 Steady-State Harmonic Model

```
clc;
clear all;
close all;

syms c_2 positive % Include assumption that c2 is positive

k = 10006;
w = 2*pi;
m = k/w^2;
% m = 500;

% Critical damping
cd =  2*sqrt(k*m);
% Set of c2 points for plotting
c_2set = cd * logspace(-8,8,2e3)';

c_1 = (k/w);

% Power equation
power = (c_1*(k^2+w^2*c_2.^2)) ./ ...
  ((k-w^2*m)^2+w^2*(c_1+c_2).^2);

% Differentiate function wrt c2
power_diff = diff(power,c_2);

% Finding peak
% Solve differentiated function
peak = solve(power_diff==0);

fprintf('The peak is at c2 = ');

% Plot a graph
figure
pset1 = eval(subs(power,c_2,c_2set));
subplot(2,1,1), plot(c_2set,pset1); hold on;
set(gca,'xscale','log'); xlabel('c_2'); ylabel('Power');

% Plot graph of differentiated function
pset2 = eval(subs(power_diff,c_2,c_2set));
subplot(2,1,2), plot(c_2set,pset2); hold on;
set(gca,'xscale','log'); xlabel('c_2'); ylabel('Power diff');

% Find the actual value of the peak
peak_pt = eval(peak);
fprintf('%s\b\b\n', sprintf('%g, ',peak_pt))
```

```
% Plot it on the graphs
minimum_power = eval(subs(power,c_2,peak_pt));
subplot(2,1,1), plot(peak_pt,minimum_power,'r+');
subplot(2,1,2), plot(peak_pt,eval(subs(power_diff,c_2,peak_pt)),'r+');

% Finding near-peak region
% Find values of power at very high or very low damping
power_caps(1) = limit(power,c_2,0);
power_caps(2) = limit(power,c_2,Inf);

power_cap_vals = eval(power_caps);
fprintf('Power caps are %g and %g\n',power_cap_vals(1),power_cap_vals(2));
% Find lower of those two
baseline = min(power_cap_vals);
% Find c2 values when power is 90% of the way from the minimum to the baseline
bad_region = solve(power == minimum_power + 0.99*(baseline-minimum_power));
% Find the actual value of the peak
bad_reg_vals = sort(eval(bad_region));
% Display the results
fprintf('Bad region is from %g to %g\n',bad_reg_vals(1),bad_reg_vals(2));

% Plot it on the graphs
subplot(2,1,1),
plot(bad_reg_vals,eval(subs(power,c_2,bad_reg_vals)),'ro-');
subplot(2,1,2),
plot(bad_reg_vals,eval(subs(power_diff,c_2,bad_reg_vals)),'ro');



figure
pset1 = eval(subs(power,c_2,c_2set));
plot(c_2set,pset1); hold on;
set(gca,'xscale','log'); xlabel('c_2 (N/m)'); ylabel('Power Extraction Rate (Ws^-^1)');
plot(peak_pt,minimum_power,'r+')
plot(bad_reg_vals,eval(subs(power,c_2,bad_reg_vals)),'ro-')
```

A3.3 Verification of Steady-State Harmonic Model

```
clc
 close all
clearvars

set(0, 'DefaultFigureWindowStyle', 'docked');
%
% % % % Theoretical case:
w =   2*pi  ;     % wave freq
k =   10006 ;     % buoy stiffness
m =   k/w^2   ;     % mass (kg)
%c1 = logspace(log10(1e-0),log10(1e10),1000);
 c1 = (k/w);
 c2 = logspace(log10(1e-2),log10(1e8),500);
%c2 = 6.338*10^5;

% % Theoretical case:
% D = 0.3125;
% k = (pi*D^2)/4*9.81*1000;
% w = (2*pi);
% m = k/(w^2);
% cd = 2*sqrt(k*m);
% c1 = logspace(log10(1e-8),log10(1e10),1000);
% c2 = 0.1;

% Physical case:
% D = 0.3125;
% k = (pi*D^2)/4*9.81*1000;
% w = (2*pi)/1;
% m = 11.63;
% cd = 2*sqrt(k*m);
% c2 = 0.159*cd;
% c1 = logspace(log10(1e-3),log10(1e7),500);

if ( length(c1)==1 && length(c2)==1 )
    error('Need a spread of values for c1 or c2');
elseif ( length(c1)~=1 && length(c2)~=1 )
    error('Both spread of values for c1 and c2 not possible with this code
yet');
end

if (length(c1)==1)

    for i3 = 1:length(c2)
        power.analytical(i3)                                          =
function_analytical_changing_one_variable(m,w,k,c1,c2(i3),'c2');
         %power.differentiated(i3)                                    =
function_differentiated_changing_one_variable(m,w,k,c1,c2(i3),'c2');
```

```
        fprintf('Calculated %i out of %i\n',i3,length(c2));
    end

elseif(length(c2)==1)

    for i3 = 1:length(c1)
        power.analytical(i3)                                                    =
function_analytical_changing_one_variable(m,w,k,c2,c1(i3),'c1');
         %power.differentiated(i3)                                              =
function_differentiated_changing_one_variable(m,w,k,c2,c1(i3),'c1');
        fprintf('Calculated %i out of %i\n',i3,length(c1));
    end
end

% Plot the power from the analytical system
figure(1);
if (length(c1)==1)
    semilogx(c2,power.analytical);
    xlabel('c2');
elseif(length(c2)==1)
    semilogx(c1,power.analytical);
    xlabel('c1');
end
ylabel('Power analytical (W)');

% Plot the power from the differentiated system
figure(2);
if (length(c1)==1)
    semilogx(c2,power.differentiated);
    xlabel('c2');
elseif(length(c2)==1)
    semilogx(c1,power.differentiated);
    xlabel('c1');
end
ylabel('Power differentiated (W)');
```

A3.3.1 Steady-State Harmonic

```
function                                power                                   =
function_analytical_changing_one_variable(m,w,k,fixed,vect,varying)

%syms c_2 positive % Include assumption that c2 is positive

%=========================================
% c1f=1;
% c2f=1;
% m=253;
%=========================================
```

```
switch varying
    case 'c1'
        c_1 = vect;
        c_2 = fixed;
    case 'c2'
        c_1 = fixed;
        c_2 = vect;
    otherwise
        error('Must specify either c1 or c2');
end

% % Displacement
u=1;
Q = ( (k+1i*w*c_2)*u ) / ( (-m*w^2) + (c_1+c_2)*(1i*w) + k );

% Power equation
power = 0.5*c_1*w^2*abs(Q)^2;
% power = 0.5 * ((w^2*c_1*k^2)/((w^2*c_1^2)+k^2))*u^2;
%       power       =       abs(       0.5*c_1*w^2*((k^2+(w^2*c_2^2))/((k-
(w^2*m)^2)+w^2*(c_1+c_2)^2))*u^2 );

save all_values k c_1 c_2 Q power
```

A3.3.2 Time Domain

```
function                                power                                =
function_differentiated_changing_one_variable(m,w,k,fixed,vect,varying
)
% clc
% clear all
% close all
%
% m=253;
% c2f=1;
% c1f=1;

switch varying
    case 'c1'
        c1 = vect;
        c2 = fixed;
    case 'c2'
        c1 = fixed;
        c2 = vect;
    otherwise
        error('Must specify either c1 or c2');
end

param.mass = m;
```

```
damping_frac = c1*w/k;

%================================================
====================
%================================================
=======

param.wave_freq = w;
param.buoy_stiff = k;
param.wave_amp = 1;

nat_freq_vary = sqrt(param.buoy_stiff / param.mass);
resonance_fraction_vary = nat_freq_vary / param.wave_freq;

param.c_1 = c1;


%% Initial conditions
y_0     = 0;              % Initial displacement y(t)
y_dot_0 = 0;                % Initial Velocity y_dot(t)
E_0 = 0;                  % Initial E, E(t)
Y_0 = [y_0,y_dot_0,E_0];      % from vector(array)of initial

% C1 * buoy_stiff(10006)/wave_freq(6.28)
param.c_1 = damping_frac*(param.buoy_stiff/param.wave_freq);

% radiation damping (C2* critical damping) - We going
% to use 5 different values for c_2 (0.01,0.05,0.1,0.5,1)
param.c_2 = c2;

%% Run ODE
%
% fprintf('Calulating %i of %i, %i of %i\n',...
%   L2,length(damping_fraction_vary),...
%   L1,length(resonance_fraction_vary));

T_max=60;
T_step = 0.001;
trange = (0:T_step:T_max)';
saad_options = odeset();
saad_options = odeset('RelTol',1E-6);

[T,y]=ode45(@(t,y)spring_v8(t,y,param),trange,Y_0,saad_options);

x = param.wave_amp*cos(param.wave_freq*T);     % reference point
motion  (given)
f = (param.buoy_stiff)*(y(:,1) - x);              % restoring Force = (k)
*displacement ( y – x )
z =     y(:,1);                    % displacement y(t)
z_dot = y(:,2);                      % Velocity y_dot(t)
```

```
E = y(:,3);                          % Energy in system (Joules)

nstep_cycle = 1/T_step;   % Number of steps in 1 cycle.
ncycles     = 10;         % Number of cycles.
power = (E(end)-E(end-(ncycles*nstep_cycle)))/ncycles;
% plot(T,x,'r',T,z,'b')

save simudata T y power


end
```

A3.4 Steady-State Harmonic Model Optimisation

```
clc
clear
% close all
%
==================================================
==================
%                    ---Mass Spring Damper System---
% Creates a structure (param) and values that correspond to properties
of
% (w=angular Frequency(rad/sec), m=mass(kg),c=dumping coefficient,
%            k=spring constant(N/m)and A=consrant )
%
==================================================
==================
% Angular frequency of waves, omega, in rad/sec (we will run the wave
at 1 Hz) (6.28 rad/sec)
param.wave_freq = (2*pi);
% Spring constant k, in N/m--rho*g*A = bouyncy stiffness 1020*9.81.1
D = 0.3125;
Area = pi*D*D/4;
param.buoy_stiff = Area*9.8106*1000;
param.mass = param.buoy_stiff/(param.wave_freq^2);
%param.mass = 19.1;

 param.buoy_stiff = 10006;
 param.mass = param.buoy_stiff/param.wave_freq^2;
 param.mass = param.mass + param.mass*0.1;
%
% % Wave amplitude, A
param.wave_amp = 1;
matsize = 100;        % step size

cd = 2*sqrt(param.buoy_stiff * param.mass);

%% First input
% Define n (fraction of natural frequency we're operating at)
C1_vary = cd * logspace(-8,8,matsize);
% C1_vary = logspace(log10(1e-4),log10(1e10),1000);

%% Second input
% damping ratio values between 0.1 to 5
% of the (buoy_stiff/wave_freq)( with 11 step size)
C2_vary = cd * logspace(-8,8,matsize);
% C2_vary = [0.01 0.02];
```

```
%%old
% m_vary = logspace(log10(16),log10(4e3),matsize);       % mass (kg) values between 16kg to 4000kg with 50 step size
% % for max mass resonance frequency (w) = 1/4 *6.28 =1.6 rad/sec---->...
% % at this frequency the mass calculate (w^2=k*m)--->m=k/w2 10006/1.6^2=4000 kg
% % for min mass resonance frequency (w) = 4 *6.28 =25 rad/sec----->...
% % at this frequency the mass calculate (w^2=k*m)--->m=k/w2 10006/25^2=16 kg

%% Initialise array for powers
Power = zeros(length(C1_vary),length(C2_vary));          % Create an array

%% Do the loops
for L1 = 1:length(C1_vary)
    % Get the value of omega_n and m we're using in this loop
    % param.nat_freq = nat_freq_vary(L1);

    param.c_1 = C1_vary(L1);

    for L2 = 1:length(C2_vary)
        param.c_2 = C2_vary(L2);


        %% Run ODE

        fprintf('Calulating %i of %i, %i of %i\n',...
            L2,length(C2_vary),...
            L1,length(C1_vary));

        k  = param.buoy_stiff;
        w  = param.wave_freq;
        m  = param.mass;

        % Critical damping
        cd =  2 * sqrt(k * m);

        % Set of c1 points for plotting
        c_1 = param.c_1;

        % Set of c2 points for plotting
        c_2 = param.c_2;

        % % Displacement
        u=1;
        Q = ( (k+1i*w*c_2)*u ) / ( (-m*w^2) + (c_1+c_2)*(1i*w) + k );
```

```
        % Power equation
        Power(L1,L2)=0.5*c_1*w^2*abs(Q)^2;

    end
end

maxPowerForEachC2 = zeros(1,size(Power,2));
c1ForMaxPowerForEachC2 = zeros(1,size(Power,2));
for c=1:length(maxPowerForEachC2);
    [maximum,ind] = max(Power(:,c));
    maxPowerForEachC2(c) = maximum;
    c1ForMaxPowerForEachC2(c) = C1_vary(ind);
end

%% Plot graphs
figure('Name','c1 vs c2 vs Power')
surf(C1_vary,C2_vary,log(Power)','FaceColor','interp','FaceLighting','ph
ong')
xlabel('c1'); set(gca,'XScale','log');
ylabel('c2');  set(gca,'YScale','log');
zlabel('log(Power(W))');
grid on
%
% figure('Name','Resonance frac vs crit frac')
%
surf(resonance_fraction_vary,damping_fraction_vary,Power','FaceColor
','interp','FaceLighting','phong')
% xlabel('Fraction of natural frequency'); set(gca,'XScale','log');
%     ylabel('Fraction     of     buoy_stiff(10006)/wave_freq(6.28)(C_1)');
set(gca,'YScale','log');
% zlabel('Power(W)');
% grid on
%
figure('Name','Contour of c1 vs c2 vs Power');
[C,h] = contour(C1_vary,C2_vary,Power',...
    (0:0.05:2.5)*1e5);
set(h,'linewidth',2);
xlabel('c1 (N/ms^-^1)'); set(gca,'XScale','log');
ylabel('c2 (N/ms^-^1)');  set(gca,'YScale','log');
zlabel('Power(W)');
clabel(C,'manual');
% grid on; view([0,90]);

figure('Name','c1 vs Power');
plot(c1ForMaxPowerForEachC2,log(maxPowerForEachC2));
set(h,'linewidth',2);
xlabel('c1 (N/ms^-^1)'); set(gca,'XScale','log');
ylabel('log(Power(W))');

figure('Name','c1 vs c2');
```

```
plot(c1ForMaxPowerForEachC2,C2_vary);  hold on;
plot(c1ForMaxPowerForEachC2,C2_vary,'*');  hold off;
% loglog(c1ForMaxPowerForEachC2,C2_vary);
set(h,'linewidth',2);
xlabel('c1 (N/ms^-^1)'); set(gca,'XScale','log','YScale','log');
ylabel('c2 (N/ms^-^1)');

figure(5); clf; hold on;
mesh(m_plot,c_plot,Power,'EdgeColor',[0.5,0.5,0.5],'FaceColor','none')
[conts,h] = contour3(m_plot,c_plot,Power);
set(h,'LineWidth',2); clabel(conts);
xlabel('Mass (N/m)'); set(gca,'XScale','log');
ylabel('Damping coefficient(Ns/m)');  set(gca,'YScale','log');
zlabel('Average Power(W)');
grid on


figure('Name','Mass vs C2')
surf(mass_vary,c_2','FaceColor','interp','FaceLighting','phong')
xlabel('Mass (Kg)'); set(gca,'XScale','log');
ylabel('C2');  set(gca,'YScale','log');
zlabel('Power(W)');
grid on
%
% maxpower = max(Power(:));
% [r,c] = find(Power==maxpower);
% fprintf('\nMax Power = %g W at damping fraction C_2 = %g and
mass = %g kg\n',...
%     maxpower,param.c_2,mass_vary(r));
```

Appendix 4A: Hydraulic Motor Calculation

The motor tests were conducted with an "open-circuit" (i.e. nothing was connected to its terminals) and a “short-circuit” (i.e. all terminals connected together) arrangement. From the difference between the two tests, the torque arising from the electrical current can be computed. The calculation is based on the assumption that the airgap torque due to the electrical current behaves like a pure damper.

Table 4A.1: Motor damping

Time (s)	Reading 1	Reading 1	Reading 1	Average
Damping	653	652	641	648.67 s
No damping	3.38	3.05	2.89	3.11 s

With Damping (everything connected)

Weight = 0.751 kg

Distance = 1.16 m

Velocity = distance/time = 1.16/648.67 = 0.0018 m/s

Force = m × g = 7.51 N and therefore

Damping constant = Force/ Velocity = 7.51/0.0018 = 4172 Ns/m.

Without damping (nothing is connected)

Weight = 0.751 kg

Distance= 1.16 m

Velocity = distance/time = 1.16/3.11 = 0.37 m/s

Force = m × g = 7.51 N and therefore

Damping constant = Force/Velocity = 7.51/0.0018 = 20.13 Ns/m.

Table 4A.2: Buoyancy force

Dimension (scale 1:16)	Prototype m	Model (scale 1:16) mm	Model (scale 1:16) m
Cylinder diameter (D)	5 m	312.5 mm	0.3125 m
Cylinder radius (r)	2.5 m	156.25 mm	0.156 m

The middle of the wave period range = 1 s, wave frequency = 1 Hz = 6.28 rad/s.

Maximum wave amplitude relative to the buoy = 9 cm = 0.09 m (peak-to-peak)

Buoy diameter = 0.3125 m

Water plane cross sectional area of buoy, $A = \pi r^2$

$= 3.14 \times (0.156)^2 = 0.0767\ m^2$

Maximum amount of submerged volume = cross sectional area of buoy $\times$ Maximum amplitude $= 0.0767 \times 0.09 = 0.0069\ m^3$

Buoyancy force = $\rho\ g\ V = 1000 \times 9.81 \times 0.00688 = 67$ N

Velocity = wave height $\times$ w = $0.09 \times 6.28 = 0.565$ m/s

Ratio of force/ velocity = 67/0.565 = 118.6 Ns/m

Optimum damping = 118.6 /2 = 59.3 Ns/m or approximately 60 Ns/m.

Multi-meter

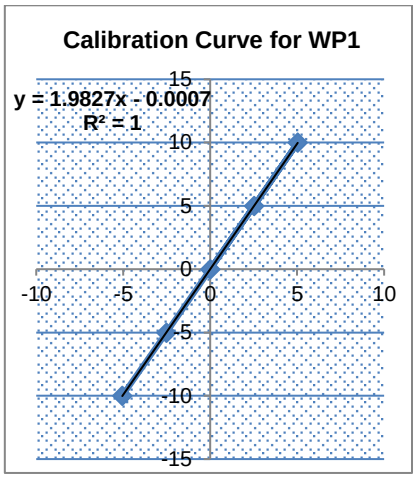
Resistance across motor terminals is measured. Three resistors (R) were connected in parallel: $R_1 = 3\Omega$, $R_2 = 3\Omega$ and $R_3 = 3\Omega$.

All three resistors were fully shorted together with a 2 m drop for maximum damping of the motor. For resistors in parallel, the equivalent circuit resistance R_T is:

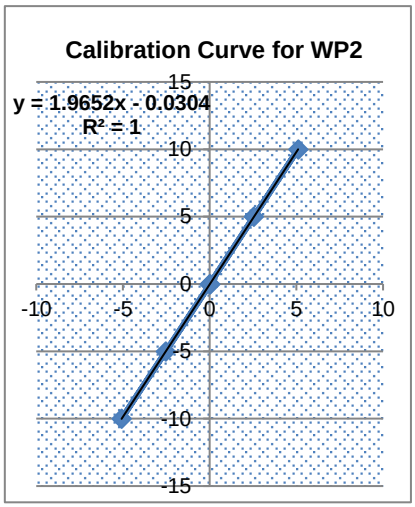
$R_T = 1/3+1/3+1/3=1\ \Omega$

Appendix 4B: Calibration Data For Waveprobes 1-6

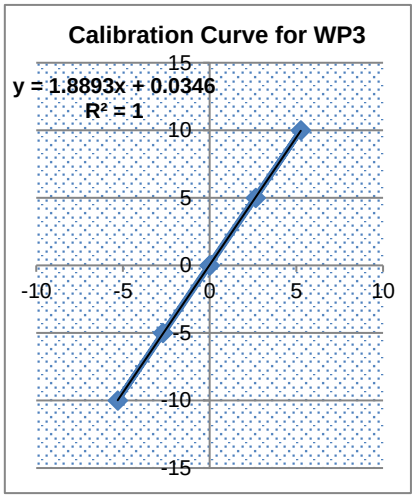
Calibration data WP1		
Volt Avg (V)	Displacement (cm)	Volt Stdv (V)
0.00	0.00	0.0005
2.53	5.00	0.0006
5.03	10.00	0.0012
-2.51	-5.00	0.0006
-5.05	-10.00	0.0005



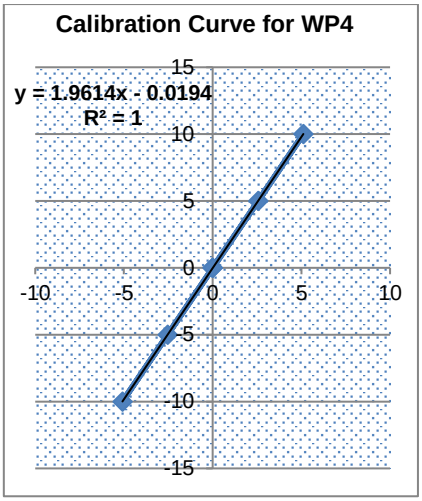
Calibration data WP2		
Volt Avg (V)	Displacement (cm)	Volt Stdv (V)
0.00	0.00	0.0005
2.55	5.00	0.0016
5.10	10.00	0.0007
-2.53	-5.00	0.0006
-5.08	-10.00	0.0004
0.04	0.00	0.0007



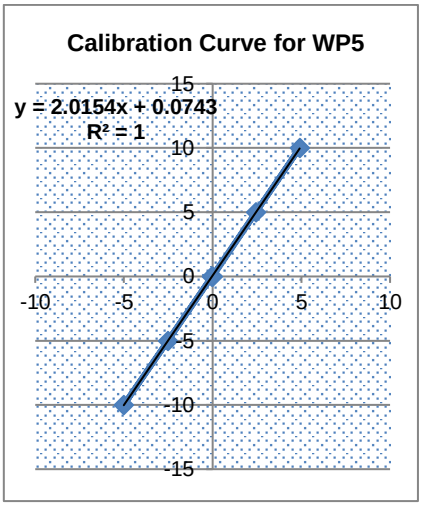
Calibration data WP3		
Volt Avg (V)	Displacement (cm)	Volt Stdv (V)
-0.01	0.00	0.0024
2.65	5.00	0.0013
5.26	10.00	0.0007
-2.70	-5.00	0.0016
-5.30	-10.00	0.0012
0.00	0.00	0.0014



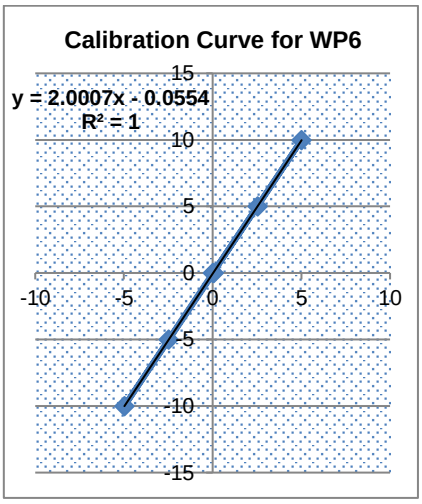
Calibration data WP4		
Volt Avg (V)	Displacement (cm)	Volt Stdv (V)
-0.01	0.00	0.0006
2.56	5.00	0.0006
5.11	10.00	0.0006
-2.53	-5.00	0.0008
-5.09	-10.00	0.0009
0.01	0.00	0.0008



Calibration data WP5		
Volt Avg (V)	Displacement (cm)	Volt Stdv (V)
0.00	0.00	0.0005
2.45	5.00	0.0006
4.91	10.00	0.0006
-2.53	-5.00	0.0007
-5.01	-10.00	0.0007
-0.04	0.00	0.0006

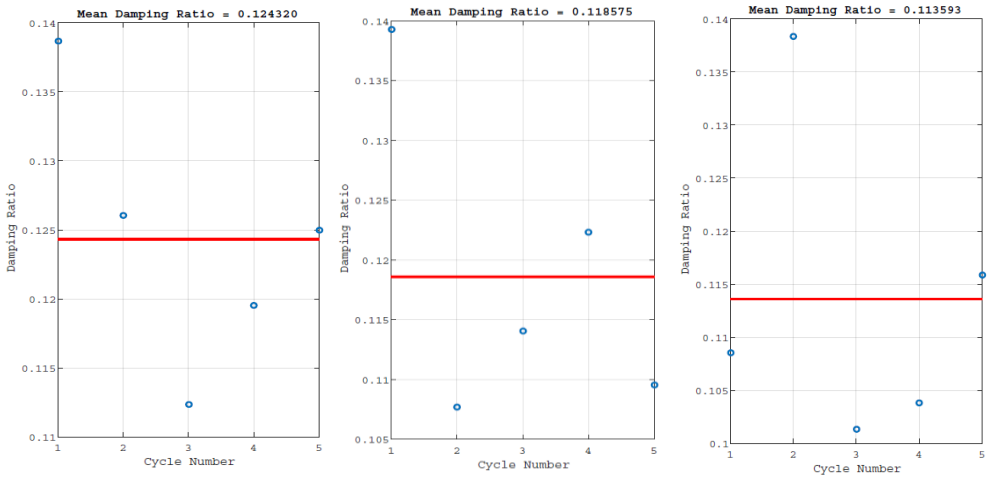


Calibration data WP6		
Volt Avg (V)	Displacement (cm)	Volt Stdv (V)
0.01	0.00	0.0006
2.54	5.00	0.0005
5.01	10.00	0.0008
-2.48	-5.00	0.0004
-4.97	-10.00	0.0007
0.06	0.00	0.0007



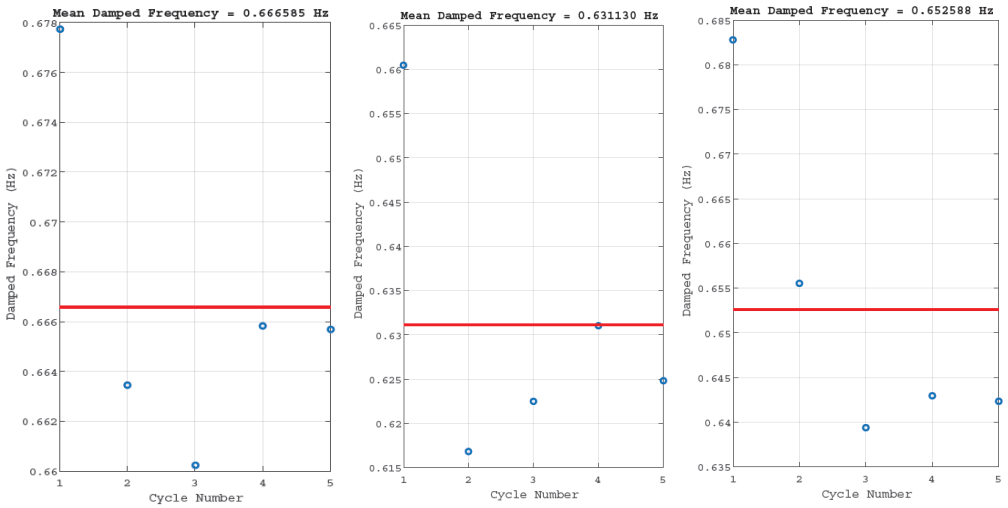
*Note: the voltage readings were taken again for a value of zero to account for any shift in the voltage reading at the start.

Appendix 4C: Decay Test Results For Each Buoy Shape



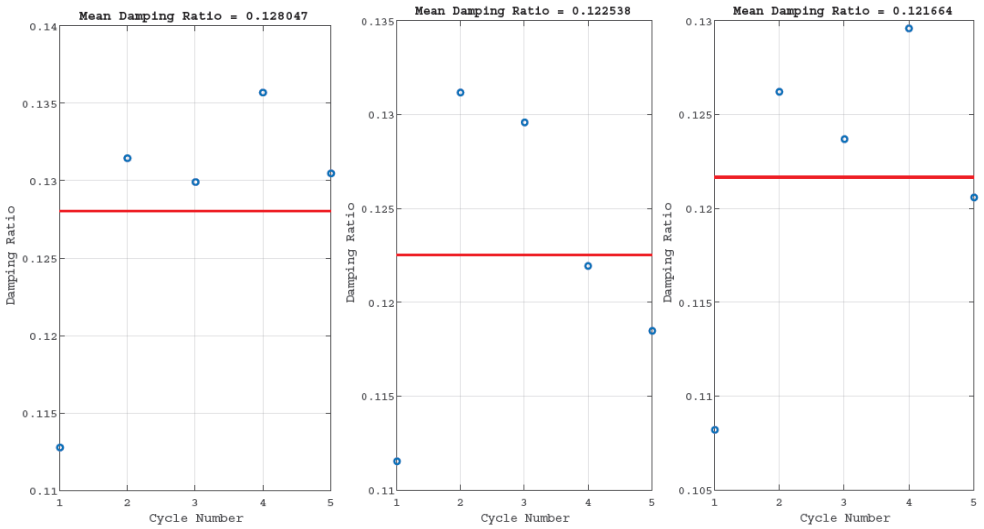
(a) Zero Damped (b) Damped (c) Extra Damped

Fig. 4D-a: Damping ratio profiles for the bullet buoy



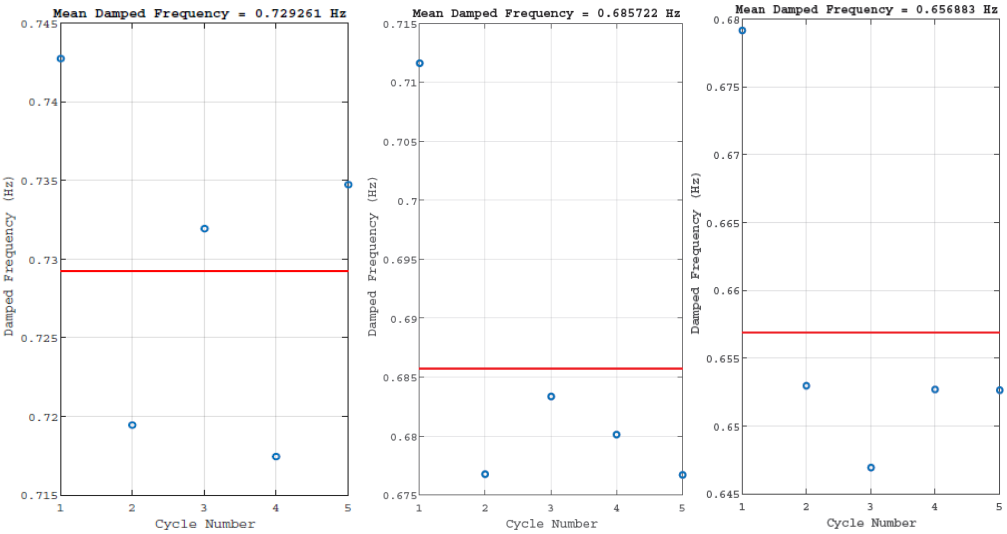
(a) Zero Damped (b) Damped (c) Extra Damped

Fig. 4D-b: Damped frequency profiles for the bullet buoy



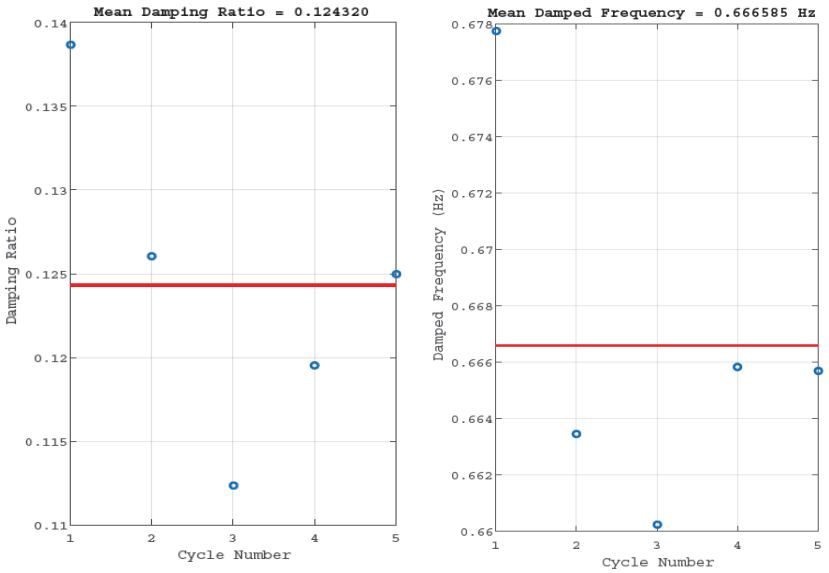
(a) Zero Damped (b) Damped (c) Extra Damped

Fig. 4D-c: Damping ratio profiles for the spike buoy



(a) Zero Damped (b) Damped (c) Extra Damped

Fig. 4D-d: Damped frequency profiles for the spike buoy



(a) Damping Ratio (b) Damped Frequency

Fig. 4D-e: Damping ratio profiles for the zero damped bi-cone buoy